School of Mechanical Engineering - University of Leeds
Thermo-Fluids System - Rolls Royce plc.

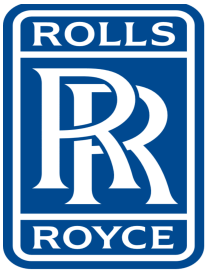

Turbine Stator Well Heat Transfer and Design Optimisation Using Numerical Methods

by

Julien Pohl

Submitted in accordance with the requirements for the degree of Doctor of Philosophy

The University of Leeds

School of Mechanical Engineering

September 2016

Intellectual Property and Publication Statements

The candidate confirms that the work submitted is his own, except where work which has formed part of jointly authored publications has been included. The contribution of the candidate and the other authors to this work has been explicitly indicated below. The candidate confirms that appropriate credit has been given within the thesis where reference been made to the work of other.

The work of modeling the deflector plate geometry in Secs. 5.1 and 5.2 of the thesis has appeared in the publication as follows:

Turbine Stator Well Cooling - Improved Geometry Benefits, June 2015, J. Pohl and V. Fico and J. A. Dixon.

I was responsible for the FEA and CFD modeling of the deflector plate geometry and for writing the paper. The contribution of the other authors was technical supervision and the revision of the paper.

The work of parametrising the deflector plate geometry and setting up the optimisation in Sec. 5.3 of the thesis has appeared in the publications as follows:

Innovative Turbine Stator Well Design Using Design Optimisation, April 2016, J. Pohl, H. M. Thompson, R. C. Schlaps, S. Shahpar, V. Fico and G. A. Clayton

Innovative Turbine Stator Well Design Using a Kriging Assisted Optimisation Method, October 2016, J. Pohl, H. M. Thompson, R. C. Schlaps, S. Shahpar, V. Fico and G. A. Clayton

I was responsible for the reduction of the model size, the parametrisation of the deflector plate geometry, the implementation into the automatic meshing system and the writing the paper. The contribution of Ralf Schlaps was the technical support in setting up the optimisation setup and successfully implementing it into the Rolls-Royce SOPHY system. The other authors guaranteed technical supervision and the revision of the paper.

The work in Secs. 6.2 and 6.3 of the thesis has appeared in the publication as follows:

Turbine Stator Well Cooling - Improved Geometry Benefits, June 2015, J. Pohl and V. Fico and J. A. Dixon.

I was responsible for the modeling, the computations, the presented comparison between the different models and for writing the paper. The contribution of the other authors was technical supervision and the revision of the paper.

The work in Chap. 7 of the thesis has appeared in the publications as follows:

Structural Deflection's Impact in Turbine Stator Well Heat Transfer, June 2016, J. Pohl, H. M. Thompson, A. Guijarro Valencia, G. López Juste, V. Fico and G. A. Clayton

Structural Deflection's Impact in Turbine Stator Well Heat Transfer, September 2016, J. Pohl, H. M. Thompson, A. Guijarro Valencia, G. López Juste, V. Fico and G. A. Clayton

I was responsible for the modeling, the computations, the presented comparison between the different models and for writing the paper. The contribution of the other authors was technical supervision and the revision of the paper.

The work in Chap. 8 of the thesis has appeared in the publications as follows:

Innovative Turbine Stator Well Design Using Design Optimisation, April 2016, J. Pohl, H. M. Thompson, R. C. Schlaps, S. Shahpar, V. Fico and G. A. Clayton

Innovative Turbine Stator Well Design Using a Kriging Assisted Optimisation Method, October 2016, J. Pohl, H. M. Thompson, R. C. Schlaps, S. Shahpar, V. Fico and G. A. Clayton

I was responsible for the conduction of the optimisation, the interpretation of the results, the validation of the outcome and for writing the paper. The contribution of Ralf Schlaps was the technical support in supervising the optimisation and post-processing the results. The other authors guaranteed technical supervision and the revision of the paper.

Acknowledgement

The research project has been funded by the European Commission within the AMEDEO EU initial training network (grant reference 316394). The results presented in this thesis are the outcome of the collaboration between industry and academia, between ROLLS-ROYCE plc. in Derby, Thermo-Fluids Methods Team, and the UNIVERSITY OF LEEDS, School of Mechanical Engineering.

First I would like to thank my mentoring Professor, Harvey THOMPSON, for his guidance through the complete research project, his valuable input to technical discussions and his constructive criticism to some of my unorthodox ideas, all with the goal of realising a successful project.

Then, I would like to thank Jeffrey DIXON as industrial supervisor and for bringing the research project into being. I appreciate it a lot that after his retirement, which was half way through the project, he still continued supervising my work. He reviewed every conference paper, listened to my presentations and also read my thesis before submission, all in his very valuable spare time.

Furthermore, I would also like to thank the European Commission and ROLLS-ROYCE again for their support within the Framework 6 Programme, Research Project MAGPI, AST5-CT-2006-030874 and for the use of the acquired test data, which was used during the numerical validation process.

Special thanks goes to Antonio GUIJARRO VALENCIA, who was my first principle technical supervisor at ROLLS-ROYCE, before he moved to the 'dark side'. He 'patiently' introduced me to the acquired MAGPI data and the ROLLS-ROYCE in-house tools HYDRA and SC03.

I would like to thank Vincenzo FICO from ROLLS-ROYCE for his support after Antonio left. First of all, I could always count on his CFD expertise and academical experience. Second of all he introduced me to the science of Italian coffee, covering every possible variations in the preparation process including the roasting and grinding.

This brings me to the coffee club, who I owe a dept of gratitude for having so many funny and distracting 'technical' conversations, which always gave me new inspiration and courage for my work. Especially, I would like to mention the coffee club representative and continuous improvement expert Alessio LENZI for his (sometimes) unintentional entertainment. But also I would like to thank Christian FERRAT and Jaime TERRON who both gave always valuable input to the discussions.

A special mention must be made to ROLLS-ROYCE colleagues in the Thermo-Fluids Methods Team, such as Christopher BARNES and Cath KIDRED for their technical support and advice using the relevant in-house software packages. Thank you to my line manager Gary CLAYTON for taking over the organisational supervision from Jeff at ROLLS-ROYCE and for hosting me in his team.

I would also like to thank the CFD Methods Team at ROLLS-ROYCE, who were always helpful to incorporate special features in their codes, which were necessary for my research. Amongst others, I would like to thank Shahrokh SHAHPAR, Stefano CALONI, Alain LEMOIGNE, Ralf TILCH, David RADFORD and Indi TISNANTO.

During my spare time I joined the ROLLS-ROYCE Badminton Club, where I met plenty of nice guys who introduced me to the English life and culture. Special thanks goes to Nigel COOK and Jake ORCHARD who explored the English cuisine in the Derbyshire area with me, to proof that there is more than Fish & Chips in the UK. I would also like to thank my team members Nick TRANTER, Ed CHRAYAH, Colin WHITAKER, Matt ARMSON and Simon SHAW, who made it very enjoyable to be in the UK.

The whole AMEDEO would not have been successful without our project manager Juliet JOPSON, who did a fantastic job in organising all trainings and meetings. Furthermore, she organised most of my business trips during the project. That is why I would like to thank her a lot.

I would also like to thank the complete AMEDEO consortium with all its early stage researchers and supervisors. We had such a good time during all our meetings and trainings, where we were able to exchange our research progress and benefit from each others knowledge.

In this context, I would also like to thank Tom VERSTRAETE from the VKI for giving me the opportunity to spend a couple of days at his research institute for a secondment on conjugate heat transfer in turbomachinery.

Special thanks goes to my (former) house mates and AMEDEO colleagues Samuel DUCKIT and Ralf SCHLAPS. We had a very good time together outside from work, where we were able to explore Derby and surroundings.

Certainly I would like to thank my family: my parents and my brother for their motivation and for supporting me spiritually throughout my whole life.

Finally, I would like to thank my girlfriend Hannah BONNIE for her motivation by her positive way of thinking and her belief in me. She gave me always courage in hard times and fully supported my work during the last few years. Special thanks goes to her parents as well, for all the nice weekends we had during my short stay-overs from the UK.

Last but not least, I would like to thank my two very good friends, Stephan MAIERHOFER and Gregory SCHNEIDER, who came over a couple of times to visit me during my stay in the UK. We definitely had some great weekends which helped to clear up our minds from the usual routines.

Summary

Engine components are commonly exposed to air temperatures exceeding the thermal material limit in order to increase the overall engine performance and to maximise the engine specific fuel consumption. To prevent the overheating of the materials and thus the reduction of the component life, an internal flow system must be designed to cool the critical engine parts and to protect them. As the coolant flow is bled from the compressor and not used for the combustion an important goal is to minimise the amount of coolant in order to optimise the overall engine performance.

Predicting the metal temperatures is of paramount importance as they are a major factor in determining the component stresses and lives. In addition, as modern engines operate in ever harsher conditions due to efficiency requirements, the ability to predict thermo-mechanical displacements becomes very relevant: on the one hand, to prevent damage of components due to excessive rubbing, on the other hand, to understand how much air is flowing internally within the secondary air system for cooling and sealing purposes, not only in the design condition but throughout the engine life-span. In order to achieve this aero-engine manufacturers aim to use more and more accurate numerical techniques requiring multi-physics models, including thermo-mechanical finite elements and CFD models, which can be coupled in order to investigate small variations in temperatures and displacements.

This thesis shows a practical application and extension of numerical methodology for predicting conjugate heat transfer. Extensive use is made of FEA (solids) and CFD (fluid) modeling techniques to understand the thermo-mechanical behaviour of a turbine stator well cavity, due to the interaction of cooling air supply with the main annulus. Previous work based on the same rig showed difficulties in matching predictions to thermocouple measurements near the rim seal gap. In this investigation, further use is made of existing measurements of hot running seal clearances in the rig. The structural deflections are applied to the existing model to evaluate the impact in flow interactions and heat transfer. Furthermore, for one test case unsteady CFD simulations are conducted in order to take into account the flow unsteadiness in the heat transfer predictions near the rim.

In addition to a baseline test case without net ingestion, a case simulating engine deterioration with net ingestion is validated against the available test data, also taking into account cold and hot running seal clearances. Furthermore an additional geometry with a stationary deflector plate is modelled and validated for the same flow cases.

Experiments as well as numerical simulations have shown that due to the deflector plate the cooling flow is fed more directly into the disc boundary layer, allowing more effective use of less cooling air, leading to improved engine efficiency. Therefore, the deflector plate geometry is embedded in a CFD-based automated optimisation loop to further reduce the amount of cooling air. The optimisation strategy concentrates on a flexible design parameterisation of the cavity geometry with deflector plate and its implementation in an automatic 3D meshing system with respect of finally executing an automated design optimisation. Special consideration is given to the flexibility of the parameterisation method in order to reduce design variables to a minimum while also increasing the design space flexibility & generality.

The parameterised geometry is optimised using a metamodel-assisted approach based on regressing Kriging in order to identify the optimum position and orientation of the deflector plate inside the cavity. The outcome of the optimisation is validated using the benchmarked FEA-CFD coupling methodology.

Contents

List of Figures

List of Tables

List of Abbreviations

ACARE	Advisory Council for Aviation Research and Innovation in Europe
AMEDEO	Aerospace Multidisciplinary Enabling DEsign
AMG	Algebraic MulitGrid
ARMOGA	Adaptive Range Multi-Objective Genetic Algorithm
BEM	Boundary Element Method
BFGS	Broydon Fletcher Goldfarb Shanno
BL	BaseLine
BSL	BaSeLine
cbc	cold build clearance
CFD	Computational Fluid Dynamics
CHT	Conjugate Heat Transfer
CSM	Computational Structural Mechanics
DOE	Design Of Experiment
DP	Deflector Plate
EU	European Union
FAS	Full Approximation Storage
FEA	Finite Element Analysis
FEM	Finite Element Method
FFTB	Flux Forward Temperature Back
FVM	Finite Volume Method
hFFB	Heat transfer coefficient Forward Flux Back
hFTB	Heat transfer coefficient Forward Temperature Back
HP	High Pressure
HPC	High Pressure Compressor
HPC	High Performance Computing
HPT	High Pressure Turbine
hrc	hot running clearance
IGB	Internal Gear Box
IP	Intermediate Pressure
IPC	Intermediate Pressure Compressor
IPT	Intermediate Pressure Turbine
LDA	Laser Doppler Anemometry
LES	Large Eddy Simulation
LHS	Latin Hypercube Sampling
LPT	Low Pressure Turbine
MA	Main Annulus
MAGPI	Main Annulus Gas Path Interaction
MDO	Multidisciplinary Design Optimisation
MOEA	Multi-Objective Evolutionary Algorithm
NS	Navier-Stokes
NGV	Nozzle Guide Vane
PIV	Particle Image Velocimetry
RANS	Reynolds-Averaged Navier-Stokes
RNG	ReNormalization Group

RPM	Revolutions Per Minute
RSM	Reynolds Stress Model
SA	Spalart Allmaras
SFC	Specific Fuel Consumption
SQP	Sequential Quadratic Programming
SSE	Sum of Squared Errors
SSG	Speziale Sarkar Gatski
SST	Shear Stress Transport
SWP	Specific Work Package
TET	Turbine Exit Temperature
TFFB	Temperature Forward Flux Back
TFSI	Thermal Fluid-Structure Interaction
TSW	Turbine Stator Well
UK	United Kingdom
URANS	Unsteady Reynolds-Averaged Navier-Stokes

List of Symbols

A	m^2	Cross-sectional area
A_s	-	Term in realizable $k-\epsilon$ model
A_0	$= 4.04$	Constant in realizable $k-\epsilon$ model
a	m	Inner radius of the stator
a^*	-	Low REYNOLDS number correction term
b	m	Outer radius of a rotating disc or cavity
Bi	-	BIOT number
C_{b1}	$= 0.1355$	Constant in SA model
C_{b2}	$= 0.622$	Constant in SA model
C_D	-	Discharge coefficient
C_d	-	Drag coefficient
C_m	-	Disc moment coefficient
C_{prod}	$= 2.0$	Constant in SA model
C_{q_r}	-	Non-dimensional through-flow rate
C_w	-	Non-dimensional fluid flow / flow coefficient
C_{w1}	-	Variable in SA model
C_{w2}	$= 0.3$	Constant in SA model
C_{w3}	$= 2.0$	Variable in SA model
$C_{\tilde{\nu}1}$	$= 7.1$	Constant in SA model
C_μ	$= 0.09$	Constant in standard $k-\epsilon$ model
c_p	$\mathrm{J\,kg^{-1}\,K^{-1}}$	Specific heat capacity at constant pressure
c_v	$\mathrm{J\,kg^{-1}\,K^{-1}}$	Specific heat capacity at constant volume
C_1	-	Term in realizable $k-\epsilon$ model
$C_{1\epsilon}$	$= 1.44$	Constant in $k-\epsilon$ model
C_2	$= 1.9$	Constant in realizable $k-\epsilon$ model
$C_{2\epsilon}$	$= 1.92$	Constant in $k-\epsilon$ model
d	m	Diameter
d'	m	Distance to the closest wall in SA model
$\mathbf{D}$	$\mathrm{s^{-1}}$	Fluid strain rate tensor
D_ω	$\mathrm{m^2\,s^{-1}}$	Cross-diffusion term $k-\omega$ model
E'	$= 9.763$	Constant in Eq. 3.38
$\mathbf{F}$	-	Deformation gradient tensor
F_1, F_2	-	Blending functions in $k-\omega$ model
$\mathbf{f}$	$\mathrm{kg\,m\,s^{-2}}$	Body force vector
f	-	Objective function
f_w	-	Damping function in SA model
$f_{\tilde{\nu}1}$	-	Viscous damping function in SA model
$f_{\tilde{\nu}2}$	-	Damping function in SA model
G	-	Cavity aspect ratio
$\mathbf{G}$	$\mathrm{s^{-1}}$	GREENS strain tensor
G_c	-	Cavity gap ratio
G_k	$\mathrm{kg\,m^{-1}\,s^{-2}}$	Term for the production of k
$G_{\tilde{\nu}}$	$\mathrm{kg\,m^{-1}\,s^{-2}}$	Turbulent production term SA model
G_ω	$\mathrm{kg\,m^{-1}\,s^{-2}}$	Term for the production of ω

g_j	-	Inequality constraints
g'	-	Function in SA model
$\mathbf{H}$	-	HESSIAN matrix
H_0	$\mathrm{J\,kg^{-1}}$	Specific total enthalpy
h	$\mathrm{W\,m^{-2}\,s^{-1}}$	Heat transfer coefficient
h_k	-	Equality constraints
h^*	m	Interstage seal fin height
$\mathbf{I}$	-	Identity matrix / identity tensor
$\mathbf{J}$	-	JACOBIAN matrix
K	-	Empirical rim geometry constant / factor
k	$\mathrm{m^2\,s^{-2}}$	Turbulent kinematic energy
k'	-	Gas specific factor
L	-	Likelihood function
l'	m	Characteristic length
M	N m	Disc moment
$\dot{m}$	$\mathrm{kg\,s^{-1}}$	Mass flow rate
Ma	-	MACH number
n	-	Unit outward normal
$\mathbf{n}$	-	Unit outward normal vector
Nu	-	NUSSELT number
Pr	-	PRANDTL number
Pr_t	-	Turbulent PRANDTL number
p	Pa	Fluid static pressure
$\mathbf{p}$	-	Smoothness control vector of the response surface
P	W	Power
$\mathbf{P}$	$\mathrm{W\,m^{-2}}$	Vector of nodal heat flows
$\dot{q}$	$\mathrm{W\,m^{-2}}$	Heat flux
$\dot{\mathbf{q}}$	$\mathrm{W\,m^{-2}}$	Heat flux vector
r	m	Radius
r^*	-	Non-dimensional radius
r'	-	Non-dimensional distance in SA model
r_i	-	Residual
R	$\mathrm{J\,kg^{-1}\,K^{-1}}$	Gas constant
R_ϵ	$\mathrm{m^2\,s^{-3}}$	Additional term in RNG model
R_ω	$= 2.95$	Constant in $k-\omega$ model
Re	-	REYNOLDS number
Re_ϕ	-	Rotational REYNOLDS number
Re_m	-	REYNOLDS number based on mass flow rate
Re_x	-	External flow REYNOLDS number
Ro	-	ROSSBY number
s	m	Axial gap between rotor and stator
$\mathbf{s}$	-	Search direction vector
s_c	m	Seal clearance gap
S	$\mathrm{s^{-1}}$	Vorticity magnitude
$\mathbf{S}$	$\mathrm{s^{-1}}$	Vorticity of rotation tensor
t	s	Time
t'	m	Thickness
t^*	m	Interstage seal fin distance
$\hat{t}$	s	KOLMOGOROV time scale
T	K	Temperature
T_{cool}	K	Cooling air inlet temperature

T_{hot}	K	Main annulus temperature
T_m	K	Metal temperature
T_w	K	Wall / surface temperature
T_0	K	Fluid total temperature
u	$\mathrm{m\,s^{-1}}$	Radial velocity
U	$\mathrm{m\,s^{-1}}$	Velocity
$\mathbf{U}$	$\mathrm{m\,s^{-1}}$	Cartesian or cylindrical velocity vector
$\mathbf{u_s}$	m	Structural deformation vector
U_τ	$\mathrm{m\,s^{-1}}$	Friction velocity
u_ς	$\mathrm{m\,s^{-1}}$	KOLMOGOROV velocity scale
v	$\mathrm{m\,s^{-1}}$	Tangential velocity
w	$\mathrm{m\,s^{-1}}$	Axial velocity
$\bar{w}$	$\mathrm{m\,s^{-1}}$	Mean axial velocity
w^*	m	Interstage seal fin tip width
w_m	-	Weighting factor
$\mathbf{x}$	-	Design vector
x_i	-	Design parameters
$\mathbf{x_s}$	-	Local coordinate of structure
$\mathbf{X_s}$	-	Initial coordinate of structure
$Y_{\tilde{\nu}}$	$\mathrm{kg\,m^{-1}\,s^{-2}}$	Turbulent destruction term SA model
Y	$\mathrm{m^2\,s^{-1}}$	Turbulence diffusivity in $k-\omega$ model
$\hat{y}$	-	Best linear unbiased predictor
y^+	-	Non-dimensional near wall spacing
y_d	m	distance of centroid to the wall
α	-	Inverse PRANDTL number
$\alpha(T)$	$\mathrm{K^{-1}}$	Thermal expansion coefficient
α_s	-	Swirl constant
α_0'	$= 1.0$	Constant in $k-\epsilon$ RNG model
β	-	Swirl ratio / swirl fraction
β'	-	Relaxation factor
β_i	-	Scaling factor
Γ_c	-	Ratio of ingress and egress discharge coefficients
Γ_k	$\mathrm{kg\,m^{-1}\,s^{-1}}$	Term for effective diffusivity of k
Γ_ω	$\mathrm{kg\,m^{-1}\,s^{-1}}$	Term for effective diffusivity of ω
γ	-	Isentropic exponent
Δn	m	Distance from cell centre to interface
Δp	Pa	Pressure difference
ΔT	K	Temperature difference
δ	m	Boundary layer thickness
ϵ	$\mathrm{m^2\,s^{-3}}$	Scalar turbulent dissipation rate
ϵ_s	-	Sealing effectiveness
$\boldsymbol{\epsilon_{th}}$	$\mathrm{s^{-1}}$	Thermal strain tensor
ζ	-	Non-dimensional boundary layer thickness
η	-	Turbine stage efficiency
η_{eff}	-	Thermal effectiveness / cooling effectiveness
Θ_0	-	Ratio of non-dimensional egress and ingress flow rate
θ	-	Non-dimensional temperature
$\boldsymbol{\theta}$	-	Spatial distribution control vector of sample points
κ	$= 0.4187$	VON KARMAN constant
λ	$\mathrm{W\,m^{-1}\,K^{-1}}$	Thermal conduction coefficient
$\boldsymbol{\lambda_s}$	$\mathrm{W\,m^{-1}\,K^{-1}}$	Thermal conduction tensor

λ_c	-	Regression constant
μ	$\mathrm{kg\,m^{-1}\,s^{-1}}$	Dynamic viscosity
μ_i	-	Average value of i-th design variable
$\hat{\mu}_r$	-	Regression model coefficient
μ_t	$\mathrm{kg\,m^{-1}\,s^{-1}}$	Dynamic turbulent eddy viscosity
μ_{t0}	$\mathrm{kg\,m^{-1}\,s^{-1}}$	Dynamic turbulent viscosity without swirl
ν	$\mathrm{m^2\,s^{-1}}$	Kinematic viscosity
$\tilde{\nu}$	$\mathrm{m^2\,s^{-1}}$	SPALART variable
ν_t	$\mathrm{m^2\,s^{-1}}$	Kinematic turbulent eddy viscosity
σ	$\mathrm{W\,m^{-2}\,K^{-4}}$	STEFAN-BOLTZMANN constant ($= 5.67 \cdot 10^{-8}$)
σ_i	-	Standard deviation of i-th design variable
$\sigma_{\tilde{\nu}}$	$= 2/3$	Constant in SA model
σ_k	-	Term in $k-\omega$ model
σ_{k1}	$= 1.176$	Constant in $k-\omega$ model
σ_{k2}	$= 1.0$	Constant in $k-\omega$ model
σ_ω	-	Term in $k-\omega$ model
$\sigma_{\omega 1}$	$= 2.0$	Constant in $k-\omega$ model
$\sigma_{\omega 2}$	$= 1.168$	Constant in $k-\omega$ model
ς	m	KOLMOGOROV length scale
$\boldsymbol{\tau}$	$\mathrm{kg\,m^{-1}\,s^{-2}}$	Stress tensor
$\boldsymbol{\tau_{turb}}$	$\mathrm{kg\,m^{-1}\,s^{-2}}$	REYNOLDS stress tensor
ρ	$\mathrm{kg\,m^{-3}}$	Density
Φ	-	Non-dimensional sealing parameter
ϕ	-	Radial basis function
ϕ_i	-	Stage flow coefficients
χ	-	Ratio of SPALART variable to viscosity
$\boldsymbol{\Psi}$	-	Correlation matrix
ψ	-	Kriging basis function
$\boldsymbol{\psi}$	-	Basis function vector
ψ_i	-	Stage work coefficients
ω	$\mathrm{rad\,s^{-1}}$	Rotational speed / angular frequency
ω	$\mathrm{s^{-1}}$	Specific turbulent dissipation rate
∇	-	Nabla operator

List of Sub- and Superscripts

abs	Absolute
ad	Adiabatic
amb	Ambient
av	Averaged value
e	Egress
eff	Effective
ent	Entrainment
eq	Equivalent
f	Fluid
i	Ingress
in	Inlet
k	Related to turbulent kinetic energy
l	Lower
max	Maximum value
min	Minimum value
mol	Molecular
out	Outlet
p	Near wall cell centroid
$\dot{q}$	Heat flux related
r	Regression
rel	Relative
s	Solid
t	Turbulent
T	Temperature related
u	Upper
w	Wall
$\hat{}$	Artificial / non-physical value
ϵ	Related to turbulent dissipation rate
ω	Related to specific turbulent dissipation rate

List of Publications

J. Pohl and V. Fico and J. A. Dixon. Turbine Stator Well Cooling - Improved Geometry Benefits. In Proceedings of *ASME Turbo Expo 2015, GT2015-42658*, Montréal, Quebec, Canada, June 2015.

J. Pohl, H. M. Thompson, R. C. Schlaps, S. Shahpar, V. Fico and G. A. Clayton. Innovative Turbine Stator Well Design Using Design Optimisation. In Proceedings of *16th ISROMAC and 1st ISIMET 2016*, Honolulu, Hawaii, USA, April 2016.

J. Pohl, H. M. Thompson, A. Guijarro Valencia, G. López Juste, V. Fico and G. A. Clayton. Structural Deflection's Impact in Turbine Stator Well Heat Transfer. In Proceedings of *ASME Turbo Expo 2016, GT2016-56428*, Seoul, South Korea, June 2016.

J. Pohl, H. M. Thompson, V. Fico and G. A. Clayton. Turbine Stator Well Geometry Benefits - Method Validation and Design Optimisation. In Proceedings of *11. ASMO UK/ISSMO/NOED 2016*, Munich, Germany.

J. Pohl, H. M. Thompson, A. Guijarro Valencia, G. López Juste, V. Fico and G. A. Clayton. Structural Deflection's Impact in Turbine Stator Well Heat Transfer. *Journal of Engineering for Gas Turbine and Power 139(4), 041901*, GTP-16-1290, October, 2016.

J. Pohl, H. M. Thompson, R. C. Schlaps, S. Shahpar, V. Fico and G. A. Clayton. Innovative Turbine Stator Well Design Using a Kriging Assisted Optimisation Method. Accepted for publication in the *Journal of Engineering for Gas Turbine and Power*, GTP-16-1472, October, 2016.

1 Introduction

1.1 Project Background

Aeroplanes are gaining ever greater importance as a means of transportation in society as well as in the economy. Since this will still be the case in the foreseeable future, the European Commission summarised different approaches, strategies and methodologies in the report *Flightpath* 2050 - *Europe's Vision for Aviation*[1] in order to maintain global leadership for European aviation. One key technology comprises the development of multidisciplinary design optimisation (MDO) methods with the target of improving the efficiency of aeroplane components (e.g. engine, wing etc.) and thus the overall efficiency of the aeroplane. Therefore the research project *Aerospace Multidisciplinary Enabling Design Optimisation* (AMEDEO)[2] (2013) has been launched as a *Marie Curie Initial Training Network*[3] bringing together leading academic researchers, partners from industry to train 13 early stage researchers. Attention is especially directed to the development of the next generation of environmentally-friendly aircraft with the target to reduce emissions, to lower production costs and time-to-market.

In Fig. 1.1 the contribution of a leading European engine manufacturer ROLLS-ROYCE plc. concerning the requested goals from the *Advisory Council for Aviation Research and Innovation in Europe* (ACARE) for 2050 is visualised. The challenging targets are defined as follows:

- CO_2 reduction by 30 % (overall ACARE goal −75 %)
- NO_x reduction by 75 % (overall ACARE goal −90 %)
- Aircraft noise reduction by 30 % (overall ACARE goal −65 %)

Within the framework of research work package SWP 3 of the AMEDEO project, which deals with the application of advanced MDO methods to aircraft engine design, sub-project 7 is conducted at the UNIVERSITY OF LEEDS in strong collaboration with the department of Thermo-Fluid Systems of ROLLS-ROYCE plc. in Derby, United Kingdom (UK). The main objective of this sub-project is the optimisation of the cooling performance of multi-stage turbine components in conventional modern high bypass turbofan engines, taking

[1] http://ec.europa.eu/transport/modes/air/doc/flightpath2050.pdf (06.12.2014)
[2] www.amedeo-itn.eu (06.12.2014)
[3] http://ec.europa.eu/research/mariecurieactions (06.12.2014)

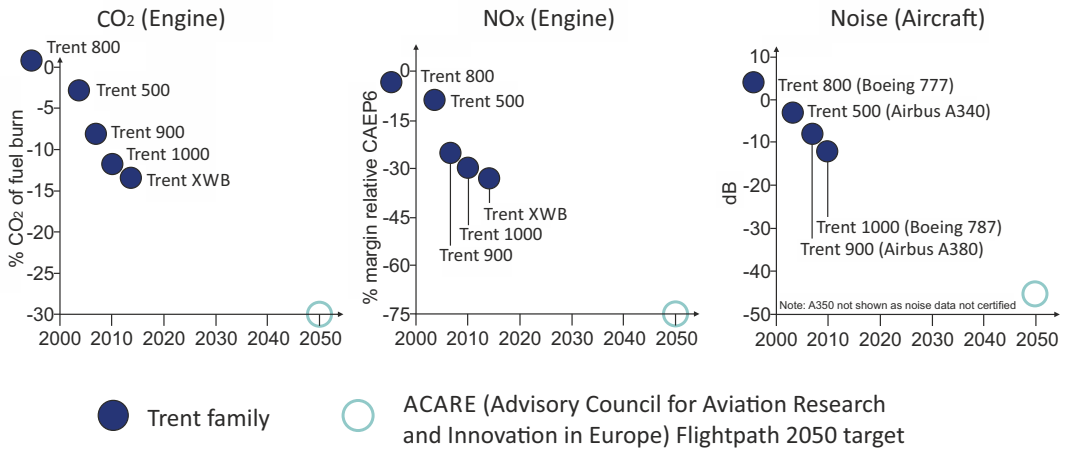

Figure 1.1: Environmental goals for 2050: Contribution of ROLLS-ROYCE TRENT engines towards CO_2 reduction (left), NO_x reduction (middle) and noise reduction (right) against Flightpath 2050 target (ROLLS-ROYCE plc., 2013)

into account different technical disciplines. In this work, the components of interest are the life critical parts forming the cavities, which are inevitably present between the rotating and stationary turbine parts. More details on the operating mode of typical aero-engines especially with respect to the importance of cooling mechanisms and the cooling air delivery will be given in later sections.

This work focuses on a multidisciplinary numerical methodology, which comprises the three disciplines *Computational Fluid Dynamics* (CFD), *Computational Structure Mechanics* (CSM) and *Conjugate Heat Transfer* (CHT). This coupled methodology is first used for benchmarking purposes in order to get confidence in the accuracy of the predictions. In a second step, an automated design optimisation is applied to the available geometry in order to minimise the required amount of cooling air whilst still ensuring appropriate cooling of the life limiting parts.

1.2 Motivation

With increasing computational power over recent decades, numerical simulations for structural, fluid and heat transfer predictions have gained more and more importance in engineering design. This especially applies to the market of aero-engine manufacturers. Since experiments with a full-size engine are very costly and since it is very challenging to implement all desired instrumentation into the engine without influencing the flow field or the component structure, it is desirable – especially from the industrial perspective – to conduct numerical simulations instead. This requires full confidence in the chosen numerical methodology, which is gained by diligent validation against well documented and recorded test data.

Furthermore, another positive side-effect of numerical simulations is the capability of analysing almost any possible shape of geometry without the necessity of manufacturing every part over and over again, which keeps costs and evaluation time to a minimum. This convenience forms the basis of an automated optimisation method, which leads to a novel improved design in a reasonable amount of time and with high confidence in accuracy of the results.

1.2.1 The Importance Of Accurate Numerical Prediction Methods

During a typical flight cycle consisting of climb, cruise, descent and landing an aero-engine undergoes different operating conditions, which cause altering temperatures, pressures, stresses and displacements to the engine components. From an engineering point of view, it is desirable to have the ability to predict these behaviours as accurately as possible in order to stay within the environmental and safety margins and to guarantee a long service life. This also avoids costly experimental engine tests and increases the competitiveness of the aero-engine company in their market sector. One of the most crucial objectives is to control component temperatures as this affects both material properties and the thermal stress levels, both of which can have a critical impact on component lives. In addition the ability to predict the displacements in a correct way is also important in order to prevent damage to components due to rubbing on the one hand and to know the exact amount of air flow passing seals for cooling or sealing purposes on the other hand. With this knowledge gained from the application of numerical modeling methods, it is then possible to optimise the distribution as well as the amount of cooling air around the vulnerable components, which ultimately results in an increase in engine performance and reduced emissions.

In the aero-engine industry, different numerical analysis methods of the solid domains are currently used in the design process, mainly modeling convective heat transfer with established empirical correlations. Nevertheless, the accuracy of these predictions is only as good as the accuracy of the applied empirical correlation, which strongly depends on the flow structure, which again, as mentioned before, varies with different operating conditions.

This type of modeling can involve a range of analyses from *thermal* only, to *thermo-mechanical*, *aerothermal* or even *aerothermo-mechanical*. In a thermal analysis the temperature distribution inside the solid components is commonly computed using the *finite element method* (FEM) in order to solve the discretised heat conduction equations. Besides assigning the relevant material properties, only thermal loads, such as discrete temperatures or convection and radiation terms, are modelled and applied as boundary conditions. This information is gained from a reliable estimation of the flow behaviour near the boundaries. This method is especially used in the preliminary design process to select appropriate component materials with respect to life and integrity considerations.

In order to fulfil a thermo-mechanical analysis, thermal as well as mechanical loads need to be applied to the boundaries. The mechanical loads typically originate from the centrifugal forces arising from rotation and pressure differences applying across structures. Besides solving the heat conduction equation, the mechanical stress-strain equation needs to be solved in the solid as well. Regarding the computation of the corresponding displacements, stresses and temperatures of the components, the equations are generally discretised using FEM.

The analysis methods with the prefix "aero" imply the presence of fluid flow dependent boundary conditions close to the edges (2D) or faces (3D) of the solid. For simple geometries, such as a flat stationary or rotating wall, the convective heat transfer boundary conditions can be implemented by taking simple analytical formulations of the flow governing equations. For more complex geometries, such as rotor-stator or rotor-rotor cavities, empirical correlations are used to model the boundaries appropriately. To correctly solve the conduction equation in the solid using these formulations or correlations, a knowledge is required of the fluid temperatures, the mass flow rates and the heat transfer coefficients plus for cavities where there is relative rotation of one or more surfaces, the swirl fraction (i.e. non-dimensional absolute tangential velocity) and the windage heating (i.e. frictional force due to relative movement between the air and a surface).

As it can be imagined, going from a more or less ideal test case, where the fluid flow is very well known, to an aero-engine configuration, where the fluid flow is very complex (e.g. due to the presence of recirculation areas, vortices, de- and reattachments), makes it very difficult to get the parameters and thus the predictions correct. Furthermore, regarding the variation of operating conditions during a flight cycle, the flow field inside the engine can change dramatically due to the different pressures and temperatures as well as the displaced components. Without reliably adapting the boundary conditions with the corresponding fluid parameters, the solution of the simulation would provide incorrect results with a large discrepancy to the real component behaviour.

One option to avoid this scenario is to make use of CFD in order to get information of the flow field adjacent to the solid components. On the one hand, CFD can be used to modify empirical correlations based on 'idealised' geometries to better represent actual engine geometry and flow structures. On the other hand, it is possible to use the CFD to automatically update the solution in the solid by coupling the CFD to the CSM. This is basically achieved by exchanging temperatures and/or heat fluxes until a defined degree of convergence between the CSM and CFD is reached. In this thesis, such a coupled methodology is applied to a *turbine stator well* (TSW) configuration and benchmarked against available experimental test data. Once enough confidence is gained in the methodology, it is used as a high fidelity model in an automated optimisation loop with the objective to reduce the required amount of cooling air in such turbine configurations.

Nevertheless, there is also a downside in using CFD. In order to solve the *Reynolds-Averaged Navier-Sokes* (RANS) equations, which describe the flow governing equations (details are given in Chap. 3), it is necessary to choose a turbulence model to calculate

the highly turbulent flow in an aero-engine. Unfortunately, there are different existing turbulence models, each performing well for a particular problem. Especially in TSWs different flow phenomena appear, such as conjugate heat transfer on the walls, mixing and ingestion near the rim as well as the presence of compressible (in the main annulus gas path) and rather incompressible flows (inside the cavities). Therefore, the performance of different turbulence models (SPALART-ALLMARAS, $k-\epsilon$ and $k-\omega-SST$) will be investigated carefully in order to highlight differences in the solutions and thus point out distinct areas where prediction uncertainties are high.

1.2.2 The Importance Of Internal Cooling Mechanisms In Aero-Engines

In this section a brief introduction into the history and the development of internal air cooling systems is given. For more details, reference is made to the work of HALLS (1967).

Over recent decades the significance of internal cooling air systems has gained more and more importance in the field of modern high bypass aero-engines. An improvement of the overall efficiency, and thus a reduction in *specific fuel consumption* (SFC), is achieved by an increase of the *turbine entry temperature* (TET) of the hot gas coming from the combustor in the main annulus gas path. Nowadays, these air temperatures exceed the thermal material limit of the directly (blades and vanes) and indirectly (cavities) exposed engine components and create threatening conditions to them. Internal cooling systems are designed to prevent damage and to protect these components from overheating. Details on how the cooling air is distributed are given in section 1.2.3 and depicted in Fig. 1.2.

According to HALLS (1967), the first aero-engine with a systematic internal cooling air system going into production was the ROLLS-ROYCE CONWAY in 1962. By using 1.2 % of the compressor flow as cooling air, the TET was allowed to go about 120 K above the blade material melting point while even increasing the life expectancy of the blades. These days, the TET is able to exceed the thermal material limits by more than 200 K without penalising the long-life cycle and safety margins (GOPALKRISHNA, 2014).

In order to maximise the overall cycle performance it is desirable to reduce the amount of cooling air to a minimum, which still ensures the optimum component life. There are mainly two reasons in favour of a reduction of the cooling air: first, the higher the amount of cooling air, the worse is the thermodynamic cycle performance of the turbine. Second, the higher the amount of cooling air reentering the main gas path at a later stage, the lower is the stage efficiency (ILLINGWORTH et al., 2005; AMIRANTE and HILLS, 2009).

1.2.3 The Secondary Air System In Modern High Bypass Aero-Engines

This section provides an overview of a typical commercial three shaft turbofan engine, i.e. the ROLLS-ROYCE TRENT 884 which is shown in Fig. 1.2 (CUMPSTY, 2009). The

following information were provided by ROLLS-ROYCE plc. during a secondment of the author in the company. Each of the three shafts couples a compressor and turbine pair:

- the *fan* (single stage) is driven by the *low pressure turbine* (LPT), consisting of 5 stages,
- the *intermediate pressure compressor* (IPC), consisting of 8 stages, is driven by the *intermediate pressure turbine* (IPT), consisting of a single stage,
- the *high pressure compressor* (HPC), consisting of 6 stages, is driven by the *high pressure turbine* (HPT), consisting of a single stage.

After the air enters the engine and passes through the fan, the air flow is divided into a so-called *bypass stream* and *core stream* (CUMPSTY, 2009). The former makes the main contribution to the engine thrust. The latter can be separated into two different air systems: on the one hand, there is the *main annulus gas path*, which is the air used for the combustion and which provides the power to the turbines (of which the LPT drives the fan, providing both main gas path and by-pass air). On the other hand, there is the

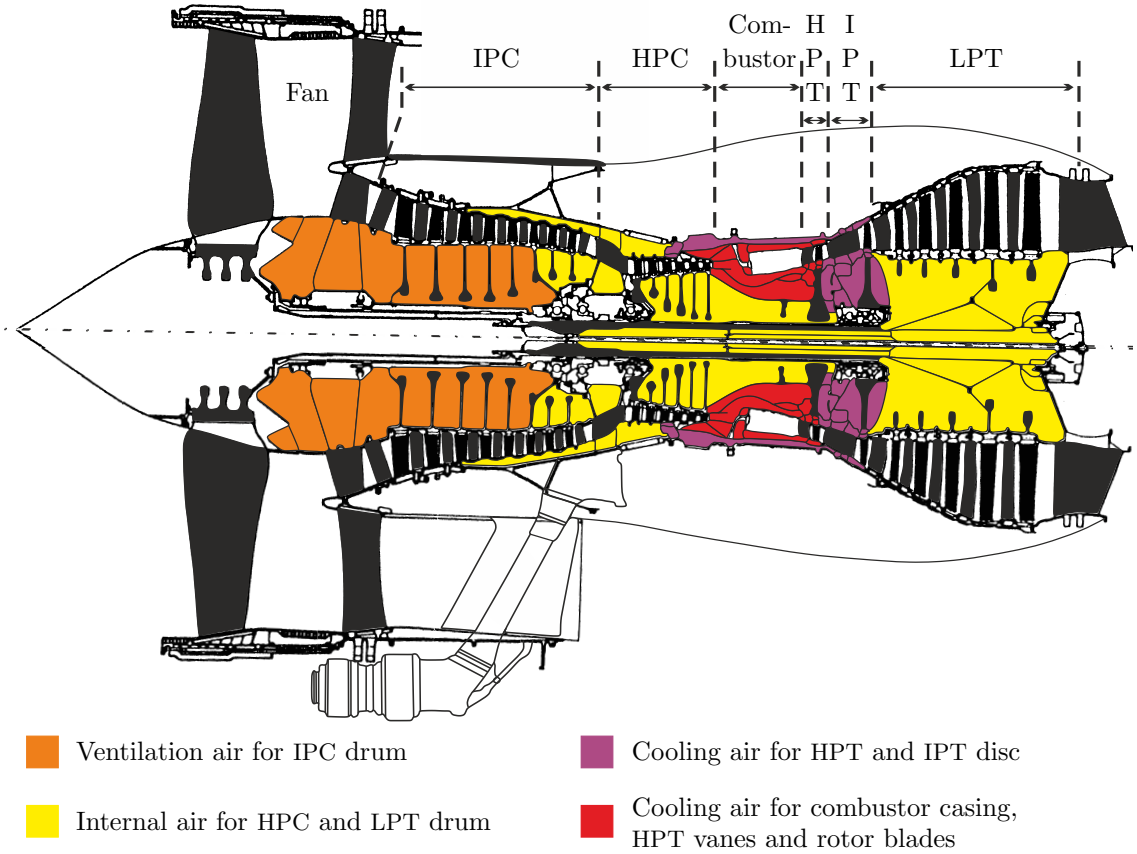

Figure 1.2: Geometry of a ROLLS-ROYCE TRENT 884 aero-engine (CUMPSTY, 2009) highlighting its secondary air system, by courtesy of ROLLS-ROYCE plc.

secondary air system, which among other things provides the required air for the cooling of critical components, for the sealing of the bearing chambers against oil leakage and for the sealing of cavities in order to prevent hot gas ingestion, which can cause damage to potentially exposed components. The total amount of air required for the secondary air system can reach up to 20 % of the main annulus flow (DIXON et al., 2013). For a given TET, these secondary air system flows penalise the engine performance. This means that any modification in design of the engine components leading to a reduction of the amount of cooling air required – without compromising on the safety and life requirements – is able to significantly improve the overall engine performance. In the following paragraphs, details of how the secondary air is distributed for cooling and sealing purposes inside the engine are given.

The secondary air system consists of four individual cooling and sealing streams, which are tagged in colour in Fig. 1.2. The orange loop is the so-called IP5 air (approximately 0.5 % of main annulus flow), which is extracted between stage 5 and 6 of the IPC and which re-enters the main annulus near the entrance of the IPC. This already compressed and heated air is used to ventilate the IPC compressor drum comprising the first five rotors and the *front bearing housing*. Once the air is extracted from the main annulus, it tends to flow towards regions of lower pressure, which, in the case of a compressor is in the opposite direction of the main annulus flow. Due to this flow behaviour the radially inboard parts of the discs are heated, which is advantageous for stress and life of these components, since the thermal gradients in radial direction on the discs are normally decreased at high power operating conditions.

The yellow stream represents the so-called IP8 air (approximately 2 % of main annulus flow), which is extracted at the last stage of the IPC. This air is distributed around the remaining compressor parts and also in the turbine section. Before entering in the turbine section, the IP8 air is used for pressurising the *Internal Gear Box* (IGB) (IPC discs 7 and 8) and venting the HPC drum (HPC discs 1 – 6) of the remaining compressor parts. In the turbine section, the air first passes through the bore of the HPT disc, sometimes heating and sometimes cooling the cob of the HPT disc, and then seals the HPT/IPT bearing chamber. Its last task is to pressurise the LPT drum in order to prevent hot gas ingestion from the main annulus in the LPT. Finally, the air is fed into TSWs through radial drive arm holes in order to protect critical components from damage. From there the air finds its way back to the main annulus through the downstream rim seal. A general overview of the existing flow pattern in such TSWs is given in section 1.2.4.

The main purpose of the commonly named HP3 air (approximately 2 % of main annulus flow), which is coloured in purple and bled from stage 3 of the HPC, is the cooling of the IPT nozzle guide vanes, the IPT blade fixings and the IPT disc. The air returns into the main annulus by mixing with the hot gas in the IPT.

The red stream is referred to as the HP6 air, which is extracted after stage 6 of the HPC. Compared to the other cooling streams in the secondary air system, this part of the cooling system bleeds the highest amount of air from the main annulus (approximately

10 % of main annulus flow). Its main task – requiring about 80 % of HP6 – is the cooling of the combustion chamber casing as well as the HPT nozzle guide vanes (NGV), which are both exposed to temperatures exceeding their thermal material limits. The remaining air is used for film cooling of the HPT blade aerofoils and for sealing the rim gap at the front of the HPT disc, before mixing with the main annulus again.

Apart from extracting air to fulfil cooling and sealing requirements, the secondary air system also provides air for utility purposes. Up to 5 % of the main annulus flow are extracted from the first and last stages of the HPC to pressurise the passenger cabin and to feed the air conditioning system. HP6 air being used at low power conditions, such as descent, and HPC inlet (or IPC delivery) air being used at higher power conditions, such as climb and cruise.

1.2.4 The Turbine Stator Well

Turbine stator wells, sometimes also referred to *interstage seal cavities*, are located between the stages of multi-stage turbines (Note: on the TRENT 884 engine example in Fig. 1.2 TSWs are only located in the LPT). These form a connection and complete the secondary air system to the turbine main annulus, providing protection to disc rims and blade fixings.

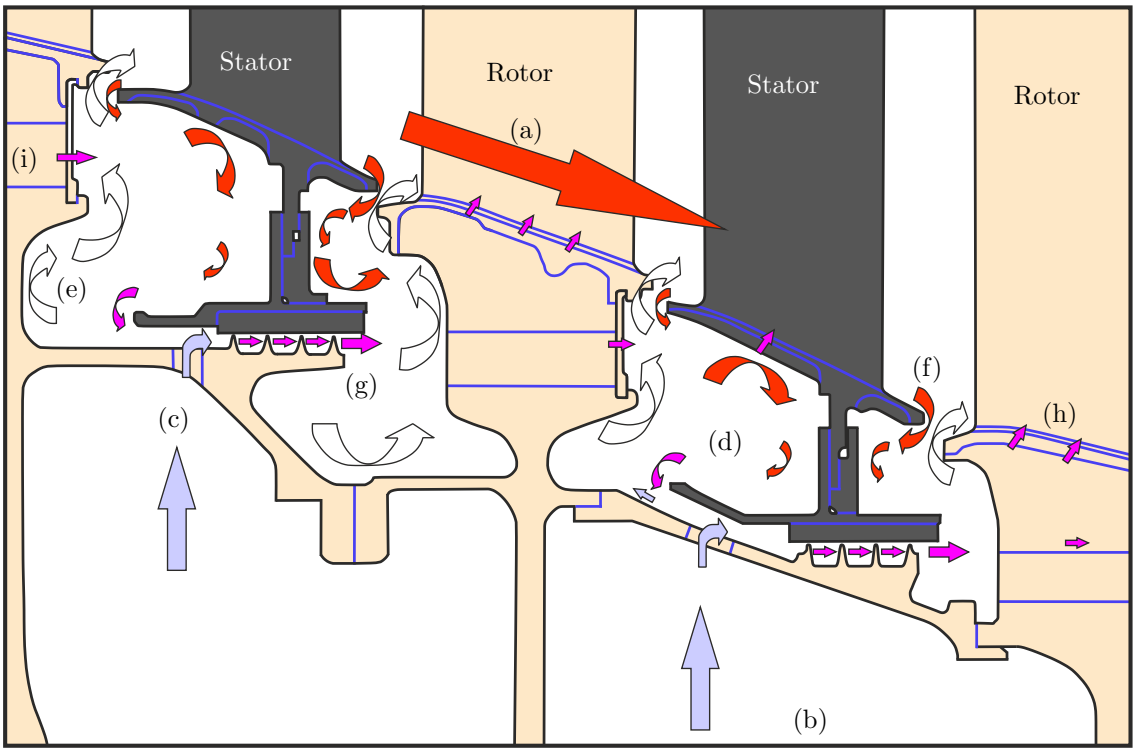

Figure 1.3: Schematical illustration of a typical turbine stator well with the main flow features, by courtesy of ROLLS-ROYCE plc.

Thus the cooling air must also be released to the main annulus again at some point and appears in the TSW, namely in the region of the *rim seals*.

A schematic illustration of a typical TSW as it can be found in an aero-engine with its main flow features (illustrated by the arrows) can be seen in Fig. 1.3. As already mentioned, the TSW is a connection between the main annulus flow (a) and the secondary air system (b). Cooling air is often introduced into the TSW cavity radially through *drive arm holes* (c). Inside the cavity a complex flow field is generated including a core flow (d) and a disc entrainment flow (e) induced by the rotating part of the turbine. The rim seal flow (f) characterises the mixing zone between the hot gas coming from the main annulus ingesting into the cavity (red arrow) and the cooling air egressing to the main annulus (white arrow). The interaction of these two flows does strongly affect the temperatures inside the cavity.

The flow of the cooling air in the drive arm holes – due to their low radial entry position into the TSW – can affect the interstage seal inlet pressure and velocity. For the flow case where the supply of cooling air approaches, or is less than the combined upstream disc rear face entrainment and the interstage seal leakage flows, hot gas is drawn into the upstream cavity of the TSW. Similarly, if the seal leakage flow is reduced below that of the entrainment flow induced on the front face of the downstream disc rim, hot gas ingestion will occur into the downstream TSW cavity.

Interstage seals (g) are used to reduce the flow of air from upstream to downstream TSW cavities. The seal flow is largely influenced by the clearance size and the pressure drop across the seal, which is a function of the upstream and downstream conditions including the pressure drop over the stage in the main annulus. Other flow phenomena, which, however, are not considered in this research, are different kinds of leakage flows, e.g. at the blade fixings (h) or the lock plates (i).

Experiments as well as numerical simulations have shown that modifications of the classical TSW geometry, such as the insertion of a deflector plate or an angled drive arm hole improve the cooling performance of the critical components (Dixon et al., 2014). Due to the insertion of a deflector plate or an angled drive arm hole the cooling flow is fed more directly into the disc boundary layer, allowing more effective use of less cooling air, leading to an improved engine efficiency.

1.3 Research Objectives

This thesis considers two main topics. First a numerical aerothermal coupling methodology between CSM using FEM and CFD using a finite volume method (FVM) is validated against available experimental test data coming from a two-stage turbine test rig facility with respect to the prediction capability of *conjugate heat transfer* (CHT) and thus metal temperature of the static and rotating components. The available test data is taken from the finalised research project *Main Annulus Gas Path Interaction* (MAGPI) (2006), which

has been funded by the European Union (EU). During this project air and metal temperature, pressure as well as displacement measurements were recorded and filed for different types of TSW geometries.

In the past, several studies were published on heat transfer prediction methods in the context of typical TSW geometries (more details on this topic follow in Secs. 2.3 and 2.4). They all have something in common, which is the fact that all studies failed to predict the metal temperatures in the rim region accurately compared to experimental test data. One reason for this inaccuracy can be related to the use of models with a so-called *cold built clearance* (cbc). Recent studies, though, highlighted the importance of taking into account the thermo-mechanical behaviour during hot running of the rig or an engine, which results in changes to the *hot running clearance* (hrc), which again influences the TSW flow structure. Another reason for the mismatch of the computations can be related to the use of steady-state CFD in the conjugate heat transfer calculations. It is known from earlier studies, that steady-state CFD computations are likely to underpredict the levels of hot gas ingestion and are limited to calculate the local mixing in the rim region accurately.

Therefore, the first objective of this research, takes these structural deformations into account, in order to further advance the understanding of the cooling flow, main annulus interaction and resultant heat transfer, in the cavities adjacent to the main annulus in multi-stage turbines. Two designated geometries of the MAGPI project are modeled to fit the purpose of CSM and CFD analyses. One *baseline* case and another modified TSW geometry with an included stationary deflector plate at the inner diameter of the stator foot. The former case has already been investigated by a range of researchers, which allows a back-to-back comparison of the results of this research compared to the previously published data. However, the latter one, is not well known yet since it has neither been validated against the experimental test data nor has the flow field been analysed in detail. Therefore, this test case is used to further extend the understanding of modified TSW flows. Both models are benchmarked for two different amounts of cooling flow rate, based on the likelihood of main stream hot gas ingestion into the cavity. In addition to benchmarking the coupled CHT methodology the respective flow fields are analysed in detail and the cooling performances of the four test cases are compared to each other. Furthermore, thermo-mechanical models are generated for each test case in order to benchmark the displacement predictions against the experimental measurements.

In addition to that, the existing aerothermal coupling method, which generally uses steady-state CFD simulations, is further extended to also take into account for the flow unsteadiness by coupling the CSM solver to time-resolved CFD solutions. This has not been done before to this particular type of cavity configurations and can end up as a strong analysis tool in turbine rim design, depending on the outcome of the calculations. In theory, this method shall capture the flow unsteadiness and the local mixing in the rim region, which will then translate in a direct impact on the heat transfer coefficient. The outcome of this simulation is then compared to the available test data and to the computational solutions using steady-state CFD.

The second part of the thesis focuses on an automated design optimisation of the TSW geometry with an included deflector plate. Earlier studies showed a positive effect with respect to the rotor disc cooling due to the implementation of such a stationary deflector plate. However, neither the influence of the deflector shape nor of its position inside the cavity were analysed in the past. Thus its full potential is still unknown, which is why the optimisation is carried out under the premise of minimising the amount of cooling air while still ensuring similar rotor disc cooling in the upstream cavity. As we have seen earlier already, a reduction of cooling air has a positive direct impact on the engine efficiency. Therefore, a clever and flexible parameterisation of the deflector plate geometry is developed, such that its shape and position inside the upstream cavity can change. The parameterised model is then incorporated into a metamodel-assisted optimisation methodology based on the regressing Kriging technique and on stand-alone CFD evaluations. The final optimised design is validated with the previously benchmarked coupled CHT methodology.

1.4 Outline of the Thesis

Chapter 1 At first a short summary of the project background and its integration in the wider research objectives are given. The second part focuses on the motivation of the current research including the importance of accurate numerical prediction capabilities in the aero-engine industry and a brief description of the engine features, which are most relevant for the understanding of this thesis (secondary air system and TSW flows). The final section summarises the main research objectives and a rough overview on the applied numerical methods.

Chapter 2 The main purpose of the second chapter is to classify the current research in already existing publications and the available state of the art numerical analysis methodologies. Primarily, the well-known available CHT methods in turbomchinery including the basic heat transfer equations are presented. In a next step, some publications according to commonly used correlations in turbomachinery, such as the free disc, typical rotor-stator flows with possible occurring interactions, such as ingestion or mixing, and seal clearance uncertainties are reviewed. Especially, the performance of the existent CHT prediction methods with respect to turbomachinery applications such as TSW flows are reviewed thoroughly. The final section focuses on state of the art optimisation techniques used in the field of turbomachinery.

Chapter 3 This chapter gives an overview of the numerical methodologies used during the research and the basic mathematical principles. At first, the flow governing equations and the fundamentals of CFD are introduced to the reader. Then the basic principles on the

structure mechanics are given including the governing equations and the introduction to the ROLLS-ROYCE in-house code SC03. The automated aerothermal coupling methodology is presented and followed by the Kriging based optimisation approach.

Chapter 4 An overview of the MAGPI two-stage turbine test rig facility is given, highlighting the experimental instrumentation for pressure, temperature and displacement measurements as well as the details of the two TSW geometries. Furthermore, the selected flow test cases, which are analysed in this work, are presented to the reader. Note that the author has not taken part in the experimental analyses and this chapter only covers the most important facts, which are needed for the understanding of the numerical analyses carried out in this research.

Chapter 5 In this chapter, the FEA and CFD models of the two different geometries are introduced to the reader. Special attention is put on the modeling approach of the deflector plate geometry. The second part of the chapter covers the parameterisation strategy of the deflector plate geometry and the actual optimisation setup.

Chapter 6 The preliminary studies point out sources of uncertainties in the numerical modeling. The impact of the near-wall mesh resolution on the wall temperature predictions as well as the influence of the overall mesh density on the TSW flow fields are summarised in the first two sections. After that, the effect of the bolts, which connect the deflector plate to the stator foot are analysed. Furthermore, a comparison of different turbulence models is conducted. The final section focuses on a comparison of the flow predictions of the two available CFD codes: FLUENT and HYDRA. This verifies the suitability of exchanging codes during the research.

Chapter 7 The numerical method validation is covered in the sixth chapter. First, the thermo-mechanical FEA model is validated against the experimental displacement measurements. The aim of the steady-state CFD results section is to present the details of the four investigated flow fields, the improved geometry benefits due to the deflector plate and to highlight the impact of the hot running clearances on the flow solutions. Furthermore, the effects of the flow unsteadiness in the rim region and inside the TSW cavities are analysed in a back-to-back comparison of RANS and URANS adiabatic CFD solutions for the two geometries. In a last step, the results of the coupled CHT method for all four test cases are presented focusing on the impact of considering the hot running clearances. In addition to this, one test case is coupled using the URANS solution and compared to the standard procedure where steady-state CFD are used.

Chapter 8 This chapter summarises the outcome of the Kriging based design optimisation of the deflector plate. The raw data of the optimisation is presented and analysed. Then the final optimum design is validated in two steps. At first, stand-alone CFD simulations of the original and the optimised deflector design with the reduced amount of cooling air are calculated in order to point out the main differences in the flow field. In a second step, the coupled CHT methodology is applied to these two cases plus to the baseline design without deflector plate and increased amount of coolant. Then the metal temperatures are compared to each other and final conclusions are drawn.

Chapter 9 The last chapter closes the thesis by summarising the main conclusions of the different chapters and by giving an outlook for potential future work in the research area of TSW flows and optimisation.

2 Literature Review – State Of The Art

This chapter introduces the reader to the already existing works and studies related to heat transfer prediction methodologies in turbomachinery and to TSW flow studies including impact of the relevant seals in the rim and interstage regions. As described in the previous chapter (compare Fig. 1.3), a TSW is formed of two rotor-stator cavities (the upstream containing a radial cooling inflow), which are connected through an interstage seal and both are linked to the main annulus by rim seals or gaps. Therefore, earlier experimental and numerical studies related to generic rotor-stator cavities are thoroughly reviewed. At first, the geometry of a *free disc* rotating in an initially stationary fluid is discussed. Then earlier important findings on rotor-stator cavity flows without and with radial inflow are summarised. With respect to TSW flows, the literature dealing with interactions between the cavities and the main annulus gas path flows has been looked into, with a special focus on the MAGPI research project. Additionally, the most relevant literature on interstage seal flows and the importance of predicting seal clearances correctly are highlighted. Finally, literature on design optimisation strategies used in the context of aero-engines and in particular in internal cooling systems is reviewed.

2.1 Conjugate Heat Transfer Methods in Turbomachinery

Within this section, the basics of heat transfer mechanisms as well as their governing equations are presented. Furthermore, the concept of conjugate heat transfer is explained with its related commonly used non-dimensional quantities. Then, different numerical methodologies, which can be found in the literature, are briefly introduced to the reader including their application to problems in turbomachinery.

2.1.1 General Heat Transfer Phenomena

In general heat transfer can be achieved by either *conduction*, *convection*, *radiation* or a combination of these mechanisms.

During conductive heat transfer thermal energy is passed on a molecular basis from a hot to a cold region within a solid, fluid or gaseous medium. The governing equation for

conductive heat transfer is given by the *law of* FOURIER:

$$\dot{q} = -\lambda \cdot \frac{\partial T}{\partial n} \tag{2.1}$$

where $\dot{q}$, λ and $\frac{\partial T}{\partial n}$ are the heat flux, the substance-specific conduction coefficient and the temperature gradient normal to a surface of constant temperature, respectively. The negative algebraic sign implies that the heat flux moves in the opposite direction to the temperature gradient.

The term convective heat transfer implies a thermal energy transport due to fluid motion and diffusion of molecules inside the fluid, and other than conduction is only present in liquid or gaseous mediums. However, the heat transfer of interest is in general the one between a moving fluid adjacent to a solid material, which is driven by a temperature difference at the solid-fluid interface, i.e. the wall. The mathematical expression of convection can be described by the *NEWTON's law*:

$$\dot{q} = h \cdot (T_w - T_f) \tag{2.2}$$

where T_w and T_f stand for the wall and fluid temperatures at the interface, respectively. The constant of proportionality h stands for the *heat transfer coefficient* (HTC) and is a function of the flow structure as well as of the fluid properties.

Radiation is achieved by emission or transmission of energy in the form of electromagnetic radiation or waves through either solid, fluid or gaseous media. The heat flux with respect to radiation only depends on the medium's absolute total temperature and is defined by the *law of* STEFAN-BOLTZMANN:

$$\dot{q} = \sigma \cdot T_{abs}^4 \tag{2.3}$$

where $\sigma = 5.67 \cdot 10^{-8} \mathrm{Wm^{-2}K^{-4}}$ is known as *STEFAN-BOLTZMANN constant* and T_{abs} is the absolute temperature of the surface of the radiating source.

An important non-dimensional quantity in fluid convective heat transfer is the *NUSSELT number*, which characterises the fluid thermal boundary layer and represents a dimensionless temperature gradient at the wall:

$$Nu = \frac{h \cdot l'}{\lambda_f} \tag{2.4}$$

where λ_f and l' are the conductivity of the fluid and the so called *characteristic length*, respectively. This ratio purely depends on the fluid properties and defines the resistance of conduction of a stationary fluid over the resistance of convection.

In multi-physical domains and environments it is very unlikely that only one type of heat transfer mechanism is significant. The combination of conductive and convective heat transfer, neglecting radiation, is referred to *conjugate heat transfer* (CHT), which is illustrated in a simple one dimensional example in Fig. 2.1. The figure shows the

schematics of a fluid flow with velocity U over a flat plate. The plate has a characteristic length of l', a thickness t' and a material conduction coefficient of λ_s. Inside the solid heat conduction takes place whereas in the boundary layer of the fluid convection is the driving heat transfer mechanism.

This leads to the two following governing equations solving the heat transfer problem:

$$\dot{q} = \lambda_s \cdot \frac{\partial T}{\partial n} = \frac{\lambda_s}{t'} \cdot (T_s - T_w) \tag{2.5}$$

$$\dot{q} = h \cdot (T_w - T_f) \tag{2.6}$$

From these two equations the non-dimensional quantity in conjugate heat transfer can be derived, the *BIOT number*:

$$Bi = \frac{h\, t'}{\lambda_s} \tag{2.7}$$

From this mathematical formulation it can be seen that the BIOT number incorporates both, solid and fluid properties - in contrast to the NUSSELT number, which only is a function of the fluid properties - and serves as a measure to compare conductive resistance of the solid with convective resistance of the fluid. In general this means that for a small BIOT number the maximum temperature gradient is in the fluid domain, whereas for a large BIOT number the maximum temperature gradient is in the solid domain.

For two or even three dimensional fluid flows over a solid body the solution of the conjugate heat transfer system becomes inevitably more complex. In general, this requires the solution of the set of the governing fluid equations, i.e. the laws of conservation of mass, momentum and energy, which will be described in Chap. 3.

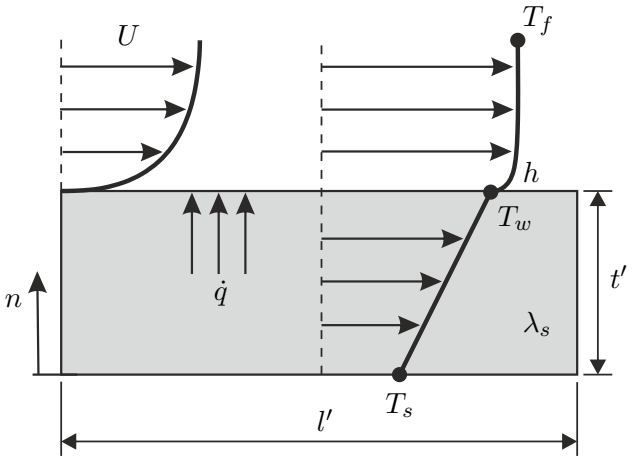

Figure 2.1: Schematic illustration of a basic conjugate heat transfer problem

2.1.2 The Uncoupled Method

One simple and cheap method to estimate temperatures in the solid is the so called *uncoupled method*, where first the fluid domain is computed to extract the HTC, which is then fed into a convecting boundary condition of the solid solver to compute the heat conduction and thus the solid's temperature. The HTC is obtained from the computation of two separate flow simulations imposing isothermal boundary conditions at the wall, defined by two different temperatures. The following system of two equations needs to be solved for that purpose, assuming a linear relation between the HTC and the wall temperature:

$$h = \frac{\dot{q}_{w,2} - \dot{q}_{w,1}}{T_{w,2} - T_{w,1}} \tag{2.8}$$

$$T_f = T_{w,1} - \frac{\dot{q}_{w,1}}{h} \tag{2.9}$$

In practical turbomachinery applications, this method was used by many authors in the field of turbine blade and vane cooling (e.g. HEIDMANN et al., 2000; CARCASCI et al., 2002; CALONI and SHAHPAR, 2015). The latter also concluded that the assumption of a one-way linear relation between the HTC and the wall temperature fails to provide accurate metal temperatures. This was also demonstrated in earlier studies carried out by PERELMAN (1969), LUIKOV et al. (1971) and HESELHAUS (1998). This latter study showed variations of the local NUSSELT number of up to 50 % between adiabatic and CHT computations. The main reason for that is the two-way interaction between the solid and the fluid, i.e. the thermal boundary condition is influenced by the HTC and vice versa. In order to obtain a fully consistent solution several iterations are required, which is then referred to as a *coupled method*.

Recently, a novel uncoupled approach was proposed by MAFFULLI and HE (2014), who also pointed out the weakness and misleading outcome using a two point uncoupled method for conjugate heat transfer problems in turbine blades. Therefore, the authors advocate the alternative use of a parabolic three point approach, which takes into account a non-linear behaviour of the HTC over a range of wall temperatures (see Fig. 2.2).

The mathematics solving this problem are based on a modified form of NEWTON's law taking into account the non-linearity of the HTC:

$$\dot{q} = (h_0 + h_1 T_w)\,(T_w - T_{w,ad}) \tag{2.10}$$

where h_0, h_1 and $T_{w,ad}$ are the unknown HTCs and adiabatic wall temperature. In order to solve this problem, three CFD simulations need to be solved, each with a different implied isotemperature. Although the method requires 50% more computational cost and time, the outcome of the calculations gave very promising results for a typical turbine blade compared to direct CHT analyses using the conjugate method (explained in Subsec. 2.1.3): the heat fluxes for the three point method were in agreement with the CHT solution whereas the two point method showed large discrepancies.

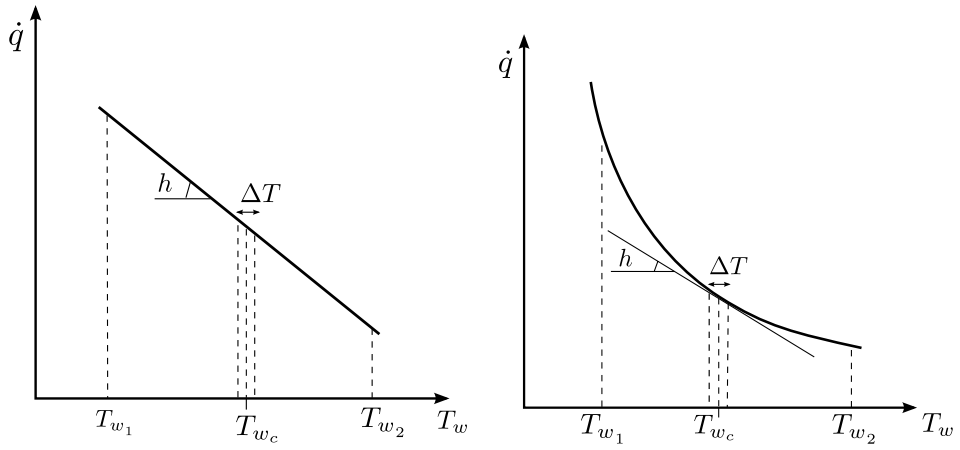

Figure 2.2: Schematics of the differences between linear (left: h independent of T_{w_c} and ΔT) and non-linear (right: h dependent of T_{w_c} and ΔT) heat flux relations when the HTC h is of interest (MAFFULLI and HE, 2014)

For another blade configuration, CALONI and SHAHPAR (2015) studied the feasibility of the three point uncoupled approach and compared the outcome to the two point method and a coupled CHT approach (explained in Subsec. 2.1.4). The outcome was in agreement with the one of MAFFULLI and HE (2014): the three point method improved the predictions of heat flux compared to the two point method and were in agreement with the coupled CHT solution.

As mentioned above, the two presented methods do not take into account the two way interaction of the fluid and the solid. Although the three point method provides promising results in calculating heat fluxes and metal temperatures for turbine blade configurations, it is not certain that this is still the case in the context of multiple components and resulting complex flow field interactions or the presence of non-linear temperature gradients. Therefore, coupled approaches are necessary. The next subsections give an overview of different computational methods to solve conjugate heat transfer problems. Basically, it can be distinguished between two main approaches, depending on the method to impose continuity of temperature and heat flux at the common boundary of the solid and the fluid domain: the *conjugate method* and the *coupled method*.

2.1.3 The Conjugate Method

In heat transfer, the conjugate method is usually referred to a monolithic numerical approach where the governing equations for the fluid and the solid are solved within a single CFD code. In order to do this, it is essential that the continuity of temperature and heat flux at the common solid/fluid boundary is ensured through an appropriate communication process by the code. Therefore, both domains need to be discretised, either separately usually resulting in a non-conformal interface at the boundary, or in a joint meshing process providing a conformal transition from fluid to solid.

In CFD the discretisation generally is achieved using a *finite volume method* (FVM) where the temperature information is saved at the cell centre. This causes an additional challenge to the code in order to calculate the correct heat flux exactly at the interface, due to the different specific heat conductivity in in the solid and the fluid. One way of doing it, as reported by VERSTRAETE (2008), is to solve the following equation:

$$\lambda_s \cdot \frac{T_s - T_w}{\Delta n_s} = \lambda_f \cdot \frac{T_f - T_w}{\Delta n_f} \tag{2.11}$$

where the subscripts s and f are related to the solid and fluid domain, respectively. The variable Δn represents the distance from the cell centre to the interface.

One obvious benefit in using the conjugate method is the use of a single code only. Although some effort is required to ensure the continuity of temperature and heat flux (not necessarily of the nodes) at the interface of both domains, no complex solution interpolations from one solver to another need to be done. Also it is possible to obtain conjugate heat transfer solutions for unsteady CFD solutions without much additional effort, although this requires high computational power (SMITH et al., 2012; YAMANE and TANAKA, 2014).

There are also a number of disadvantages and limitations using the conjugate method, which are basically due to the limitations of one single code. In CSM, the *finite element method* (FEM) is the preferred method to solve the structural governing equations, whereas in CFD, the FVM is commonly used to solve the flow governing equations. Currently available CSM and CFD codes are not able to handle two different solving techniques at the same time. Therefore, in CHT problems, one computational technique needs to be adapted, which is generally done in the solid domain, which is solved using the FVM. This is definitely not the best way and also requires interpolation strategies for the surface values (from cell center to the nodes). If one was interested in carrying out additional structural analyses like stress and life predictions, the temperature solution needs to be interpolated to a structural solver. This requires a different mesh as well as a suitable interpolation technique. In the field of turbomachinery, it is of interest to simulate transient flight cycles with multiple time steps and different running conditions, which makes conjugate method computing times and costs impractical with current solvers and computing hardware.

Furthermore, VERSTRAETE (2008) mentioned the difficulties of simulating 2D to 3D models within one single solver. This approach is very much appreciated for large domains as the run time is reduced significantly by using an axisymmetric fluid model.

Regardless of advantages and disadvantages of the method, it has been successfully applied to turbomachinery problems. In the history of turbine blade and vane cooling a lot of studies can be found in the literature, e.g. HAN et al. (2000), FACCHINI et al. (2004), MONTOMOLI et al. (2004), TAKAHASHI et al. (2005) or MAFFULLI and HE (2014). In the area of the secondary air system the studies of OKITA and YAMAWAKI (2002), GUIJARRO VALENCIA et al. (2012), SMITH et al. (2012) and LÜCK et al. (2014a) are worthy of mention. More details on their works and the outcome are given in later sections.

2.1.4 The Coupled Method

In the coupling method two different solvers are used to solve the decoupled governing equations of the solid and fluid domains separately. In order to consider the two way interaction at the common interface, the two solvers need to update each other with temperatures, heat flux or HTCs. Generally, the coupled computation starts from a steady-state or time-averaged unsteady adiabatic CFD solution of the fluid domain, which is updated by the boundary output of the solid domain computations and vice versa until continuity at the boundary is achieved. In such computations the time limiting factor is the expensive CFD computation, which takes orders of magnitude longer than the heat conduction calculations.

The solid domain is in general computed using a FEM, which requires a much coarser mesh for an efficient computation of the heat conduction through the metal. The solution of the fluid is obtained using a FVM, either implicitly or explicitly, and requires a much finer mesh than the solid, in order to resolve the flow physics accurately. This is especially of importance near the walls, where the heat transfer takes place, to make sure that the boundary layers are resolved accurately.

As for the conjugate method, the coupled method has advantages but also drawbacks. The most obvious advantage is the flexibility of the method due to the possibility of choosing the most suitable codes for solving the solid and the fluid regimes, respectively. This reduces the uncertainty of obtaining misleading results due to the choice of a non-optimal code. The separate grid generation also allows the generation of optimum meshes for each domain without having to consider cell expansion ratios at the interface, which would result in an unnecessarily large cell count for the solid. This is applicable due to the capability to handle non-conformal meshes at the interface, where information is passed by interpolating the FVM solution to the FEM and vice versa. For axisymmetric models, the possibility of coupling 2D FVM models to 3D FEM models in order to save computational resources while using the same interpolation techniques as for the 3D to 3D coupling. Depending on the FEM solver, it is also possible to simulate transient flight cycles or stress and life analyses in parallel without the need of generating new FEM models and interpolating temperatures onto a new mesh.

The main drawbacks of the coupling method are found at the solid-fluid interfaces where a suitable interpolation technique needs to be applied in order to ensure a fully consistent solution in the both domains and especially at the joint boundaries. Depending on the interpolation technique, this can raise the complexity of solving the CHT problem. Furthermore, a separate robust communication tool needs to be designed, which ensures the exchange of information, the correct application of the interpolation technique and the monitoring of convergence.

So far four different coupling methods exist in the open literature, which were thoroughly described and discussed by Verstraete and Braembussche (2008; 2009) and which are known as:

- Flux Forward Temperature Back (FFTB) method
- Temperature Forward Flux Back (TFFB) method
- Heat transfer coefficient Forward Temperature Back (hFTB) method
- Heat transfer coefficient Forward Flux Back (hFFB) method

Furthermore, the same authors derived respective convergence criteria as a function of the BIOT number for each of the four methods. Since, in this work, the hFTBmethod is applied to the heat transfer problem, as it has proven to be the most stable approach in TSW geometries, only this method is presented and described in the upcoming subsection. In order to obtain the full details of the four methods, reference is made to the publications of VERSTRAETE and BRAEMBUSSCHE (2008; 2009).

2.1.4.1 The hFTB Method

The hFTB coupling method flowchart is illustrated in Fig. 2.3 and is based on the convective heat transfer approach (see Eq. 2.2) to provide a boundary input for the FEM domain. In general, the coupling process starts with either an adiabatic flow solution or one with an imposed wall temperature distribution T_w at the solid/fluid interface. This

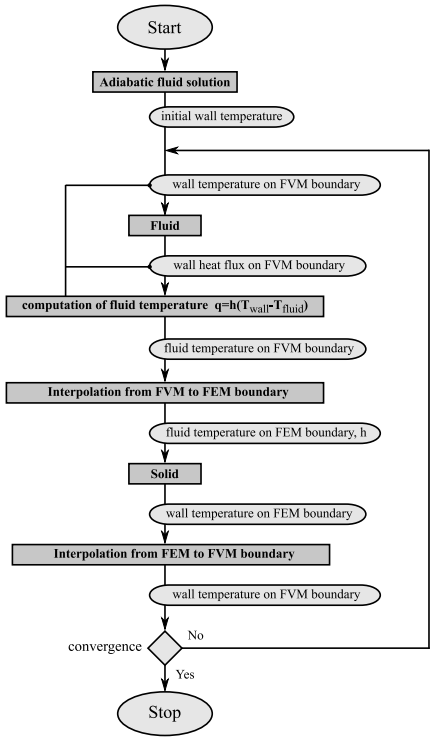

Figure 2.3: Flowchart of the hFTB CHT coupling method (VERSTRAETE, 2008; VERSTRAETE and BRAEMBUSSCHE, 2009)

initial solution then gives an estimation of two artificial numerical values: $\hat{h}$ and $\hat{T}_f$, which are passed to the FEM domain. In return, the calculated wall temperature distribution at the boundary is then passed to the fluid domain. This process is repeated until a fully consistent solution is achieved.

As one convective heat transfer equation (Eq. 2.2) is not sufficient to solve the problem with two unknowns ($\hat{h}$ and $\hat{T}_f$) a further equation is necessary. Therefore, MONTENAY et al. (2000) and VERDICCHIO (2001) proposed a problem solution where a second flow calculation is conducted for a different wall temperature distribution. Under the assumption that the values for $\hat{h}$ and $\hat{T}_f$ stay the same and substituting the two equations leads to an expression for $\hat{h}$ only depending on the heat fluxes $\dot{q}_{w,1}$ and $\dot{q}_{w,2}$ and the wall temperatures $T_{w,1}$ $T_{w,2}$ of both flow solutions:

$$\dot{q}_{w,2} - \dot{q}_{w,1} = \hat{h} \cdot (T_{w,2} - T_{w,1}) \tag{2.12}$$

With this equation it is then possible to calculate $\hat{T}_f$ only as a function of the respective values for the imposed wall temperature T_w and the wall heat flux $\dot{q}_w$. According to MONTENAY et al. (2000) - in order to avoid an ill-posed conduction problem - it is essential to only have positive heat transfer coefficients $\hat{h}$ along the entire solid/fluid boundary. One possibility to achieve that is by initialising the HTC to a constant positive value and updating the fluid temperature $\hat{T}_f$ at each CFD simulation. The continuity of heat flux and temperature can then be checked using one equation only:

$$\dot{q}_w^{fem^i} - \dot{q}_w^{fvm^i} = h \cdot \left(T_w^{fvm^{i+1}} - T_w^{fvm^i} \right) \tag{2.13}$$

In that way $\hat{h}$ does not affect the solution itself but instead influences the stability and convergence time of the CHT computation. According to VERSTRAETE and BRAEMBUSSCHE (2008; 2009) the hFTB method converges for:

$$\hat{Bi} > \frac{Bi - 1}{2} \tag{2.14}$$

with $\hat{Bi}$ being the artificial BIOT number, which is defined as:

$$\hat{Bi} = \frac{\hat{h} \cdot t'}{\lambda_s} \tag{2.15}$$

That means, that the discussed coupling method for CHT problems with $Bi < 1$ is stable for any value of $\hat{h}$ and is only stable for problems with $Bi > 1$ if $\hat{h}$ is chosen appropriately. Since the BIOT number is not always known a sufficient but not necessary criterion for convergence can also be formulated as:

$$\hat{h} > \frac{h}{2} \tag{2.16}$$

From these last equations it can be seen that it is not obvious how to set up the CHT problem in the most effective manner, i.e. obtaining a converged solution robustly and quickly at the same time. As a best practice it is suggested to guess a constant value for $\hat{h}$ for every wall making sure it is larger than the maximum value of h. In that case convergence is guaranteed, but the computational time might not be optimal (VERSTRAETE, 2008).

The first attempts in using the hFTB method were carried out by MONTENAY et al. (2000) and VERDICCHIO (2001) who both calculated the conjugate heat transfer in cavities of the secondary air system of an aero-engine using 2D models. After the successful computations of VERDICCHIO, the method was then integrated into the ROLLS-ROYCE in-house CSM solver SC03, in order to communicate with the commercial CFD code FLUENT. This coupled method was applied to a set of different secondary air system geometries: ILLINGWORTH et al. (2005) carried out an analysis on the pre-swirl system of an engine using the method whereas GUIJARRO VALENCIA et al. (2012) presented a study on an engine representative TSW geometry adjacent to a main gas path in order to predict heat transfer in the stator well with ingestion. DIXON et al. (2014) extended the functionality of the method by adding the capability to couple SC03 to the in-house CFD code HYDRA and presented a study on the same TSW geometry for a balanced cavity with no net ingestion due to additional cooling.

SUN et al. (2010) demonstrated the suitability of the method analysing four different test cases. Amongst others real axisymmetric engine geometries such as a LPT cavity and an HPC drive cone cavity were thermally analysed simulating a transient flight cycle. The computational results agreed well with the experiments. A further study of SUN et al. (2012) showed the applicability of the method to a 3D engine HPT cavity model. In order to deal with oscillations coming from the CFD computations due to unsteady flow phenomena, the authors extended the coupling method and proposed a *pseudo-unsteady* approach. Instead of passing the last computed heat flux - which might be at a maximum or minimum peak of the oscillation - a mean value for the heat flux averaged over a defined range is passed to the FEA solver.

In the area of the main gas path, the hFTB method was firstly used by HESELHAUS et al.(1992; 1998) and LASSAUX et al. (2004) for 3D cooled turbine blades and vanes. Furthermore, CALONI and SHAHPAR (2015) successfully applied the method to a internally cooled turbine blade using the CSM solver SC03 coupled to the ROLLS-ROYCE CFD solver HYDRA.

Regarding the stability of the method, VERSTRAETE (2008) conducted a CHT computation of a flow over a flat plate. As in that test case, the HTC at the leading edge of the plate was approaching infinity, very high values for h needed to be defined. It was shown that if a too small value is chosen, the solution diverges after a few CHT iterations. However, the stability and the computational time until convergence does not only depend on the HTC but also on the number of inner CFD iterations. Therefore, it is essential to

find an optimum balance between number of iterations and the initial guess of h to obtain a good and quick solution.

2.2 The Free Disc

The rotating free disc in a quiescent environment is a simple configuration, which has been analysed for nearly a century (VON KARMAN, 1921). This section gives only a short introduction into the main characteristics of the phenomena appearing in the flow and presents some derived correlations. For more details, reference is made to the books of OWEN and ROGERS (1989), SHEVCHUK (2009) and CHILDS (2011), also to the report of HARMAND et al. (2013).

In Fig. 2.4 a typical free disc configuration with its associated flow is presented. The disc of radius b rotates around the z-axis at an angular frequency of ω in a initially stationary fluid, which is of density ρ and has a kinematic viscosity ν. On the disc a boundary layer of thickness δ is formed, in which the fluid is pumped radially outwards with a velocity of u. To balance this flow, an axial entrainment flow $\dot{m}_{ent}$ of velocity w is developed. This was first discovered and described by VON KARMAN (1921).

Typically, analytical expressions for a free disc are given in a non-dimensioned form. The entrained mass flow can be expressed by a so called *entrainment flow coefficient* $C_{w,ent}$, which is defined as follows:

$$C_{w,ent} = \frac{\dot{m}_{ent}}{\mu\, b} \tag{2.17}$$

where μ is the dynamic viscosity of the fluid and b the outer radius of the disc.

The disc moment can be described by a *disc moment coefficient* C_M, which can be expressed as follows:

$$C_M = \frac{M}{\frac{1}{2}\,\rho\,\omega^2\,b^5} \tag{2.18}$$

where M, ρ, ω and b are the disc moment, the fluid density, the angular velocity and the outer radius of the disc, respectively.

For convective heat transfer problems on a rotating free disc, the NUSSELT number Nu is defined as:

$$Nu = \frac{\dot{q}\, r}{\lambda_f\, \Delta T} \tag{2.19}$$

where $\dot{q}$ is the heat flux, λ_f is the thermal conductivity of the fluid, r the radius and ΔT is the difference of disc surface temperature T_w and ambient fluid temperature $T_{amb,f}$.

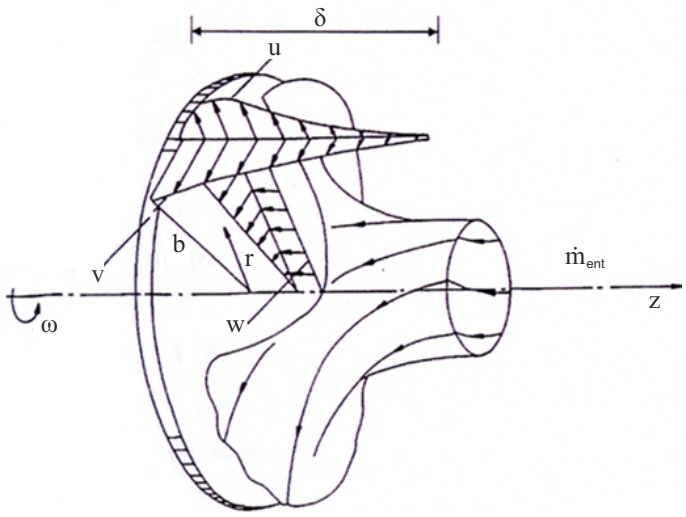

Figure 2.4: Rotating free disc in a quiescent environment (SCHLICHTING and GERSTEN, 2006)

Another important non-dimensional quantity is the rotational REYNOLDS number Re_ϕ, which is used to characterise the transition from a laminar to a turbulent flow. The definition is as follows:

$$Re_\phi = \frac{\rho\,\omega\,b^2}{\mu} \tag{2.20}$$

According to SHEVCHUK (2009) there is no fixed value for Re_ϕ to define transition. Depending on the experimental setup and the instrumentation a range between 1.8×10^5 (TIEN and CAMPBELL, 1963) and 3.6×10^5 (ELKINS and EATON, 1997) were determined.

The pioneer in deriving an analytical expression for rotating free disc flows was VON KARMAN (1921), who approximated the NAVIER STOKES equations for laminar and turbulent incompressible axisymmetric flows by ordinary differential equations. By doing that, he found out that the thickness of the boundary layer near the rotating disc is dependent on the angular velocity and the kinematic viscosity of the fluid.

This attempt was followed up by COCHRAN (1934), who for a laminar flow derived a solution for the boundary layer thickness δ as:

$$\delta = 2.8 \left(\frac{\nu}{\omega}\right)^{0.5} \tag{2.21}$$

where ν is the kinematic viscosity. This shows that the kinematic boundary layer is of constant thickness and thus the convective heat transfer coefficient only depends on the angular velocity and not on the radial position (HARMAND et al., 2013).

Furthermore, he defined the moment and the entrainment flow coefficients as a function of the rotational REYNOLDS number Re_ϕ. These are given by:

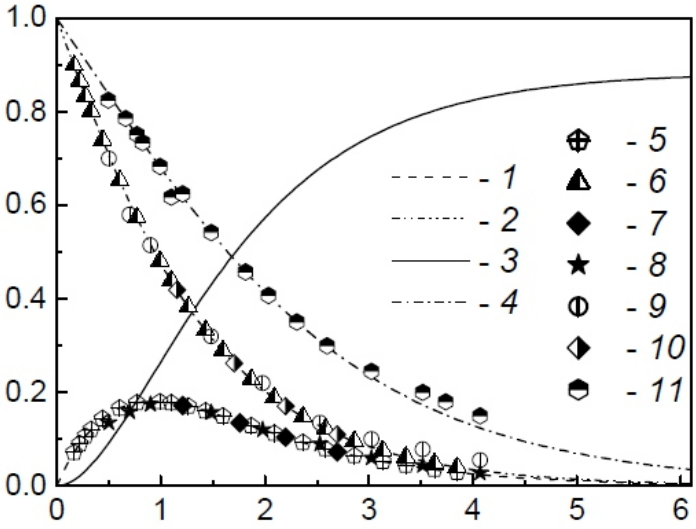

Figure 2.5: Velocity and temperature profiles in laminar flow over a free rotating disc (SHEVCHUK, 2009): computations (1 − 4) of non-dimensional radial, axial, tangential velocity and temperature, respectively, for an isothermal disc ($T_w = const$) and $Pr = 0.71$ by SHEVCHUK (2009), compared to experiments from ITOH and HASEGAWA (1994) (5 and 8), ELKINS and EATON (1997) (6, 9 and 11) and LINGWOOD (1996) (7 and 10)

$$C_{w,ent} = 2.779\, Re_\phi^{0.5} \tag{2.22}$$

$$C_M = 1.935\, Re_\phi^{-0.5} \tag{2.23}$$

For turbulent flows, assuming a one-seventh power-law distribution[1] for the radial and tangential velocity components, VON KARMAN derived the following expressions from the integral-momentum equations:

$$\frac{\delta}{r} = 0.526\ Re_\phi^{-0.2} \tag{2.24}$$

$$C_{w,ent} = 0.2186\, Re_\phi^{0.8} \tag{2.25}$$

$$C_M = 0.0729\, Re_\phi^{-0.2} \tag{2.26}$$

In contrast to the laminar case, the boundary layer thickness depends on both the angular velocity of the disc as well as the radius, the same applies to the convective heat transfer, which increases with both increasing parameters.

The impact on the convective heat transfer of a rotating free disc was thoroughly investigated by DORFMAN (1963). By approximating the energy equation with a power-law radial temperature distribution in a laminar flow, he obtained the following expressions for the NUSSELT number:

[1] $\zeta \leq 1$, where $\zeta = z/\delta(r)$, $u = \alpha(r)\,\omega\, r\, \zeta^{1/7}\,(1-\zeta)$ and $v = \omega\, r\,(1-\zeta^{1/7})$ and $\alpha(r)$ is a non-dimensional amplitude factor

$$Nu = 0.308\,(n+2)^{0.5}\,Re_{\phi}^{0.5}\,Pr^{0.5} \tag{2.27}$$

where Pr stands for the PRANDTL number, which is a measure of the momentum diffusivity versus the thermal diffusivity, and is defined as:

$$Pr = \frac{\mu\, c_p}{\lambda_f} \tag{2.28}$$

with c_p being the specific heat capacity of the fluid at constant pressure.

For the turbulent flow case, DORFMAN obtained the following expression:

$$Nu = 0.0197\,(n_t+2.6)^{0.2}\,Re_{\phi}^{0.8}\,Pr^{0.6} \tag{2.29}$$

where n_t is the exponent coming from the interpolation expression of the radial temperature distribution ($T(r) = T_0 + \beta^* r^{n_t}$).

Furthermore, DORFMAN derived a correlation for the disc entrainment flow, which only depends on the rotational REYNOLDS number:

$$C_{w,0} = 0.219\,Re_{\phi}^{0.8} \tag{2.30}$$

which was refined by CHEW (1988) to fit the flow entrainment for partial rotors, as they are commonly present in the field of turbomachinery. This refinement lead to following equation:

$$C_{w,ent} = C_{w,0}\left[1 - \left(\frac{a}{b}\right)^5\right] \tag{2.31}$$

where a and b are the inner and outer disc radii, respectively.

In Fig. 2.5 computed velocity and temperature profiles over a free disc using self-similar solutions as presented above are compared to different experimental measurements (SHEVCHUK, 2009). It can be seen that the corresponding curves are nearly perfectly superimposed, which leads to the conclusion that free disc correlations are effective for free disc or equivalent flows.

This last statement was also reinforced by recent investigations. Amongst others, AUTEF (2007) and JAVIYA (2012) carried out numerical simulations in order to compare the NUSSELT numbers from their numerical predictions to experimental measurements of NORTHRUP and OWEN (1988) and the correlations developed by VON KARMAN (1921). Using the two different CFD solvers HYDRA and FLUENT from ROLLS-ROYCE and ANSYS, respectively, while applying a standard $k-\epsilon$ turbulent model with wall functions and enhanced wall treatment to solve the governing equations, very good agreement between the simulated results and the measurements as well as the correlation were achieved.

2.3 Rotor-Stator Cavity Flows

This section introduces the reader to the fundamentals of rotor-stator cavities with through-flow, as they can be found in different domains in modern aero-engines. Experimental and theoretical studies carried out and developed in the past, which can be found in the open literature, are presented in the following subsections. At first cavities without main gas path interactions are considered. In a second step, the complex interactions between both fluid flows (cavity and main gas path) are taken into account and explained. The last part of this section focuses on the MAGPI research project, where experimental data from a TSW test rig was gained and well documented in order to obtain information on the flow behaviour and to benchmark different numerical methods. An overview of the work completed so far is given.

2.3.1 Rotor-Stator Cavities Without The Main Gas Path

Considerable experiments for an enclosed rotor-stator flow were carried out by DAILY and NECE (1960), who separated the observed flow types into four different regimes. Fig. 2.6 shows the strong dependency of these regimes on the rotational REYNOLDS number Re_ϕ and the cavity aspect ratio $G = s/b$, with s and b being the axial gap between rotor and stator and the cavity outer radius (see Fig. 2.7). Basically the flow can either be laminar (regimes I and II) or turbulent (regimes III and IV) with merged (regimes I and III) and non-merged (regimes II and IV) boundary layers of the rotor and the stator (explanations of the terms 'merged' and 'non-merged' follow below).

In principle, the flow structure consists of two main features: a large recirculation zone in the core region, where tangential velocities are dominant, and a secondary flow in the

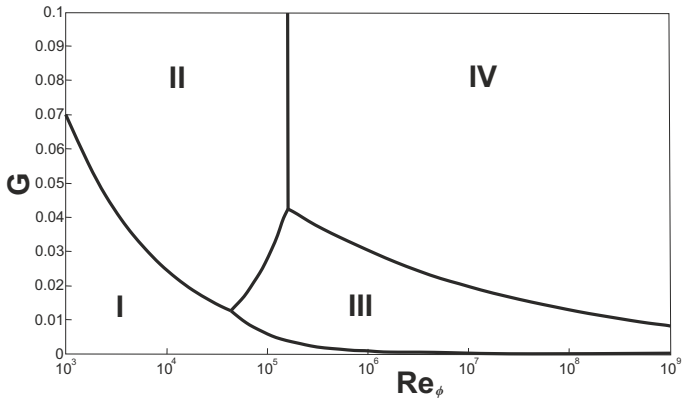

Figure 2.6: Flow regimes in a rotor-stator system. I: laminar flow with merged boundary layers; II: laminar flow with non-merged boundary layers; III: turbulent flow with merged boundary layers; IV: turbulent flow with unmerged boundary layers (DAILY and NECE, 1960)

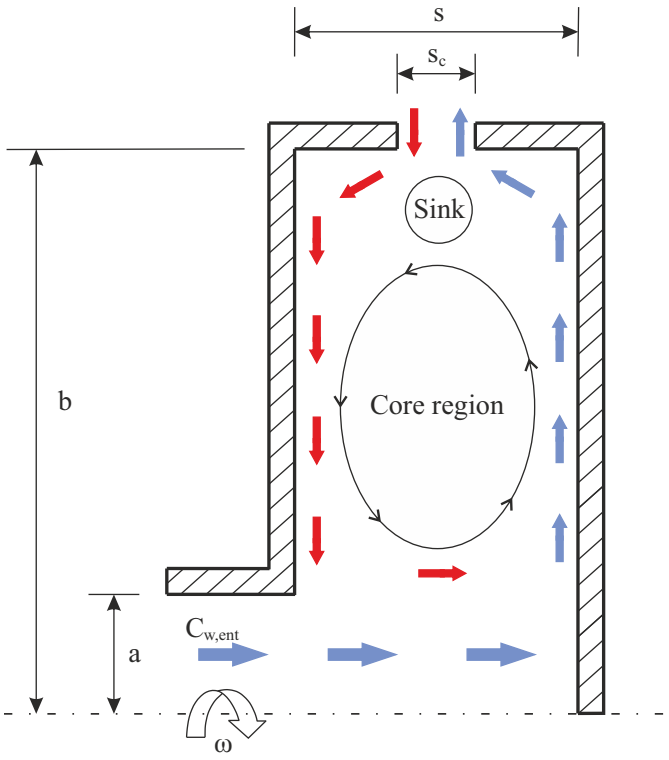

Figure 2.7: Schematic diagram of the flow structure in a shrouded rotor-stator cavity with axial seal gap and axial inlet (EASTWOOD, 2014)

meridian plane. The properties of the latter define whether the boundary layers are merged or not.

In the case of the non-merged boundary layers (II and IV) a so-called BATCHELOR (for finite disc length) or STEWARTSON (for open-end flows) flow structure is present (BRADY and DURLOFSKY, 1987; CHILDS, 2011), referring to the similarity analysis of BATCHELOR[2] (BATCHELOR, 1951) and STEWARTSON (STEWARTSON, 1953), which appears for rotor-stator configurations with a large gap s between both discs. In a BATCHELOR type of flow, the flow field is separated into two separate boundary layers and an inviscid core region. The boundary layer along the rotor is known as EKMAN or VON KARMAN layer, while on the stator wall it is called BÖDEWADT layer. In the case of the STEWARTSON type of flow, only one boundary layer, the EKMAN layer, on the rotor disc is present with the inviscid core flow.

The case of merged boundary layers (I and III) is only present for geometries with a very small gap between the discs. An earlier numerical study from RANDRIAMAMPIANINA et al. (1997) report the presence of a COUETTE flow structure, where the inviscid core is absent and only one viscous region is present.

[2]The governing differential equations aere solved under the assumption of a stationary axisymmetric flow between to infinite discs

Analytical expressions for the cavity aspect ratio G to distinguish between merged, non-merged and free disc behaviour were formulated by OWEN (1984). He defined the lower and upper limit for non-merged boundary layers as:

$$G_{min} = 0.23\, Re_{\phi}^{-0.2} \tag{2.32}$$

$$G_{max} = 1.05\, Re_{\phi}^{-0.2} \tag{2.33}$$

Values of G smaller than G_{min} refer to merged boundary layers, i.e. COUETTE type flow structure, and values of G bigger than G_{max} refer to free disc flows.

A typical shrouded rotor-stator configuration is depicted in Fig. 2.7 with a schematically illustrated flow field as it is present in regimes II and IV. A disc rotating with the angular velocity ω faces a stationary wall at a certain axial distance s. The geometry of the whole system is given by the inner radius of the stator a, the cavity outer radius b, the axial gap between rotor and stator s and the seal clearance s_c. The non-dimensional entrained fluid flow $C_{w,ent}$, which is also sometimes referred as sealing flow, enters the cavity axially and is pumped radially outward inside the boundary layer of the rotor wall. After impinging the shroud the flow is deflected in the axial direction and then partially exits the configuration through the seal and partially stays inside the cavity.

The portion staying inside the cavity impinges the stator wall and is then entrained radially inwards inside the stator boundary layer until it is turned again near the hub, by conservation of mass and momentum, to be pumped radially outwards again. The sink region in proximity to the seal clearance develops if air from outside the cavity ingests through the seal and mixes with the sealing flow. This happens when the sealing flow is smaller than the required amount of sealing air at the disc rim gap, causing a smaller pressure inside the cavity.

BAYLEY and OWEN (1970) analysed experimentally the sealing air requirements for a shrouded rotor-stator cavity with an axial seal clearance. For rotational REYNOLDS numbers $Re_{\phi} \leq 4 \times 10^6$ without external flow, they defined a correlation for the minimum required sealing mass flow rate as a function of the cavity gap ratio $G_c = s_c/b$ and Re_{ϕ}:

$$C_{w,min} = 0.61\, G_c\, Re_{\phi} \tag{2.34}$$

Later studies carried out by PHADKE and OWEN (1980) for a larger range of G_c and $Re_{\phi} \leq 1 \times 10^6$ derived the following correlation for the minimal amount of sealing flow:

$$C_{w,min} = 0.14\, G_c^{0.66}\, Re_{\phi} \tag{2.35}$$

Furthermore, a comparison of the required sealing mass flow for axial against radial seals was carried out by PHADKE and OWEN (1983). It was stated that radial seals require

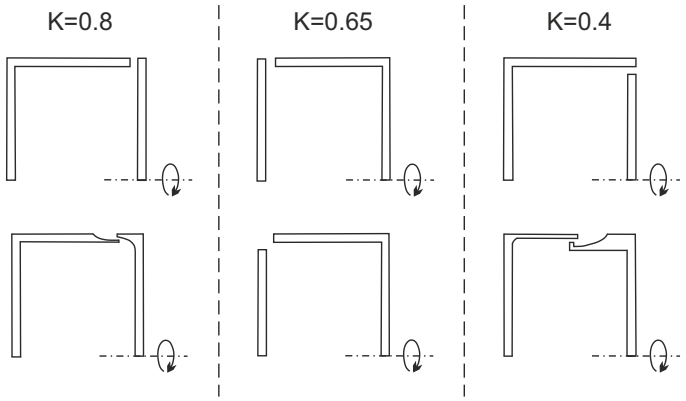

Figure 2.8: Corresponding K values for different rim seal geometries (CHEW et al., 1992)

less sealing flow which is due to a so called *pressure inversion effect*, which results in an increase of pressure in the cavity due to an increase in rotational speed.

CHEW et al. (1992) investigated the sealing of a rotor-stator cavity in the absence of an external flow as well. They derived a mathematical model to calculate the minimum required sealing flow for three different rim seal types and a range of gap sizes. The results calculated by the model were compared to experimental measurements and were stated to be in good agreement. The equation is similar to the correlations cited above but more general and applicable for a range of seal geometries. It is as follows:

$$C_{w,min} = 2\,\pi\,K\,\left(\frac{u}{\omega\,b}\right)\,G_c\,Re_\phi \tag{2.36}$$

where K is a value dependent on the type of seal (see Fig. 2.8) and u is the radial velocity at the outer radius b of the rim gap.

Regarding numerical achievements in the area of rotor-stator flows, CHEW and VAUGHAN (1988) set up a 2D axisymmetric RANS simulation using the finite difference method with a mixing length turbulence model and compared the results to the data from DAILY and NECE (1960) as well as to the data from DAILY et al. (1964). The authors concluded that their predictions were sufficiently accurate for most engineering tasks, although the velocities inside the core region were underpredicted.

With regard to heat transfer mechanisms in rotor-stator cavities different experimental and numerical studies have been carried out in the last two to three decades. For example STAUB (1992) discovered an interdependency of the swirl ratio, the sealing flow and the heat transfer in a typical rotor-stator cavity with a radial outlet. If the sealing flow is higher than the entrainment flow in the rotor boundary layer, then heat transfer is driven by the swirl flow and thus the correlation of the NUSSELT number is dependent on the swirl REYNOLDS number, which is based on the sealing flow inlet. For small sealing flows, the heat transfer is driven by the rotor speed and thus the correlation depends on the rotational REYNOLDS number Re_ϕ.

The swirl ratio β represents a dimensionless quantity for the absolute tangential velocity v_{abs} and is defined as:

$$\beta = \frac{v_{abs}}{\omega r} \tag{2.37}$$

A combined experimental and numerical study setting up a rotor-stator test rig with an axial inlet and radial outlet with a heated rotor wall was carried out by CHEN et al. (1994). Within the experiments, *Laser Doppler Anemometry* (LDA) was used to measure radial and tangential velocities as well as thermocouples and flux meters inside the rotor for measurements of metal temperatures and heat fluxes were implemented. The numerical analysis was achieved by solving the RANS equations using a low REYNOLDS number $k-\epsilon$ turbulence model. As they did not include the modelling of radiation in their numerical study, a large discrepancy in the NUSSELT number between their predictions and the measurements were detected. But as soon as they corrected the measured heat flux by subtracting the radiation term, the computed results were in better agreement with the predictions.

DJAOUI et al. (2001) carried out experimental and analytical analyses of turbulent flows and heat transfer in rotor-stator cavities with radial inflow for different cavity aspect ratios and ROSSBY numbers Ro. The latter describes the ratio between the inertial and the Coriolis forces and is defined as follows for a typical rotor-stator cavity:

$$Ro = \frac{2\,\dot{m}}{\rho\,\omega\,s\,b^2} = \frac{2\,s_c\,Re_m}{s\,Re_\phi} \tag{2.38}$$

with $Re_m = \dot{m}/\mu\,s_c$ being the REYNOLDS number based on the mass flow rate $\dot{m}$.

It was found out that the value of $Ro \approx 0.01$ defines the transition between rotationally and through-flow dominated regimes. Also it was stated by RAIMUNDO et al. (2002) that the heat transfer seems to have its minimum for this value of Ro. An empirical correlation for the averaged NUSSELT number Nu_{av} was defined by YUAN et al. (2003), who analysed the heat transfer on the stator disc of an opened rotor-stator system. For a STEWARTSON flow the empirical relationship is as follows:

$$Nu_{av} = -1.016\,Re_\phi^{0.4664} + 18.15\,Re_\phi^{0.6426}\,G_c - 126.3\,Re_\phi^{0.7485}\,G_c^2 + 707.5\,Re_\phi^{0.7749}\,G_c^3 \tag{2.39}$$

Furthermore, they were able to increase the average heat transfer for an optimum value of G_c and a given rotational REYNOLDS number.

More recently, PONCET et al. (2005a) carried out experimental measurements in water for a BATCHELOR type of flow in a turbulent flow in a rotor-stator cavity to study the behaviour of the entrainment flow coefficient $C_{w,ent}$ as a function of the REYNOLDS number Re_ϕ, of the through-flow rate C_{q_r} and the cavity aspect ratio G. The authors derived a correlation following a five-seventh power-law and benchmarked their correlation against

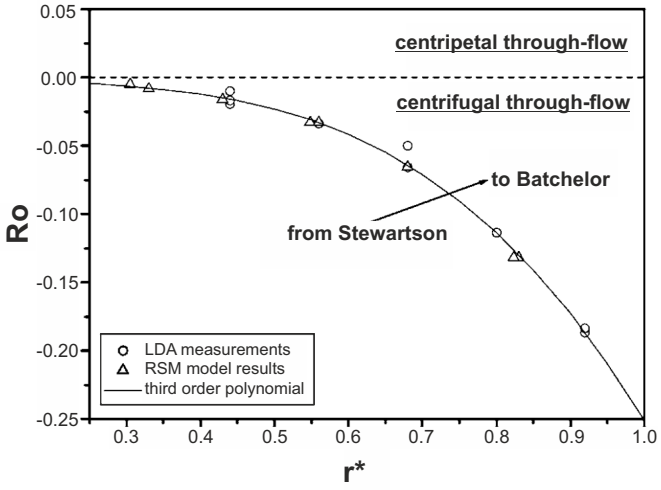

Figure 2.9: Transition diagram between BATCHELOR and STEWARSTON flow structure in the Ro-r^*-plane (PONCET et al., 2005b)

the velocity and pressure results obtained from the experiments. The final simplified expression is given as follows:

$$C_{w,ent} = 2\,(\hat{a}\,C_{q_r} + \hat{b})^{5/7} - 1 \tag{2.40}$$

where $\hat{a}$ and $\hat{b}$ are two experimental constants.

In another study, PONCET et al. (2005b) characterised the transition from a BATCHELOR type flow to a STEWARTSON type flow for a given radius and ROSSBY number. Fig. 2.9 shows the transition diagram in the Ro-r^*-plane. The ROSSBY number Ro is a function of the non-dimensional radius r^* and is fitted to the experimental and numerical data using a third degree polynomial function. The final single correlation is defined as:

$$Ro = 0.0088 - 0.0998\,r^* + 0.3048\,r^{*\,2} - 0.4646\,r^{*\,3} \tag{2.41}$$

In another combined analytical, numerical and experimental study, NOUR et al. (2009) investigated the turbulent flow behaviour in a shrouded rotor-stator system. Using hot-wire anemometry for the experiments and the second order RANS approach with a REYNOLDS stress model (RSM) for the numerical study, the authors derived an analytical expression and concluded that the core swirl ratio is only dependent on the pre-swirl ratio and the radial in- and outflow. Furthermore, it is stated that the chosen numerical approach is able to predict the flow field as is obtained during the experiments. DA SOGHE et al. (2011b) improved the prediction capability of their simplified one dimensional in-house code by introducing a new correlation for the friction coefficient of both, the rotor and the stator discs. The correlation was compared to an earlier correlation defined by HAASER et al.

(1987) and to CFD analysis results, which were obtained by solving the RANS equations using the $k-\omega-SST$ turbulence model. The in-house code uses empirical correlations to solve the governing equations for 1D steady-state axisymmetric flows. With the new correlation accounting for the friction coefficient, the discrepancies in the core swirl ratio were noticeably reduced.

2.3.2 Rotor-Stator Cavity/Main Gas Path Interactions

In the previous section, the fundamentals of rotor-stator cavities in a quiescent environment are given. By adding an external main annulus gas path, the complexity of the rotor-stator flows increases dramatically. This is mainly due to the nature of the external flow, which is hotter and of higher velocity than the cavity flow. Furthermore, it is highly asymmetric and unsteady, which is caused by the presence of 3D features, such as rotor blades and stator vanes moving relative to each other. This unsteadiness and asymmetry lead to a pressure profile above the rotor-stator cavity rim, which is also unsteady and asymmetric, provoking either *egress* or *ingestion* (blue hyphen and red plus sign, respectively, in Fig. 2.10). Ingestion means that the hot gases from the main annulus enter the cavity, whereas egress is the opposite, meaning that the cool air from the cavity enters the main annulus.

The ability to accurately predict component temperatures has always been one of the major tasks in the aero-engine industry, never more so than now as cycle temperatures increase and design margins are reduced. This also means that ingestion and egress play a key role in the design of turbine disc cavities in order to minimise the required amount of cooling air.

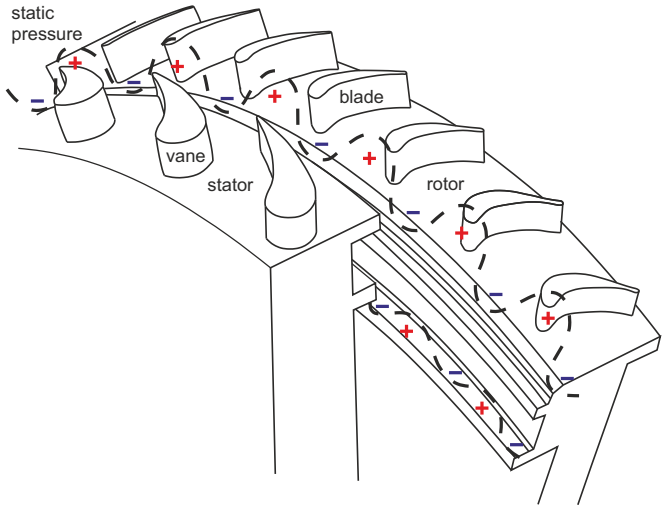

Figure 2.10: Variation of static pressure in a turbine main annulus for a double rim seal (positive and negative pressures with respect to the rotor-stator cavity) (SANGAN et al., 2014)

As already mentioned in the previous section, BAYLEY and OWEN (1970) carried out investigations on ingestion into rotor-stator cavities but without taking into account an external flow. The influence of the main annulus and its circumferential pressure variations on the cavity flow were investigated by ABE et al. (1979). The authors carried out experiments to study six different rim seal geometries using an upstream stator vane and a rotating disk. By visualising the flow with an oil paint method and by measuring static pressure and velocities in the rim region, it was found out that ingestion depends on the sealing air and main annulus flow velocities as well as on the rim seal size and type.

A few years later, PHADKE and OWEN (1988b; 1988c) carried out a set of experiments to analyse the effect of different seal geometries in an axisymmetric and asymmetric main annulus environment, respectively, but still without including an engine representative blade passage in the main annulus. For all seal geometries, the authors distinguished two dominant regimes causing hot gas ingestion: a *rotation-dominated* and a *external-flow-dominated* regime. Both regimes can be described as a function of the ratio of the external flow REYNOLDS number $Re_x = \bar{w}b/\nu$ (with $\bar{w}$ being the mean value of the axial velocity in the inner part of the main annulus) to the cavity rotational REYNOLDS number Re_ϕ. For low values of Re_x/Re_ϕ the ingestion is dominated by the rotation, whereas for large values of Re_x/Re_ϕ the ingestion is dominated by the main annulus, which is also known as "externally induced" ingestion (EASTWOOD, 2014). Two correlations for the minimum required sealing flow $C_{w,min}$ were derived for both regimes. In the case of a rotationally dominated regime, $C_{w,min}$ increases with Re_ϕ and the disc pumping effects dominate:

$$C_{w,min} \propto G_c^m \, Re_\phi^n \tag{2.42}$$

where m and n are seal shape dependent values.

For the regime with dominant externally induced ingestion $C_{w,min}$ is proportional to Re_x instead and the following correlation was derived from the experiments:

$$C_{w,min} = 2\,\pi\,K\,G_c \left(\frac{\Delta p_{max}\, Re_x^2}{\rho\, \bar{U}^2} \right)^{0.5} \tag{2.43}$$

with K and Δp_{max} being an empirical constant varying for different rim seal geometries and the maximum circumferential pressure difference in the main annulus, respectively. Furthermore, the authors showed that $C_{w,min}$ increases with increasing circumferential asymmetries.

Further experimental work was carried out in an axial turbine test rig including two radial rim seals by DADKHAH et al. (1992) and GREEN and TURNER (1994). Two different rim seal geometries were analysed, one with an upstream overlapping stator shroud and the other with an upstream overlapping rotor shroud. The first study only comprised stator vanes in the main annulus but no rotor blades. The comparison of both rim seal geometries with respect to their sealing effectiveness showed that in the case with the

upstream stator, the minimum required sealing flow is lower than in the case with an upstream rotor. Furthermore, it was observed that the amount of locally ingested air was lower for the upstream rotor configuration as soon as the entrainment flow was lower than the minimum required sealing flow.

The authors of the second study included the blade rows in the test rig. After evaluating the measurement results the authors concluded that the presence of the blades reduces the minimum required sealing flow. Furthermore, it was stated that the complete sealing of a rotor-stator cavity depends on the pressure inside the cavity: the pressure inside the cavity should be equal to the maximum pressure in the main annulus at the rotor blade leading edge. However, BOHN et al. (2000)'s experimental and numerical simulations for a different rim seal geometry found that the presence of the blades reduced the sealing performance.

DANIELS et al. (1992) conducted experiments to evaluate the sealing effectiveness of four different rim seal geometries for diverse flow conditions. In order to determine the rim seal ingestion, a gas tracing methodology using CO_2 as the tracer was implemented into the rig setup. It was found that a reduction of the radial gap improves the sealing effectiveness rather than increasing the axial overlap.

Another experimental and numerical study on hot gas ingestion into a rotor-stator cavity was that of CHEW et al. (1994). They concluded that in a external-flow-dominated regime the asymmetric pressure distribution downstream of the NGV is very likely to be the driving parameter to having an influence on the sealing effectiveness. The pumping effect coming from the rotor disc is rather of secondary importance in such regimes. From a numerical point of view, HILLS et al. (2001) carried out CFD simulations of a rotor-stator cavity geometry in order to reproduce the ingestion observed from experimental measurements. By doing that it was found that steady-state RANS solver solutions tend to significantly underpredict the level of hot gas ingestion. Solving the governing equations using an unsteady approach gives a better agreement but still fails to predict the level of ingestion accurately.

SCANLON and WILKES (2004) developed a preliminary design tool for main annulus gas ingestion predictions in a rotor-stator cavity. They presented a simple method to derive the pressure asymmetries in the main annulus coming from the rotor blades, which then can be used to calculate the amount of ingested air. The model was benchmarked against two different experimental test cases with generally good agreement. Nevertheless, besides the fluctuations arising from the blade passage, the authors discovered the presence of lower frequency fluctuations inside the rim gap, which their model was not able to predict. Therefore they came to the conclusion that these unsteady pressure fluctuations are of importance to ingestion problems.

Similar observations were amongst others made by CAO et al. (2004) experimentally and numerically. In this study a two stage turbine rig at engine conditions was equipped with fast response pressure transducers in order to measure the flow features in the rim. The obtained measurements were compared to the steady and unsteady CFD simulations.

Good agreement was achieved for the time-averaged pressure calculations using an unsteady approach, as was already suspected by CHEW et al. (1994). Besides confirming the presence of lower frequency fluctuations in the rim seal region, the authors showed that by reducing the rim gap, the ingestion could be reduced and also the instabilities could be suppressed.

BOUDET et al. (2005, 2006) conducted numerical simulations of an engine representative turbine stage where they also detected the instabilities mentioned above: the high frequency fluctuations arising from the potential effects of the blades as well as the low frequency flows forming in the rim seal. Furthermore, it was shown that the lower frequency instabilities are generated due to the presence of a non-linear coupling with the blade passing frequency. Another study on rim seal geometries with respect to external flow ingestion was accomplished by BOHN et al. (2006), who conducted experiments on a 1.5-stage turbine rig. After comparing the sealing effectiveness of conventional axial seals to radial seals with an axial offset, it was suggested that the radial seal gaps were more effective.

ROY et al. (2007) investigated the rim seal in a single stage axial turbine. Both, the rotor blades and the stator vanes were included in the external flow path, which was connected to the cavity by an radial overlapping rim seal. During experiments, *Particle Image Velocimetry* (PIV) was used to visualise the flow field near the rim. Additionally three-dimensional unsteady CFD simulations were carried out. The authors detected two different flow regimes: firstly, there was a highly swirled flow, i.e. a flow with high tangential velocity, at the outer radius of the rim, which according to the authors, is related to the blade passage and which is ingested into the cavity. Secondly, there is a second flow with low swirl near the rim, which is attributed to air coming from the cavity and which enters the main annulus (egress). These observations lead to the conclusion that it is crucial to have three dimensional time-resolved flow fields to make predictions of ingestion.

ZHOU et al. (2009) did a follow-up study on the same facility. They analysed the effect of different aspect ratios of the rotor-stator cavity on the interaction in the rim gap and compared the results from experiments (PIV and concentration measurements) to the results of a three-dimensional CFD sector model solution. As in previous studies, the CFD underpredicts ingestion. Here, the authors brought forward the argument that the sector model failed to capture the circumferentially rotating, low pressure areas near the rim seal.

In his two part paper, OWEN (2010; 2012) solved the incompressible orifice flow equations for the regimes of rotationally-induced and combined ingress, respectively. The analytical solution for the rotationally-induced ingress shows that the sealing effectiveness ϵ_s depends on the ratio of the non-dimensional egress ($C_{w,e}$) and ingress ($C_{w,i}$) flow rate Θ_0, the minimum non-dimensional sealing flow rate $C_{w,min}$, the ratio of the discharge coefficients for ingress and egress $\Gamma_c = C_{D,i}/C_{D,e}$ and the swirl ratio of the external flow β. The comparison to the experiments by GRABER et al. (1987) showed good agreement for a large range of rotational REYNOLDS numbers and swirl ratios. As the author did not

consider diffusion effects in his calculations, at the higher values of ϵ the calculated results are over-predicting the experimental measurements.

In order to benchmark the solution of the orifice model for the combined internal and external induced ingress, the authors used the experimental data from PHADKE and OWEN (1988c). It was concluded that the driving mechanism for the combined ingress is solely dependent on the ratio of the axial REYNOLDS numbers in the main annulus Re_x to the rotational REYNOLDS numbers Re_ϕ. This assumption was confirmed by the experiments. Furthermore, the authors suspected that the orifice model in the *saw-tooth version*, as it was used in this study, can be taken to determine a minimal required sealing flow for any value of Re_ϕ. This would only require one set of experimental measurements. However, this theory still needs to be confirmed.

Further investigations on the orifice flow model were conducted by ZHOU et al. (2011) to estimate the sealing effectiveness at engine representative conditions. They improved the predictions for the test case of GRABER et al. (1987) by adapting the values for the ratio of the discharge coefficients Γ_c and the minimum required sealing flow rate using a statistical matching approach against empirical data. The predictions for externally induced ingress were in good agreement to the data of JOHNSON et al. (2008) and OWEN (2010). Furthermore, ZHOU et al. (2013) carried out CFD simulations for an axial rim seal geometry model and compared the results to those from the orifice model. Both predictions were in good agreement which underlines the assumption that at engine representative conditions the ingress and egress is driven by pressure fluctuations in the main gas path.

These findings were supported by the experimental study of SANGAN et al. (2012a; 2012b; 2013), who additionally analysed radial seal geometries as well as double seals. Results of the experimental measurements in comparison to the orifice model equations

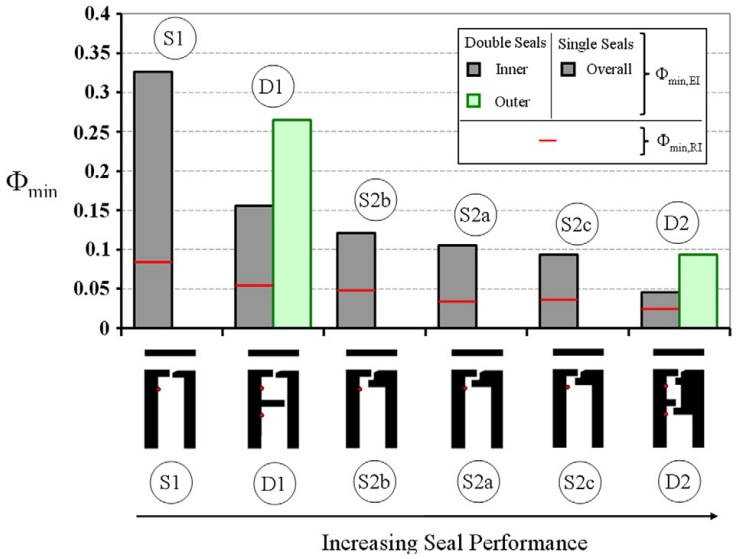

Figure 2.11: Ranking of sealing performance in order of magnitude of the non-dimensional minimum sealing parameter Φ_{min} for different rim seal geometries (SANGAN et al., 2013)

solutions were compared and found to be in very good agreement. Fig. 2.11 depicts a ranking of the analysed seal configurations. It can be seen that a single axial seal geometry has the worst sealing performance and that a radial double seal configuration performs best. Besides this, the authors concluded that a double seal geometry approximately reduces the required amount of sealing flow rate by 50 % compared to its corresponding single seal type.

2.3.3 The Main Annulus Gas Path Interactions (MAGPI) Research Project

This section gives a brief introduction into the EU-funded research project MAGPI (2006). A two-stage axial turbine rig - including a main gas path and a secondary air system - was designed and built at the University Of Sussex, with the purpose of gaining test data for an improved understanding of turbine disc heat transfer, of hot gas ingestion and of the spoiling effects of cooling air flow with respect to the overall engine performance and the cooling mechanism itself. The rig geometry, comprising the blade profile design as well as all the seals, such as the rim seal or the interstage seal in the TSW, and the operating conditions during testing were designed to be engine representative. After having conducted the tests, the well documented experimental data was used for validation purposes of available design tools in order to improve the prediction capability for the provision of adequate secondary air system flows, especially when interacting with the main annulus. During the last couple of years some of the experimental data obtained during the project was analysed and validated by the members of the MAGPI consortium.

Dixon et al. (2013) analysed the effect of cooling flow entry locations with respect to the cooling effectiveness of the rear face of the upstream rotor disc. Two cases were analysed and compared using adiabatic steady-state CFD: a radial inlet through a drive arm hole and an axial inlet through a lock plate slot in the first rotor disc. The results of how the thermal effectiveness ($\eta_{eff} = (T_{hot} - T)/(T_{hot} - T_{cool})$) changes with changing amount of cooling air are depicted in Fig. 2.12. The coloured numbers in the graph, represent the turbine stage efficiency η, which was additionally calculated for each case. From those results, it can clearly be seen that the lock plate geometry is outperforming the conventional drive arm hole geometry by means of cooling air requirements for a given disc temperature. Also it can be seen that the stage efficiency decreases with increasing cooling air mass flow, which is due to the egress of the cooling air into the main annulus. Furthermore, the authors carried out a manual linking between the in-house codes SC03 (CSM) and HYDRA (CFD) in order to predict metal temperatures.

In a related study, Guijarro Valencia et al. (2011) presented an automated coupling methodology for heat transfer and metal temperature predictions using the in-house tools SC03 for the solid and HYDRA for the fluid side (hFTB method). Both tools communicate through a proprietary communication library and exchange heat flux and temperatures through applied convective boundary conditions. In this study, a 2D axisymmetric CFD solution is coupled to a 3D CSM model. The authors benchmarked their

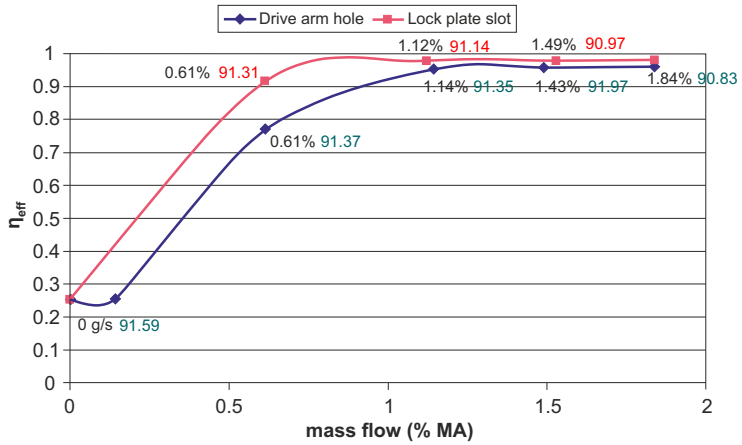

Figure 2.12: Thermal effectiveness η_{eff} on the rear face of the rotor 1 disc for different cooling flows including calculated values for the turbine stage efficiency (DIXON et al., 2013)

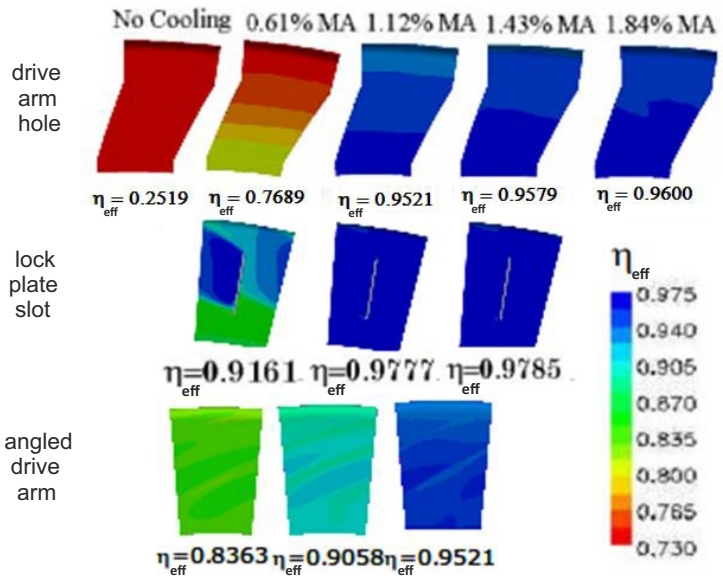

Figure 2.13: Contours of thermal effectiveness on the rear face of the rotor 1 disc for three different cooling air inlet configurations for different amounts of cooling efflux (GUIJARRO VALENCIA et al., 2011)

method against the data from a non-cooled re-ingestion experiment. The results were very promising in comparison to the experimental measurements and the predictions coming from the manually linked method. Only on the stator wall in the region of the interstage seal clearance were larger discrepancies detected. This was explained by an increase of this clearance during hot running, which was not considered in the numerical calculations.

Besides the validation of that test case, the authors presented numerical adiabatic steady-state CFD results for a cooled geometry with an angled drivearm hole. These results were compared to the calculations from DIXON et al. (2013). In Fig. 2.13 the contours

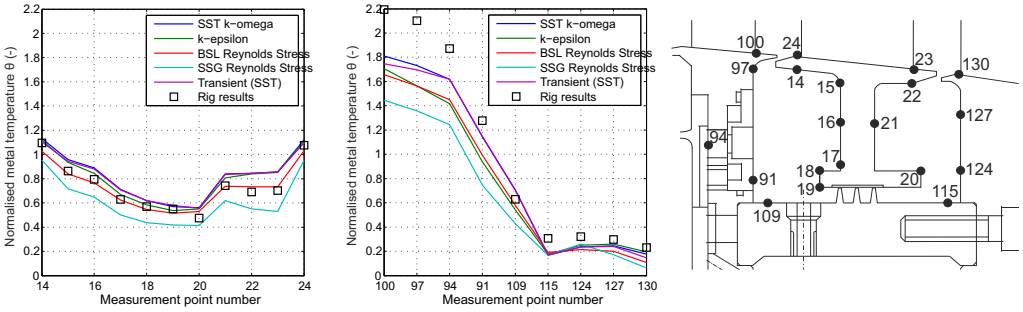

Figure 2.14: Stator foot (left) and rotor disc (middle) normalised metal temperatures θ in the TSW with the respective thermocouple locations in the rig (right) (SMITH et al., 2012)

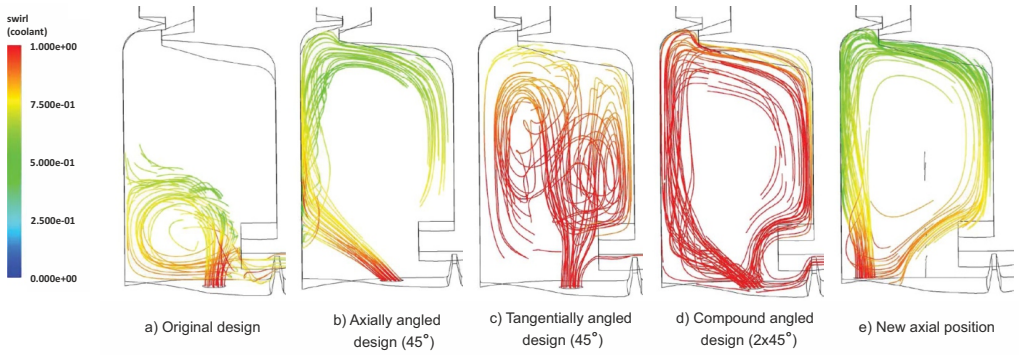

Figure 2.15: Cooling air streamlines coloured by swirl fraction for different drive arm hole angles and positions for the flow case with low ingestion (DA SOGHE et al., 2011a)

of thermal effectiveness on the rear face of the upstream rotor disc for the three different configurations are visualised for varying amounts of cooling efflux. The area-averaged value is given below each contour plot. The authors showed that the performance of the angled drive arm hole geometry lies between the other two configurations.

SMITH et al. (2012) conducted a numerical study on a cooled TSW using the conjugate method, where the solid and fluid regimes are solved within one single code (see Subsec. 2.1.3). Different turbulence models, such as $k-\omega-SST$, $k-\epsilon$ and REYNOLDS stress models, were compared to each other with the aim of accurately reproducing the experimental measurements. The results of the normalised wall metal temperatures ($\theta = (T - T_{cool})/(T_{hot} - T_{cool})$) for both the rotor and the stator, can be seen in Fig. 2.14. The conjugate method reproduced the metal temperatures very well on the stator foot, but had problems calculating the correct values on the rotor disc in the rim region (measurement point numbers 100, 97 and 94). These deviations were explained with a possible problem with the main annulus solution due to the choice of non-ideal turbulence models, which do not correctly capture the secondary flows in the blade passage, which might have a stronger impact on the heat transfer on the outer disc radius than expected. Although a transient solution was presented, the authors strongly advised not to use it for practical purposes due to its long run time.

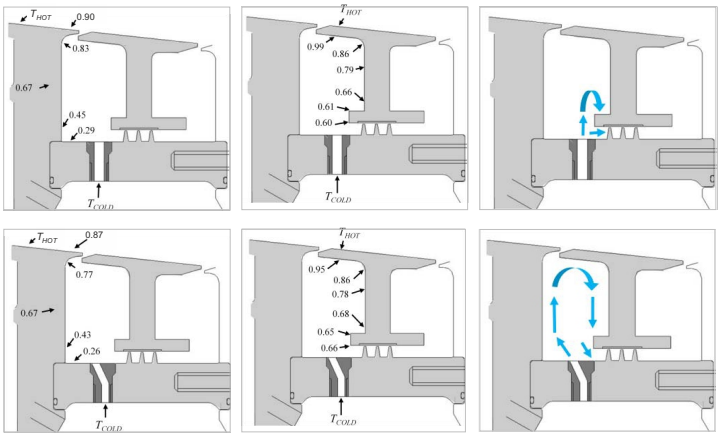

Figure 2.16: Measured normalised metal temperature data and schematic flow structure for a straight (top) and axially angled (bottom) radial cooling efflux (Coren et al., 2011)

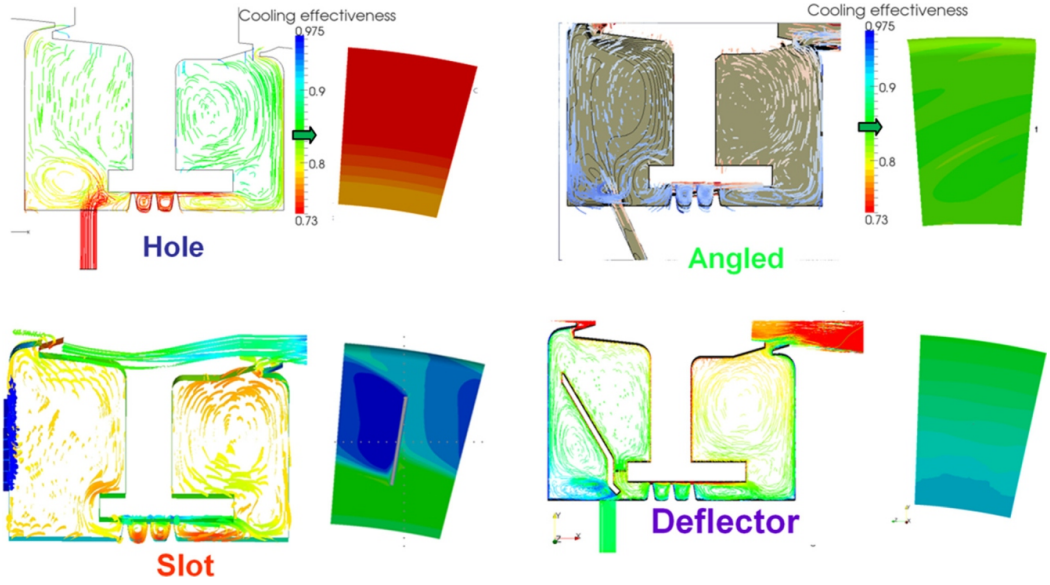

Figure 2.17: Streamlines coloured by cooling effectiveness (=thermal effectiveness) for the three different TSW configurations with $30\,\mathrm{g\,s^{-1}}$ cooling air efflux (Dixon et al., 2014)

After reviewing a range of different turbulence models, it was suspected that the models with ω-based near wall treatment (SST and BSL Reynolds stress model) were best suited to capture the rig flow physics. However, in the overall performance, it was concluded that the $k-\omega-SST$ turbulence model is most suitable for pressure, metal and fluid temperature predictions. In addition to that, it is also more robust than the Reynolds stress model.

Da Soghe et al. (2011a) conducted a numerical study on a cut-down model of the complete geometry, which only comprised the second stator vane and the TSW. Following the conjugate method for steady-state RANS with a $k-\epsilon$ turbulence model in its standard high Reynolds formulation, cases with three different amounts of cooling air mass flow rate (55, 70 and $90\,\mathrm{g\,s^{-1}}$) were validated against experimental metal temperature mea-

surements on the stator foot. The comparison showed good agreement in predicting the trends of the measured temperatures. However, the higher the cooling air mass flow rate was chosen, the less accurate the calculations compared to the experiments.

Furthermore, the authors analysed the cavity sealing performance for different drive arm hole angles and positions. A numerical parameter study was conducted in order to get an idea of the impact of different cooling air supply configurations on the thermal effectiveness at the walls. Fig. 2.15 shows the results of the flow case with low ingestion from the main annulus. All modifications promote a deeper penetration of the cooling air into the cavity compared to the original design. With regard to the thermal effectiveness, it was shown that the modified configurations perform better as well. The same observations were made for the flow case with high ingestion from the main annulus.

Based on that study, Coren et al. (2011) conducted experiments with an angled drive arm hole. After a numerical optimisation process to detect the optimum angle, which was carried out by Andreini et al. (2009) and due to manufacturing restrictions, the bore hole was inclined by 25°. Results of the non-dimensional metal temperature on the disc are depicted in Fig. 2.16. These results support the findings from Da Soghe et al. (2011a) that the cavity cooling is improved by the implementation of an axially angled drive arm hole. Due to the angled inlet the cooling air momentum is increased and the air flow is directed towards the rotor disc where it first impinges the wall. Then it is pumped radially outwards and finds its way back to the interstage seal along the stator wall, whereas in the case with the straight drive arm hole the air tends to turn directly towards the interstage seal.

For the non-cooled TSW Dixon et al. (2014) improved the CFD to CSM coupling methodolgy for metal temperature predictions presented by Guijarro Valencia et al. (2011) by using a 3D geometry to solve the governing equations in the fluid. Although the 2D results were already promising, the implementation of a 3D CFD option gave the opportunity to also couple non-axisymmetric geometries, such as cooled TSW. They compared the results from a coupled solution for the $55\,\mathrm{g\,s^{-1}}$ case and were able to reproduce the metal temperatures within 2 K compared to the experiments. Only, near the rim region, as stated by Smith et al. (2012), larger discrepancies were detected. This was also related to the inability of capturing ingestion properly by the chosen turbulence model (Spalart-Allmares) and in general by other available turbulence models.

Besides validating the coupling methodology, the authors presented a new TSW configuration including a mounted deflector plate to the stator foot. As a follow-up study of Dixon et al. (2013), the authors conducted steady-state CFD simulations of the deflector plate geometry and classified the performance of thermal effectiveness and turbine stage efficiency of the four different configurations (straight and angled drive arm hole, lock plate slot, deflector plate). It was concluded that the configurations with the lock plate slot and the deflector plate provide the best the rotor disc cooling. In Fig. 2.17 streamlines inside the TSW coloured by thermal effectiveness (in this study named cooling effectiveness) are visualised with their corresponding rear face of the first rotor disc for all geometries. On

this basis, it was also shown that the lock plate slot achieves the best rotor disc cooling just ahead of the chosen deflector plate geometry.

Guijarro Valencia et al. (2012) published a joint paper (Rolls-Royce, Siemens, Turbomeca and University Of Florence) on a numerical study to predict re-ingestion. Different flow solvers, including in-house (HYDRA) as well as commercially available ones (CFX and FLUENT) were used to reproduce the amount of ingestion measured experimentally. The authors compared different turbulence models (Spalart-Allmares with wall functions, $k-\omega-SST$, $k-\epsilon$ standard and realisable both with wall functions) and also conducted steady-state and unsteady RANS simulations. After comparing the numerical results to the experimental test data, it was concluded that steady-state CFD cannot predict ingestion levels accurately. URANS solutions instead are able to predict ingestions partially, however, the predicted ingestion is still significantly lower than the measured value. This was attributed to the limited capability of RANS to predict the diffusion of a jet in cross-flows. In order to obtain more accurate predictions it is necessary to look into higher order turbulence models, e.g. large eddy simulations (LES) (O'Mahoney et al., 2011; Zhou et al., 2011).

In a practical aero engine context - outside the MAGPI project - Young et al. (2012) analysed the effect of a deflector plate attached to the rotating component with regard to improve the cooling effectiveness of the rotor disc. Due to the deflector plate the cooling air is entrained in the direction of the disc after entering the cavity, which results in a better cooling of this engine life critical component. The outcome was that promising that it has been patented successfully and included in subsequent engine design.

2.4 Interstage Seal Flows And Seal Clearance Uncertainties

Interstage seals are used in modern gas turbine applications to maintain stage efficiency by means of controlling and reducing the air flow rate from high to low pressure cavities. In

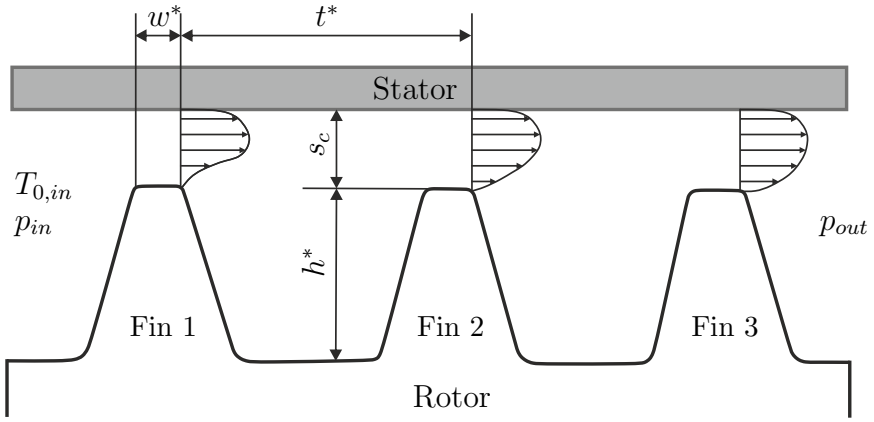

Figure 2.18: Straight through labyrinth seal with main geometrical features (Zimmermann and Wolff, 1998)

general the seals are designed in a labyrinth configuration, either in a *straight through* or a *stepped* arrangement. A schematic illustration of a straight through three fin labyrinth seal as it can be found in a TSW can be seen in Fig. 2.18. The seal flow is largely influenced by the number of fins, the clearance size s and the static pressure drop across the seal, which is a function of the upstream and downstream conditions including the pressure drop over the stage in the main annulus.

The seal flow can be calculated using the ST. VENANT-WANTZELL equation for an ideal isentropic nozzle flow together with a single discharge coefficient. The mathematical formulation is as follows:

$$\dot{m} = C_D \cdot \dot{m}_{ideal} \tag{2.44}$$

with

$$\dot{m}_{ideal} = \frac{p_{in} A}{\sqrt{T_{0,in}}} \cdot \left(\frac{p_{out}}{p_{in}}\right)^{\frac{1}{\gamma}} \cdot \sqrt{\frac{2\gamma}{R\,(\gamma - 1)} \left[1 - \left(\frac{p_{out}}{p_{in}}\right)^{\frac{\gamma-1}{\gamma}}\right]} \tag{2.45}$$

where $\dot{m}$ is the air mass flow through the seal, C_D the discharge coefficient, p_{in} and p_{out} the fluid static inlet and exit pressures, respectively, A the cross-sectional area between the fin tip and the stator foot, $T_{0,in}$ the fluid total inlet temperature, γ the isentropic exponent and R the gas constant.

In the past, numerical studies were carried out in order to derive correlations of discharge coefficient predictions for different labyrinth seal types and for a variety of fin numbers covering a range of pressure ratios and clearance sizes. Amongst others, WITTIG et al. (1987) achieved good agreement with experiments by solving the 2D time averaged NAVIER-STOKES equations for different straight through and stepped labyrinth seals and different numbers of fins. ZIMMERMANN and WOLFF (1998) later derived a set of correlations for labyrinth seal flow predictions for practical applications by adding design dependent correction factors to the correlations of HODKINSON (1940). More recently, KIM and CHA (2009) carried out CFD simulations for straight through and stepped seal arrangements. The authors compared the outcome of the simulations to experiments as well as to results from an analytical expression. It was stated that an improvement in seal flow predictions was achieved by using CFD instead of the analytical expression.

From these seal flow studies, one common conclusion can be drawn: it is crucial to have the correct geometrical measures and details of the seal in order to predict seal flows accurately. As an aero-engine undergoes different operating conditions during a typical flight cycle, i.e. varying temperatures, stresses and resulting component displacements, the seal clearances vary as well. From an engineering perspective, it is desirable to have the ability to accurately predict these behaviours in order to stay within the environmental and safety margins and to maximise component performance and life. As modern engines

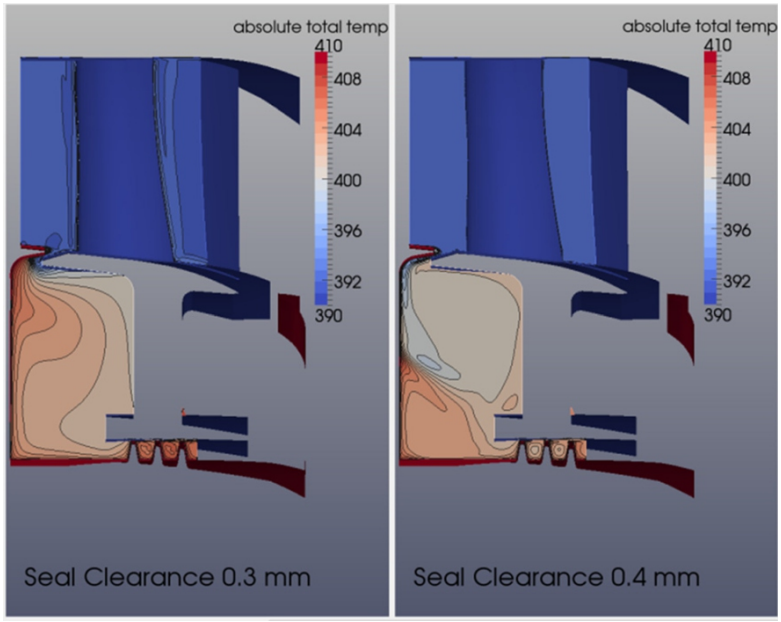

Figure 2.19: Contours of absolute total fluid temperature in the upstream cavity of a TSW for cold (left) and hot (right) running clearances (DIXON et al., 2014)

are required to provide ever improving performance, often at harsher operating conditions, the ability to predict temperatures and displacements becomes very relevant: on the one hand, to prevent damage of components, on the other hand, to know the exact amount of air flowing internally within the secondary air system, not only in the design condition but throughout the engine life-span.

Within the MAGPI project, DIXON et al. (2014) analysed the effect on the flow structure in a non-cooled TSW for two different interstage seal clearances, in cold built and hot running conditions. The meshes were generated independently. Steady-state and unsteady adiabatic CFD simulations as well as a thermal coupled CFD-CSM simulation were carried out and showed significant differences of hot gas ingestion near the rim, which gave different flow fields and temperatures in both upstream and downstream cavities. In Fig. 2.19, the contours of absolute total fluid temperature show that the level of ingestion is higher for the hot running clearance.

Based on these findings, other researchers have also been involved in developing methods which enable mesh modifications to allow for changes in seal clearances. In order to do that, it is essential to determine a method, which is able to modify the mesh to the changed geometry. According to LIU et al. (2006) and AMIRANTE et al. (2012a,b) there are two ways in achieving that: either by regenerating the mesh or by deforming the mesh. The former is robust and flexible to handle large geometry changes but has limited mesh control. The latter will keep the mesh topology and is robust for small geometrical perturbations but cannot handle large deformations and is limited to multi-block structured mesh movements. In the field of turbomachinery and aero-engines, several studies on the aircraft external aerodynamics (REUTHER et al., 1996; BYUN and GURUSWAMY, 1998) as

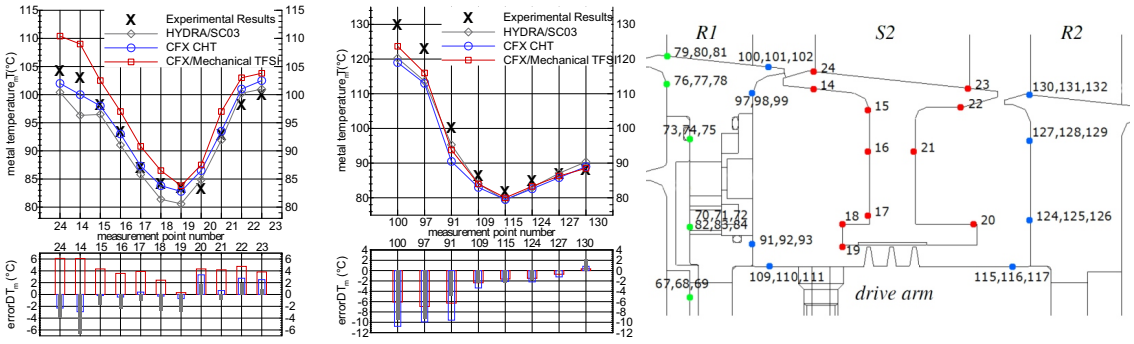

Figure 2.20: Comparison of predicted metal temperatures to experimental measurements at the stator (left) and the rotor (right) walls taking structural deflections into account (blue and red lines) (LÜCK et al., 2014a)

well as on aero-engine main annulus aerodynamics (BLOM and LEYLAND, 1997) can be found.

The application to secondary air system geometries has only been developed in recent years. AMIRANTE et al. (2012a,b,c) extended the existing aero-thermal coupling approach between the CFD code HYDRA and the CSM code SC03 by including an additional iteration loop, which takes into account the structural deflections. The mesh adaptation was achieved using a torsional spring analogy, which was already implemented successfully in earlier 2D and 3D studies (FARHAT et al., 1998; DEGAND and FARHAT, 2002; MARCOU et al., 2007). The full coupling algorithm is explained in detail in (2012a). Within the study of AMIRANTE et al. (2012c) an axisymmetric TSW model is simulated where the focus lies on the practicability of the method throughout a transient cycle. The application of the method has been further extended by the same authors (AMIRANTE et al., 2012b) to a 3D thermo-mechanical model giving promising results on temperature predictions, which were compared to results produced with empirical correlations. Even at initially balanced ingestion/egress conditions, a change of seal clearance changes the solution inside the cavities significantly, either provoking more ingestion or egress for a larger or smaller interstage seal clearance, respectively.

Another study analysing the influence of seal clearances on metal temperature predictions in a TSW was carried out by LÜCK et al. (2014a). The authors compared two different available numerical strategies using the commercial fluid and solid solvers CFX and Mechanical, both from ANSYS. It was shown that the use of a conjugate heat transfer (CHT) method and a *thermal fluid-structure interaction* (TFSI) approach, which both accounted for the mesh motion solving the *displacement diffusion equation* as it is implemented in CFX, the discrepancies in metal temperature predictions compared to experimental test data could partially be reduced. A summary of the comparison of the two applications against test data and previously published predictions (DIXON et al., 2014) can be found in Fig. 2.20. Using the CHT method, the predictions were significantly improved at the stator walls whereas at the rotor walls the discrepancies in the rim region were still very

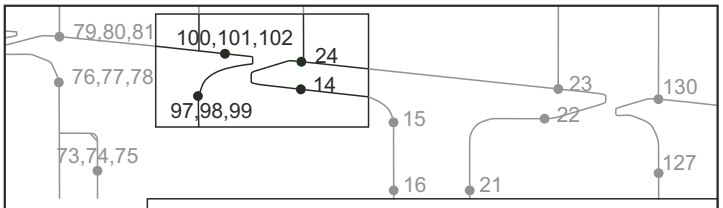

	ΔT at the rim gap thermocouples (K) Predicted - Measured			
	Rotor		Stator	
	MP97	MP100	MP14	MP24
DIXON	-9.5	-9.3	-3.9	-6.6
SMITH	-8.1	-7.9	-0.8	-1.0
DA SOGHE	*N/A*	*N/A*	*N/A*	*N/A*
LÜCK	-7	-6	+6	+4

Figure 2.21: Compilation of previous computational results at the rim seal compared to experiments (DIXON et al., 2014; SMITH et al., 2012; DA SOGHE et al., 2011a; LÜCK et al., 2014a)

large. The use of the TFSI approach led to a slight reduction of the discrepancies at the rotor rim but to a significant overprediction of the stator rim temperatures.

A summary of the metal temperature discrepancies between computations and experiments of the MAGPI TSW rig is given in Fig. 2.21. It clearly shows the difficulties of matching the temperatures near the rim, although slight improvements were achieved by LÜCK et al. in considering the hot running seal clearances.

From a stochastic point of view, MONTOMOLI et al. (2014) analysed the effect of rare events on the metal temperatures of a TSW geometry during the transient. An *uncertainty quantification* study was carried out to quantify the impact of *black swans* on the temperature predictions. It was shown that on the one hand, the variations in predicting the mean temperature values were considered minor, but on the other hand, the variation of thermal gradients could reach up to two orders of magnitude. In order to reduce these uncertainties, an optimisation of the transient cycle was carried out, leading to the conclusion that a slow acceleration is beneficial to reduce the temperature gradients.

2.5 Optimisation Methods in Turbomachinery

Optimisation methods have their origin in mathematics and date back to the 1940's, where they were firstly used to solve rather simple quantitative problems. Over the years, these methods were enhanced and applied amongst others to problems in economics, physics, computer science and engineering. With ever increasing computational power, it is possible

to solve optimisation problems of increasing size as well as complexity. This is especially of importance in the field of engineering and turbomachinery, where the use of expensive CFD and CSM calculations in the preliminary design process is inevitable. In the upcoming subsections the reader is introduced to a typical optimisation problem definition, some existing optimisation algorithms as well as metamodeling approaches as they have been successfully used in turbomachinery problems.

2.5.1 General Optimisation Problem Definition

Two different optimisation problems have been identified: a *single-objective* and a *multi-objective* optimisation. As one would imply by the names, a single-objective optimisation only minimises or maximises one objective whereas in a multi-objective several objectives are minimised or maximised at the same time. In general, an optimisation problem is defined by one or more so called *objective functions* $f_m(\mathbf{x})$, which are sought for minimum values, while satisfying a number of problem dependent constraints:

$$\begin{aligned}
&\text{Minimise} && f_m(\mathbf{x}), && m = 1, 2, ..., M; && (2.46)\\
&\text{Subject to} && g_j(\mathbf{x}) \geq 0, && j = 1, 2, ..., J; && (2.47)\\
& && h_k(\mathbf{x}) = 0, && k = 1, 2, ..., K; && (2.48)\\
& && x_i^l \leq x_i \leq x_i^u, && i = 1, 2, ..., n; && (2.49)\\
&\text{With} && \mathbf{x} = [x_1, x_2, ..., x_n]^T && && (2.50)
\end{aligned}$$

where $\mathbf{x}$ is the *design vector* containing the n *design parameters* $x_1, ..., x_n$. The superscripts l and u define the lower and upper limit of a particular design parameter x_i. Such design parameters can for example be a length or the thickness of a component, a distance of one component to an other or an angle between two components or any other geometrical engineering parameter.

Typical objective functions in the aero-engine sector can be the minimisation of the engine specific fuel consumption or the weight of a component or the maximisation of the engine efficiency. As the basic strategy is a minimisation of the objective function, maximisation problems can be tuned in such a way that the inverse value is minimised.

Equation 2.48 represents the so called *inequality constraints*, which have to be satisfied while minimising the objective function. Such constraints can be upper temperature limits, which must not be exceeded or minimum stress levels inside components to guarantee a defined minimal life of a component.

The *equality contraints* in Eq. 2.49, define the relationship between particular design parameters. These constraints can be eliminated from the optimisation problems by a suitable choice of design parameters.

In a single-objective optimisation problem it is possible to find one optimum solution or one optimum design while ensuring that the defined constraints are satisfied. In a multi-

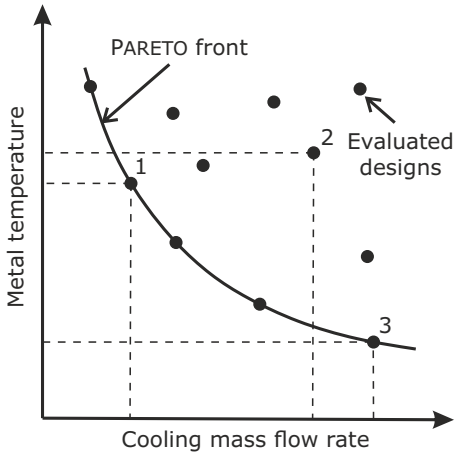

Figure 2.22: Typical PARETO front of a 2D multi-optimisation problem

objective optimisation this is not the case anymore, as the multiple objectives usually conflict with each other. The solution of such a problem is known as a *PARETO front*, i.e. none of the objective functions can be improved without increasing another objective function. An example for a two-objective PARETO front is depicted in Fig. 2.22, where both objectives need to be minimised.

Comparing the points 1 and 2, it can be seen that point 1 performs better than point 2 for both the metal temperature as well as the cooling mass flow rate. The comparison of points 1 and 3 instead do not show dominance of any design as for 1 the cooling mass flow rate is lower than for 3 but the metal temperature behaves in the opposite way. Therefore designs 1 and 3 are both PARETO optimal. In order to determine the optimal solution it is necessary to very carefully consider, which objective is the most important one and should be weighted accordingly.

A further possibility to solve a multi-objective optimisation problem is to transform it into a pseudo-single-objective optimisation problem. This means, that only one objective function is optimised, which is defined as the weighted sum of the multiple objective functions:

$$F(\mathbf{x}) = \sum_{m=1}^{M} w_m \cdot f_m(\mathbf{x}) \tag{2.51}$$

where w_m is the weighting factor for the m-th objective function. The final solution then corresponds to one PARETO optimum, depending on the weighting coefficients for each objective.

The challenge in solving optimisation problems in engineering, either single- or multi-objective, is the complexity of the engineering problem itself. It is not uncommon to have large 3D CFD and CSM models dealing with unsteady and mixing flows including conjugate heat transfer at the walls. In such a case, one single evaluation can take several hours or days and as a result the optimisation can take several weeks to find the optimum solution. Therefore, it is essential to have a robust and reliable optimisation strategy to

get to the final design as quickly as possible and thus reduce the overall computational time of the optimisation. Furthermore, it is essential to reduce the dimensionality of the optimisation problem to a minimum, i.e. keep the number of design parameters minimal while still ensuring complete design space coverage, as the addition of one extra dimension to that design space results in an exponential increase of the design volume ($\propto n^k$). In optimisation, this relationship is often referred as the *curse of dimensionality*.

2.5.2 Optimisation Algorithms

This subsection gives an overview of some of the available optimisation algorithms, which can be applied to the optimisation problems stated in the previous subsection. They can be subdivided into two major groups, depending on their approach for getting from one iteration $\mathbf{x}_i$ to the next iteration $\mathbf{x}_{i+1}$, following the equation:

$$\mathbf{x}_{i+1} = \mathbf{x}_i + \beta_i \cdot \mathbf{s}_i \tag{2.52}$$

where $\mathbf{s}_i$ is the search direction going from the i-th to the $(i+1)$-th iteration and β_i is a scaling factor of the search direction.

The two major methods are commonly known as *gradient-free* or *zero order* algorithms and *gradient-based* or *first/second order* algorithms. Depending on which algorithm is chosen, the search direction as well as the scaling factor are determined. In order to get a full overview of existing optimisation algorithms it is referred to the literature, such as the books of Rao (2009); Belegundu and Chandrupatla (2011) and Arora (2012).

2.5.2.1 Gradient-Free Algorithms

There are a number of gradient-free algorithms available in the literature. Most of them are based on either a statistical or a heuristic method to find a global optimum. However, the major drawback of gradient-free algorithms is the necessity of evaluating a large number of designs to get to the optimum solution. Especially for CSM- and CFD-based optimisation problems this drawback becomes the limiting factor. As a result, this led researchers to further develop the algorithms and make them more engineering friendly and suitable for expensive designs.

In general, there are very simple statistical optimisation algorithms like the *random search* or the *random walk*, which however are not suitable for complex engineering tasks as they need an infeasible number of design evaluations to find an optimum solution. Furthermore, it is not guaranteed that the optimisation will find a global optimum but instead end up in a local one.

A more effective statistical method to find a global optimum is the so called *simulated annealing*, which was was introduced by Kirkpatrick et al. (1983). This method is based on the analogy of the cooling process of a metal, in which the final cooled result

corresponds to the optimum solution. Similar to the random walk, an existing design $\mathbf{x}_i$ is perturbed randomly and then evaluated as a new design $\mathbf{x}_{i+1}$. In the case that the new design outperforms the previous design the algorithm is repeated for the new design. However, in order to avoid the optimisation getting trapped in a local minimum, even if the new design is worse than the previous design, it can still be treated as a better design to make the algorithm continue from that solution. By doing that, it is ensured that the global optimum is found. This method improves the convergence quality of the optimisation compared to the two previous methods but still is computationally expensive for large designs and models.

Popular heuristic approaches are the *evolutionary algorithms*, which have been developed in the early 70's by RECHENBERG (1973) and HOLLAND (1975) and are global searching techniques. Their basic principles are related to the evolutionary character in nature, where a defined number of designs represent the generation of the parents and the children are generated by different evolutionary mechanisms such as selection, crossover and mutation. The main difference of these approaches compared to the previously presented ones is the fact, that they are population based and require the entire population per iteration rather than just one single design. Two different forms of evolutionary algorithms can be distinguished: the *genetic algorithms* (GOLDBERG, 1989) and the *differential evolution* (PRICE and STORN, 1997). The former is based on the mechanisms of reproduction and crossover, whereas the latter is based on replacement.

Although the evolutionary algorithms provide the most effective optimisation technique and are more robust than the statistical methods, the main drawback is the need of a large amount of design evolutions in order to find the global optimum in the design space. Therefore, different strategies have been developed to increase the efficiency of the search algorithms and reduce the number of designs to be evaluated.

This can for example be done using *distributed evolutionary algorithms* where the entire population is subdivided into different sub-populations or islands, which all evolve separately. After a couple of evolutions, the best individuals of each sub-population are exchanged between each other for further evolutions, which eventually will result in an optimum individual/design. This method especially gained importance with advanced capabilities in parallel computing MÜHLENBEIN et al. (1991). In an aero-engine context, this method was successfully tested for the aerodynamic compressor blade design by KARAKASIS et al. (2007). It was shown that the optimisation process was accelerated by using the distributed evolutionary algorithm leading to a better design.

Another possibility is the use of *hierarchical evolutionary algorithms*, which describe a strategy of using low fidelity models in order to accelerate the design evaluations. In general, low fidelity models represent the same design as the high fidelity model but can have a coarser mesh or a less expensive evaluation method, i.e. are less accurate. In order to make sure that a suitable design is obtained at the end of the optimisation using the low fidelity model, it is essential to re-evaluate promising designs with the high fidelity model. Overall, the computational time can be decreased significantly as a smaller number

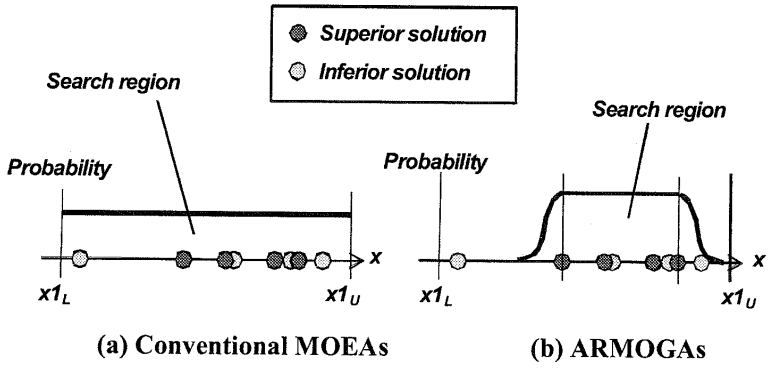

Figure 2.23: Sketch of search region for a conventional MOEA (left) compared to an ARMOGA (SASAKI and OBAYASHI, 2005)

of expensive high fidelity models are evaluated during the optimisation process. Often this hierarchical approach is used in conjunction with the distributed approach, where low and high-fidelity sub-populations are generated. The most promising low-fidelity individuals are then fed into the high-fidelity sub-population and re-evaluated with the more accurate method in order to validate the outcome of the low-fidelity sub-population. Thus it is possible to explore the design space in more detail at reduced computational costs and only re-evaluate promising individuals with an expensive evaluation tool. This approach was successfully tested by WHITNEY et al. (2002) in the field of aerodynamic shape optimisation. As mentioned before, KARAKASIS et al. (2007) used a combination of the distributed and hierarchical approach to optimise a compressor blade cascade. GONZÀLEZ et al. (2006) applied the hierarchical evolutionary algorithm for an aero-structural optimisation of a high aspect ratio aircraft wing, whereas RIBEIRO et al. (2012) carried out an optimisation of a wind turbine.

Further improvement can be achieved by using a so called *metamodel assisted evolutionary algorithm*. This approach is based on an interpolation model, which is typically known as *metamodel*, *response surface* or *surrogate model*. Details on different interpolation models and their level of accuracy are given in Subsec. 2.5.4. Instead of evaluating low-fidelity designs, which can still be expensive in computational time in addition to their inaccuracy, in the metamodel-assisted approach, several high-fidelity models are evaluated and their outcome is used for an interpolation of the design space. The more designs are evaluated the better the interpolation will be. Obviously, the interpolation gives inaccurate results in regions far away from evaluated designs. However, due to their very low computational cost, they can be used to explore the design space much more quickly. Once a promising design is found it is re-evaluated using the high-fidelity model, which leads to a new interpolation of the design space with the updated points. In the aero-engine sector, this approach was for example successfully tested for expensive 3D CFD based optimisations of the main annulus aerodynamics (SHAHPAR et al., 2008; POLYNKIN et al., 2010; SCHLAPS et al., 2014) as well as for blade (VERSTRAETE et al., 2013) and disc cooling (LÜCK et al., 2014b).

One further option in reducing the number of evaluations is the use of evolutionary algorithms with and included range adaptation, which adapts the search region according to the probability of a better solution. SASAKI and OBAYASHI (2005) introduced an *adaptive range multi-objective genetic algorithm* (ARMOGA) and demonstrated its suitability to solve analytical optimisation problems. The range adaptation is based on a Normal distribution and changes according to the population statistics of the standard deviation σ_i as well as the average value μ_i of the i-th design variable:

$$x_{i+1} = \frac{x_i - \mu_i}{\sigma i} \tag{2.53}$$

A comparison of the adaptation of the search region in comparison to a *multi-objective evolutionary algorithm* (MOEA) can be seen in Fig. 2.23. Other than in the conventional technique, the search region in the ARMOGA is reduced after a few design evaluations by taking into account the population statistics mentioned before. This ensures a quicker convergence due to a decreased search area. It was also concluded by the authors that ARMOGAs would be useful for expensive high-fidelity CFD based optimisations.

2.5.2.2 Gradient-Based Algorithms

In addition to evaluating the design vector $\mathbf{x}$, gradient-based algorithms also evaluate the gradient information of the objective function as a function of the same evaluated design. Depending on which order is employed, either first or second, the first order gradients or additionally the HESSIAN matrix need to be computed:

$$1^{\text{st}} \text{ order gradient}: \qquad \nabla f(\mathbf{x}) = \left(\frac{\partial f}{\partial x_1}, \frac{\partial f}{\partial x_2}, ..., \frac{\partial f}{\partial x_n} \right) \tag{2.54}$$

$$\text{HESSIAN matrix}: \qquad \mathbf{H}(\mathbf{x}) = \begin{bmatrix} \frac{\partial^2 f}{\partial^2 x_1} & \frac{\partial^2 f}{\partial x_1 \partial x_2} & \cdots & \frac{\partial^2 f}{\partial x_1 \partial x_n} \\ \frac{\partial^2 f}{\partial x_2 \partial x_1} & \frac{\partial^2 f}{\partial^2 x_2} & \cdots & \frac{\partial^2 f}{\partial x_2 \partial x_n} \\ \vdots & \vdots & \ddots & \vdots \\ \frac{\partial^2 f}{\partial x_n \partial x_1} & \frac{\partial^2 f}{\partial x_n \partial x_2} & \cdots & \frac{\partial^2 f}{\partial^2 x_n} \end{bmatrix} \tag{2.55}$$

The most common methods to calculate the gradients is by using the *finite difference method* or the *adjoint method* (PIRONNEAU, 1984; ROTH, 2012). The former is a rather simple approach, where the gradient for a design point is computed by evaluating the objective function for slightly perturbed design variables. For a large number of design variables, this method becomes very expensive. The latter method computes the gradients on the basis of the concept of LAGRANGIAN multipliers, which results in one additional equation to be solved, the *adjoint equation*. The additional computation of the adjoint equation can be very expensive but is independent of the number of design variables.

Regarding first order methods, there are several algorithms in the open literature. Possibly the simplest but also least efficient one is the *steepest descent*. This method imposes the search direction $\mathbf{s}_i$ of Eq. 2.5.2 as the negative first order derivative (Eq. 2.54). The computation time strongly depends on the choice of the scaling factor β_i. Its value must be restricted to prevent too large a descent. However, if its value is chosen to be very small, the iteration process will require a lot of design evaluations.

An acceleration of the convergence of the steepest descent method can be achieved by using conjugate gradients. The new search direction takes into account the gradient of the i-th design plus the gradient information of the previous iteration $(i-1)$. Popular algorithms using that scheme are the Polak-Robiere and Fletcher Reeves algorithms.

Second-order methods, like the NEWTON method (BONNANS et al., 2003), require the additional evaluation of the HESSIAN matrix to determine the search direction. The main advantage of this method is that a quadratic function can be optimised within one single iteration as the search direction $\mathbf{s}_i$ and the scaling factor β_i are calculated directly. The disadvantage of the evaluation of the HESSIAN matrix, is that this additional computational effort is very expensive. Moreover, the second-order derivatives are very sensitive towards noise, which is typically observed in CFD computations. Therefore, generally so called *quasi-NEWTON methods*, such as the *sequential quadratic programming* (SQP) (WILSON, 1963; HAN, 1976, 1977; GILL et al., 1981; POWELL, 1983), are preferred in the field of optimisation. In SQP the HESSIAN matrix is approximated using a quadratic polynomial to the true function, i.e. a second order TAYLOR series expansion:

$$f(x+h) = f(x) + h \cdot f'(x) + \frac{h^2}{2!} \cdot f''(x) + O(h^3) \tag{2.56}$$

This equation is then used for finite differencing in order to calculate the gradients. Another approach is the *BFGS-method* - named after its originators BROYDON, FLETCHER, GOLDFARB and SHANNO - which considers previous iterations to calculate the search direction and scaling factor, similar to the conjugate gradients method. It has been proven that this method also performs well in non-smooth optimisations (AVRIEL, 2009).

The main drawbacks of the gradient-based algorithms compared to the gradient-free methods, is the additional computational effort, which is required for the calculations of the gradient information. Furthermore, the gradient-based methods only work properly for continuous and smooth objective functions. Otherwise, there is a danger of getting trapped in a local minimum instead of finding the global one.

2.5.3 Design of Experiment

Prior to embarking into the different approximation techniques (i.e. metamodels), it is essential to define an initial database as this is the basis and starting point for all approximation models. One efficient way to explore the design space is the so called *Design of Experiment* (DOE) approach. In general the approximations produced with these sur-

rogate or metamodels are more accurate in close proximity to evaluated designs and the inaccuracy increases the further away. One way to effectively cover a multi-dimensional design volume is the use of *space-filling* techniques, which give a uniform stratified distribution of points as an initial DOE. The simplest way of achieving that is by means of rectangular grids of points. Depending on the dimensionality of the problem, this method can produce very large DOEs.

In order to avoid this large amount of data evaluations another method has been proposed, which generates a sampling plan that is stratified for each dimension. This technique is generally known as *Latin Hypercube Sampling* (LHS), which distributes a desired amount of initial database points homogeneously within the design space in such a way that each point is the only one in a certain axis-aligned hyperplane (McKay et al., 1979; Stein, 1987). From a stochastic point of view, this method provides the best interpolation dataset for an unknown behaviour of an objective function within a defined design space.

In order to choose the number of database points for the initial DOE, different strategies have proven to be successful. The most popular are factorial, fractional factorial, central composite (Montgomery, 2000) and LHS techniques. Researchers have developed problem dependent 'rules-of-thumb' for the optimum amount of initial data points. Jones et al. (1998) suggested the use of ten times the number of design variables for an initial DOE ($10 \times n$). Verstraete et al. (2013) initialised the DOE with a $(2^{n-p} + 1)$ factorial design, with n being the total number of design variables and p defining the lower order parameter combinations. Another recommendation for a purely continuous design space of a surrogate based optimisation was given by Baert et al. (2015). The authors took five times the number of design variables ($5 \times n$) for an initial DOE.

2.5.4 Metamodeling

As already mentioned earlier, metamodels can be used to enhance the optimisation process and speed up the overall simulation run time by use of appropriate approximation methods. There are several different ways of approximating a design space via interpolation. Therefore, the purpose of this subsection is to give the reader an overview of some of the different available metamodeling techniques. A more detailed description follows for the Kriging method, which proved to be very efficient in particular for large scale optimisation problems.

2.5.4.1 Overview of Metamodeling Techniques

Data fitting and approximation can be achieved by carrying out a *regression analysis*. One popular and simple approach is the *method of least squares*. In general, a dataset (x_i, y_i) for $i = 1, ..., n$ points, is approximated by polynomial functions such as the following

quadratic equation:

$$\hat{y}_r(x_i, \beta_m) = \beta_0 + \beta_1 x_i + \beta_2 x_i^2 \tag{2.57}$$

where $\hat{y}_r$ is the predicted value (r for regression) for an input variable x_i and β_m ($i = 0, ..., m$) are the so called *regression coefficients* of the polynomial. In general the system is overdetermined, meaning that $i < m$. Therefore, in the least squares method the appropriate regression coefficients are determined by minimising the *sum of squared errors* (SSE):

$$SSE = \frac{1}{n} \cdot \sum_{i=1}^{n} r_i^2 \tag{2.58}$$

with

$$r_i = y_i - \hat{y}_r\left(x_i, \beta_m\right) \tag{2.59}$$

where r_i is the residual, which is defined as the difference of the actual value y_i and the predicted value $\hat{y}$. Reformulating Eq. 2.57 for a sampled data in matrix form leads to:

$$\begin{bmatrix} y_1 \\ y_2 \\ \vdots \\ y_n \end{bmatrix} = \begin{bmatrix} 1 & x_1 & x_1^2 \\ 1 & x_2 & x_2^2 \\ \vdots & \vdots & \vdots \\ 1 & x_n & x_n^2 \end{bmatrix} \begin{bmatrix} \beta_0 \\ \beta_1 \\ \beta_2 \end{bmatrix} \tag{2.60}$$

and thus

$$\mathbf{y} = \mathbf{x}\beta_m \tag{2.61}$$

Solving this matrix system for the regression coefficients results in the least square estimation:

$$\beta_m = \left(\mathbf{x}^T\mathbf{x}\right)^{-1}\mathbf{x}^T\mathbf{y} \tag{2.62}$$

where $\mathbf{x}^T$ is the matrix transpose of $\mathbf{x}$.

After having determined the optimum regression coefficients minimising the sum of squared errors, one single polynomial equation can be defined, which gives the relation between input and output variables. This kind of analysis can be extended to any degree of polynomial equation by simply including the appropriate amount of regression coefficients. As one can imagine, it is very difficult and rare to capture the whole range of a dataset with one single equation. Even using very high order polynomials does not lead to satisfying results as they tend to oscillate between the data points (Sasena, 2002).

Another possibility to approximate a dataset in a more accurate way are piecewise interpolation methods such as splines. A spline is subdivided into several separate curves, which can be defined by different appropriate polynomial equations. At the connections of each of the curves, it is necessary to define a certain degree of continuity. In that manner, it is also possible to fit highly non-linear datasets. Usually, the connection between two curves is guaranteed with C^2 continuity, which ensures the same value, slope and curvature of the so called *knot point* for both curves.

Different from the two previously mentioned techniques, where the interpolation is based on a polynomial fit, there are also methods available in the literature, which approximate a dataset with higher degrees of freedom. Two examples for that are *fuzzy logic* and the *neural networks*. ROSS (1995) describes the principle of the fuzzy logic in his work: the design variables of the dataset are categorised in different groups (e.g. low, medium, high) and then rules are described on how the dependent variables y_i react for the different inputs x_i. The approximate response surface is then generated by analysing the response behaviour of an input, i.e. how close the input belongs to a certain group.

The method of neural network is analogous to the learning process of a human brain and therefore is very useful for unknown non-linear behaviours. In this method an input and a corresponding output need to be known at the start. The input value is passed to a so called *hidden layer*, a layer of nodes which alters the data using transform functions. The outputs of the hidden layer nodes is then passed to the output by recombination and scaling mechanisms. In order to predict the output correctly, the hidden layer is trained using non-linear optimisation techniques. This method also allows the implementation of multiple parallel hidden layers and nodes, which gives the opportunity to predict highly non-linear behaviours. Therefore, this method has gained popularity in the field of optimisation in recent years. VERSTRAETE et al. (2013) used this method for example to optimise a U-bend internal turbine blade cooling channel.

One further category of approximation methods is the *radial basis function metamodel*, which is closely related to the neural network method. In fact it can be associated to a single layer neural network, where the radial coordinates are the neurons, featuring an input $\mathbf{x}_i$, hidden units ϕ, weights w_i, linear transfer functions and an output $\mathbf{y}$. The particularity of radial basis functions is that they are real-valued functions, which depend either on the Euclidian distance or the distance to a centre point between the sampled data point and the predicted point. Typical known radial basis functions are the Gaussian, multiquadratic, inverse quadratic or thin plate splines. The mathematical formulation of the approximation is as follows:

$$\hat{y}_r(\mathbf{x}) = \sum_{i=1}^{N} w_i \phi \left(||\mathbf{x} - \mathbf{x}_i|| \right) \tag{2.63}$$

where w_i is a weighting coefficient, ϕ is the radial basis function for an associated centre $\mathbf{x}_i$. This method was successfully introduced by DYN et al. (1986) and then continuously improved, also allowing noisy data to be approximated (POGGIO and GIROSI, 1990).

2.5.4.2 Kriging

A particular and powerful approximation technique for complex optimisation problems is the so called *Kriging* technique, which is able to replicate accurately a complex function while also accounting for a degree of uncertainty in its values. In general a Kriging inter-

polation is generated through a set of data points in a one- or multi-dimensional space, where for each data point a confidence interval is obtained from a normal distribution indicating the upper and lower bounds of such interval.

Historically, this method was developed in the field of geology, where it was aimed to predict the most likely distribution of gold in a reef complex in South Africa based on only a few samples from different locations (KRIGE, 1951). Later on, this method was also found to be applicable in different areas such as geography (OLIVER and WEBSTER, 1990), statistics and geostatistics (JOURNEL and HUIJBREGTS, 1978; MATHERON, 1963), environmental science (BAYRAKTAR and TURALIOGLU, 2005) as well as in the aerospace sector (VERSTRAETE et al., 2013; LÜCK et al., 2014a; BROOKS et al., 2011; JOUHAUD et al., 2007). It is out of the scope of this thesis to derive the equations in detail of the Kriging method. Therefore only the most relevant facts are summarised in the following paragraphs. For more details the reader is referred to the early literature of KRIGE (1951) and MATHERON (1963) and for practical guidance in engineering to the book of FORRESTER et al. (2008).

In general Kriging can be described as a least squares interpolation method (see the previous subsection), which provides a stochastic prediction of an unknown function by minimising its mean square error. Its original basis function is given in the form:

$$\psi^{(i)} = \exp\left(-\sum_{j=1}^{k} \theta_j |x_j^{(i)} - x_j|^{p_j}\right) \tag{2.64}$$

where $\mathbf{p} = [p_1, ..., p_j]^T$ and $\boldsymbol{\theta} = [\theta_1, ..., \theta_j]^T$ are vectors to control the smoothness of the response surface and the spatial distribution of the influence of a sample point, respectively. These vectors are typically known as *tuning* or *hyper parameters* to build the Kriging model.

Of particular interest in CFD based optimisations is the ability to filter out noise coming from the numerical calculations. Therefore, the *regressing Kriging* was introduced by FORRESTER et al. (2006) and BROOKS et al. (2011), which is based on the classical Kriging approach with an additional parameter to filter out scatter or noise.

Applying mathematical simplifications to the likelihood maximisation of the model, leads to the maximum likelihood estimate for the *best linear unbiased predictor* $\hat{y}_r$, which is defined as:

$$\hat{y}_r = \hat{\mu}_r + \boldsymbol{\psi}^T(\boldsymbol{\Psi} + \lambda_c \mathbf{I})^{-1}(\mathbf{y} - \mathbf{1}\hat{\mu}_r) \tag{2.65}$$

where $\boldsymbol{\psi}$ is the vector containing the basis functions, $\boldsymbol{\Psi}$ is the correlation matrix and λ_c is the regression constant. $\hat{\mu}_r$ is the regression model coefficient and defined as:

$$\hat{\mu}_r = \frac{\mathbf{1}^T(\boldsymbol{\Psi} + \lambda_c \mathbf{I})^{-1}\,\mathbf{y}}{\mathbf{1}^T(\boldsymbol{\Psi} + \lambda_c \mathbf{I})^{-1}\,\mathbf{1}} \tag{2.66}$$

where $\mathbf{I}$ is an $n \times n$ identity matrix, leading to $|\mathbf{x}^{(i)} - \mathbf{x}| \to 0$ and $\mathrm{cor}(\mathbf{x}^{(i)}, \mathbf{x}) = 1 + \lambda$. This makes sure that no interpolation along with the noise is done, which leads to a smoother

and more accurate estimation of the response surface. The least squares estimate of the residual process variance is given by:

$$\hat{\sigma}_r^2 = \frac{(\mathbf{y} - \mathbf{1}\hat{\mu}_r)^T (\mathbf{\Psi} + \lambda \mathbf{I})^{-1} (\mathbf{y} - \mathbf{1}\hat{\mu}_r)}{n} \tag{2.67}$$

These maximum likelihood estimates (variables with circumflex) are then fed back into the likelihood maximisation, which leads to the so called *concentrated log likelihood function*:

$$\ln(L) = -\frac{n}{2} \ln(\hat{\sigma}_r^2) - \frac{1}{2} \ln\left(|(\mathbf{\Psi} + \lambda \mathbf{I})|\right) \tag{2.68}$$

This function is then maximised to find the tuning parameters $\hat{\boldsymbol{\phi}}$, $\hat{\mathbf{p}}$ and λ which represent the solution accurately. In general this is done by using automated search techniques such as optimisation algorithms (see Subsec. 2.5.2).

As mentioned above, Kriging was successfully applied to aero-engine design processes. VERSTRAETE et al. (2013) optimised a 2D U-bend geometry, which is typical for internal cooling channels of turbine blades, using a coupled CFD and CSM approach, which was embedded into a metamodel assisted evolutionary algorithm. Another Kriging based optimisation of the MAGPI cavity was carried out by LÜCK et al. (2014b).

2.6 Summary

This chapter gave a detailed overview of the previously published analytical, computational and experimental studies, which are related and relevant for the understanding of the current research. In summary the following research areas were covered:

1. First the fundamentals of heat transfer phenomena in general and in particular in turbomachinery were given. The governing equations for the three driving heat transfer mechanisms, conduction, radiation and convection were introduced and explained. In a next step, the mechanism of conjugate heat transfer was defined and different computational methods for accurately calculating the CHT were summarised step-by-step. Each section contains a detailed discussion of a particular CHT calculation approach, pointing out its advantages and disadvantages. In addition to that, a range of earlier research studies where the respective CHT methods were applied in a turbomachinery context are summarised. With respect to the current research special attention was put on the CHT studies of the MAGPI geometry and also on ROLLS-ROYCE publications with their method of favour.

2. In a next step, the basics on TSW relevant flows were presented. At first, the very simplistic free disc test case were presented with its respective flow field and the most important non-dimensional quantities. This type of flow is generally present along every rotating wall. The results and conclusions of earlier studies were discussed and

analytically derived correlations for the disc entrainment flow, moment coefficient and NUSSELT number were summarised. This is of particular interest for the thermal modeling during this work, when applying boundary conditions to the CSM model in areas where no CFD solution is available.

3. Similar to the free disc, a typical rotor-stator cavity flow was introduced and different numerical and experimental studies were presented from which empirical correlations were derived in the past. At first it was looked into stand-alone cavities without an external flow and then into cavities adjacent to a main gas path. Finally, special focus was turned towards the MAGPI research project, which plays an important role in this thesis. As already mentioned, different studies on CHT method validation were discussed as well as preliminary studies on disc cooling improvements.

4. The importance and the function of interstage seals in the area of TSW studies were discussed. Furthermore, the importance of predicting seal clearances correctly with respect to flow field changes and the influence on the heat transfer predictions were explained by referring to published work in the literature. This is an area of great potential with respect to heat transfer validation tasks and takes an important role in this thesis

5. The last section covered the field of optimisation methods in the field of turbomachinery. It was started with the general optimisation problem definition, then different gradient-free and gradient-based algorithms were presented with their advantages and disadvantages. In addition to that, useful space-filling techniques and approximations with metamodels were introduced to the reader. Published works dealing with optimisation problems in turbomachinery were also mentioned for a better understanding and classification in the current context. As it is out of the scope of this chapter to present every available optimisation method, the focus was only turned to relevant methods, which are applicable to the current TSW design and which are available and were tested at ROLLS-ROYCE.

3 Numerical Methodology

The purpose of this chapter is to introduce the numerical methodology used in this work. Before this, some theoretical background on the flow and heat governing equations in fluids and solids is given including the numerical modelling of these equations in typical engineering computations. In addition, an overview of the computational codes used in this work is given as well as the application strategy. In the last sections of this chapter, the actual automated numerical aerothermal coupling method and the metamodel assisted optimisation approach are presented.

3.1 Flow Governing Equations

In general, the fluid flow is governed by the NAVIER-STOKES (NS) equations. In a three dimensional space this system of equations consists of a continuity equation for mass conservation, three scalar equations for the conservation of momentum, a scalar equation for the conservation of energy plus one additional state equation, which is related to the fluid species. Due to the non-linearity of the equations, which are all coupled, it is not possible to obtain an exact solution for turbulent flows, i.e. for high REYNOLDS number flows.

In the next paragraphs the final derived equations for a three dimensional compressible flow in vector notation are summarised. As it is out of the scope of this study to derive these equations and not necessary for the understanding of the proposed methodology in this thesis, the interested reader is referred to the book of DURST (2006) for more details.

For viscous flows in a closed fluid system, the equations are as follows: the continuity equation is defined as

$$\frac{\partial \rho}{\partial t} + \nabla \cdot (\rho \mathbf{U}) = 0 \tag{3.1}$$

with $\mathbf{U}$ being the velocity vector. The momentum equations are defined as

$$\frac{\partial (\rho \mathbf{U})}{\partial t} + \nabla \cdot (\rho \mathbf{U} \times \mathbf{U}) = -\nabla p + \nabla \cdot \boldsymbol{\tau} + \rho \mathbf{f} \tag{3.2}$$

where p is the static pressure, $\mathbf{f}$ is the body force vector and $\boldsymbol{\tau}$ is the stress tensor. The latter can be defined by

$$\boldsymbol{\tau} = 2\mu_f \left[\mathbf{D} - \frac{1}{3} (\nabla \cdot \mathbf{U}) \mathbf{I} \right] \tag{3.3}$$

with $\mathbf{D}$ being the fluid strain rate tensor, which is given by

$$\mathbf{D} = \frac{1}{2}\left[\nabla\mathbf{U} + (\nabla\mathbf{U})^T\right] \tag{3.4}$$

and $\mathbf{I}$ being the identity tensor.

The energy equation is defined as:

$$\frac{\partial(\rho H_0)}{\partial t} + \nabla\cdot(\rho\mathbf{U}H_0) = \frac{\partial p}{\partial t} + \rho\mathbf{U}\mathbf{f} + \nabla\cdot(\mathbf{U}\boldsymbol{\tau}) - \nabla\cdot\dot{\mathbf{q}} \tag{3.5}$$

where H_0 is the specific total enthalpy, which is defined by

$$H_0 = c_p T + \frac{1}{2}\mathbf{U}^2 + k'\frac{p}{\rho} \tag{3.6}$$

with $k' = 0$ and $k' = 1$ for perfect gases and incompressible flows, respectively, T the static temperature and $\dot{\mathbf{q}}$ being the heat flux vector due to conduction according to Eq. 2.1:

$$\dot{\mathbf{q}} = -\lambda_f \nabla T \tag{3.7}$$

where λ_f is the thermal conductivity of the fluid.

The most common and general approach to write this system of equations is to use the Cartesian coordinates x, y, z with the corresponding velocity components u, v, w. In the field of turbomachinery, it is often more convenient to use the cylindrical coordinate representation of the NS equations. This requires a substitution of the Cartesian coordinates x, y, z with the respective cylindrical coordinates: radius r, tangential or azimuthal position ϕ and axial position z. These coordinates are defined as $x = r\cos\phi, y = r\sin\phi$ and z being the rotational axis. The absolute velocity components along the cylindrical coordinates r, ϕ, z are u, v, w.

3.2 Computational Fluid Dynamics

As already mentioned in the section above, it is only possible to find an approximated solution of the NS equations in most 'real' flow situations. In this context, computational fluid dynamics (CFD) represents a numerical modeling strategy to solve this system of partial differential equations using digital computers. The partial derivatives in the NS equations are replaced by discretised algebraic formulations, which are solved to obtain approximate values of the flow field variables at discrete points in space and/or in time.

In the upcoming subsections, the reader is introduced to the CFD modeling techniques used during this study. As for the previous section, the author is aware of the presence of further modeling approaches in the literature, which might also be suitable for the current study. Therefore, the interested reader is referred to the CFD text books of J. D. Anderson (1995); Wilcox (1998); Pope (2000); Ferzinger and Perić (2002)

for further information. In addition to summarising the modeling approaches, an overview of the CFD codes is given as well as the CFD methodology as it is applied in the current work.

3.2.1 Turbulence Modeling

In aero-engines, air and gas flows are generally turbulent and therefore a turbulence modeling strategy is needed to solve the governing equations. In turbulent flows highly fluctuating velocity fields in space and time are present, which contain a large number of eddies of varying size (RICHARDSON, 1922; POPE, 2000). According to RICHARDSON, the large eddies are very unstable and break up into smaller eddies, which then again break up into even smaller eddies until a stable state is obtained where the remaining energy of the eddies is dissipated through viscous actions.

Based on these findings, KOLMOGOROV (1941) postulated that at every time large eddies break up into smaller ones, the velocity and the time scales of the large turbulent eddies decrease. Once the eddies reach a certain minimum eddy length scale, they do not break up any more and only depend on the kinematic viscosity of the fluid ν and the turbulent energy dissipation ϵ. This led to the following definitions:

$$\text{length scale:} \qquad \varsigma \equiv \left(\frac{\nu^3}{\epsilon}\right)^{\frac{1}{4}} \tag{3.8}$$

$$\text{velocity scale:} \qquad u_\varsigma \equiv (\epsilon\nu)^{\frac{1}{4}} \tag{3.9}$$

$$\text{time scale:} \qquad \hat{t} \equiv \left(\frac{\nu}{\epsilon}\right)^{\frac{1}{2}} \tag{3.10}$$

In order to correctly calculate all eddy structures, it is necessary to solve the flow at all length and time scales, including the KOLMOGOROV scales. In this context *correct* is defined as a solution, which only contains a numerical and a truncation error. As the length and time scales correlate negatively with the REYNOLDS number ($\varsigma \equiv Re^{-3/4}$ and $\hat{t} \equiv Re^{-1/2}$, respectively) (POPE, 2000), a *direct numerical simulation* (DNS) of these eddy structures is only applicable to moderately complex flow cases as at low REYNOLDS numbers. For high REYNOLDS number and complex flow structures, it is still beyond the reach of today's supercomputers to conduct a DNS.

For that reason, statistical approximation techniques were invented to provide accurate solutions at reduced computational costs. In this work - as a well established method in the gas turbine and aero-engine community (see Chap.2) - the REYNOLDS averaged NAVIER-STOKES (RANS) equations are used as an approximation technique, including three different *BOUSSINESQ* or *eddy viscosity models* to calculate the engine flow. The key information for understanding the thesis is given below, but for more detail, reference is made to the publications of WILCOX (1998) and POPE (2000).

3.2.1.1 REYNOLDS-Averaged NAVIER-STOKES Equations

As mentioned above, the RANS equations are an approximation technique to solve turbulent flows. This method was developed by REYNOLDS (1894) for incompressible flows, who decomposed the instantaneous flow variables into a sum of mean and fluctuating quantities. For the velocity vector this results in:

$$\mathbf{U} = \overline{\mathbf{U}} + \mathbf{U}' \tag{3.11}$$

where $\mathbf{U}$, $\overline{\mathbf{U}}$ and $\mathbf{U}'$ represent the instantaneous, mean and fluctuating velocity vectors, respectively. The scalars such as pressure or energy are decomposed in the same way, resulting in:

$$\psi = \overline{\psi} + \psi' \tag{3.12}$$

Substituting these instantaneous quantities into the continuity and momentum equations (Eqs. 3.1 and 3.2 neglecting the density fluctuations, which is commonly used for reasons of simplicity, gives the following time-averaged equations:

$$\frac{\partial \rho}{\partial t} + \nabla \cdot \left(\rho \overline{\mathbf{U}}\right) = 0 \tag{3.13}$$

$$\frac{\partial \left(\rho \overline{\mathbf{U}}\right)}{\partial t} + \nabla \cdot \left(\rho \overline{\mathbf{U}} \times \overline{\mathbf{U}}\right) = -\nabla \overline{p} + \nabla \cdot \left[2\mu_f \left(\overline{\mathbf{D}} - \frac{1}{3}\left(\nabla \cdot \overline{\mathbf{U}}\right)\mathbf{I}\right)\right] + \rho \overline{\mathbf{F}} + \boldsymbol{\tau_{turb}} \tag{3.14}$$

with

$$\overline{\mathbf{D}} = \frac{1}{2}\left[\nabla \overline{\mathbf{U}} + \left(\nabla \overline{\mathbf{U}}\right)^T\right] \tag{3.15}$$

By comparing these time-averaged equations to the *real* equations, it can be seen that the instantaneous quantities were replaced by the mean values and that one additional non-linear term $\boldsymbol{\tau_{turb}}$ was added in the time averaged momentum equation (Eq. 3.14). This term is known as the *REYNOLDS stress tensor*, which is symmetric and includes six additional unknown components - the *REYNOLDS stresses* - which make the whole system of equations under-determined.

According to WILCOX (1998), there is one stress transport equation for each transport phenomena, which are the following: convection, turbulent and molecular diffusion, stress production, pressure strain and dissipation. The interested reader is referred to the literature of WILCOX (1998) for the mathematical formulations of each of these transport phenomena.

One approach to close the RANS equation system is to apply the dependent unknown stresses to the existing mean quantities, which is commonly known as the *eddy viscosity approach* introduced by BOUSSINESQ in 1897 (POPE, 2000). In analogy to the modeling of the dynamic viscosity of the fluid μ_f, a new quantity is defined, the so called *turbulent eddy viscosity* μ_t, which is not a fluid property as a such, but describes the increase of viscosity due to the turbulent fluctuations to the flow and is defined as:

$$\mu_t = \rho \cdot \nu_t \tag{3.16}$$

The estimation of the turbulent viscosity is the basis of turbulence modeling, but is out of the scope of this study. For a detailed overview, reference is again made to the books of WILCOX (1998) and POPE (2000).

In addition to the turbulent kinetic energy, another quantity is needed to approximate the REYNOLDS stresses. This quantity is known as the *turbulent kinetic energy* k, which is characterised by the root-mean-square velocity fluctuations:

$$k = \frac{1}{2}\overline{\mathbf{U}' \cdot \mathbf{U}'} \tag{3.17}$$

With these two quantities it is then possible to describe the REYNOLDS stresses as follows:

$$\boldsymbol{\tau_{turb}} = \rho\overline{\mathbf{U}' \times \mathbf{U}'} = \frac{2}{3}\rho k\mathbf{I} - \mu_t\left[\nabla\overline{\mathbf{U}} + \left(\nabla\overline{\mathbf{U}}^T\right)\right] \tag{3.18}$$

From this equation it can be seen that in addition to the mean values, it only consists of two additional dependent variables, μ_t and k. One way of estimating values for these two unknowns, is by zero-equation or algebraic models, which are derived from empirical correlations or boundary layer theory. The main drawback of this approach is the uniformity of the turbulence modeling in the complete domain, i.e. the turbulence model does not adapt to varying flow conditions such as turbulence entrainment due to convection from one region to another.

A range of different one and two equation turbulence models have been derived in the past. The most relevant models for this work are presented in the upcoming subsections. First the RANS system needs to be completed with the time-averaged energy equation, which is as follows:

$$\frac{\partial\left(\rho H_0\right)}{\partial t} + \nabla\cdot\left(\rho\overline{\mathbf{U}}H_0\right) = \frac{\partial\overline{p}}{\partial t} + \rho\overline{\mathbf{U}\mathbf{F}} + \nabla\cdot\left\{\overline{\mathbf{U}}\left[2\mu_{eff}\left(\overline{\mathbf{D}} - \frac{1}{3}\left(\nabla\cdot\overline{\mathbf{U}}\right)\mathbf{I}\right)\right]\right\} - \nabla\cdot\dot{\mathbf{q}} \tag{3.19}$$

where similar to the two other time-averaged equations, the instantaneous quantities are replaced by their mean values and slightly different terms occur. As a new artificial quantity, the effective viscosity μ_{eff} is included, which is the sum of the viscosity of the

fluid μ_f and the turbulent viscosity μ_t. The mean heat flux vector $\overline{\dot{\mathbf{q}}}$ is defined by the mean temperature:

$$\overline{\dot{\mathbf{q}}} = -\lambda_f \nabla \overline{T} \tag{3.20}$$

and can be rewritten by substituting the thermal conductivity λ_f with the turbulent PRANDTL number Pr_t and the turbulent viscosity to yield:

$$\overline{\dot{\mathbf{q}}} = -\frac{\mu_t \cdot c_p}{Pr_t} \nabla \overline{T} \tag{3.21}$$

3.2.1.2 The SPALART-ALLMARAS Turbulence Model

The SPALART-ALLMARAS turbulence model is a one equation turbulence closure model, which was derived in 1992 by the two authors SPALART and ALLMARAS. The basic principle of this approach is that a transport equation is solved for a modified turbulent kinematic eddy viscosity, the so called *SPALART variable* $\tilde{\nu}$. Furthermore, the turbulent kinetic energy k is not calculated in the SPALART-ALLMARAS model, i.e. the last term in Eq. 3.18 is neglected when estimating the REYNOLDS stresses. That leads to the following definition of the turbulent viscosity:

$$\mu_t = \rho \tilde{\nu} f_{\tilde{\nu}1} \tag{3.22}$$

with $f_{\tilde{\nu}1}$ being the *viscous damping function* defined as:

$$f_{\tilde{\nu}1} = \frac{\chi^3}{\chi^3 + C_{\tilde{\nu}1}^3} \tag{3.23}$$

where χ is the ratio of the SPALART variable $\tilde{\nu}$ to the molecular kinematic viscosity of the fluid ν_f and $C_{\tilde{\nu}1}$ is a constant of 7.1.

According to POPE (2000), the transport equation for the SPALART variable $\tilde{\nu}$ is as follows:

$$\frac{\partial (\rho \tilde{\nu})}{\partial t} + \nabla \cdot \left(\rho \tilde{\nu} \overline{\mathbf{U}} \right) = G_{\tilde{\nu}} + \frac{1}{\sigma_{\tilde{\nu}}} \Big\{ \nabla \cdot \left[(\mu_f + \rho \tilde{\nu}) \nabla \tilde{\nu} \right] + C_{b2} \rho (\nabla \tilde{\nu})^2 \Big\} - Y_{\tilde{\nu}} \tag{3.24}$$

where $G_{\tilde{\nu}}$ is a term for the production of turbulent viscosity and $Y_{\tilde{\nu}}$ is a term for the destruction of turbulent viscosity near the wall, which is due to viscous damping and wall blocking. The variables $\sigma_{\tilde{\nu}} = 2/3$ and $C_{b2} = 0.622$ are constants.

The production term $G_{\tilde{\nu}}$ is defined as

$$G_{\tilde{\nu}} = C_{b1}\rho\tilde{S}\tilde{\nu} \tag{3.25}$$

with

$$\tilde{S} \equiv S + \frac{\tilde{\nu}}{\kappa^2 d'^2} f_{\tilde{\nu}2} \tag{3.26}$$

and

$$f_{\tilde{\nu}2} = 1 - \frac{\chi}{1 + \chi f_{\tilde{\nu}1}} \tag{3.27}$$

where $C_{b1} = 0.1355$, the VON KARMAN constant $\kappa = 0.4187$, d' is the distance from the wall and S is a magnitude of mean deformation, which is estimated using the vorticity magnitude of the rotation tensor $\mathbf{S}$:

$$S \equiv \sqrt{2\mathbf{SS}} \tag{3.28}$$

A further development of the model was proposed by DACLES MARIANI et al. (1995), who suggested to include both, the effect of the vorticity as well as the effect of the mean strain rate on the turbulence production. This results in following description of S:

$$S \equiv \sqrt{2\mathbf{SS}} + C_{prod} \min\left(0, \sqrt{2\mathbf{DD}} - \sqrt{2\mathbf{SS}}\right) \tag{3.29}$$

where $C_{prod} = 2.0$ and $\mathbf{D}$ is the mean strain rate tensor. By including both the rotation and strain tensors, the production of eddy viscosity is reduced in regions where the mean vorticity exceeds the mean strain rate magnitude. This is of particular interest in vortical flows, where the flow near the core of a vortex is purely dominated by rotation and turbulence is known to be suppressed.

The turbulence destruction term $Y_{\tilde{\nu}}$ is approximated by:

$$Y_{\tilde{\nu}} = C_{w1}\rho f_w \left(\frac{\tilde{\nu}}{d'}\right)^2 \tag{3.30}$$

with

$$f_w = g' \left[\frac{1 + C_{w3}^6}{g'^6 + C_{w3}^6}\right]^{\frac{1}{6}} \tag{3.31}$$

$$g' = r' + C_{w2}\left(r'^6 - r'\right) \tag{3.32}$$

$$r' \equiv \frac{\tilde{\nu}}{\tilde{S}\kappa^2 d'^2} \tag{3.33}$$

where $C_{w2} = 0.3$, $C_{w3} = 2.0$ and the constant C_{w1} is given by

$$C_{w1} = \frac{C_{b1}}{\kappa^2} = \frac{1 + C_{b2}}{\sigma_{\tilde{\nu}}} \tag{3.34}$$

It is assumed that the modified turbulent kinematic viscosity $\tilde{\nu}$ on the wall is equal to zero. For fine meshes, which resolve the viscosity-dominated sublayer, the wall shear stresses are obtained using the laminar stress-strain relationship:

$$U = U_\tau y^+ \tag{3.35}$$

where U is the velocity parallel to the wall, U_τ is the friction velocity and y^+ is the non-dimensional distance from the wall. The latter two are given by:

$$U_\tau = \sqrt{\frac{\tau_w}{\rho}} \tag{3.36}$$

and

$$y^+ = \frac{\rho U_\tau y_d}{\mu_f} \tag{3.37}$$

where y_d is the distance of the centroid of a wall adjacent cell from the wall. In case, the mesh is not fine enough to resolve the viscous sublayer, it is assumed that the centroid of the wall-adjacent cell falls within the logarithmic region of the boundary layer, the *law-of-the-wall* is applied:

$$U = \frac{U_\tau}{\kappa} ln\left(E' y^+\right) \tag{3.38}$$

with the constant $E' = 9.763$.

3.2.1.3 The $k-\epsilon$ Turbulence Model

The $k-\epsilon$ turbulence model is a two-equation model, which consists of two separate transport equations allowing the independent determination of the turbulent velocity and length scales of a flow field. These equations are for the turbulent kinetic energy k $(= 0.5 \cdot \overline{\mathbf{U}' \cdot \mathbf{U}'})$ and the turbulent dissipation rate ϵ. There are different forms of the $k-\epsilon$ model in the literature, which basically vary on how the turbulent viscosity is calculated, on the effect of the turbulent PRANDTL number governing the turbulent diffusion of k and ϵ, and on the generation and destruction terms in the ϵ equation. In this section three forms are presented:

- the standard $k-\epsilon$ model (LAUNDER and SPALDING, 1974)
- the RNG $k-\epsilon$ model (YAKHOT and ORSZAG, 1986)
- the realizable $k-\epsilon$ model (SHIH et al., 1995)

At first we consider the standard $k-\epsilon$ model. The transport equations for k and ϵ by neglecting the buoyancy and compressibility effects are given by

$$\frac{\partial(\rho k)}{\partial t} + \nabla \cdot (\rho k \mathbf{U}) = \nabla \cdot \left[\left(\mu_f + \frac{\mu_t}{Pr_{t,k}} \right) \nabla k \right] + G_k + \rho\epsilon \tag{3.39}$$

and

$$\frac{\partial(\rho \epsilon)}{\partial t} + \nabla \cdot (\rho \epsilon \mathbf{U}) = \nabla \cdot \left[\left(\mu_f + \frac{\mu_t}{Pr_{t,\epsilon}} \right) \nabla \epsilon \right] + C_{1\epsilon} \frac{\epsilon}{k} G_k - C_{2\epsilon} \rho \frac{\epsilon^2}{k} \tag{3.40}$$

where $Pr_{t,k} = 1.0$ and $Pr_{t,\epsilon} = 1.3$ are the turbulent PRANDTL numbers for k and ϵ, respectively, $C_{1\epsilon} = 1.44$ and $C_{2\epsilon} = 1.92$ are constants, μ_t is the turbulent viscosity and G_k is the term for the generation of turbulence kinetic energy due to the mean velocity gradients, both defined as

$$\mu_t = \rho C_\mu \frac{k^2}{\epsilon} \tag{3.41}$$

with $C_\mu = 0.09$ and

$$G_k = -\rho \overline{\mathbf{U}' \mathbf{U}'} \nabla \cdot \mathbf{U} \tag{3.42}$$

Approximating this term with the BOUSSINESQ hypothesis leads to:

$$G_k = 2\mu_t \mathbf{D}\mathbf{D} \tag{3.43}$$

As the standard $k-\epsilon$ turbulence model is a high REYNOLDS number model and Eqs. 3.39 and 3.40 are only valid in the region up to the outer edge of the buffer layer ($y^+ > 30$) and in the core, additional methods for the wall treatment are required. Basically, two approaches are available depending on the mesh density. For a resolved laminar sublayer, the near-wall flow can be calculated using the linear stress rate of strain relation to estimate the shear stress. This can for example be done using the *enhanced wall treatment* approach, where a separate equation for a low REYNOLDS flow is solved to evaluate the effective turbulent viscosity for fine near wall meshes (FLUENT, 2009).

For coarser meshes, however, a different approach needs to be taken into account. A logarithmic profile for the mean velocity is used for the adjacent cell layer, from where the wall shear stress and effective viscosity are estimated. The production term G_k in Eq. 3.39 is altered to

$$G_k = \frac{\tau^2}{\kappa \rho C_\mu^{0.25} k_p^{0.5} y_p} \tag{3.44}$$

and the dissipation rate is calculated using following formulation:

$$\epsilon_p = \frac{C_\mu^{0.75} k_p^{1.5}}{\kappa y_p} \tag{3.45}$$

where the subscript p stands for the near wall cell centroid.

As already mentioned at the beginning of this section, there are some alternative approaches available which improved the standard turbulence model. One of these, is the RNG $k-\epsilon$ model, which was derived from the instantaneous NAVIER-STOKES equations, using a mathematical technique called *renormalization group* (RNG) method (ORSZAG et al., 1993). The main advantages of the RNG model at a glance are (FLUENT, 2009):

- due to an additional term in the ϵ equation, the accuracy for rapidly strained flows is significantly improved
- accuracy of swirling flows is improved due to taking into account the effect of swirl on the turbulence
- analytical formulations for turbulent PRANDTL numbers are used instead of constant values, allowing a wider range of flows to be covered
- an analytically-derived differential formula for effective viscosity is provided accounting for low-REYNOLDS number effects

This leads to the following representation of the transport equations, while again neglecting buoyancy and compressibility effects:

$$\frac{\partial(\rho k)}{\partial t} + \nabla \cdot (\rho k \mathbf{U}) = \nabla \cdot \left(\alpha_k \mu_{eff} \nabla k\right) + G_k + \rho\epsilon \tag{3.46}$$

and

$$\frac{\partial(\rho \epsilon)}{\partial t} + \nabla \cdot (\rho \epsilon \mathbf{U}) = \nabla \cdot \left(\alpha_\epsilon \mu_{eff} \nabla \epsilon\right) + C_{1\epsilon}\frac{\epsilon}{k} G_k - C_{2\epsilon}\rho\frac{\epsilon^2}{k} - R_\epsilon \tag{3.47}$$

The quantities α_k and α_ϵ are the inverse effective PRANDTL numbers for k and ϵ, respectively, derived from the following analytical expressions in RNG theory:

$$\left|\frac{\alpha - 1.3929}{\alpha_0 - 1.3929}\right|^{0.6321} \left|\frac{\alpha + 2.3929}{\alpha_0 + 2.3929}\right|^{0.3679} = \frac{\mu_{mol}}{\mu_{eff}} \tag{3.48}$$

where $\alpha_0 = 1.0$. In the high REYNOLDS number limit ($\mu_{mol}/\mu_{eff} \ll 1$), $\alpha_k = \alpha_\epsilon = 1.393$.

The effect on turbulence due to rotation and swirl in the mean flow is included in the RNG model by modifying the turbulent viscosity appropriately:

$$\mu_t = \mu_{t0}\ f\left(\alpha_s, \beta, \frac{k}{\epsilon}\right) \tag{3.49}$$

where μ_{t0} is the value of turbulent viscosity without taking swirl into account. β is the swirl number and α_s is a swirl constant, which assumes different values for either swirl-dominated or barely swirling flows.

The biggest difference between the standard and the RNG model is the presence of the additional term R_ϵ in Eq. 3.47, which is defined as:

$$R_\epsilon = \frac{C_\mu \rho \eta^3 \left(1 - \eta/\eta_0\right)}{1 + \beta\eta^3} \frac{\epsilon^2}{k} \tag{3.50}$$

with $\eta = Dk/\epsilon$, $\eta_0 = 4.38$ and $\beta = 0.012$.

A large strain rate ($\eta > \eta_0$), the term R_ϵ makes a negative contribution, leading to a smaller destruction of ϵ, i.e. leading to a higher ϵ and smaller k, and thus reducing the effective viscosity. As a result, the RNG model is more responsive to the effects of rapid strain and streamline curvature than the standard $k-\epsilon$ model.

As a second alternative $k-\epsilon$ turbulence model to the standard one, is the *realizable* $k-\epsilon$ model. According to the literature (e.g. POPE (2000) or FLUENT (2009)), it performs best for separated flows, jets, recirculation and flows with complex secondary flow features. However, in multiple reference frame simulation, i.e. having different stationary and rotating domains, which are connected via mixing (steady-state) or sliding (unsteady) interfaces, non-physical turbulent viscosities are produced and therefore one should carefully check the solution before drawing any conclusions.

Realizable means that the model satisfies certain mathematical constraints on the REYNOLDS stresses, which are consistent with the physics of the turbulent flow. This is not the case for either of the previously mentioned models. This also means that the transport equations are different in the realizable model. First, a new formulation for the turbulent viscosity was introduced, involving a variable C_μ, which was originally proposed by REYNOLDS (1987). Second, a new transport equation for the dissipation rate ϵ was derived based on the dynamic equation of the mean-square vorticity fluctuations.

The turbulent viscosity μ_t is defined as previously ($= \rho C_\mu k^2\, \epsilon^{-1}$), with the only difference that C_μ is no longer constant but defined as:

$$C_\mu = \frac{1}{A_0 + A_s \frac{kU^*}{\epsilon}} \tag{3.51}$$

where

$$U^* \equiv \sqrt{\mathbf{DD} + \tilde{\mathbf{S}}\tilde{\mathbf{S}}} \tag{3.52}$$

and

$$\tilde{\mathbf{S}} = \mathbf{S} - 2\boldsymbol{e}\omega \tag{3.53}$$

$$\mathbf{S} = \overline{\mathbf{S}} - \boldsymbol{e}\omega \tag{3.54}$$

where $\overline{\mathbf{S}}$ is the mean rate-of-rotation tensor viewed in a rotating reference frame with the angular velocity ω. The model constants are given by $A_0 = 4.04$ and $A_s = \sqrt{6}\cos\phi$, where

$$\phi = \frac{1}{3}\cos^{-1}\left(\sqrt{6}W\right), \text{with } W = \frac{S_{ij}S_{jk}S_{ki}}{\tilde{S}^3}, \text{and } \tilde{S} = \sqrt{\mathbf{SS}} \tag{3.55}$$

From that definition, it can clearly be seen that C_μ is a function of the mean strain and rotation rates as well as the turbulence variables k and ϵ.

The transport equation for k is the same as for the standard model (see Eq. 3.39) and therefore not mentioned again. However, the transport equation for ϵ has changed to:

$$\frac{\partial(\rho\epsilon)}{\partial t} + \nabla\cdot(\rho\epsilon\mathbf{U}) = \nabla\cdot\left[\left(\mu_f + \frac{\mu_t}{Pr_{t,\epsilon}}\right)\nabla\epsilon\right] + \rho C_1 S\epsilon - \rho C_2\frac{\epsilon^2}{k+\sqrt{\nu\epsilon}} \tag{3.56}$$

where

$$C_1 = \max\left[0.43, \frac{\eta}{\eta+5}\right], \qquad \eta = \sqrt{2\mathbf{SS}}\frac{k}{\epsilon}, \qquad C_2 = 1.9, \qquad Pr_{t,\epsilon} = 1.2 \tag{3.57}$$

The main difference in this new equation compared to the previous ones is that the production term ($\rho C_1 S\epsilon$) does not contain the production of k any more and therefore is considered to better represent the spectral energy transfer (FLUENT, 2009).

3.2.1.4 The $k-\omega-SST$ Turbulence Model

The $k-\omega$ *Shear-Stress Transport* (SST) turbulence model is a two equation model developed and improved by MENTER (1994) and MENTER et al. (2003) based on the two transport equations for the turbulence kinetic energy k and the specific dissipation rate ω. It is a hybrid model, which is based on the standard WILCOX $k-\omega$ and on a $k-\epsilon$ turbulence model, which is transformed into a $k-\omega$ formulation. Due to the combination of these two turbulence models, it is possible to accurately resolve the near-wall region using the standard $k-\omega$ formulation and to solve the flow in the far field using the transformed $k-\epsilon$ formulation.

This combination is achieved by multiplying both models with a blending function and adding them together. The blending function can take two values: it is zero away from the surface, which activates the transformed $k-\epsilon$ model and it is one in the near-wall region, which activates the $k-\omega$ model. This leads to following representation of the two

transport equations for k and ω, respectively:

$$\frac{\partial(\rho k)}{\partial t} + \nabla \cdot (\rho k \mathbf{U}) = \nabla \cdot (\Gamma_k \nabla k) + G_k - Y_k \tag{3.58}$$

and

$$\frac{\partial(\rho \omega)}{\partial t} + \nabla \cdot (\rho \omega \mathbf{U}) = \nabla \cdot (\Gamma_\omega \nabla \omega) + G_\omega - Y_\omega + D_\omega \tag{3.59}$$

where Γ_k and Γ_ω are terms for the effective diffusivity of k and ω, respectively, G_k is a term for the production of k due to the mean velocity gradient and G_ω is a term for the production of ω. The terms Y_k and Y_ω represent the turbulence diffusivity of k and ω, respectively, and D_ω is a cross-diffusion term, which is present due to the transformation of the $k-\epsilon$ equations to a function of k and ω.

The effective diffusivities are modeled as:

$$\Gamma_k = \mu_f + \frac{\mu_t}{Pr_{t,k}} \tag{3.60}$$

$$\Gamma_\omega = \mu_f + \frac{\mu_t}{Pr_{t,\omega}} \tag{3.61}$$

where $Pr_{t,k}$ and $Pr_{t,\omega}$ are the respective turbulent PRANDTL numbers and μ_t is the turbulent viscosity, which is described as:

$$\mu_t = \frac{\rho k}{\omega} \frac{1}{\max\left[\frac{1}{\alpha^*}, \frac{SF_2}{\alpha_1 \omega}\right]} \tag{3.62}$$

with S the strain rate magnitude. σ_k and σ_ω are respectively defined as:

$$\sigma_k = \frac{1}{\frac{F_1}{\sigma_{k,1}} + \frac{1-F_1}{\sigma_{k,2}}} \tag{3.63}$$

$$\sigma_\omega = \frac{1}{\frac{F_1}{\sigma_{\omega,1}} + \frac{1-F_1}{\sigma_{\omega,2}}} \tag{3.64}$$

with $\sigma_{k,1} = 1.176$, $\sigma_{k,2} = 1.0$, $\sigma_{\omega,1} = 2.0$ and $\sigma_{\omega,2} = 1.168$. The coefficient a^* is a low-REYNOLDS number correction term, which damps the turbulent viscosity, and is defined as:

$$\alpha^* = \alpha^*_\infty \left(\frac{\alpha^*_0 + \frac{Re_t}{R_k}}{1 + \frac{Re_t}{R_k}} \right) \tag{3.65}$$

with $Re_t = \rho k \left(\mu_f \omega\right)^{-1}$, $R_k = 6$, $\alpha^*_0 = \beta_i/3$ and $\beta_i = 0.072$. The terms F_1 and F_2 are the blending functions defined as:

$$F_1 = \tanh\left\{ \left\{ \min\left[\max\left(\frac{\sqrt{k}}{0.09\omega y}, \frac{500\mu_f}{\rho y^2 \omega} \right), \frac{4\rho k}{\sigma_{\omega,2} D^+_\omega y^2} \right] \right\}^4 \right\} \tag{3.66}$$

$$F_2 = \tanh\left\{\left[\max\left(\frac{2\sqrt{k}}{0.09\omega y}, \frac{500\mu_f}{\rho y^2 \omega}\right)\right]^2\right\} \tag{3.67}$$

where y is the distance to the nearest surface and D_ω^+ is the positive portion of the cross-diffusion term, defined as:

$$D_\omega = 2\left(1 - F_1\right)\rho\sigma_{\omega,2}\frac{1}{\omega}\nabla k \nabla\omega \tag{3.68}$$

and

$$D_\omega^+ = \max\left[2\rho\frac{1}{\sigma_{\omega,2}\omega}\nabla k\nabla\omega, 10^{-10}\right] \tag{3.69}$$

The production term of k is given by:

$$G_k = \min\left[\mu_t S^2, 10\rho\beta^* k\omega\right] \tag{3.70}$$

and the one for the production of ω is given by:

$$G_\omega = \frac{\alpha}{\nu_t}G_k \tag{3.71}$$

where the coefficient α is defined as:

$$\alpha = \frac{\alpha_\infty}{\alpha^*}\left(\frac{\alpha_0 + \frac{Re_t}{R_\omega}}{1 + \frac{Re_t}{R_\omega}}\right) \tag{3.72}$$

where $R_\omega = 2.95$ and α_∞ is a function of the blending function F_1 and not a constant compared to the standard k-ω model. It is defined by the following relationship:

$$\alpha_\infty = F_1\alpha_{\infty,1} + \left(1 - F_1\right)\alpha_{\infty,2} \tag{3.73}$$

where

$$\alpha_{\infty,1} = \frac{\beta_{i,1}}{\beta_\infty^*} - \frac{\kappa^2}{\sigma_{\omega,1}\sqrt{\beta_\infty^*}} \tag{3.74}$$

$$\alpha_{\infty,2} = \frac{\beta_{i,2}}{\beta_\infty^*} - \frac{\kappa^2}{\sigma_{\omega,2}\sqrt{\beta_\infty^*}} \tag{3.75}$$

The respective terms for the turbulence dissipation are:

$$Y_k = 0.09\rho k\omega \tag{3.76}$$

and

$$Y_\omega = \rho\beta_i\omega^2 \tag{3.77}$$

where the coefficient β_i is a function of the blending function F_1.

The wall boundary condition for the k equation is similar to the enhanced wall treatment presented in Eqs. 3.35 and 3.38, where coarse near-wall meshes correspond to the wall function approach and the finely resolved meshes are determined by an appropriate low-REYNOLDS number approach.

For the wall treatment of the ω equations, the value at the wall is defined as:

$$\omega_\omega = \frac{\rho \left(u^*\right)^2}{\mu_f} \omega^+ \tag{3.78}$$

with its asymptotic value ω^+ in the laminar sublayer:

$$\omega^+ = \min \left[\omega_\omega^+, \frac{6}{\beta \left(y^+\right)^2} \right] \tag{3.79}$$

In the turbulent (i.e. logarithmic) region, ω is defined as:

$$\omega = \frac{U^*}{\kappa y \sqrt{\beta_\infty^*}} \tag{3.80}$$

with the value of ω^+ given by:

$$\omega^+ = \frac{1}{\sqrt{\beta_\infty^*}} \frac{du_{turb}^+}{dy^+} \tag{3.81}$$

3.2.2 CFD Methodology

Now that we have obtained a brief overview on the flow governing equations and the mathematical background on how to solve these equations using different approximation methods, it is time to introduce the reader to the CFD methodology used in the current research. In the upcoming subsections, an overview is given on the meshing and discretisation techniques, the CFD solver used, the treatment of multi-stage setups and the implementation of the multigrid method. Finally, the requirements on the convergence of the simulations are given.

3.2.2.1 Meshing and Discretisation

The first step of a CFD analysis, is to prepare and mesh the geometry of interest. Depending on the complexity of the model, in general, the choice is between structured, multi-block structured and unstructured meshes. In this work, two different meshing tools are used to generate the mesh: the ROLLS-ROYCE in-house tool PADRAM (Parametric Design and Rapid Meshing) (SHAHPAR and LAPWORTH, 2003), which generates automatically and robustly high fidelity 3D multi-block structured as well as unstructured

meshes. And secondly, the commercial meshing tool ICEM from ANSYS, which allows the generation of high-fidelity multi-block structured meshes for complex geometries using a user-defined blocking approach.

As one aim of the present work is the automation of the methodology, the meshes are preferably generated in PADRAM, which generates multi-block hexahedral meshes for the blades and vanes in the main annulus and also for the *baseline cavity* design, which is introduced in the next chapter. The *deflector plate cavity* geometry, which is also presented in the next chapter, is meshed in a multi-block hexahedral way in ICEM as well as in an unstructured way in PADRAM for comparison. For both geometries a mesh independency study is carried out, in order to avoid of getting an inaccurate solution due to the grid resolution.

In all meshes it is aimed for a fine near-wall resolution to resolve the viscosity-dominated sublayers (i.e. $y^+ < 1$). Details on that are given in the next chapter, where the geometries and the discretised models are presented.

To solve the NS equations numerically in a finite domain, this domain needs to be appropriately discretised using a discretisation technique such as the *finite difference method* (FDM), the *finite element method* (FEM), the *finite volume method* (FVM) or the spectral method. For industrial applications it has been proven most convenient to use the FVM in CFD applications as it is a conservative method and also easily applicable to both structured and unstructured meshes. Conservative in this context means that by applying the FVM, the equations for the conservation of mass, momentum and energy are always satisfied, not only in every single control volume but also in the complete discretised domain.

3.2.2.2 CFD Solvers

Two different CFD solvers are used here, both using the FVM as discretisation scheme of the domains. The most important settings for the understanding of the current work are given and explained in the next paragraphs. For more details on the codes and different solver settings, reference is made to the two respective user guides of the codes, FLUENT (2013) and HYDRA (2009).

FLUENT One CFD code used in this research, is the commercial code FLUENT from ANSYS, which is a cell centre based solver and thus computes and stores the variables in the cell centre. This code is used for the validation of the numerical methodology and compared against experimental data. From two available solver options in FLUENT, either density or pressure based, the latter option is picked, as it is considered to perform in a superior way in incompressible flows as they are typically present in turbine cavities. The pressure based solver solves the continuity and momentum equations in either a coupled or a segregated way, whereas the scalar equations, such as the ones for the energy and the turbulence, are solved in a sequential way. In the pressure based coupled solver, both

momentum and continuity equations are solved at the same time, whereas in the segregated solver, first the momentum equations are solved and then a pressure correction is applied by solving the continuity equation. In this work, all simulations are carried out using the pressure based coupled solver.

In order to calculate the fluxes due to convection along the faces, a spatial discretisation of the RANS equations is necessary. From a range of different discretisation options in FLUENT, it is decided to discretise each of the equations in a first step using the first order upwind scheme and then in a second step using the second order upwind scheme. According to ROLLS-ROYCE's best practices, this two step converged solution is robust and stable, guaranteeing an appropriate drop in residuals and giving the opportunity to monitor the simulation step-by-step. For steady-state simulations the flow field is calculated iteratively until convergence is reached (see Subsec. 3.2.2.5). For unsteady simulations the implicit dual time stepping algorithm is used, which solves a defined number of inner steady-state iterations for each time step before advancing to the next one.

HYDRA The second solver used in the second part of this study, is the ROLLS-ROYCE in-house CFD code HYDRA, which solves the RANS equations for the discretised domain using the FVM formulation in a node based manner, calculating and storing the variables in the nodes during the computation. HYDRA is used to carry out an automated design optimisation purely using available ROLLS-ROYCE in-house tools. For that reason, the simulation results in HYDRA are compared against the ones in FLUENT, to guarantee the validity of using the codes interchangeably. Other than FLUENT, HYDRA is a fully coupled density based solver, which in general is most suitable for compressible flows, as they are present in the main annulus of an aero-engine. Density based solvers are still able to solve incompressible flows but usually at a higher computational cost. As in FLUENT, the spatial discretisation of the conservation equations in HYDRA is achieved using a second order upwind scheme. The simulations in HYDRA are calculated in steady-state during the optimisation.

3.2.2.3 Multi-Stage Setup

As the geometry of interest consists of rotating and stationary components, which requires the definition of different rotating and stationary domains, it is necessary to define a way for these domains to communicate with each other. For steady-state calculations, i.e. not time resolved, the *mixing plane* approach is a popular option to couple multiple zones, where as for unsteady simulations, i.e. time resolved, the *sliding plane* approach is the more favoured option.

Mixing Planes While using mixing planes for CFD calculations, the different domains or zones are set as completely independent models and can be meshed separately and also

be defined in different reference frames. This is typical for modeling turbine stages, where the rotor zone containing the rotor blades is defined in a rotating reference frame, but the stator zone containing the vanes is defined in a stationary reference frame, instead. The requirements for a communication between these different reference frames is rather simple: for rotating domains, only the position of the interface or the common boundary needs to be at an identical axial coordinate. The respective sector angles do not have to be identical and can vary for the computation.

Each domain is treated as a steady-state problem and solved accordingly. The communication is achieved through a mixing plane boundary, which pairs an upstream outflow from a blade or vane passage to the downstream inflow of another vane or blade passage. Basically, spatially averaged flux variables are passed from the upstream zone outflow to the downstream zone inflow. Due to the averaging of the fluxes, all unsteadiness arising from circumferential variations in the passage-to-passage flow field, such as wakes or shocks, are lost. Despite this lost of information, the mixing plane model is considered to provide reasonable approximations at a low computational cost, but still keeping in mind the limitations of this approximation technique.

Sliding Planes Sliding planes, also known as sliding meshes, are commonly chosen to solve transient CFD simulations involving different zones with differential translation or rotation. Other than the mixing plane approach, the sliding plane approach only works for identical sectors of the different zones, which are defined as separate dynamic meshes. Dynamic in this context means, that the different cell zones slide relative to one another along the common mesh interface in discrete time steps. In rotating domains in general it is sought for a time-periodic simulation, i.e. a solution which repeats within a certain period, which is related to the rotational speed of the domains. Although, the outcome of the simulation using sliding meshes is considered to be more accurate, as the stage interactions are not lost, there is one main drawback of using sliding planes, which is the much higher computational cost compared to the steady-state simulation.

Interior Planes An interior plane is a particular way to connect a stationary to a rotating reference frame domain, passing the flux information through a conformal mesh interface. By doing this, the need to average the flow field in the space at the interface is avoided and the information is passed on a node-to-node connectivity from one domain to another, instead. This feature is of particular interest, when different stationary and rotating 3D features, such as bolts or holes, are present in close proximity. However, it is recommended to use interior planes only in flow regions where the likelihood of secondary flow features or unsteadiness is low.

3.2.2.4 Multigrid

The rationale for including multigrid methods into the solver is to accelerate the convergence of the simulation. For a fine grid, standard iterative solvers perform well in eliminating so called *high frequency errors*, but are much less efficient at reducing the *low frequency errors*. A way to accelerate the elimination of these low frequency errors is by using coarser grids, where the low frequency errors effectively transform into high frequency errors, which are easier to eliminate.

Both CFD solvers use a multigrid method to accelerate the convergence of the low frequency errors. FLUENT uses the so called *algebraic multigrid* (AMG) technique, where the coarser level equations are generated mathematically without generating and storing separate coarser grids. In HYDRA the *full-approximation storage* FAS method, which uses geometric multigrids with several coarser levels, is used.

The main advantage of the AMG method is the reduced usage of memory as well as the reduced computation time compared to the FAS method. However, the mathematical formulations of the coarser levels are linearised expressions, which results in a loss of non-linear behaviours.

3.2.2.5 CFD Convergence

In FLUENT, the convergence of the numerical simulations is primarily assessed by monitoring the normalised unscaled residuals of the mass, energy, and momentum equations. The normalised residuals are obtained by dividing the unscaled residuals with the maximum residual value obtained from the first five iterations. A general recommendation, given by FLUENT (2009), in order to check convergence is that the normalised unscaled residuals should drop to 10^{-3}.

The same criterion is valid for the unsteady simulations. Each inner steady-state time step should end in a residual drop of 10^{-3}, which can be controlled in the size of the time step or the amount of inner iterations.

In HYDRA the root mean square of the non-dimensionalised residuals of the non-dimensionalised governing equations is summed up and monitored at each iteration. According to HYDRA (2009) an acceptable tolerance for a steady-state simulation is set to a value of 10^{-16}. However, these residuals criteria may not be appropriate for particular geometries, such as rotating multi-stage flows. Therefore, as an additional criterion for convergence, the mass and enthalpy balance of the solution is checked to ensure that errors in these parameters are smaller than 0.1 % and smaller than 3 %, respectively (FICO, 2013).

3.3 Finite Element Analysis

The finite element method (FEM), also called finite element analysis (FEA) is a discretisation technique of a system of partial differential equations. This method is the standard methodology for thermal and structural analyses in solids. In the next subsections, a brief overview is given on the governing equations for the structural mechanics as well as on the discretised equations as they are implemented and solved in the ROLLS-ROYCE in-house FEA code SC03. In the last part, the two methodologies for metal temperature predictions and component displacement calculations, as they are used in this work, are presented.

3.3.1 Governing Equations for Structural Mechanics

The law of FOURIER states, that the heat flux in any direction is proportional to the temperature gradient along the same direction, which in a solid is known as heat conduction or diffusion. The mathematical formulation in its differential transient form is given by

$$\frac{\partial T}{\partial t} = \frac{1}{c_v}\left[-\nabla \cdot (\boldsymbol{\lambda_s} \nabla T) + \dot{q}\right] \tag{3.82}$$

where c_v is the specific heat per unit volume of solid, $\boldsymbol{\lambda_s}$ is the anisotropic thermal conductivity tensor and $\dot{q}$ is the internal heat generation rate per unit volume.

In order to solve this equation, it is essential to define an initial condition, from where the calculation starts. There are basically two different options: first, there is the so called *DIRICHLET boundary condition*, where an initial temperature is specified. The second option is the so called *NEUMANN boundary condition*, where an initial heat flux is specified. The latter needs to satisfy the energy balance across the surface using the following heat flux definition:

$$\dot{q} = \boldsymbol{n} \boldsymbol{\lambda_s} \nabla T \tag{3.83}$$

where $\dot{q}$ is the heat flux into the volume and $\boldsymbol{n}$ is the unit outward normal vector.

The calculation of the structural deformations $\mathbf{u_s}$ is calculated by taking the difference of the local coordinates of the structure $\mathbf{x_s}$ and an initial position $\mathbf{X_s}$:

$$\mathbf{u_s}\left(\mathbf{X_s}, t\right) = \mathbf{x_s}\left(\mathbf{X_s}, t\right) - \mathbf{X_s} \tag{3.84}$$

In order to calculate the non-linear stress-strain behaviour of the solid, the displacements are calculated using the *deformation gradient tensor* $\mathbf{F}$, which accounts for the deformation as well as for the rigid body movement of the solid. It is defined as:

$$\mathbf{F} = \mathbf{I} + \frac{\partial \mathbf{u_s}}{\partial \mathbf{X_s}} \tag{3.85}$$

and also is used to define the *GREENS strain tensor* $\mathbf{G}$, defined as:

$$\mathbf{G} = 0.5\left(\mathbf{F}^T\mathbf{F} - \mathbf{I}\right) \tag{3.86}$$

with $\mathbf{I}$ being the identity tensor.

Thermal strains are calculated using the thermal strain tensor $\boldsymbol{\varepsilon_{th}}$, which - for isotropic materials - is a volumetric tensor integrated over a temperature interval of an initial and operating temperature:

$$\boldsymbol{\varepsilon_{th}} = \mathbf{I}\int_{T_0}^{T_1} \alpha\left(T\right) dT \tag{3.87}$$

where $\alpha(T)$ is the thermal expansion coefficient of the material and is a function of the temperature.

As the focus of this research lies on the temperature, heat transfer and displacement analysis, the structural equations to calculate the material stresses are not presented. The interested reader is referred to LOVE (1905); IRONS and AHMAD (1992).

3.3.2 FEA Code - SC03

All simulations of the solids are carried out using the ROLLS-ROYCE in-house code SC03, which spatially discretises the governing equations inside the solid using the finite element method and temporally using the finite difference method. The code is time-marching and as a such starts from an initial condition, i.e. an initial metal temperature distribution for each node in the solid. For full details, reference is made to the SC03 user guide (1999), whereas a short description of the most relevant facts is given in the next paragraphs.

The mesh is generated automatically inside SC03, subdividing the finite solid domain into a finite number of simple geometrical elements, each possessing a distinct number of nodes at their edges. These elements are typically six-noded triangles in 2D and ten-noded tetrahedrals in 3D. Within a single element, the temperature distribution is assumed to have a spatial variation following:

$$\mathbf{T} = N^e T^e, \text{ with } e = 1, 2, ..., p \tag{3.88}$$

where e is the number of element nodes, N^e is the shape function of the element e, which depends on the element type chosen, and T^e is the temperature associated to that same element.

The variation of temperature over the domain bounds follows the summation approximation

$$\mathbf{T} = \mathbf{N^j T^j} = \left[N_1 \;\; N_2 \;...\; N_p\right]\left[T_1 \;\; T_2 \;...\; T_p\right]^T \tag{3.89}$$

with N^j being a shape array, assembling all shape functions, and T^j being the nodal temperature vector, assembling the respective node temperature. The weak formulation

of the temperature in an element, as it is commonly used in finite element codes (for details reference is made to standard finite element literature), is only dependent on the surrounding nodes, i.e.:

$$N_j(x_i) = \begin{cases} 1, & \text{if } \; i = j \\ 0, & \text{if } \; i \neq j \end{cases} \tag{3.90}$$

Substituting the approximated temperature distribution of Eq. 3.89 into the transient heat equation (Eq. 3.82) and integrating over the solid domain leads to following conduction equation:

$$\mathbf{M}\frac{d\mathbf{T}}{dt} + \boldsymbol{\lambda}\mathbf{T} = \mathbf{P} \tag{3.91}$$

where $\mathbf{M}$ is the specific heat matrix, $\boldsymbol{\lambda}$ is the conductivity matrix, $\mathbf{T}$ is the vector of nodal temperatures and $\mathbf{P}$ is the vector of nodal heat flows.

For a boundary contribution of NEUMANN type to this spatially discretised equation, the temporally discretised equation leads to:

$$\mathbf{M}^{n+1}\left(\frac{\mathbf{T^{n+1}} - \mathbf{T^{n}}}{\Delta T}\right) + \boldsymbol{\lambda}^{n+1}\theta'\mathbf{T}^{n+1} + \boldsymbol{\lambda}^{n+1}\left(1-\theta'\right)\mathbf{T}^{n} = \mathbf{P}^{n+1} \tag{3.92}$$

where θ' can have the value of 0, 0.5, 2/3 or 1 for an explicit forward differencing, a central differencing, a GALERKIN or EULER scheme, respectively. Assuming a constant thermal conductivity as well as a constant material heat capacity, the residual vector $\boldsymbol{R}^{n+1}$ is given by

$$\boldsymbol{R}^{n+1} = \mathbf{P}^{n+1} + \left[\frac{\mathbf{M}}{\Delta t} - \boldsymbol{\lambda}\left(1-\theta'\right)\right]\mathbf{T}^{n} - \left[\frac{\mathbf{M}}{\Delta t} + \boldsymbol{\lambda}\theta'\right]\mathbf{T}^{n+1} \tag{3.93}$$

with its JACOBIAN:

$$\mathbf{J}^{n+1} = \frac{\partial \boldsymbol{R}^{n+1}}{\partial \mathbf{T}^{n+1}} = \frac{\partial \boldsymbol{P}^{n+1}}{\partial \mathbf{T}^{n+1}} - \left[\frac{\mathbf{M}}{\Delta t} + \boldsymbol{\lambda}\theta'\right] \tag{3.94}$$

The final solution is then obtained solving the equations using a quasi-NEWTON approach of the NEWTON-RAPHSON iterative solver, i.e. the derivatives of $\mathbf{M}$ and $\boldsymbol{\lambda}$ are neglected:

$$\mathbf{T}_{k+1}^{n+1} = \mathbf{T}_{k}^{n+1} - \beta'\left(\mathbf{J}^{n+1}\right)^{-1}\boldsymbol{R}_{k}^{n+1} \tag{3.95}$$

where β' is the relaxation factor. The non-linear heat flux vector can be either computed using the same empirical correlations as the ones presented in Chap. 2 or by coupling the

FEA code to a CFD solver. At each time step, Eq. 3.95 is iterated until the residual becomes less than a user-defined threshold. Then the boundary conditions are updated and a new time step starts. In order to obtain a steady-state solution in SC03, it is necessary to time-step the simulation until a steady-state condition is reached.

The discretisation of the structural deformations is done in a similar way. The deflections are discretised with nodal values U^e and interpolating shape functions:

$$\mathbf{u} = N^e u^e, \text{ with } e = 1, 2, ..., p \tag{3.96}$$

where the shape function N^e again depends on the particular element type.

As mentioned above, it is necessary to imply distinct boundary conditions in order to obtain a solution. The most common boundary conditions used in SC03 are the *stream*, the *convecting zone*, the *void* and the *joints*. In a stand-alone SC03 simulation, all these boundary conditions are related to a range of user-defined empirical heat transfer correlations. User-defined in this context means, that the user can first of all choose an appropriate correlation and fine tune it by varying the input parameters, such as mass flow rates, temperatures or pressures. The complete documentation on the available correlations can be found in the SC03 user guide.

A stream in SC03 is defined as a mass flow rate of specified fluid, e.g. air, with a prescribed initial temperature. The stream can exchange energy with the solid and the air temperature changes accordingly. The user specific variables are the fluid properties, mass flow rates, the initial temperature and the heat transfer coefficient.

A convecting zone is defined as a source boundary condition, where the temperature of the fluid is not affected by the addition or removal of heat. The user input variables are the heat transfer coefficient and the fluid temperature. This boundary is generally used for coupling purposes to a CFD code (see next section on aerothermal coupling for details). In this study, convecting zones are also used in order to validate the displacement models, where the experimentally measured metal temperature is applied to the boundary as an air temperature with a very high heat transfer coefficient. Details on this procedure are given in Subsec. 3.3.3.

A void represents air with negligible heat capacity and hence is instantly in equilibrium with its surroundings. The main user inputs are the heat transfer coefficient, the power input and the pressure.

Joints are a structural boundary condition and can be defined as fixed, sliding or non-linear and cyclic. Fixed describes a welded-like behaviour of two adjacent components. Sliding or non-linear means that one component can slide over the other by still allowing tension transmission through the boundary. Cyclic joints are used for periodic surfaces.

3.3.3 FEA Methodology

Different FEA models of the test geometry (2D axisymmetric and 3D sector models) are generated using the code SC03. The details of the geometry and the meshes are given in the next chapter. Appropriate solid properties, e.g. thermal conductivity as a function of the metal temperature, are modelled and applied in the boundary condition panels.

During this research, thermal as well as thermo-mechanical models are set up and solved accordingly. In case of a purely thermal simulation, the option in SC03 is chosen, to only solve the conduction equation by switching off the mechanical stress-strain equations. In the case where a thermo-mechanical simulation is carried out in order to predict component displacements, the mechanical equations are switched on again.

The purpose of the thermo-mechanical simulation is to evaluate the effects of thermal and centrifugal growth with respect to the relative displacements of the rotating and stationary components and to compare the numerical predictions to the experimental measurements. The rotor is manufactured from titanium (Ti318), whereas the stator is manufactured from stainless steel (St304). Both material properties are modeled in SC03 as a function of temperature. For that a simplified 2D FEA model is generated, where as thermal boundary conditions only convecting zones and thermal contacts are defined. The setup of the convecting zones follows the approach proposed by Eastwood (2014). At each experimental temperature measurement location, a convecting zone is defined in the according FEA model, with an artificially high heat transfer coefficient to impose surface temperatures in the model. Furthermore, thermal contacts are defined, where different parts touch. The structural boundary conditions are limited to dynamic restraints and joints, in order to fix the model in space and to model the component contact. These boundary conditions are obtained from a read-across of the calibrated complete rig model from a previous work within Rolls-Royce.

Convergence of the mesh is checked at the end of a simulation. The result is considered to be mesh independent when the temperature error of the final solution is smaller than a user-defined tolerance, which is chosen to be 1.25 K in this work.

3.4 Aerothermal Coupling Methodology

The previous sections gave an overview on stand-alone CFD and FEA analyses and how the governing equations are solved for the fluid and solid domains, respectively. As already discussed in Chap. 2.1, heat transfer between a fluid and a solid domain is a two way interaction, and referred to as conjugate heat transfer combining heat conduction in the solid and convection in the fluid. In this research, the hFTB coupled method is used, as has been introduced in Subsec. 2.1.4.1.

This method was already successfully applied to rotor stator flows adjacent to the main gas path in the past, and has proven to be reasonably stable (see Chap. 2). Having a look

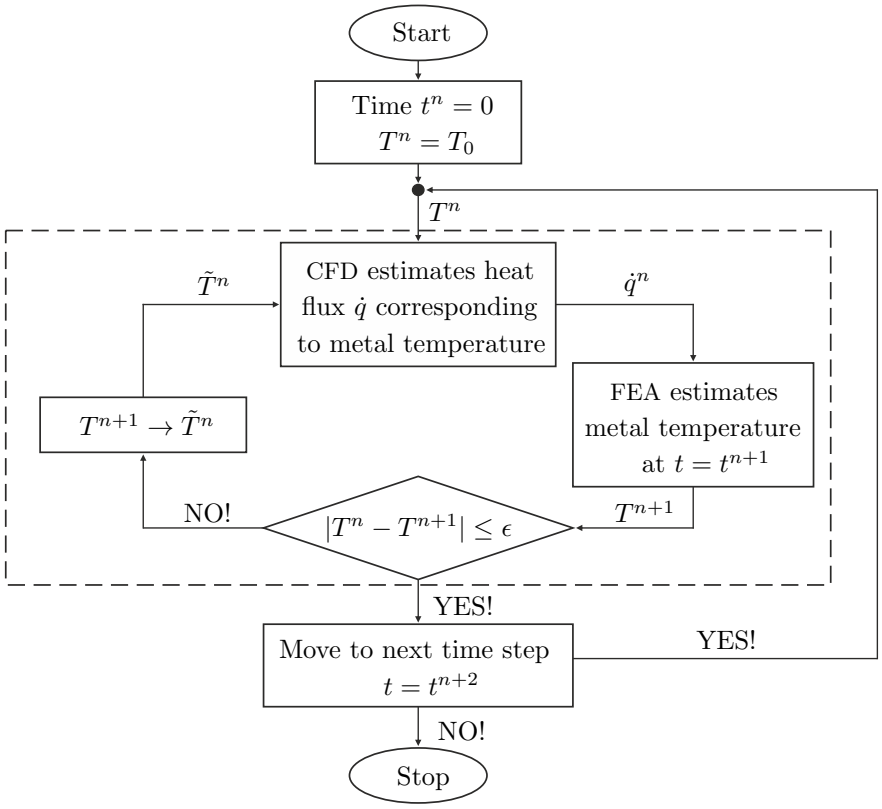

Figure 3.1: Schematic representation of the aerothermal coupling process

at the convergence criterion derived by VERSTRAETE (2008) (see Subsec. 2.1.4), which depends on the local BIOT number at the coupled walls, supports this choice. Carrying out two different isothermal CFD simulations of the TSW sector gives an estimate of the NUSSELT numbers at the discs and the blades and thus the according heat transfer coefficients, following the approach:

$$\hat{h} = \frac{\dot{q}_2 - \dot{q}_1}{T_2 - T_1} \tag{3.97}$$

The maximum HTC is in the range of $\hat{h} = 500\,\mathrm{W\,K^{-1}\,m^{-2}}$ and present in the rim regions and the fin tips at the labyrinth seal. Due to the fact that the temperature gradients at the rig operating conditions are rather small compared to real engine conditions ($\Delta T_{hot-cool} \approx 100\,\mathrm{K}$), the BIOT numbers in the overall domain are below 1. According to VERSTRAETE the hFTB method is always stable for such conditions.

A flowchart of the coupling procedure between the ROLLS-ROYCE in-house FEA solver SC03 and the commercially available CFD code FLUENT is shown in Fig. 3.1. Both codes communicate through a ROLLS-ROYCE proprietary library. It is within this functionality that the user specifies one or more coupled walls, outlining a CFD domain, which may cover a part or the whole of the finite element model. For the boundary condition setup in SC03 this means, that at the coupled walls convecting zones are applied to obtain and exchange information with the fluid. At all non-coupled walls, standard boundary conditions

such as streams and joints are applied, coming from a read-across of thermal matching against experimental test data, which was already done prior to this research. A brief summary of the coupling method is given below, whilst a more detailed description is given by ILLINGWORTH et al. (2005); VERDICCHIO (2001).

The general setup of the coupling process inside SC03 is equivalent to the stand-alone FEA analysis. Within SC03, the user defines a transient analysis by specifying an analysis cycle for the particular geometry under investigation, i.e. the evolution of a set of environment parameters through the time span simulated. These are user-input parameters and include mass flow rates, operating temperatures and pressures. The code is time marching and as such SC03 needs an initial condition, i.e. an initial metal temperature distribution for each node in the solid. To solve the heat equation in the solid, SC03 uses an implicit time discretisation and a NEWTON-RAPHSON solver (see previous section for details).

The aerothermal coupling process is schematically depicted in Fig. 3.1. First, the system calls the fluid solver passing to it the current values of boundary temperatures T^n, (n indicating that these quantities refer to the time t^n). The choice of these initial values strongly effects the convergence of the coupling process: the closer the initial guess is to the final solution, the quicker the simulation will converge. Therefore, in this study, it is started from interpolated temperatures obtained from a read-across from previous thermally matched models. It is assumed that the solid time response is much slower than the fluid instantaneous temperature variations. Therefore, steady or time averaged unsteady CFD calculations can be employed using the boundary conditions passed by the finite element code.

More precisely, the CFD solver applies the wall temperature boundary conditions passed from the SC03 model and runs either a steady-state or an unsteady case to find the solution corresponding to these prescribed wall temperatures. After a certain degree of convergence is achieved, based on user inputs, the CFD solver outputs the heat fluxes $\dot{q}^n$ computed on the wall boundaries. Typically, for steady-state CFD simulations 20 iterations are sufficient to update the solution, whereas for unsteady simulations, three blade revolutions with 20 inner iterations at each CFD time step are used to obtain an updated averaged flow field. The calculated heat flux values are returned to SC03, which runs the NEWTON-RAPHSON solver to obtain an improved estimate of the temperature field at time t^{n+1}. The CFD solver and the FEA NEWTON-RAPHSON solver loop is then repeated until the solution has stabilised to within a user defined tolerance ϵ. In this study, the tolerance is chosen to be smaller than 1.25 K. When the temperatures are stabilised, (typically this requires around 20 iterations), the analysis moves to the next time step t^{n+2} in the analysis cycle.

As the coupled walls are non-conformal interfaces due to the different meshing and solver approach of the respective solvers, it is necessary to interpolate the solution from one mesh to another. The basic principle of the relationship between the SC03 integration points and the CFD node points, for passing the metal temperatures at a coupled wall boundary, providing a smooth, continuous, wall temperature profile which can be read into the CFD model, is illustrated in Fig. 3.2. For achieving that, each CFD node point is

considered, meaning that the nearest SC03 integration points, either side of a each CFD node, are identified in the first place. Having done this, the metal temperatures from these SC03 integration points are interpolated with respect to distance, to determine the metal temperature at the location of the CFD node.

The interpolation of heat fluxes passed from the CFD node points to the SC03 integration points, is more complex and the general approach is illustrated in Fig. 3.3. It is assumed that the SC03 integration points are always more sparsely distributed than the CFD node points, which should always be the case, since the CFD model always requires a much finer mesh than the FEA model, in order to provide an accurate solution of the fluid flow.

As for the temperature interpolation, each CFD node point is considered. The nearest SC03 integration point to each CFD node is identified, and then all the CFD nodes are grouped together, according to the SC03 integration point to which they are associated. Since each CFD node has an individual cell area and heat flux attributed to it, it is possible to pass a value of heat flux to the SC03 integration points, which accounts for any spikes of heat transfer occurring between the SC03 integration points.

The heat flux passed to each SC03 integration point is defined as:

$$\dot{q} = \frac{\text{total power}}{\text{total CFD cell area}} \tag{3.98}$$

where the *total CFD cell area* is the sum of all the individual CFD cell areas, to each associated SC03 integration point, and the *total power* is the sum of the power apportioned to each CFD cell within the grouping. The power attributed to each CFD cell is calculated by multiplying the individual cell area by the cell's heat flux.

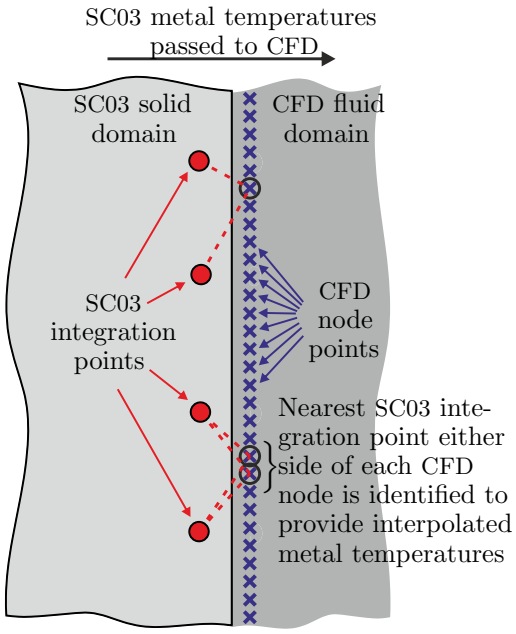

Figure 3.2: Interpolation of SC03 metal temperatures at a coupled wall

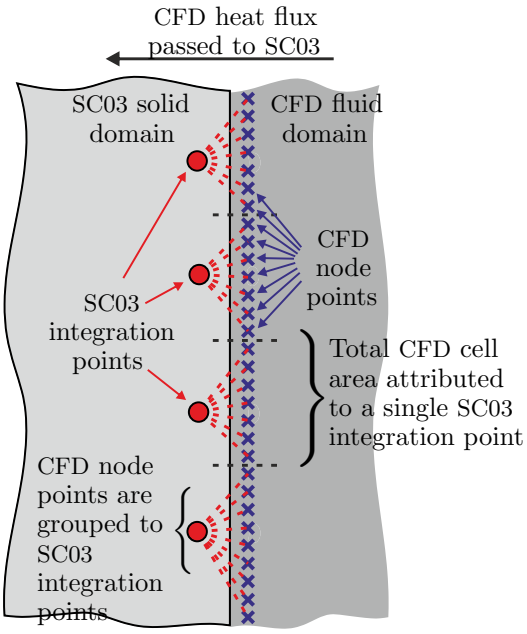

Figure 3.3: Interpolation of CFD heat fluxes at a coupled wall

These two interpolation techniques ensure a robust and accurate exchange of information between the two solvers. Furthermore, once a coupled simulation is converged, a fully consistent solution along the coupled interfaces is obtained.

The thermal coupling presented here is used to validate the methodology for TSW heat transfer. Therefore, cold and hot running geometries of different test cases are analysed and compared to available experimental test data. Considering cold and hot running clearances highlights the impact of the structural deflections on the heat transfer and thus the metal temperature predictions inside the TSW. In the second part, the design optimisation, the aerothermal coupling is used to verify the outcome of the optimisation using standalone CFD, and to extract the metal temperatures of the optimised and non-optimised designs.

3.5 Kriging Based Optimisation Methodology

One of the goals of this research is to detect a better geometrical design of a TSW and a rotor stator cavity, in order to reduce the required amount of cooling mass flow rate, but still ensuring efficient cooling of the life critical components. Therefore an automated optimisation technique is applied to the MAGPI geometry with a deflector plate in order to find the optimum shape and position of that deflector plate. Due to the excessive run time of the aerothermal coupling for each simulation, it is decided to run only adiabatic CFD simulations during the optimisation process and to validate the outcome with the aerothermal coupling afterwards.

Another desired requirement is to run the optimisation using only Rolls-Royce inhouse tools, i.e. HYDRA for the CFD, whereas the aerothermal coupling is conducted using FLUENT. In order to ensure that the two solvers provide similar results, the results for both adiabatic simulations using the two different codes are compared to each other.

For complex engineering problems, the aim is to get to the optimum solution as fast as possible, i.e. with a minimum number of simulations. Therefore, mathematical or statistical approximation models are used to speed up the optimisation. In the technical literature, these models are known as surrogate models, metamodels or response surface models (RSM), as they are described in Subsec. 2.5.4. In this study, the optimisation is conducted by using the regressing Kriging technique, which is able to replicate accurately a complex multi-dimensional function with the ability to filter out scatter or noise coming from numerical calculations such as CFD (Forrester et al., 2006; Brooks et al., 2011).

The optimisation is conducted using the Rolls-Royce SOPHY system (SOFT, PADRAM, HYDRA) (Shahpar, 2005). SOFT (Smart Optimisation For Turbomachinery) (Shahpar, 2002) provides a library of different optimisation algorithms and communicates through python scripts with the other codes in order to execute them in batch mode, to evaluate the results of the simulation. In general, these computations are run in parallel on an HPC cluster in order to reduce the overall run time.

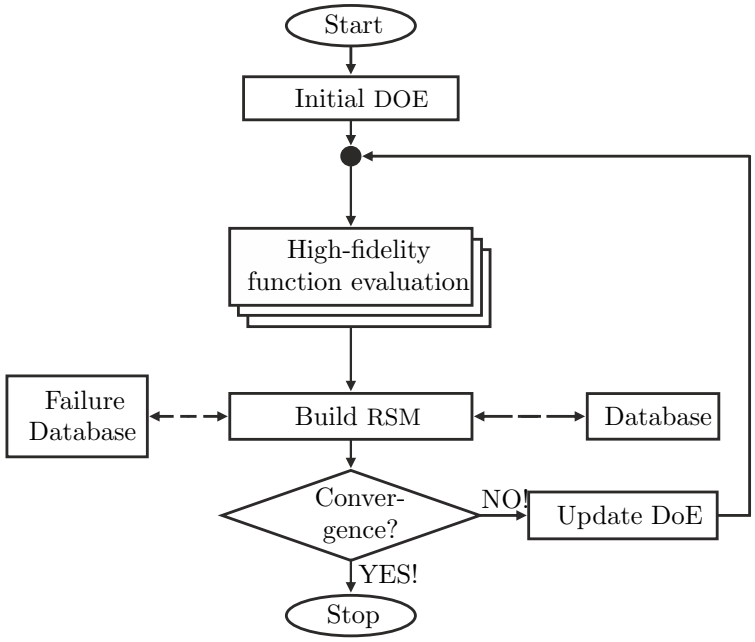

Figure 3.4: Schematic representation of the optimisation strategy using regressing Kriging in SOFT

The 2D geometry is generated parametrically using a python programme and then fed to the meshing tool PADRAM (Parametric Design and Rapid Meshing) (SHAHPAR and LAPWORTH, 2003). PADRAM then generates automatically and robustly 3D structured and unstructured meshes for the main annulus and for the cavity domain, respectively. The discretised 3D model is passed to the HYDRA system (LAPWORTH, 2004) for pre-processing and finally solves the RANS equations. The converged CFD solution is then fed to the post-processing tool Paraview, where the solution is evaluated with respect to the figure of merit, i.e. the objective function, then passed to the optimiser. The details on the geometry and the parameterisation including the optimisation setup are given in Sec. 6.1.

A schematic representation of the optimisation process based on Kriging as it is implemented in SOFT for this study, can be seen in Fig. 3.4. Starting from an initial LHS DOE set, the obtained initial designs are evaluated in parallel and saved in a database or in case of failure, in a failure database. The number of samples for the initial DOE is defined as five times the number of design variables, following the recommendations of BAERT et al. (2015). This seems to be a reasonable approach in this study, due to a defined low dimensional design space (8 dimensions as we will see later in Sec. 5.3). Once the designs are evaluated, a RSM is built using regressing Kriging and the convergence of the RSM is checked using the efficient leave-one-out cross-validation method (see BROOKS et al. (2011); DUBRULE (1983)). If the RSM is within the desired accuracy, the optimisation stops. Otherwise, the initial DOE is updated by additional points in order to iteratively get to a more accurate solution.

In order to refine the DOE and to find a new set of update points, the RSM is searched using global and local optimisation techniques. Therefore, two optimisation algorithms are chosen from the SOFT library: as a global optimiser, ARMOGA is chosen, and for a local optimiser, the SQP method is used (both presented in Chap. 2.5.2). The searching criteria follow a list of preferences until the maximum number of update points, also known as infill points, is reached. In this study, the maximum number of update points is set to six points in total per update. Initially a search is made for the *best constrained generalised expected improvement* (CGEI) (FORRESTER et al., 2008). In a second step - if no CGEI could be found or the maximum number of update points has not been reached yet - the *maximum Kriging error* is sought in order to find the location of maximum uncertainty. In a third step a search is made for the *best Kriging prediction*. In the case that the maximum number of update points still is not reached, random points are included.

The requirements for the convergence of the CFD simulations as well as for the aerothermal coupling used for validation purposes, follow the criteria mentioned in Subsec. 3.2.2.5 and Sec. 3.4, respectively.

3.6 Summary

This chapter has outlined the methods used in the overall modeling and optimisation process of this research. In summary the following topics were covered and presented:

1. The NAVIER-STOKES equations have been reviewed and the simplifications due to REYNOLDS-averaging for computational purposes were explained. In addition to that, three different turbulence models in the context of RANS were presented, highlighting their main advantages and drawbacks in CFD problems. The performance of these models in the MAGPI cavity model is evaluated in Chap. 6 and the major differences between the solutions are discussed.

2. The details on the CFD methodology including the meshing and discretisation approaches (ICEM and PADRAM), the different CFD solvers (pressure-based (FLUENT) and density-based (HYDRA)) and the solution setup including calculation speed-up strategies such as multigrid methods and convergence criteria are outlined. This is important for the stand-alone CFD analyses as they are shown in Sec. 7.2 and used during the automated design optimisation (Chap. 8).

3. The equations for structural mechanics (thermal and thermo-mechanical) including their discretisation within the RR in-house FEA code SC03 have been discussed in detail. The different types of boundary conditions available in SC03, which are relevant to this work, were presented and the basic principles of the solution algorithm have been explained. The thermo-mechanical prediction capabilities of SC03 are benchmarked against experimental displacement measurements in Sec. 7.1 and

the thermal predictions are used within the coupled aerothermal method validation (Sec.7.4 and 7.5).

4. A separate section summarised the aerothermal coupling methodology, which is based on the hFTB method. A detailed overview of the iterative process, as it is implemented in a proprietary library of SC03, and the interpolation procedure between the CFD and the FEA solutions at the solid-fluid interface are given. This method is used for benchmarking purposes in Chap. 7, where the computational results are compared to experimental measurements. Furthermore, this method is used to validate the optimised deflector plate design in Chap. 8.

5. In the final section of this chapter an optimisation technique to modify the local geometry of interstage cavity components to improve the performance of the sealing and cooling system in a TSW. Details on the optimisation strategy are introduced to the reader and the choice of the individual optimisation methods available in the RR library SOFT was justified by referring to the literature review in Chap. 2. The presented optimisation loop is used for the design optimisation of the deflector plate inside the upstream TSW cavity. Details on the parameterisation and the optimisation setup are presented in Sec. 5.3. The results are then discussed in Chap. 8.

4 The MAGPI Turbine Test Rig

After having introduced the scientific problem of interest in the previous chapters, it is now time to introduce the reader to the experimental apparatus, the MAGPI turbine test rig. First the main operating conditions and the general rig design are summarised. Then the details on the instrumentation are given, which is followed by the selection of the test cases.

4.1 The Turbine Rig Test Facility

All experiments were carried out by other researchers at the UNIVERSITY OF SUSSEX, Thermo-Fluid Mechanics Research Centre in an earlier EU funded project, MAGPI (2006). The assembly of the complete experimental setup can be seen in Fig. 4.1 including a close-up view of the drive arm and the first rotor-stator stage. A brief overview is given in this thesis. In order to obtain the full details, reference is made to the work of COREN et al. (2010) or EASTWOOD et al. (2012); EASTWOOD (2014).

The test section of the rig comprises a two-stage turbine, rated at $P \approx 400\,\mathrm{kW}$, spinning at $\omega \approx 10630\,\mathrm{RPM}$, with a pressure ratio $p_1/p_2 \approx 2.5$ at the design condition. The flow coefficients are $\phi_1 \approx 0.51$ and $\phi_2 \approx 0.62$, the work coefficients are $\psi_1 \approx 1.6$ and $\psi_2 \approx 1.4$ for the first and the second stage, respectively. The main annulus air is supplied to the rig by an adapted aero engine driven compressor plant at $\dot{m}_{MA} \approx 4.8\,\mathrm{kg\,s^{-1}}$, an absolute

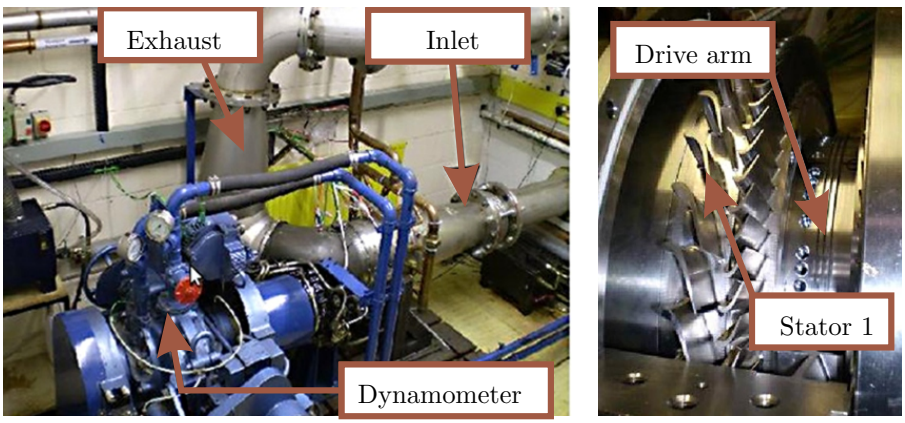

Figure 4.1: Experimental setup of the test rig

pressure of $p_{abs} \approx 3.3\,\text{bar}$ and an absolute total temperature $T_{0,abs} \approx 170\,^{\circ}\text{C}$. An Atlas Copco screw type compressor is used to provide the various cooling air supplies. The cross-section of the rig test section has been designed to represent the key features of a TSW. The average MACH number behind the stator vanes is $Ma \approx 0.6$, which generate realistic potential fields at the up- and downstream rim gaps. The turbine has also been designed to suit the subsequent FEA and CFD analyses, with 39 vanes and 78 rotor blades for each stage. Thus the analysis models can be set-up as a sector model at 1/39 th of the complete rotor-stator system keeping the accuracy and the computational costs within the limits of the modest computing capability used in this study. Within the second test phase, a deflector plate was included into the TSW. It was attached by 18 bolts to the stator foot. A modelling approach for that is presented below.

Cooling Air Supply

Fig. 4.2 depicts a technical drawing of the complete rig highlighting the rotating parts in green and the coolant delivery path in light blue. The cooling air is supplied to the hub region of the test section via insulated transfer tubes. The rig has a split casing and is designed to allow rapid geometry changes. In the current research, the cooling air is introduced radially into the upstream cavity through 39 drivearm holes. Different rig setups for supplying the cooling air into the cavity are presented by DIXON et al. (2014).

In order to achieve accurate metering of the cooling air into the stator wells, the delivery path is separated from the outer wheelspace by a balance cavity sealed by two labyrinth seals. During testing this cavity is pressure balanced against the cooling air supply of higher pressure to prevent leakage; effectively a blown seal is formed. The balance air is

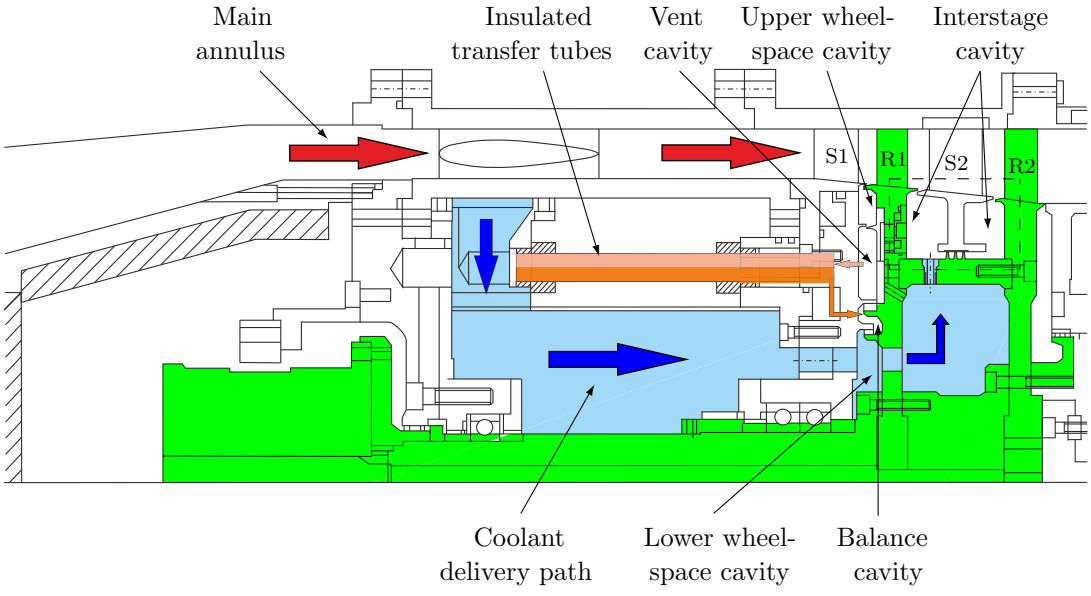

Figure 4.2: CAD drawing of the experimental setup

measured upstream of the rig, and vented from the intermediate wheelspace to prevent egress into the main annulus. This arrangement also allows a known rate of egress to be specified. Cooling air flow rates were determined using hot film air mass meters.

Instrumentation

Turbine main annulus conditions are measured by temperature and pressure probes built into the leading edges of the nozzle guide vanes (NGV), avoiding the blade passage restrictions inherent with interstage probes. The TSW and surrounding regions have been instrumented with metal and air thermocouples as well as static pressure tappings. An overview of the location of all sensors within the experimental setup can be seen in Fig. 4.3. The static thermocouples have been calibrated within a range of accuracy of $\pm 0.1\,\mathrm{K}$ in the measurements whilst the rotating thermocouples precision is of $\pm 0.2\,\mathrm{K}$. The mass flows within the cooling system are measured with an uncertainty of $\pm 0.5\,\mathrm{g\,s^{-1}}$.

Fig. 4.4 provides a more detailed overview of the temperature and pressure instrumentation inside the upstream and downstream cavity, which is the area of interest during this research. Besides measuring the temperatures and pressures, two additional high precision *Micro-Eddy current sensors* were installed in the rig in order to capture the radial and axial displacement of the rig components and thus to obtain a reliable measurement of the interstage seal radial clearance and any effect of axial movement on rim gaps etc.. These displacement sensors were able to measure movements of the magnitude of $10^{-5}\,\mathrm{m}$ with a measurement uncertainty of $\pm 6\,\mu\mathrm{m}$.

During the second test phase of the MAGPI project, the deflector plate was added inside the upstream cavity, attaching it to the stator foot with 18 bolts (also called spacers in some studies). However, no additional measurement instrumentation than the original was

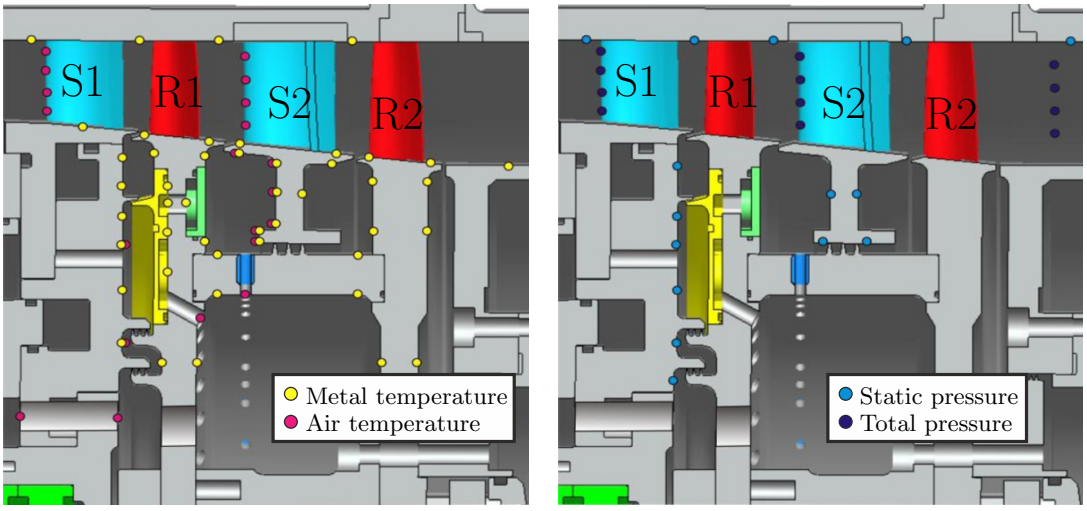

Figure 4.3: Temperature (left) and pressure (right) sensor positions inside the two-stage turbine rig test facility, by courtesy of Rolls-Royce plc.

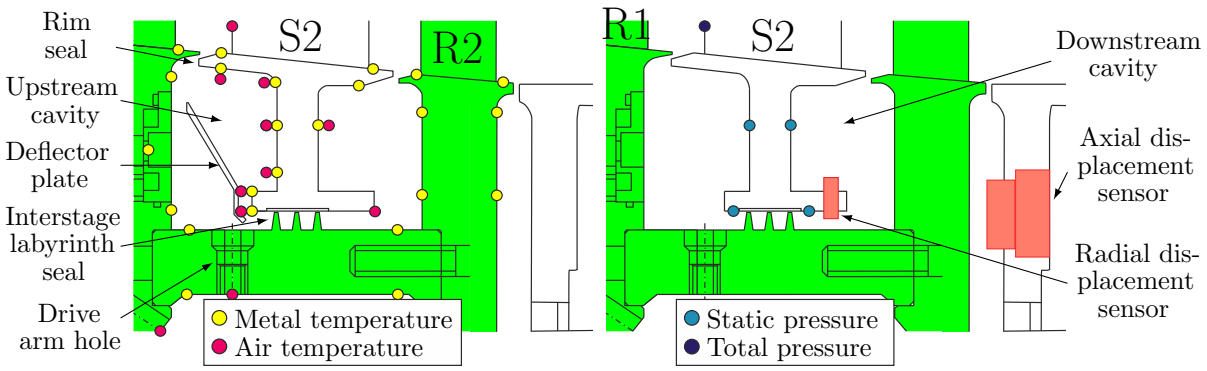

Figure 4.4: Temperature, pressure and displacement sensor positions inside the TSW with (left) and without (right) mounted deflector plate

included along the deflector plate. In order to obtain the full details on the experimental instrumentation, reference is made to EASTWOOD (2014).

4.2 Overview of Selected Test Cases

Prior to embarking on the modeling strategies description, an overview of the test cases relevant to this study is given. The configuration in which the air is inserted radially through 39 drive arm holes is selected as baseline geometry whilst the deflector plate geometry, whose benefits were studied by POHL et al. (2015), is used for comparison. From a vast range of test data available, two flow cases per geometry are chosen. Regarding levels of the cooling flow, two values of mass flow are selected based on the likelihood of main stream hot gas ingestion into the cavity. Based on the measured egress and ingestion rates (see Fig. 4.5), the choice is made for two cooling mass flow rates: The first with a high likelihood of net ingestion, $\dot{m}_{cool,1} \approx 30\,\mathrm{g\,s^{-1}}$ and the second with almost no net ingestion,

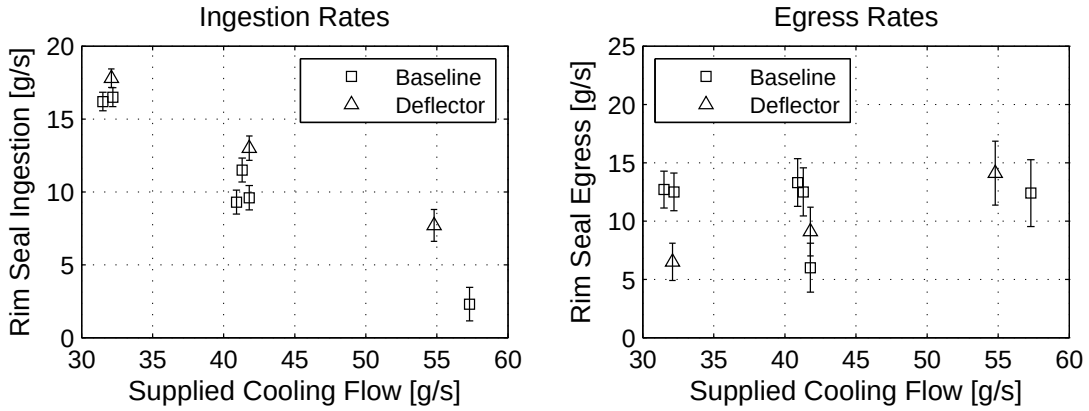

Figure 4.5: Indicated rim seal ingestion and egress rates for a selection of test cases taken from EASTWOOD (2014)

Case #	$\dot{m}_{cool}/\dot{m}_{MA} \times 10^{-2}$	$C_{w,cool} \times 10^3$	T_{cool}/T_{hot}	$Re_\phi \times 10^6$	λ_T
BL1	0.64	9.89	0.82	1.92	0.09
BL2	1.14	17.81	0.78	1.92	0.16
DP1	0.62	9.61	0.83	1.91	0.09*
DP2	1.12	17.4	0.75	1.91	0.16*

Table 4.1: Flow conditions for the four test cases

$\dot{m}_{cool,2} \approx 55\,\mathrm{g\,s^{-1}}$. The flow details of these four test cases is given in Tab. 4.1, where the indices *BL* and *DP* are introduced for the baseline and the deflector plate geometry, respectively. The indices *1* and *2* stand for the a high and low likelihood of ingestion, respectively.

From that table it can be seen that the operating conditions are very similar for all the test cases. By calculating the turbulent flow parameter, the relative strength of the throughflow to rotation can be estimated. From the literature, it is known that for values of $\lambda_T \leq 0.1$ the cavity flow is dominated by the rotation, which is the case for the flow cases with small cooling mass flow rate (BL1 and DP1). However, for the deflector plate geometries (highlighted by the asterisks), it is not certain that this correlation is valid due to the change of the cavity geometry.

Two more definitions of technical terms in the context of seal clearances are necessary for the understanding of the next chapters and sections. On the one hand, there is the term *cold built* or simply *cold* for the geometries at non-operating conditions and on the other hand, there is the term *hot running* or *hot* for the deformed cases during hot running. The latter are based on the measurements of the radial displacement sensor installed in the rig.

4.3 Summary

This chapter summarised the main technical information of the experimental turbine test apparatus, which is required for the understanding of the upcoming numerical studies. First, the MAGPI turbine rig test facility was presented including the information of the main operating conditions. The experimental sensor instrumentation was shown and an overview of the relevant flow cases was given. Based on the likelihood of hot gas ingestion two different coolant flow cases for the two geometries (baseline and deflector plate) have been chosen as benchmarking test cases. The experimental test results serve as inlet and outlet boundary conditions for the respective FEA and CFD models, which are presented in the upcoming chapter, as well as for the validation of the aerothermal coupling methodology.

5 Numerical Modeling

In this chapter, it is time to introduce the reader to the numerical models, which are based on the experimental test rig setup presented in the previous chapter. The numerical models as they are used for the FEA as well as for the CFD analyses are presented in detail. The last part of this chapter focuses on the cut-down CFD model as it is used in the optimisation process. The model is presented including the geometry parameterisation and the optimisation setup.

5.1 FEA Modeling

In this section a step-by-step introduction of the various finite element models used during this work is given. At first the stand-alone thermal and thermo-mechanical 2D axisymmetric FEA models are presented including the modeling strategy and boundary condition definition. This is followed by introducing the reader to the 3D sector model used for the aerothermal coupling to CFD, also including the model setup assumptions. All models are generated using the ROLLS-ROYCE in-house code SC03, where appropriate solid properties, e.g. thermal conductivity as a function of the metal temperature, are modelled.

5.1.1 2D Models

The first model (Fig. 5.1) was used in the rig design phase to help establish operating temperatures and stresses using empirical correlations (the author did not contribute to

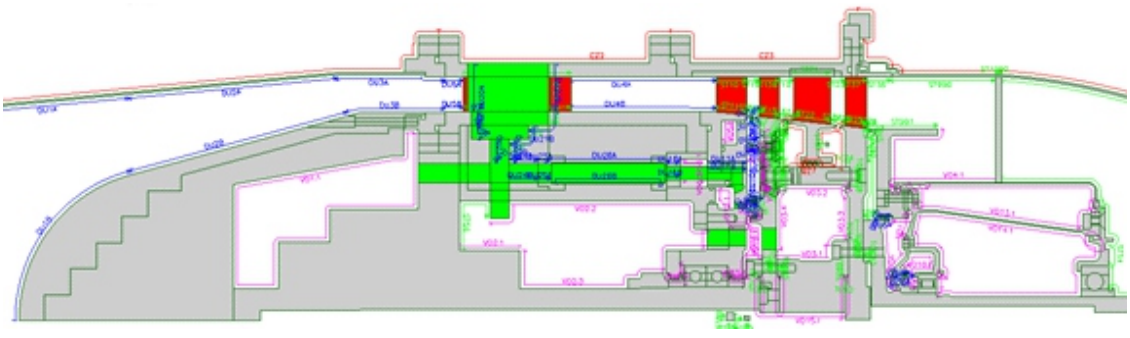

Figure 5.1: 2D finite element model for thermal analysis

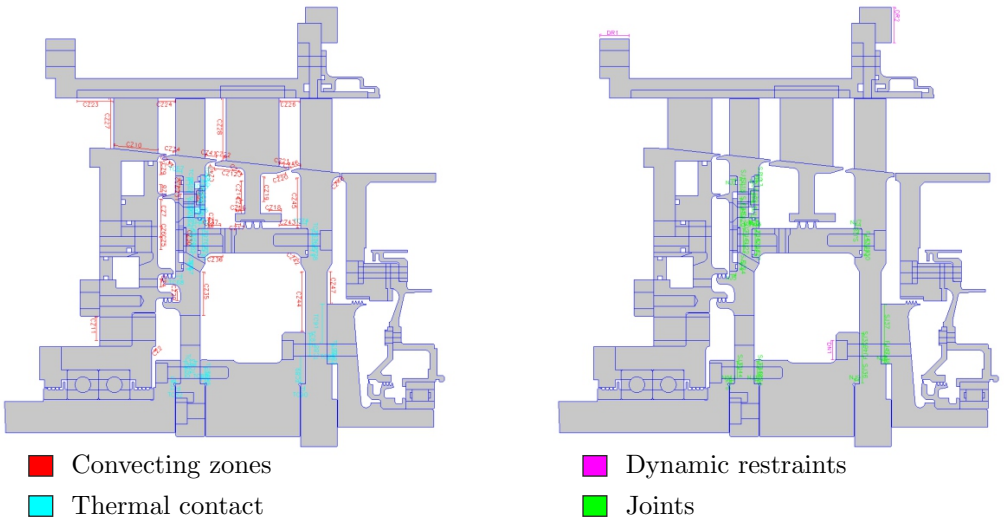

Figure 5.2: 2D FEA models with appropriate thermal (left) and structural (right) boundary conditions to predict displacements

Figure 5.3: 2D FEA mesh for the baseline (left) and the deflector plate (right) geometry

that work, but is familiar with the process). The extent of the geometry in this model covers the entire test section plus the internal air system and the telemetry unit placed in the front cone. At a later stage, this model of the rig was used to calculate the metal temperatures to allow benchmarking between the existing test results and the stand-alone thermal FEA analysis. During this research, this model is used to provide matched (validated) thermal and structural boundary conditions for both cut-down models, 2D and 3D, where no CFD is coupled to the FEA.

The second type of model (one for each geometry and test case) is a cut-down section of the rig, as it can be seen in Figs. 5.2 and 5.3. Thermal boundary conditions are applied

in the form of convecting zones and thermal contacts. At each thermocouple measurement position a convecting zone is defined to prescribe the measured temperature. The regions where two components touch, is modeled using temperature continuity at the contact point. From a structural point of view, dynamic restraints are defined to fix the geometry against non-physical axial and radial absolute movements. Two faces of the casing are fixed for that purpose, one radially and the other axially, as it is read-across from the whole rig model. All touching areas between components non-linear and sliding joints are defined, also coming from the read-across of the complete rig model.

Both geometries are meshed within SC03 and can be seen in Fig. 5.3. All elements are second-order six-node triangles with a distortion ratio of 5.3 and general tolerance of 10^{-12} as it is recommended in the SC03 user manual and guidance materials. The overall node count for both geometries is around 100.000.

5.1.2 3D Sector Models

The 3D models, shown in Figs. 5.4 and 5.5, are 1/39 th sectors containing the rotor blade rows and discs, the second stage stator vane and the discs, the connecting drive arm and the stator foot. The deflector geometry additionally contains the sector of the deflector plate and one scaled bolt (Pohl et al., 2015). The scaling of the bolt is explained in the CFD modeling section. The models are set up to run thermally only. The boundary conditions in the regions of the TSW as well as in the rotor 1 blades and stator 2 vane are coupled to the CFD models, which are the red walls representing the convecting zones. The remaining non-coupled boundary conditions are obtained from a read-across from a matched model against test data. This allows a back-to-back comparison of measured thermocouple test data obtained from the experiments against the numerically predicted wall metal temperatures, thus giving the opportunity to qualify and quantify the accuracy

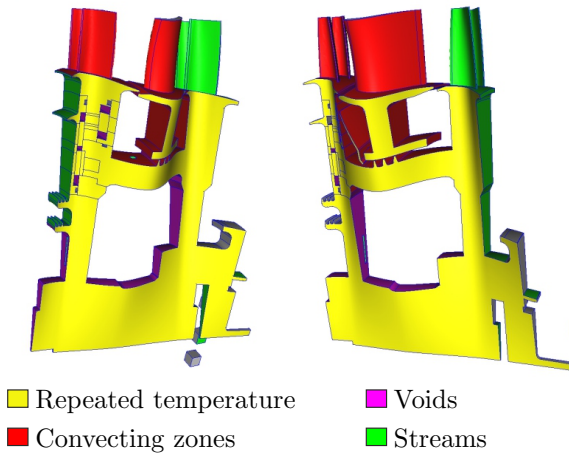

Figure 5.4: 3D baseline (left) and deflector (right) FEA models highlighting the thermal boundary conditions

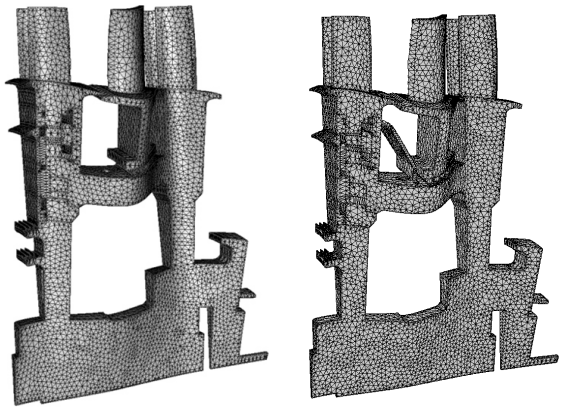

Figure 5.5: 3D baseline (left) and deflector (right) meshed FEA models for coupled aerothermal analyses

of the numerical heat transfer method. (Note: this is often referred to as model validation).

The meshes of the two sector geometries are shown in Fig. 5.5. The discretised models contain roughly 50.000 second order tetrahedral cells with about 100.000 nodes at a minimum distortion aspect-ratio of 3.

5.2 3D CFD Sector Modeling

Over the recent years, following the conclusion of the MAGPI project, CFD modelling capabilities to analyse the flow and heat transfer in the TSW have already been developed. It was shown that this requires both steady and unsteady CFD calculations in full 3D, particularly where cooling efflux and annulus gas ingestion are finely balanced. Although the suitability of a sector model is still not certain, initial results are encouraging and it is chosen to keep the computational requirements within the capability of available computer facilities by using a 1/39 th sector model of the rig geometry.

Figure 5.6 shows the extent of the CFD sector model superimposed with the FEA sector model. The modeling follows some lessons learnt from previous studies and internal reports, which were carried out at ROLLS-ROYCE. In order to save computer memory and computational run time, the upper wheelspace and vent cavities are not modeled in this study. Instead this whole domain is chopped down to one mass flow inlet accounting for the flow egressing from the upper wheelspace into the main annulus, obtained from a read-across of the complete model. Furthermore, the cavity is modeled with straight walls, which do not fit the curvature of the FEA model. The aerothermal coupling, however,

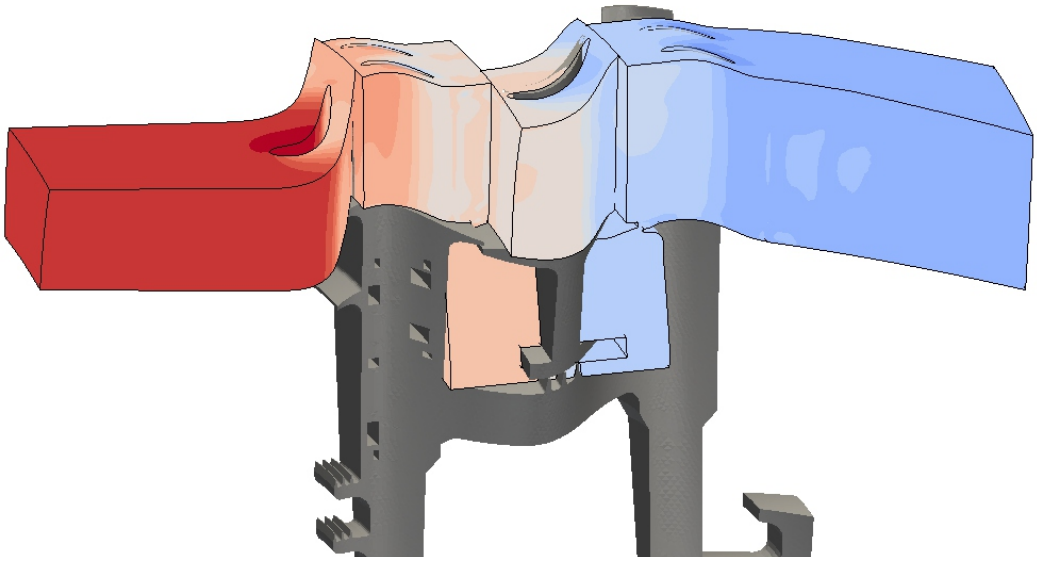

Figure 5.6: Extent of the 3D CFD sector geometry contoured by total temperature superimposed with the 3D SC03 sector model (grey)

accounts for that by interpolating from the periodic boundaries. The advantage of this meshing approach is to use the automated in-house meshing tool PADRAM. The main drawback is that the second rotor blade row cannot be coupled due to the offset.

In the next subsections, the various CFD meshes used in this research are presented in detail. At first the main annulus mesh is shown, which is followed by the two cavity meshes. As this work is a follow up study of the MAGPI project, where the mesh dependency of high-quality meshes for the main gas path and the baseline cavity were already thoroughly investigated (DIXON et al., 2013; GUIJARRO VALENCIA et al., 2012; DIXON et al., 2014), this work is not repeated here. The same mesh files are provided by the courtesy of ROLLS-ROYCE. However, special attention is put into the modeling of the deflector plate cavity geometry, demonstrating the suitability of different approaches using different meshing tools and geometry approximations.

5.2.1 Main Annulus Geometry

The mesh of the main annulus consists of one vane and two blades per stage and the individual meshes can be seen in Figs. 5.7 - 5.10, where only the surface meshes of the blades and the platforms are visualised. All four meshes are generated in an automated multi-block structured way using the in-house tool PADRAM. For all vanes and blades a clustering strategy is chosen to obtain a fine resolution near the blade and in the wake region. Furthermore, the tip gap of the first rotor blades to the casing is highly resolved using a fine clustering of 24 cell layers.

As mentioned previously, the domain of the first stator vane consists of two mass flow inlets, one for the main annulus conditions and the other one simulating the air flow egressing from the vent cavity into the main annulus. The latter is highlighted with the black arrow as a patch inlet in Fig. 5.7. The rotor domains possess apart from one inlet and outlet, an additional patch, where the TSW cavities can be merged together. This is explained in the upcoming subsections, where the cavity modeling is explained.

This meshing approach results in a mesh count of just over a million nodes per blade pair and vane, respectively, with a near wall-resolution of $y^+ < 20$, as it can be seen in Fig. 5.11. In most regions, y^+ values of around unity are obtained due to the chosen clustering approach. Only in the area of the first rotor platform and the second rotor (which is not coupled to the FEA), are larger y^+ values detectable. Although the two stages are modeled in the CFD model, only the first rotor and the second stator stage are coupled to the FEA code later on. Therefore, it is considered reasonable to save computational resources by emplying a coarser mesh for the second rotor stage including the outlet.

For accurately predicting the conjugate heat transfer, it is necessary to resolve the boundary layer accurately. In earlier studies, e.g. carried out by GUIJARRO VALENCIA et al. (2011), the CFD simulations were run in HYDRA using the SPALART-ALLMARAS turbulence model using the standard wall treatment of LAUNDER and SPALDING (1974) for

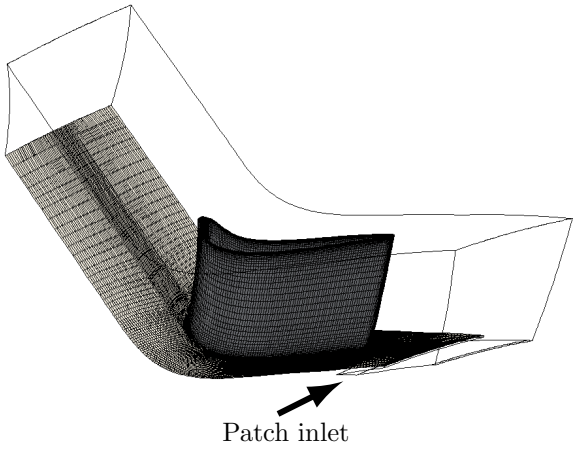

Figure 5.7: Stator 1 mesh

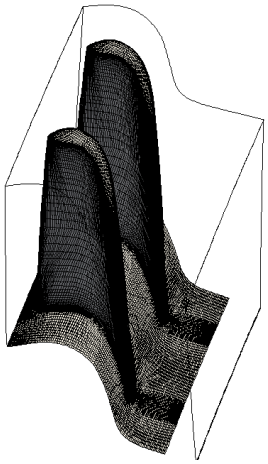

Figure 5.8: Rotor 1 mesh

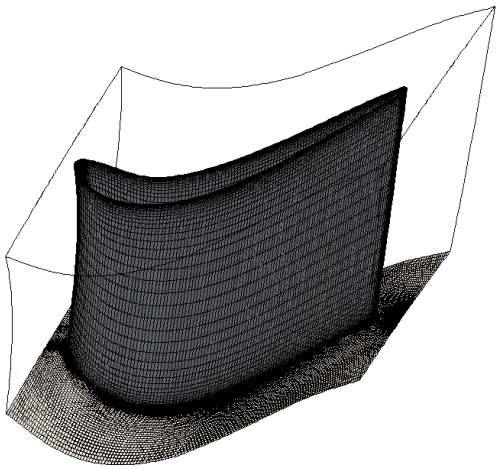

Figure 5.9: Stator 2 mesh

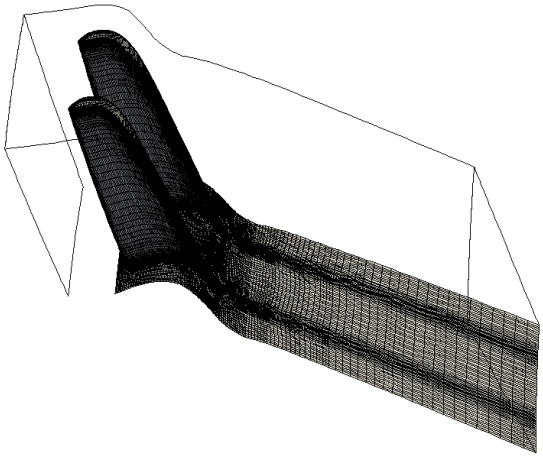

Figure 5.10: Rotor 2 mesh

near-wall distances of 20 - 40 and the low-REYNOLDS model for smaller distances. However, later results showed that the use of a two-equation turbulence model, such as the $k-\omega-SST$ model of MENTER produces more accurate results, especially when coolant flows and rim seal flow interactions are present (GUIJARRO VALENCIA et al., 2012; SMITH et al., 2012; WILCOX, 1998). While in HYDRA, the same wall treatment applies to the $k-\omega$ turbulence model, the setup in FLUENT for this turbulence model typically requires a high resolution of the boundary layer, in order to solve the near-wall flow accurately. Therefore, advantage is taken of the mesh refinement feature in FLUENT, to adjust the near-wall resolution to appropriate values. A near-wall mesh sensitivity study is presented in Sec. 6.1 in order to determine the areas which need to be refined in the coupled domain.

The mesh interfaces are highlighted as well in Fig. 5.11. After each stationary vane and each rotating blade pair an interface is placed in order to achieve a communication between the stationary and the rotating reference frames. Within the main gas path, three mesh interfaces are defined, either as mixing plane in steady-state calculations or as sliding interface, for time-resolved CFD calculations.

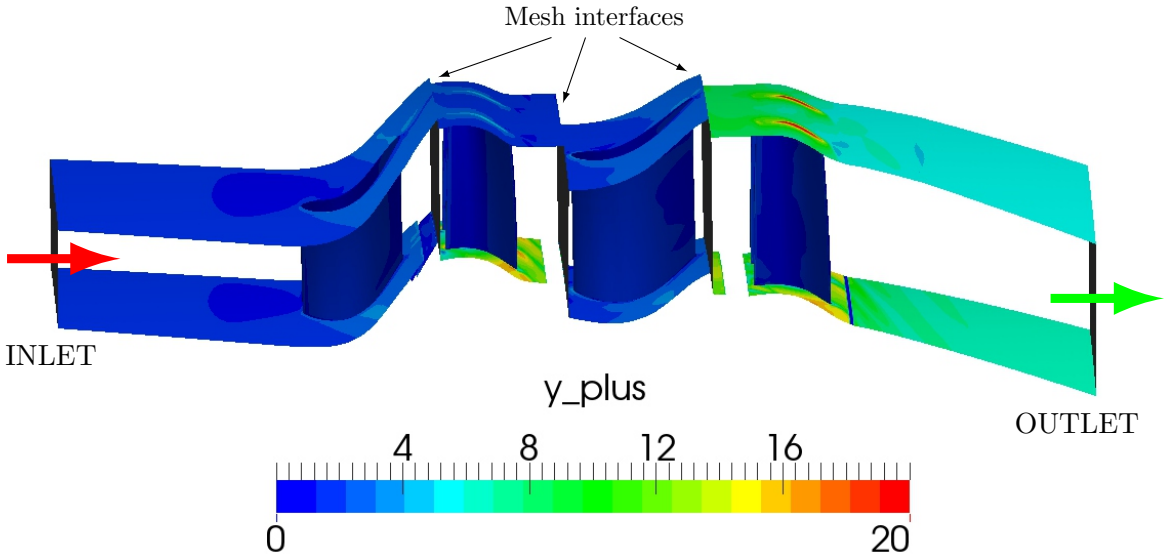

Figure 5.11: y^+ contours for the main annulus mesh generated automatically in PADRAM

5.2.2 Baseline Cavity Geometry

The baseline cavity geometry is meshed in a multi-block structured way in PADRAM and merged conformally to the main annulus mesh at the rim seals using the pre-processing tools available in HYDRA and FLUENT. The extent of the CFD model can be seen in Fig. 5.12, where the cooling mass flow rate is introduced radially through the drive arm hole. The parts highlighted in green are stationary components, whereas the red parts are rotating. A more detailed illustration of the baseline cavity mesh can be seen in Fig. 5.13, where close-up views of the up- and downstream rim as well as of the interstage seal are depicted.

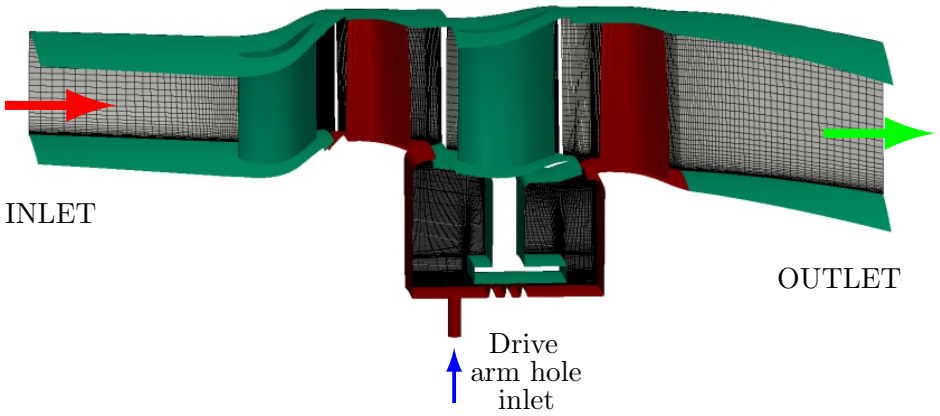

Figure 5.12: Extent of the 3D CFD sector model including the baseline cavity

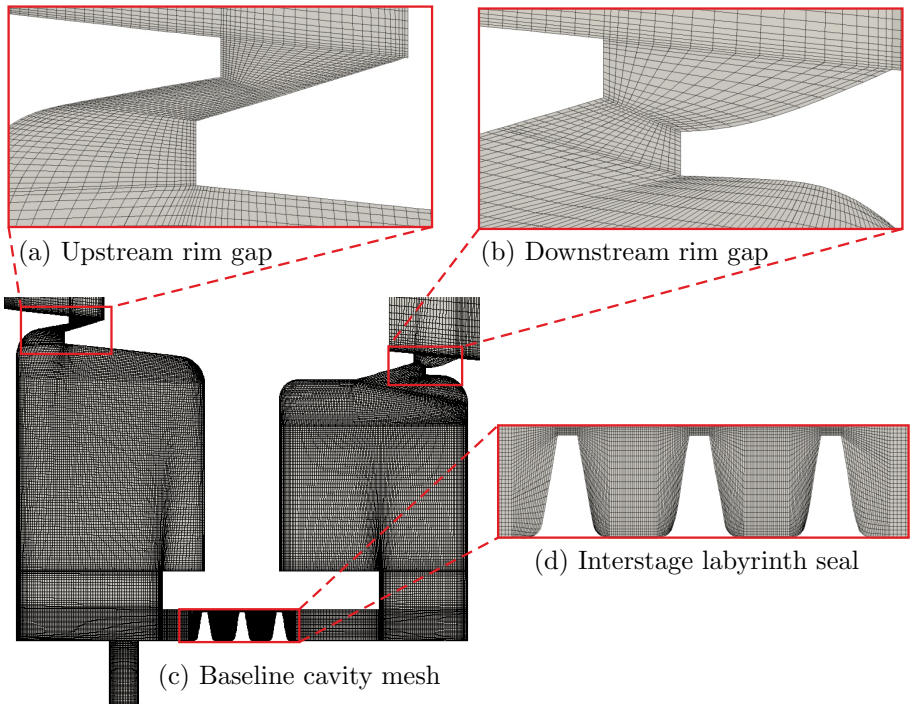

Figure 5.13: Close-up views of the CFD baseline cavity mesh and according seals

The illustrated cavity mesh contains around 4.5 million cells with a near-wall resolution of $y^+ \leq 40$, as was used in previous studies already (DIXON et al., 2013, 2014). Similar to the main annulus mesh, the near-wall distance is adapted to unity for the CFD simulations in FLUENT, while HYDRA copes with the larger resolution using the near-wall treatment of LAUNDER and SPALDING (1974). With the mesh refinement, the overall mesh size including the main annulus increases to around 10 million cells.

5.2.3 Deflector Plate Cavity Geometry

In this subsection, the details on the modeling of the deflector plate cavity are given. Three different approaches are presented: first two multi-block structured approaches using the commercial meshing tool ICEM from ANSYS are presented and second a hybrid unstructured meshing method using PADRAM is shown. Furthermore, different approximations are presented for the different meshing techniques and compared to each other. The extent of the CFD model is shown in Fig. 5.14.

5.2.3.1 Deflector Geometry with Bolt – Structured

As mentioned above, the current CFD model is 1/39 th of the full rotor-stator system, i.e. incorporating 1 vane, two rotor blades per stage and one cooling air hole. Due to the fact

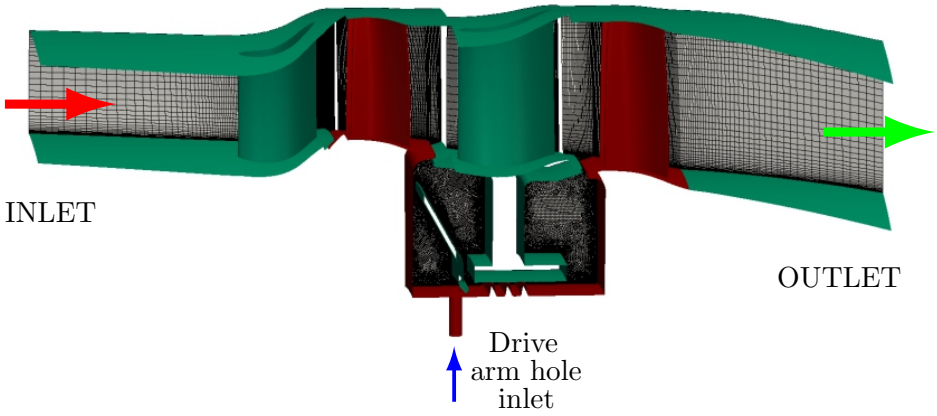

Figure 5.14: Extent of the 3D CFD sector model including the deflector plate cavity

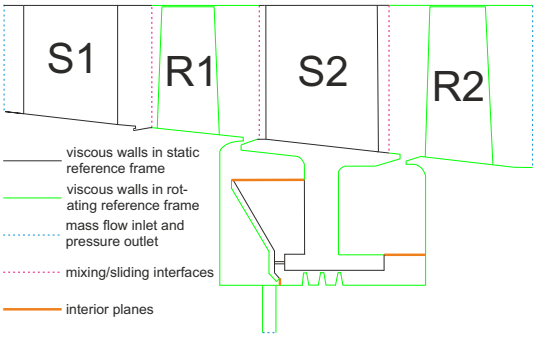

Figure 5.15: Extent of the CFD domain for the structured mesh with bolt

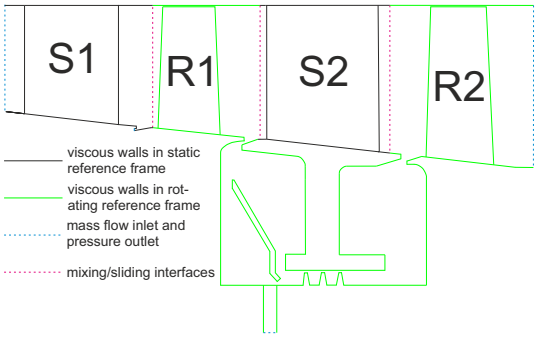

Figure 5.16: Extent of the CFD domain for the structured and unstructured mesh without bolt

that there are 18 bolts along the deflector plate but a 1/39 th sector model is analysed, the first step consists of calculating an equivalent bolt for each sector. It is assumed that the total globally generated drag by the 18 real bolts of diameter d is equal to the drag generated by the equivalent 39 bolts. The following equation is solved for the modelling approach:

$$18 \cdot A \cdot C_d = 39 \cdot A_{eq} \cdot C_{d,eq} \tag{5.1}$$

where A and C_d are the bolt cross-sectional area and the drag coefficient of the bolt, respectively. The subscript eq stands for the equivalent geometry.

Estimating a constant drag coefficient for both cylindrical bolts results in an equivalent diameter of $d_{eq} = 0.4615\, d$.

At first, the computational domain of the cavity with deflector is generated in a multi-block structured way using the commercial meshing tool ICEM from ANSYS. An O-grid is generated along the walls in order to achieve a near-wall distance of $y^+ \leq 1$ in order to resolve the boundary layer properly. Since the cavity domain possesses two 3D features,

one stationary (the connecting bolt) and one rotating (the cooling hole), the cavity domain needs to be split into separate static and rotating zones or one 3D feature needs to be neglected.

Fig. 5.15 depicts one possible solution, which is chosen for this work. To generate the structured cavity mesh the cavity is subdivided into three zones: one rotating zone comprising the cooling hole, which then is connected to the first rotor platform, one stationary zone comprising the stationary connecting bolt and another rotating zone, which is connected to the second rotor platform. These three zones communicate through "interior" surfaces, which impose continuity between two adjacent zones and which are set up in FLUENT. Unlike mixing planes or interfaces, the flow field is not averaged over the surfaces and the fluid information is passed on a node-to-node basis. The main assumption behind the use of interior surfaces for multiple reference frame applications, is that the cyclic variation of thermo-fluid variables associated with the relative movement between the zones can be locally neglected. The last step consists of merging the cavity mesh to the main annulus. The connection of the cavity and the main annulus is done by non-conformal interfaces. A mesh sensitivity study of this setup is carried out for four different mesh sizes to guarantee mesh independence of the solution. These results are presented in Sec. 6.2. The fine mesh, which contains around five million cells in the cavity domain, is shown in Fig. 5.17.

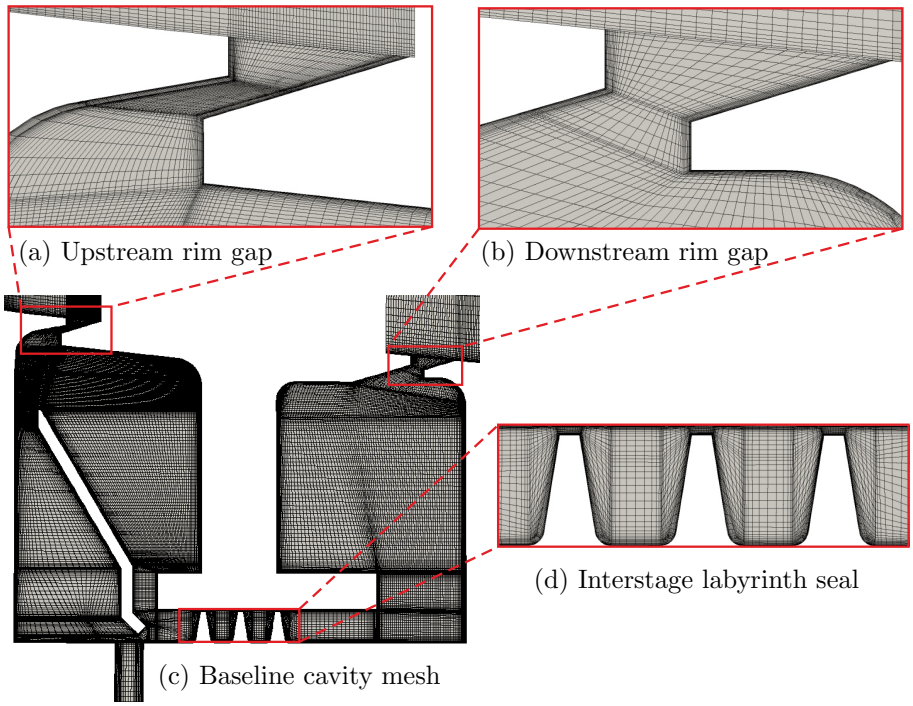

Figure 5.17: Close-up views of the structured CFD deflector plate cavity mesh and according seals produced in ICEM

5.2.3.2 Deflector Geometry without Bolt – Structured

Another possibility of meshing the deflector geometry can be done by neglecting one 3D feature. In this study, the connecting bolt is neglected in order to mesh the cavity in one single zone. This domain setup is shown in Fig. 5.16. Apart from the change in geometry, the mesh generated in ICEM is identical. This setup is used to analyse the effect of the bolt on the flow field inside the cavity. The outcome is discussed in Sec. 6.3.

5.2.3.3 Deflector Geometry without Bolt – Unstructured

Finally, a hybrid unstructured mesh of the cavity is generated using PADRAM. This allows a parametric automated creation of the mesh, which is beneficial for automated design optimisation studies. The geometry configuration for this unstructured mesh is identical to the structured setup without bolt in the section before (see Fig. 5.18). The mesher generates a 2D mesh based on a DELAUNAY triangulation with an O-grid determined by the user, allowing an accurate near-wall resolution in most parts of the cavity. Only in the region, where the bolt used to be present, as well as in the interstage seal region are higher y^+ values obtained. In FLUENT these values are corrected appropriately using the mesh refinement capability mentioned above. In HYDRA these regions are treated using the near-wall treatment of LAUNDER and SPALDING (1974). Then the mesh is swept in

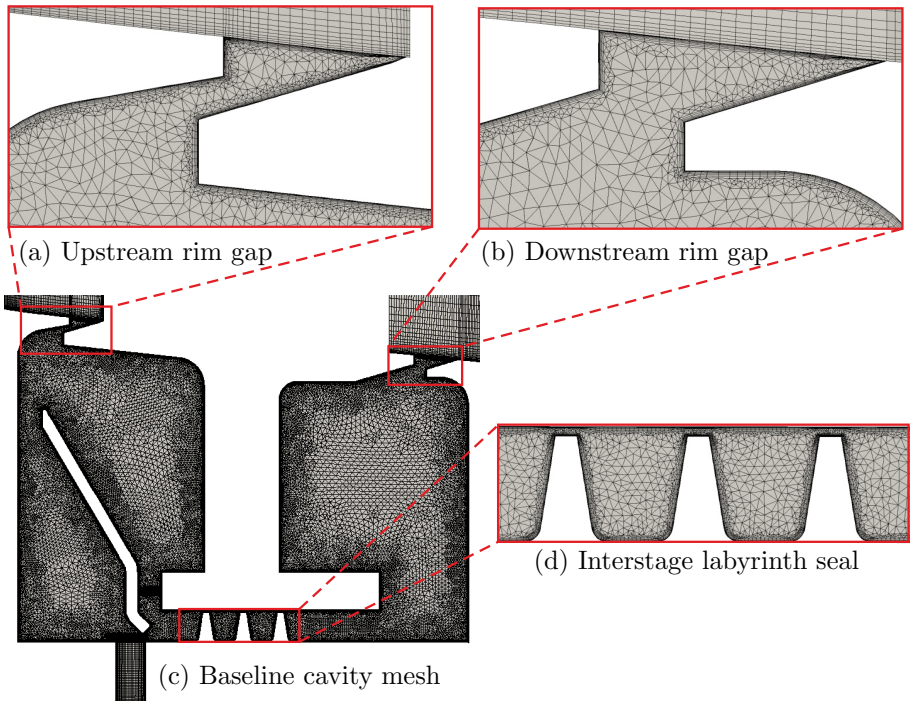

Figure 5.18: Close-up views of the unstructured CFD deflector plate cavity mesh and according seals produced in PADRAM

the tangential direction to generate the 3D sector. By applying this method, the mesh is generated within seconds. As a guideline for the mesh density, the results published by DIXON et al. (2014) are picked up and compared to the structured grid solutions. Unlike the structured ICEM meshes, this PADRAM mesh of the cavity is merged to the mesh of the main annulus in a conformal way. However, from the close-up views of the up- and downstream rim region it can be seen that the prism layer could not be removed when merging the meshes, which is certainly not ideal when computing the flow solution in this area. This drawback is kept in mind when evaluating the results later on. Overall, the mesh contains around six million cells.

5.3 CFD-Based Design Optimisation

In this section, the reader is introduced to the CFD model used during the design optimisation. The geometry simplifications as well as the parameterisation strategy are presented first while the second part focuses on the optimisation setup.

5.3.1 CFD Model and Geometry Parameterisation

Figure 5.19 shows the extent of the 3D CFD sector as it is used during the optimisation process. In comparison to the models presented in the previous sections, the current model only consists of the first rotor blade row and the upstream TSW cavity including the deflector plate. By doing that, the overall mesh count is reduced while still capturing the main flow features caused by the deflector plate.

The cooling air inlet is defined as a mass flow inlet with a fixed temperature whereas the inlet for the main annulus is defined as a pressure inlet. The latter is a total pressure distribution obtained from the solution of the complete main annulus. Similar approximations are taken for the outlets in the main annulus and the fin, where the static pressure distributions are taken from the full sector model run. The walls are defined as adiabatic, to keep the computation within a reasonable time scale.

During the optimisation process, the cavity as well as the rotor blade geometries are not changed. Only the shape and the position of the deflector plate are modified. The parameterisation of the deflector plate is done in 2D and is shown in Fig. 5.20. It is chosen to define the midsection of the deflector plate by four control points, defining three separate B-spline curves (1 - 3), which in this work are defined as straight lines. There are mainly two reasons for this: first, to make the parameterisation as general as possible by avoiding hard-coded values. Second, to generate a manufacturable solution, which also could be mounted to the stator foot, meaning that it is necessary to have a vertical curve 2.

The points of the B-splines of the midsection are then projected orthogonally in positive and negative directions with a distance of half the thickness $t/2$ of the deflector plate. It can also be seen that the angle of curves 1 and 2 do not have to be the same. The degrees of freedom of the four control points are depicted in Fig. 5.21. In total seven geometrical design parameters are defined:

- $d_{U,x}$ and $d_{U,r}$, which define the axial and radial degree of freedom of the upper point
- $d_{D,x}$, which defines the axial distance of curve 2 to the stator foot
- $d_{D,r}$, which defines the radial degree of freedom of the point connecting curve 1 to curve 2 with respect to the outer radii of the stator foot
- l_D, which defines the length of curve 2
- $d_{L,x}$ and $d_{L,r}$, which define the axial and radial degree of freedom of the lower point

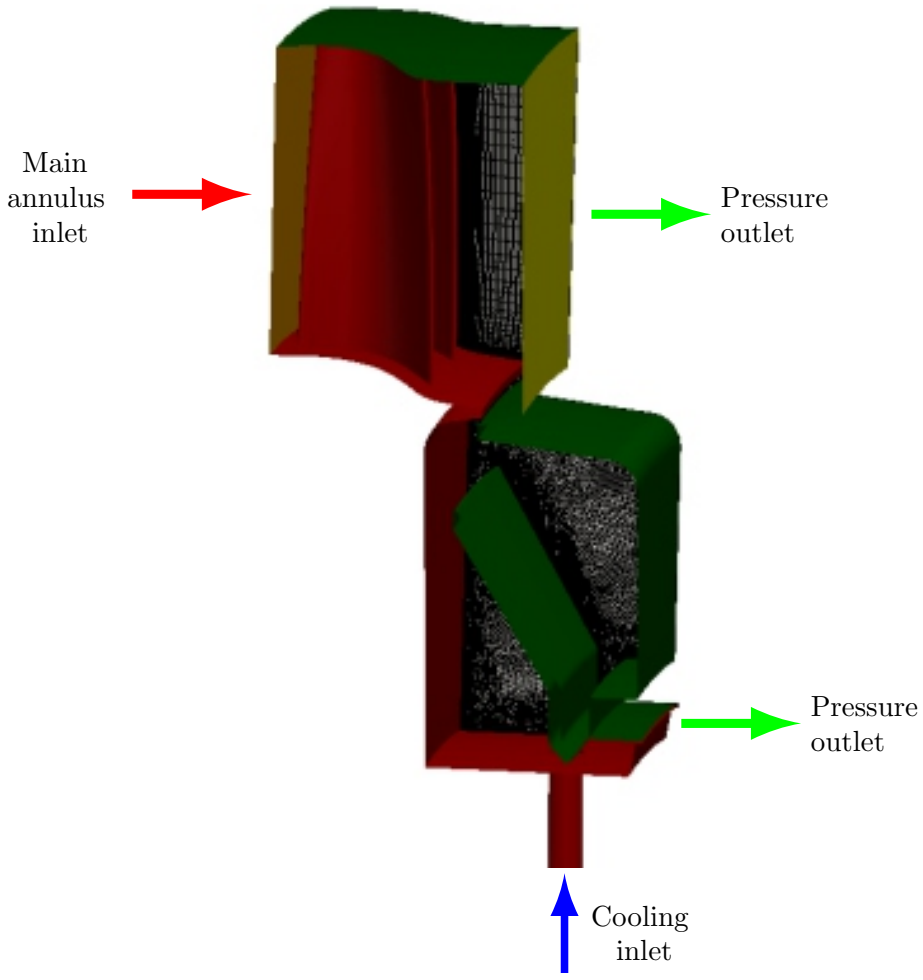

Figure 5.19: Extent of the 3D CFD sector model used during the design optimisation

Before setting up the optimisation it is checked that the generated geometry after applying the thickness to the midsection does not cut or touch lines of the remaining non-changed cavity geometry. Second, checks are made to ensure that the most extreme geometries, i.e. the one with the tightest gaps between parts, can be reliably meshed in PADRAM without corrupting the defined boundary layer resulting in mesh failures.

5.3.2 Optimisation Setup

In order to finally setup the automated optimisation loop, the objective function as well as the constraints have to be defined, both depicted in Fig. 5.21 in blue and red, respectively. The objective of this optimisation is to minimise the cooling air mass flow rate entering the cavity through the drive arm hole and defined as follows:

$$f(\mathbf{x}) = \dot{m}_{cool} \tag{5.2}$$

with $\mathbf{x}$ being the design vector consisting of eight design parameters (seven geometrical and one for the cooling air mass flow rate). Also one constraint $g_j(\mathbf{x})$ is defined (see Fig. 5.21):

$$g_j(\mathbf{x}) = \theta^{max}_{disc,ad} - \theta_{disc,ad,j} \geq 0 \tag{5.3}$$

where $\theta^{max}_{disc,ad}$ is the non-dimensional maximum allowable area mean adiabatic wall temperature at the disc and $\theta_{disc,ad,j}$ the computed value for a particular design j during

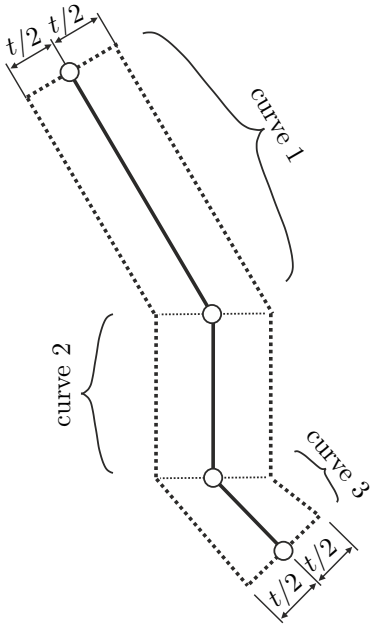

Figure 5.20: Definition of the shape parameters of the deflector plate

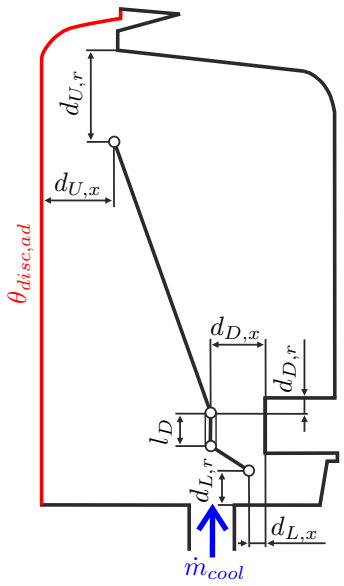

Figure 5.21: Definition of the deflector plate position inside the cavity

the optimisation. The maximum temperature value $\theta^{max}_{disc,ad}$ is taken from the results of a numerical simulation of the baseline geometry and an initial cooling mass flow rate of $55\,\mathrm{g\,s^{-1}}$, which is set to $100\%\,\dot{m}_{cool}$. An additional tolerance of $1.5\,\%$ is added to the computed value as it is assumed that this amount of coolant is *"a conservative guess for an optimum disc cooling. Basically a recognition that it would be unwise to reduce the cooling flow to the bare minimum in case of unforseen operational factors"* (DIXON, 2015).

By defining 8 design parameters ($n = 8$), the initial DOE contains 40 different designs, following the approach of BAERT et al. (2015) presented in Sec. 3.5. The actual optimisation is conducted in parallel on a Linux HPC cluster. The meshes are generated in serial mode using a single core. Same applies for setting up the boundary conditions and the post-processing of the CFD results. The FAS multigrid generation (see Sec. 3.2.2.4) is done in parallel using 12 cores, whereas each CFD simulation is run in parallel on 24 cores.

5.4 Summary

This chapter summarises the numerical modeling strategies for the FEA, CFD and optimisation analyses. The main topics were:

1. First, the different 2D and 3D FEA models for the thermal and thermo-mechanical analyses highlighting the applied boundary conditions are presented in detail.

2. The CFD modeling approaches of the main annulus and the TSW geometries are given. The variation of y^+ values is discussed and solutions on appropriately treating this non-uniformity are proposed. The results of the impact of the y^+ values on the flow solution are presented in Sec. 6.1. Special attention is put on the modeling and meshing of the deflector plate geometry. The results of the mesh independence study for this particular geometry are discussed in Secs. 6.2 and 6.3.

3. The last section covered the parameterisation of the deflector plate geometry and the modeling strategy within the automated optimisation framework. The objective function was defined as the cooling mass flow rate, which is aimed to be minimised, and one constraint (the averaged disc temperature) is set up, which must not be exceeded for a valid design. The outcome of this analysis is summarised in Chap. 8.

6 Preliminary Studies

Before validating the CHT methodology some preliminary tests are carried out, in order to establish the accuracy of the numerical models and methods. This chapter focuses on the 3D CFD sector models presented in the previous chapter. Mesh sensitivity studies are conducted for the near-wall mesh resolution as well as for the deflector plate cavity. The effect of the connecting bolt on the flow field is analysed as well as the effect of using different turbulence models to solve the RANS equations. The last section compares the results of one simulation setup for the two flow solvers FLUENT and HYDRA. This is done as a preliminary study to ensure that the code exchange from FLUENT (used for the aerothermal coupling) to HYDRA (used during the optimisation) for the optimisation is valid.

6.1 Near-Wall Mesh Resolution

Near-wall mesh resolution in CFD is an important factor to solve a CHT problem accurately. In the previous chapter, we have seen that the near-wall distance of the cells in the generated meshes reaches values larger than 1 in certain areas. As a consequence, this requires either the use of wall functions or an additional mesh refinement in the near-wall

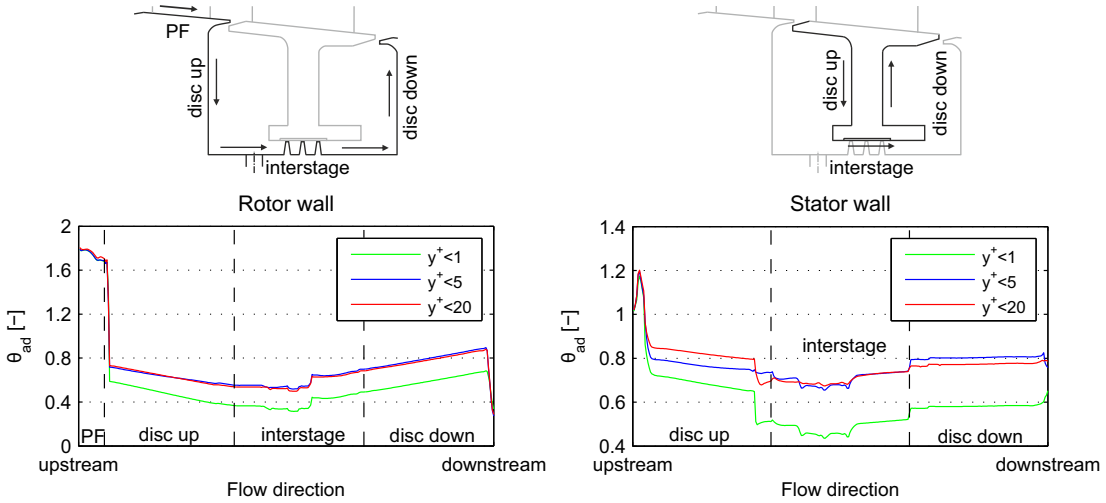

Figure 6.1: Non-dimensional adiabatic wall temperatures at the rotor (left) and stator (right) wall for the three different near-wall resolved meshes: $y^+ < 1$, $y^+ < 5$ and $y^+ < 20$

resolution in these particular regions. The literature showed that the $k-\omega-SST$ turbulence model performs better than other turbulence models in TSW flows adjacent to the main gas path and this is chosen as the preferred method to solve the turbulence closure (a turbulence model sensitivity study is conducted in Sec. 6.4). A general recommendation using this turbulence model without wall functions - as it is the case in FLUENT - is to resolve the boundary layer with y^+ values around unity (POPE, 2000; FLUENT, 2009). However, previous studies also showed that similar results could be achieved using larger y^+ values.

Therefore, three different near-wall refined meshes are compared to each other in this section. The respective near-wall resolutions are $y^+ < 1$, $y^+ < 5$ and $y^+ < 20$. Figure 6.1 shows a comparison of non-dimensional adiabatic wall temperatures θ_{ad} for the three different meshes along the TSW walls of the domain. The rotating walls contain the rotor platform (PF), the up- and downstream rotor discs as well as the interstage seal disc as it can be seen in the sketch above the graphs. The stationary walls are shown accordingly on the right hand side. The flow direction is illustrated by the arrows and the graphs show the temperatures from the upstream to the downstream direction.

Assuming that the plots for $y^+ < 1$ predict the *correct* adiabatic wall temperatures, we now compare the performance of the coarser meshes to see whether mesh refinement is needed in particular regions and thus save computational effort and time. Inspecting the curves for $y^+ < 5$ and $y^+ < 20$, it can be seen that the temperatures only agree with the temperatures predicted for the very fine mesh with $y^+ < 1$ in the area of the platform. The remaining temperatures are consequently overpredicted compared to the very fine mesh. Therefore, for the remaining calculations in FLUENT, the mesh along the platform is not refined but the remaining cavity parts are adapted to $y^+ < 1$. For HYDRA this adoption is not necessary since adaptive wall functions are applicable.

6.2 Mesh Independence Study for the Deflector Plate Cavity

Six different cavity meshes are generated, four in ICEM using a multi-block structured approach including the modeling of the scaled bolt (see Subsec. 5.2.3.1), one in ICEM also using a multi-block structured approach neglecting the bolt modeling (see Subsec. 5.2.3.2) and one in PADRAM using a hybrid unstructured approach without modeling the bolt based on a 2D Delaunay triangulation (see Subsec. 5.2.3.3). Details on the case names and the cavity mesh approach as well as on the model size are summarised in Tab. 6.1. Furthermore, the moment coefficients C_m induced by the viscous heating of the rotating cavity parts are shown. In addition to the absolute values, the relative percentage values for the meshes compared to the very fine mesh are shown in the last column. This indicates which of the solutions can be considered mesh independent.

The last column shows that the C_m of the coarse mesh deviates from the value of the very fine mesh by almost 6%. The more the mesh is refined the smaller is the deviation.

Case #	Meshing tool	Mesh type	Nodes $\times 10^6$	$C_m \times 10^{-3}$	C_m [%]
coarse	ICEM	struct.	1.8	13.16	94.36
normal	ICEM	struct.	3.5	13.65	97.84
fine	ICEM	struct.	5.1	14.02	100.53
very fine	ICEM	struct.	6.2	13.95	100.00
no bolt fine	ICEM	struct.	3.8	13.00	93.16
PADRAM	PADRAM	unstruct.	5.6	13.85	99.29

Table 6.1: Summary of the different meshes including their type and size plus their according predicted viscous moment coefficients

For the fine mesh, it can be considered that the solution is mesh independent as the C_m is only 0.5% larger. The same applies to the PADRAM unstructured mesh, where the C_m is also off by less than 1%. Interestingly, the case *no bolt fine*, which is based on the fine mesh largely underpredicts the C_m compared to the fine and very fine mesh. This can be due to two factors: first, the use of an interior plane in close proximity to the cooling air inlet influences the flow field more than expected and second, the effect of the bolt on the flow field is also larger than expected. However, the use of the unstructured mesh which also neglects the bolt does not support the latter theory.

Therefore, further investigations are necessary. In Figs. 6.2-6.5 plots of circumferentially averaged non-dimensional total temperature and swirl ratio in four cavity cutting planes are shown for the six different meshes. The plots are taken from two axial and two radial cutting planes in the up- and downstream cavities. In brief, the evaluation of these plots gives us following information:

Fig. 6.2 This figure shows the temperature and swirl plots extracted from an axial cutting plane in the upstream cavity in close proximity to the rotor disc. From these contours, some differences between the mesh solutions can be observed. The temperature plots as well as the swirl plots show large differences at lower radii for the different meshes. These are most likely to be due to the complex flow field structure in the area where the cooling jet enters the cavity and impinges the deflector plate. For the cases where the bolt is modeled, it can be seen that the temperatures at lower radii reduce with finer meshes and almost become constant. For the swirl ratio an almost linear trend can be seen by refining the mesh. Similar to the moment comparison, which only differs by approximately 0.5%, it can be stated that the solutions of the fine and the very fine mesh are very close. However, unlike other results, the solution using the PADRAM mesh is not in as good agreement with the fine and very fine mesh solutions. Especially at lower radii, the PADRAM solution gives higher temperature and lower swirl values and does not show the linear trends mentioned before. This might be related to highly complex recirculation region, where small differences in the mesh can result in a different vortex structure. The structured mesh without a bolt ("no bolt fine") shows a similar trend in temperature predictions at lower radii, to the PADRAM mesh and does not flatten out.

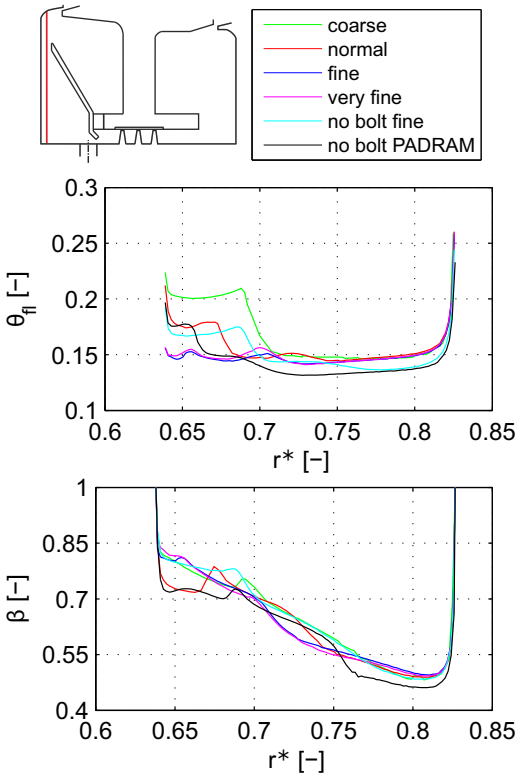

Figure 6.2: Plots of adiabatic fluid temperature (top) and swirl (bottom) in an axial cutting plane in the upstream cavity

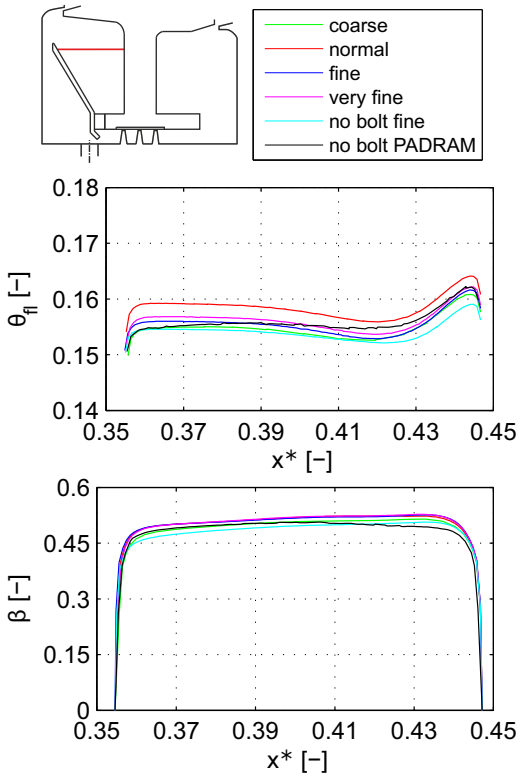

Figure 6.3: Plots of adiabatic fluid temperature (top) and swirl (bottom) in a radial cutting plane in the upstream cavity

This can be an indicator for the assumption that the internal plane close to the cooling air inlet impacts the flow solution and is not suitable.

Fig. 6.3 The comparison of the plots in the upstream radial cutting plane show only minor differences in the temperature predictions depending on the mesh density and even smaller differences in the swirl ratio predictions. Again the solutions using the fine and very fine mesh show very similar results and also the PADRAM mesh solution is in good agreement, although the PADRAM solution shows a rather constant temperature profile compared to the other mesh solutions, which are slightly wavy. The same constant flow behaviour can be seen from the swirl ratio for the PADRAM mesh solution, whereas the swirl ratio results for the structured meshes show a slightly progressive swirl ratio in the core from left to right, which is most likely to be related to the mesh density in this particular area. These differences are most likely related to the different meshing approaches. Possibly the transition from the structured boundary layer to the unstructured cells in the cavity core is not fine enough in the PADRAM mesh to resolve the flow features exactly. However, the differences are only very minor and can be considered negligible.

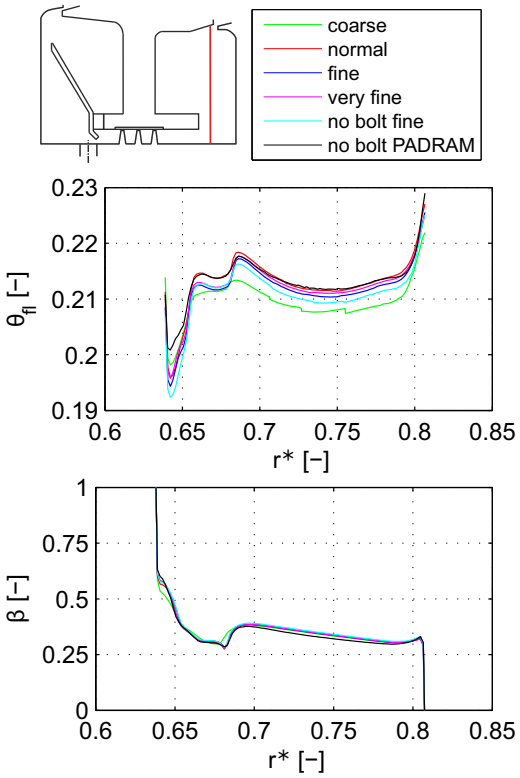

Figure 6.4: Plots of adiabatic fluid temperature (top) and swirl (bottom) in an axial cutting plane in the downstream cavity

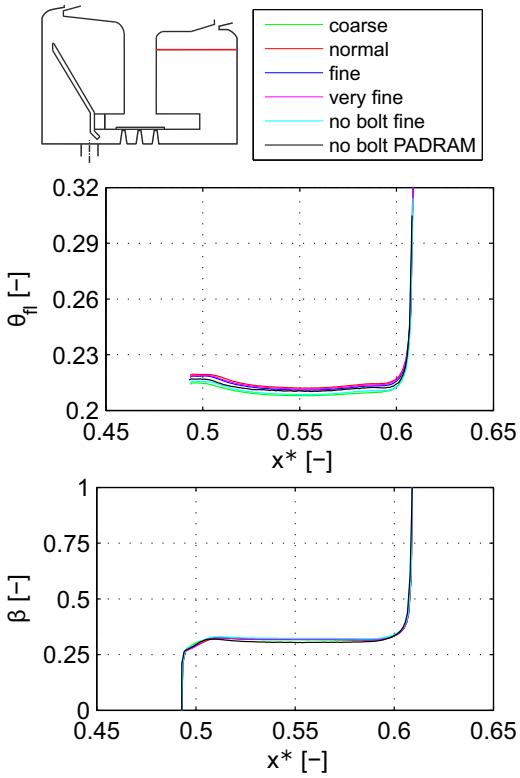

Figure 6.5: Plots of adiabatic fluid temperature (top) and swirl (bottom) in a radial cutting plane in the downstream cavity

Fig. 6.4 Considering the different results in the axial cutting plane in the downstream cavity, significant differences are only observed at lower radii. This is a recirculation region and the differences in these solutions can purely be associated to the mesh variations in that area. As in the previous plot discussions, barely any differences between the fine and the very fine mesh are present. However, the coarse mesh solution underpredicts the temperatures at higher radii. The comparison of the swirl ratio does not show significant differences between the meshes. Only the results of the coarse mesh show some slight deviations in the recirculation zone at lower radii. Interestingly, the PADRAM mesh results predict a higher fluid temperature at lower radii, whereas at higher radii the temperatures are marginally underpredicted compared to the results of the fine and very fine mesh. This again is related to the recirculation zone prediction, which for the PADRAM mesh is associated with more air recirculating. The structured mesh without bolt modeling predicts comparable results to the fine and very fine mesh results. Therefore, the differences between the meshes with modeled bolt and without can hardly be associated to the interior plane included in close proximity to the lower radii.

Fig. 6.5 Similar to the results from the radial cutting plane in the upstream cavity, the differences in the temperature and swirl ratio predictions using different meshes are small.

From these observations, we can conclude that the fine mesh case can be considered as a converged mesh when the bolt is modeled as there are almost no differences to the very fine case. However, the comparison of solutions using these meshes with those using a similar mesh without a modeled bolt, there are still uncertainties in the solution associated with the use of the non-conformal mesh interface at the rim as well as the use of interior planes. The PADRAM mesh, which was stated in previous studies to provide mesh independent solutions, shows some differences in the results compared to the structured meshes as well. This case is therefore used as a reference test case, especially because the mesh at the rim can be merged in a conformal way, reducing one source of uncertainty already. Another reason for further investigations on the PADRAM mesh, is the fact that within PADRAM the mesh can be automatically generated within seconds and used in an automated optimisation framework. It is also possible to use this type of mesh with the ROLLS-ROYCE in-house CFD solver HYDRA. However, the uncertainties of the results in the recirculation areas coming from this mesh need to be considered while evaluating the results and validating the numerical conjugate heat transfer methodology.

6.3 Effect of Bolt in Deflector Plate Cavity

In addition to sources of error from neglecting the bolt, further errors may result from the implementation of interior planes inside the cavity and the use of non-conformal interfaces in the rim region. These are further investigated in this section. Therefore, the flow field in proximity to the cooling air inlet and the bolt are qualitatively analysed.

The contours of non-dimensional adiabatic fluid temperature and swirl ratio are shown in Figs. 6.6 and 6.7, respectively. These figures show the respective contours in two angular and axial cutting planes perpendicular to each other taken in the upstream cavity close to the cooling air inlet and the bolt.

From the temperature results, it can be seen that, in both setups, the cooling air jet enters the cavity at the same temperature and then impinges onto the lower deflector part, which results in a increase in temperature at the stagnation region. Then the jet splits into two parts, one going towards the area enclosed by the rotor disc and the deflector and the other going towards the interstage labyrinth seal. One major difference from comparing these two figures is the size of this stagnation region, the dark red contour at lower radii of the deflector plate, and thus the split ratio of the coolant jet. The stagnation area is larger for the case with a modeled bolt and as a result, the cool spot (in blue) right from the lower deflector plate tip is smaller than the one in the case without the bolt, meaning that only a small amount of coolant goes towards the seal. These findings are also reflected in the swirl ratio contours, where a smaller area of non-swirled fluid (in blue) can be seen

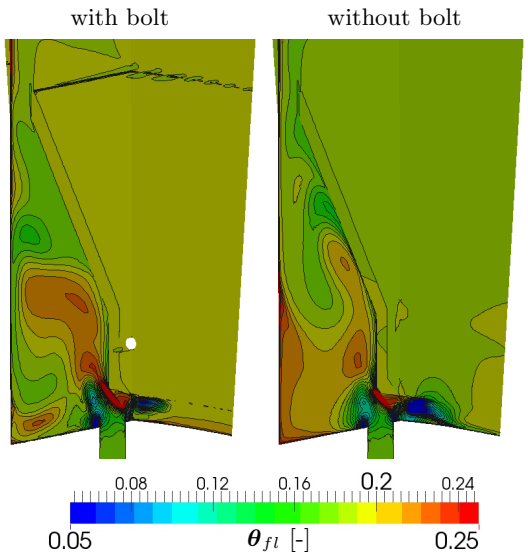

Figure 6.6: Contours of fluid temperature in two perpendicular cutting planes in the upstream cavity in proximity to the bolt, once with (left) and once without modeled bolt (right)

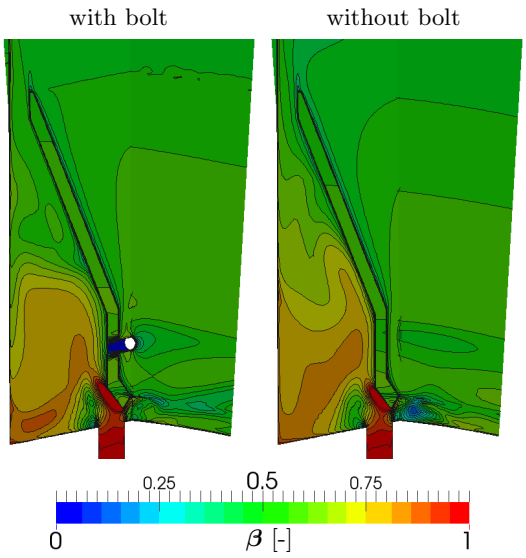

Figure 6.7: Contours of swirl ratio in two perpendicular cutting planes in the upstream cavity in proximity to the bolt, once with (left) and once without modeled bolt (right)

in the contours of the case with a modeled bolt compared to the reference case without a bolt.

Furthermore, from the temperature contours, some small dots representing different temperature values are visible in the axial cutting plane of the bolt modeled case at lower radii. These structures are in the area of an interior plane and strongly suggest that the flow information, i.e. the fluid temperatures and the swirl ratio, is not passed correctly between the reference frames, leading to noisy results. This is even more significant at the upper deflector tip, where a straight line can be seen in the angular cutting plane and the same kind of dotted contours on the axial cutting plane. This is also reflected in the swirl contours of the modeled bolt case, which show a wavy contour line in the axial cutting plane. This is not seen in the case where the bolt is not modeled. Similar to the structures at the lower deflector tip, this noisy behaviour at the upper tip is exactly in the region of an interior plane. Although the mesh is already very fine, it might be possible that this non-physical noisy behaviour could be removed with a further local grid refinement in the region of the interior plane. However, this would result in more computational power and time. This does not seem reasonable in the current research due to different available modeling techniques and due to the presence of the noise at only local regions without progressing further.

Some minor differences are visible in the swirl ratio contours in the area enclosed by the deflector plate and the stator foot, especially in proximity to the bolt, where the air is disturbed due to the presence of the bolt.

From the evaluation of these contours, new conclusions on the suitability and independence of the mesh can be drawn. As already suspected, the use of interior planes is a problem, leading to some noisy and non-physical results in their proximity. Furthermore,

the ratio of coolant going towards the interstage seal is smaller for the case with a modeled bolt resulting in slightly different flow structure. With respect to the subsequent work, where a CFD model must be coupled to an FEA model in order to extract metal temperatures, it is decided to use the PADRAM mesh without a bolt and a conformal interface at the rim for the later studies. As before, the limitations and differences found in this and the previous section are still kept in mind while analysing and understanding the results.

6.4 Turbulence Modeling

Now, that we analysed the uncertainties coming from the mesh, it is necessary to get an understanding on the impact of using different approximation methods in solving the RANS equations. Therefore, the results of four different turbulence models are compared to each other using the PADRAM mesh of the deflector plate geometry.

The four different turbulence models are the $k-\omega-SST$, $k-\epsilon$ realizable, RNG and SPALART-ALLMARAS ones as they are presented in Chap. 3. The ϵ-based turbulence models use the mesh with a non-refined near-wall resolution, since wall functions are applicable for these models in FLUENT. For the two other models, the near-wall resolution is refined as explained in Sec. 6.1.

At first, the predicted relative adiabatic rotor and stator wall temperatures are compared to each other, which are shown in Fig. 6.8. For a better understanding of the temperature variations along the walls, the relationship between absolute and relative temperatures as a function of the swirl ratio is given here:

$$T_{rel} = T_{abs} - \frac{r^2\omega^2}{2c_p}(2\beta - 1) \tag{6.1}$$

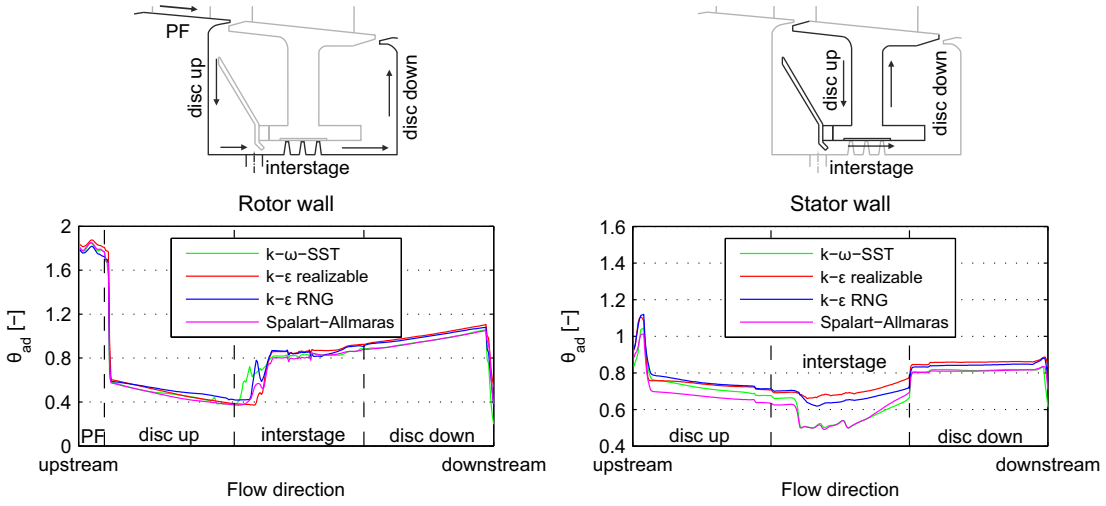

Figure 6.8: Non-dimensional adiabatic wall temperature predictions at the rotor (left) and stator (right) wall using four different turbulence models

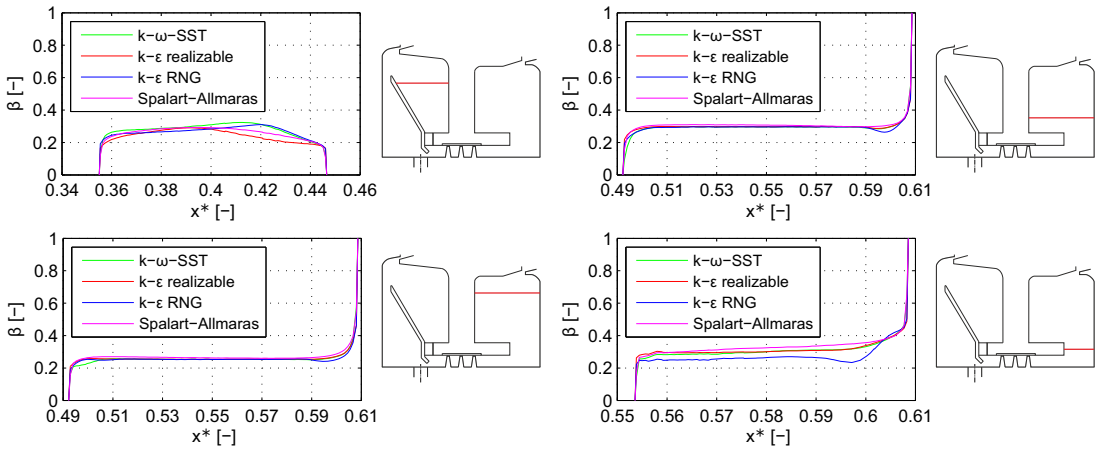

Figure 6.9: Swirl ratio predictions in four radial cutting planes in the upstream and downstream TSW cavity for four different turbulence models

First, we are having a look at the rotor wall temperature predictions going in stream wise direction (indicated by the arrows in the graphs). At the rotor platform (PF) a small peak in temperature can be seen which is related to the blade passage, where the fluid area is reduced. Only marginal differences are detectable between the different solutions, which are slightly more conspicuous close to the rim, where the rotor stator interaction starts to gain importance. The $k-\epsilon$ realizable model predicts slightly higher temperatures than the other models, which indicates a smaller swirl ratio estimation. The $k-\epsilon$ RNG model, however, predicts slighlty lower temperatures than the $k-\omega-SST$ and the SA model. This is an indicator for a higher swirl ration estimation instead.

It is hard to find an explanation for these differences, especially because they are only minor. But one reasonable explanation might be due to different predictions of the mixing behaviour between the main annulus and the cooling air near the rim of the respective models. Another possibility for the temperature differences in the rim might already arise at the coolant inlet where the jet splits into different portions when impinging onto the lower deflector tip for the different turbulent models. As a consequence different amounts of cooling mass flow rate are entrained radially upwards to the rim resulting in a different rim temperature.

These two last statements are reinforced by examining the upper disc temperatures. Just at the upper radii in the rim region, a temperature peak can be seen for the $k-\epsilon$ realizable model, whereas the other models predict an instant temperature drop. This suggests that the different turbulence models either capture the turbulent mixing in a different way or predict model particular entrainment flows. As a result the $k-\epsilon$ realizable model predicts more hot gas ingestion into the cavity and a different heat transfer due to a different swirl prediction.

Going further downstream along the rotor disc, the slight differences in temperature predictions persist. However, in this region both ϵ-based models predict the higher temperatures than the other two. This can be associated with the use of the different near-wall treatment approaches of the models, meaning that the accuracy of using wall functions in

the ϵ-based models can be questioned. Another possibility is the modeling of the coolant jet entering the cavity and impinging the deflector plate. As we have seen in the previous section, different meshes result in a different jet impingement behaviour and the choice of different turbulence models may lead to different dissipation losses or increased production terms. Furthermore, the flow structure predictions of the recirculating vortices is most likely to be affected by the choice of turbulent models and can lead to significant differences.

This last statement is supported by the temperature predictions at the interstage, where the largest discrepancies between the different models can be found. Due to the very turbulent flow entering the cavity and the mixing phenomenon when going towards the interstage seal the differences are most likely related to model uncertainties. These larger discrepancies reduce to smaller values in the fin region again and propagate constantly towards the downstream rim gap, showing that the ϵ-based models predict slightly higher temperatures than the ω-based and the SA model.

The relative adiabatic stator wall temperature predictions for the different turbulence models, demonstrate a similar trend. From these plots it can be seen that the ϵ-based models overpredict the stator temperatures compared to the two other models. Similar to the rotor temperatures, the differences in the stator temperatures are most likely related the differences in predicting the turbulent mixing in the rim and also solving complex vortex flow structures. The use of wall functions poses another uncertainty for the ϵ-based models. However, it is not certain that the solutions from the $k-\omega-SST$ and the SPALART-ALLMARAS models, which show a very similar trend again, provide the correct solutions.

From the plots of swirl fraction in four different radial cutting planes inside the two TSW cavities shown in Fig. 6.9 further differences in the solution can be observed. The swirl ratio plot from the upstream cavity (top left) shows that the $k-\omega-SST$ model predicts the slightly higher swirl than the other models. The $k-\epsilon-$ RNG predicts a similar trend whereas the two remaining turbulence models infer a different vortex structure in that area. This is a very interesting observation since all the other plots show pretty good agreement between all the turbulence models except for the $k-\epsilon-$ RNG. This again shows the difficulties in choosing the right turbulence model to solve the complex cavity flow adjacent to the main annulus, generating strong turbulent mixing regions in the rim.

From the paragraphs above, we now need to select the most appropriate turbulence model. Account is also taken of some of the previous analyses published in literature (see Sec. 2.3.3), where it has been shown that the $k-\omega-SST$ turbulence model is most likely to provide the most accurate results in such flow domains (SMITH et al., 2012; LÜCK et al., 2014a), although the SPALART-ALLMARAS model did also provide acceptable results for one particular flow case (DIXON et al., 2014). Another reason to pick the $k-\omega-SST$ model is the fact that we analyse flow cases with a high likelihood of ingestion. In case of ingestion, the literature recommends the use of the $k-\omega-SST$ model (WILCOX, 1998). Furthermore, now that we have an impinging jet at the lower tip of the deflector plate,

the literature has also shown that the $k-\omega-SST$ model is superior in predicting these impinging flow structures compared to other turbulence models (ZUCKERMANN and LIORD, 2005).

Another source of uncertainty in the current comparison of turbulence models, is the use of wall functions for the ϵ-based turbulence models, which cannot be influenced or manipulated in the current setup. However, in the next chapter, where the aerothermal coupling method is validated, the uncertainties and limitations of the turbulence model approximations are considered during the evaluation process.

6.5 Verification of CFD Code Exchange

Due to the fact that during the automated CFD based design optimisation of the deflector plate, the ROLLS-ROYCE in-house density-based flow solver HYDRA is used and during the validation process of the CHT method, the pressure-based coupled solver in FLUENT is used, it needs to be verified that both codes provide comparable results. As only the upstream cavity is optimised, this last section of the preliminary studies, compares qualitatively the solutions of the two flow solvers in that region. The prediction of fluid temperature as well as swirl ratio are shown in Figs. 6.10 and 6.11, respectively. The upper figures represent the solution obtained from FLUENT and the lower ones the flow solution from HYDRA.

Let us first consider the disc temperature predictions shown on the very left. From these contours, it can be seen that generally a similar trend is predicted, although the results in HYDRA look more continuous in angular direction, indicating a more homogeneous distribution of the cooling air inside the cavity compared to the FLUENT solution. Also at lower radii, HYDRA predicts lower temperatures which gradually increase in the radial direction, whereas the FLUENT solution does not show this evenly distributed temperature field. These differences can be associated to the different wall treatments of the respective codes. Whereas HYDRA uses wall functions, FLUENT uses a refined mesh in the near-wall region.

Similar information can be taken from the angular cutting planes shown on the left of Fig. 6.10 and in Fig. 6.11. The temperature as well as the swirl ratio contours indicate a more structured distribution of the cooling air in HYDRA along the rotor disc. In the rim region it can be seen that FLUENT predicts a slightly bigger area of high temperature - designated in red - at the rotor wall compared to the HYDRA predictions. However, averaging the temperature over the complete surface, as it is done in the optimisation process to imply the constraint, shows that the difference between the two flow solutions is within 1 K, which equates to less than 2 % of the temperature difference between the cooling air supply and the main annulus gas path temperature.

More obvious differences in the flow solution can be seen along the stator wall, where HYDRA predicts higher temperatures. This might be related to differences in predicting

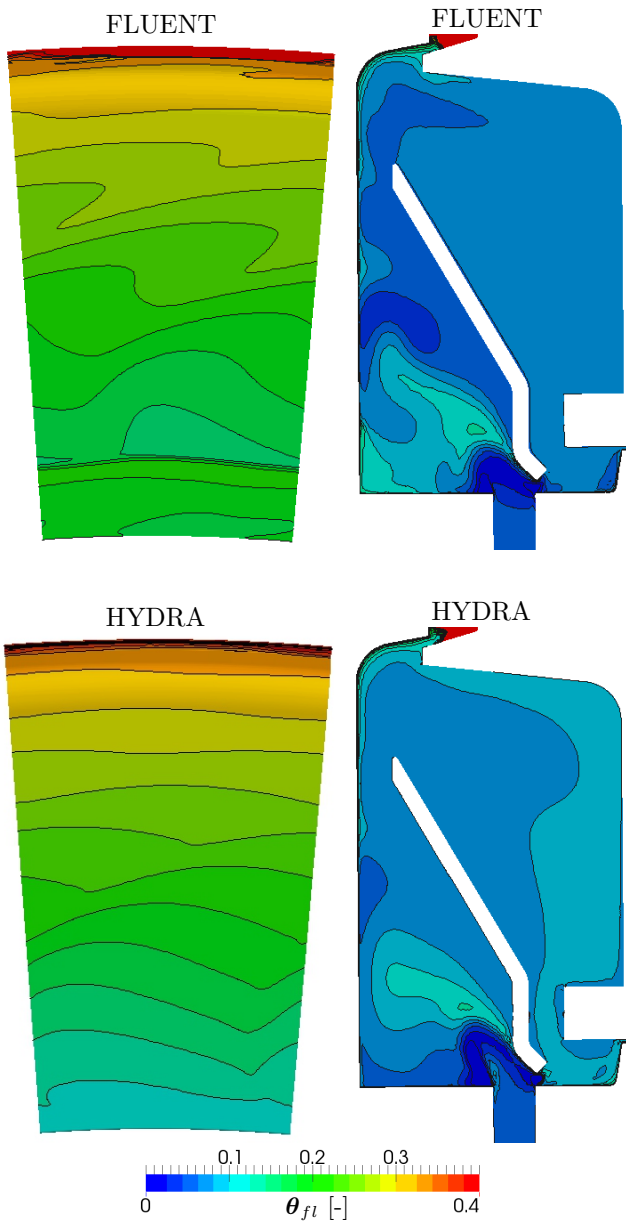

Figure 6.10: Comparison of the non-dimensional fluid temperature predictions at the upstream rotor disc (left) and inside the upstream cavity (right) obtained from the two CFD solvers FLUENT (upper) and HYDRA (lower)

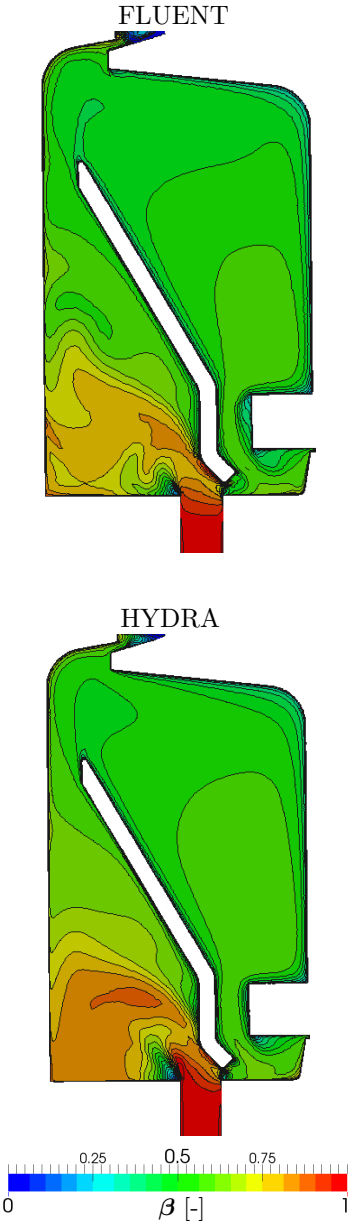

Figure 6.11: Comparison of the swirl ratio predictions inside the upstream cavity obtained from the two CFD solvers FLUENT (upper) and HYDRA (lower)

the rim seal flow where the turbulent mixing and pressure fluctuations dominate the flow structure and are difficult to capture using steady-state CFD. Nevertheless, the stator disc is not considered in this optimisation frame work and therefore the differences are not important in that area. However, for the final evaluation of the design, these differences pose another source of uncertainty, which need to be considered in the conclusion of the results.

Although, this preliminary test shows good agreement between the solutions of the two codes, the comparison is done using one particular flow case at one particular deflector plate

design. Therefore, the validation of the final optimised design with the appropriate flow case incorporates a similar comparison as presented here to further rule out uncertainties related to the code choice.

6.6 Summary

The purpose of this chapter was to give an overview of a range of possible sources of uncertainty due to the choice of distinct numerical modeling approaches. The chapter summarised the outcome of some preliminary studies, which were considered important, before embarking into validation of the aerothermal coupling method. In brief, the following topics were discussed:

1. The importance of the near-wall mesh resolution on the adiabatic wall temperatures was discussed and it was concluded that in most regions the use of y^+-values of around unity is inevitable when wall functions are not applicable. Therefore, the mesh refinement feature in FLUENT is applied to the mesh before starting the CFD simulation.

2. Different meshes of the deflector plate geometry were generated in ICEM (structured) and PADRAM (hybrid unstructured) and the respective CFD results were compared to each other. It was found that the flow solution is independent for the structured 'fine' mesh and that the unstructured PADRAM mesh provides slightly different solutions which is most likely due to numerical errors arising from the transition of the prism layer to the unstructured cells. Furthermore, the impact of non-conformal interfaces in the rim region, where the meshes of the main annulus and the cavity are merged, was analysed. The flow solution did neither show any non-physical behaviour nor did it vary from the conformal solution, and therefore can be considered as a reasonable modeling approach.

3. The effect of the bolt inside the cavity was discussed. It was concluded that the flow field is only affected locally and therefore it is not necessary to make the additional effort of including the bolt into the model. Special attention was put on the setup of interior planes inside the cavity when modeling the bolt. This has shown to cause problems in the flow solution giving oscillating temperature lines in the proximity of the planes. Therefore, the mesh of preference should be modeled without bolt in order to avoid the use of the interior planes. With respect to the optimisation task and the conclusions of the mesh studies, PADRAM is used as meshing tool for the upcoming analyses.

4. Turbulence models pose a source of uncertainty when analysing turbulent and mixing flows. The performance of four turbulence models was compared to each other and to the literature. It was concluded that the $k-\omega-SST$ model is most likely to

provide the most accurate flow solutions for TSW flows adjacent to the main gas path. Therefore, this model is used during the method validation and the optimisation but still considering its limitations during the evaluation of the results.

5. As a final step, the suitability of exchanging the CFD codes FLUENT and HYDRA was evaluated. Both codes provide similar results with respect to disc temperature predictions and swirl ratio inside the cavities. Therefore, HYDRA is used during the design optimisation and FLUENT is used for the validation of the final optimised design.

7 Numerical Method Validation

This chapter of the thesis deals with some of the open questions proposed as further work in two previous studies (Dixon et al., 2013, 2014) and extends the scope, deepening in the study of alternative optimised geometries (Pohl et al., 2015). The aim of this thesis is to further advance the understanding of the cooling flow, annulus gas interaction and resultant heat transfer, in the cavities adjacent to the main annulus in multi-stage turbines. In particular, attention is turned to the impact of the seal clearances in the cavity flow structures as well as to the heat transfer within the rotor walls and the rim gaps, paying attention to the main annulus platforms and rim seal.

Therefore, the FEA and CFD models as presented in the previous chapter are used to further improve the analysis tool-set and best practices for TSW design, linking fluid and solid domains by appropriate meshing and applying automatic FEA-CFD coupling. Stand-alone thermal and thermo-mechanical FEA simulations as well as stand-alone steady-state CFD solutions are presented for the two different TSW geometries and two different amounts of cooling flow, respectively. The predictions for radial component displacement from the thermo-mechanical model are validated against experimental test data. The steady-state CFD analyses are used on the one hand to highlight the rotor disc cooling benefits due to the deflector plate and on the other hand to analyse the benefits of taking the hot running clearances into account. In addition, unsteady CFD analyses of the two geometries for one flow case are conducted to ascertain the difference between time accurate and the steady-state solutions. Furthermore, each case is simulated using a coupled FEA-CFD approach in order to compare the calculated air and metal temperatures to measured test data. In a final step, one unsteady CFD solution is coupled to the FEA analysis in order to highlight the effect of the flow unsteadiness on the TSW heat transfer.

7.1 Thermo-Mechanical Displacement Analyses

The results of the 2D thermo-mechanical SC03 models are shown in Fig. 7.1 and 7.2. Figure 7.1 shows the non-dimensional metal temperature contours including isotherms based on the direct application of the respective test data at the walls. Both geometries (baseline on the left and deflector plate on the right hand side) with the two relevant flow cases ($30\,\mathrm{g\,s^{-1}}$ and $55\,\mathrm{g\,s^{-1}}$ on the upper and lower views respectively) are run, and the computational results are compared to the experimental measurements of the thermocouples

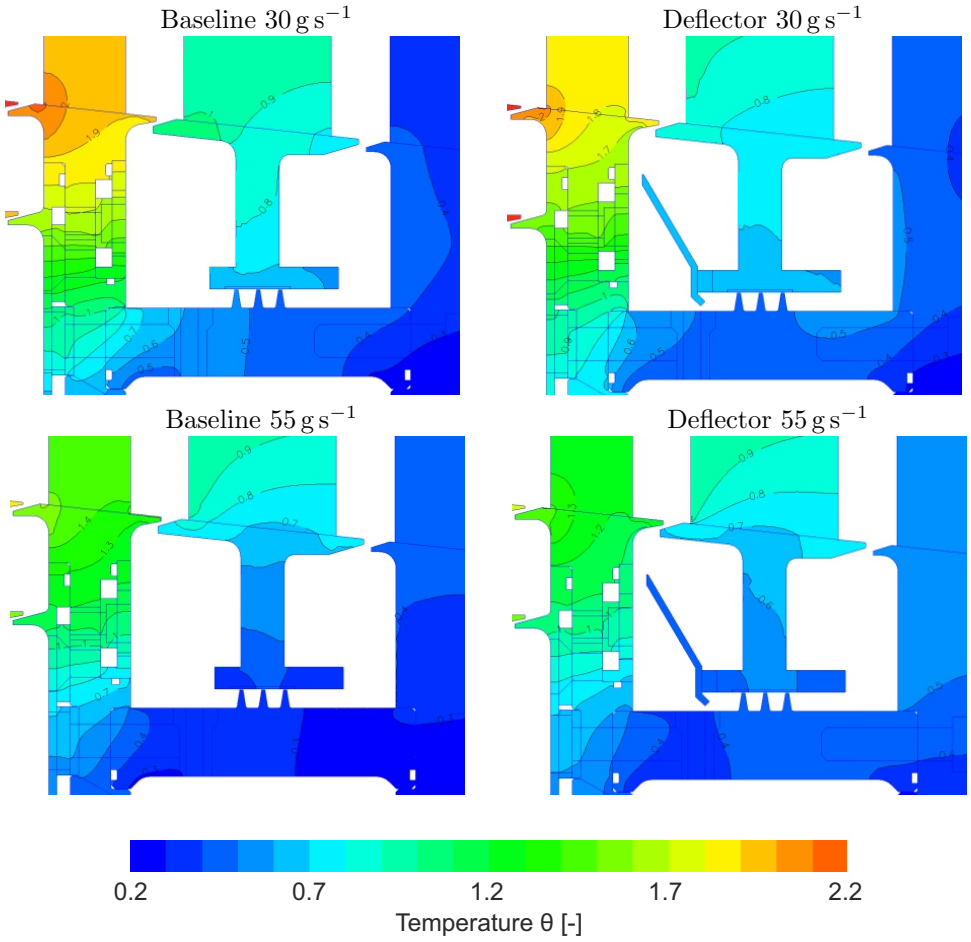

Figure 7.1: Temperature contours from the 2D FEA model for the four test cases (30 g s^{-1} top, 55 g s^{-1} bottom)

Geometry	Flow case	Δr^*_{exp}	Δr^*_{SC03}	Δr^*_{error} [%]
Baseline	30 g s^{-1}	N/A	1.25	N/A
	55 g s^{-1}	1.35	1.32	−2.2
Deflector	30 g s^{-1}	1.39	1.26	−9.3
	55 g s^{-1}	1.46	1.35	−7.5

Table 7.1: Overview of hot running interstage seal clearances for the four test cases compared to test data EASTWOOD (2014)

installed inside rotor disc 1 to verify the correct prediction of the conduction across the components. This comparison shows only marginal differences (within the prediction and measurement tolerances).

The purpose of these models is primarily to validate the displacement predictions from the SC03 models, the cooling performances of these four test cases are discussed later on in this chapter. Although further comments will be made when looking at the results of the adiabatic CFD and FEA-CFD coupled analyses, from a first look at the rim gap temperatures, some comments can be made. For each test case, Fig. 7.1 shows that the

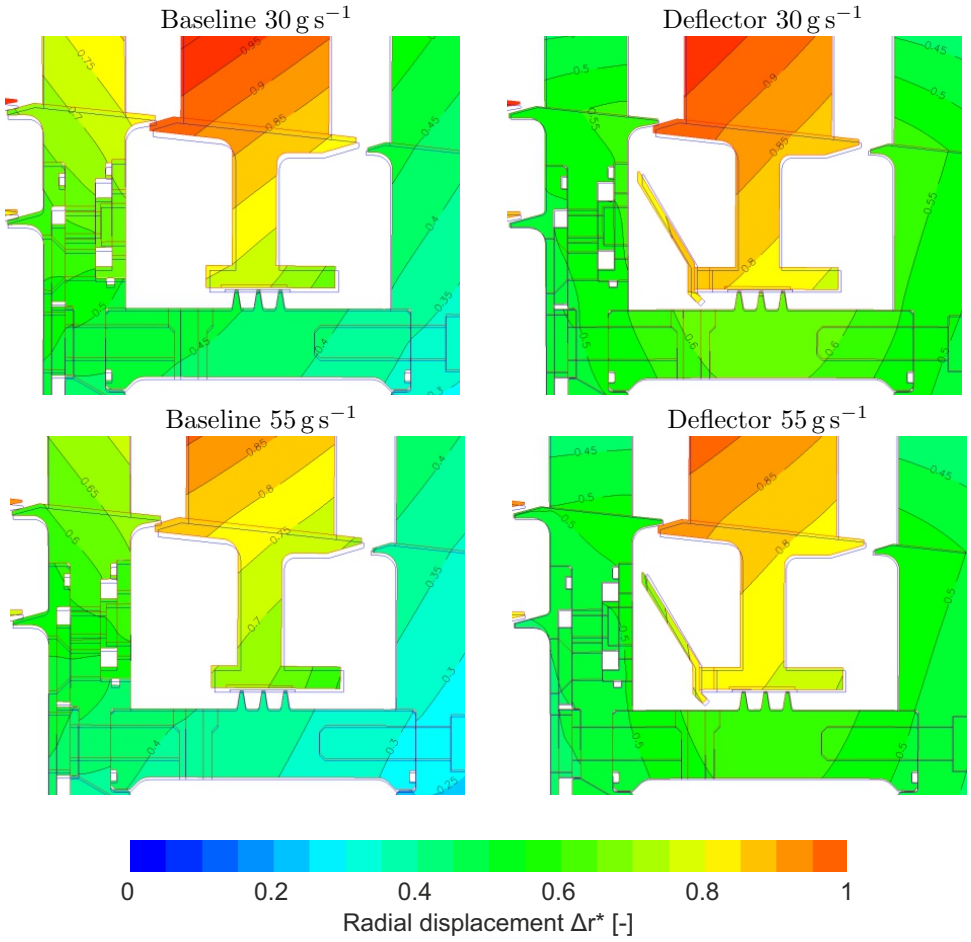

Figure 7.2: Contours of non-dimensional radial displacement from the 2D FEA model for the four test cases ($30\,\mathrm{g\,s^{-1}}$ top, $55\,\mathrm{g\,s^{-1}}$ bottom)

rim at the rotor side is significantly hotter than radially inboard where cooling air is introduced, while at the stator side, as can be seen from the contours (isotherms), almost vane temperature is reached. However, in the region of the stator foot and the labyrinth seal fins, it can be observed that the stator is slightly hotter than the rotor. This is more evident for the lower flow rate cases.

Figure 7.2 shows contours of radial displacement (normalised over the cold built clearance) in the rig based on the previous temperature distribution as well as the centrifugal forces and pressure loads, which are read across from the complete rig model. It can be seen that the clearances increase during hot running, which means that the thermal growth of the stator foot, which is pulled radially outwards by the casing, is more than the combined effects of the centrifugal forces and thermal loads induced in the rotor.

The growth of the seal clearances for each test case is summarised in Table 7.1. An average value from the three fins is calculated in the model and is compared to the experimental displacement measurements from Eastwood (2014) where available. Based on the measurement uncertainty of the seal clearance of 2.5 % Eastwood (2014) it can be deduced that the displacement predictions for the baseline geometry is in good agreement

with the measurements. However, for the deflector plate geometry, the discrepancies are larger and outside the measurement tolerance of the sensor. This might be due to the additional modeling of the deflector plate and the bolts. Especially the latter, which is a non-axisymmetric feature and modelled using a thickness property, might lead to different heat transfer behaviour in the area between the deflector to the stator foot compared to the experiments. However, despite the larger discrepancies, it is noteworthy mentioning that for the deflector plate cases, the seal clearances are larger than for the baseline geometry and this trend is consistently captured.

As the axial displacements measured during the experiments were considered to be small, i.e. being within the sensor measurement tolerance, it is not sensible to carry out a detailed comparison. However, this conclusion from the experiments is supported by the numerical results, where only very minor axial displacements are calculated.

7.2 Steady-State CFD Results

Having benchmarked the thermo-mechanical models with respect to the displacements, this section brings us to the steady-state CFD results. The CFD results are thoroughly reviewed before and after running through the coupled process, i.e. adiabatically and with applied wall temperatures. The purpose is to isolate the effect of heat transfer and to benchmark the heat pickup in the cavity due to coolant mixing and windage versus hot gas ingestion. It is divided into four subsections: first, we will analyse the two respective cavity flow fields of the baseline geometry followed by the cavity flow fields of the deflector plate geometry. The third part contains a back-to-back comparison of the four flow cases with respect to the cooling performance of the life-critical features inside the TSWs. In the final subsection, the four CFD models are updated with the hot running clearances (from the experiments where available) and a comparison between the *cold* against *hot* geometry for each test case is conducted.

7.2.1 Baseline Geometry

Figure 7.3 summarises the steady-state CFD results of the baseline geometry for the $30\,\mathrm{g\,s^{-1}}$ flow case at the top and the $55\,\mathrm{g\,s^{-1}}$ at the bottom. On the left hand side a surface *line integrated convolution* (LIC) representation is given (a method to visualise a flow or a vector field (Cabral and Leedom, 1993)), which is contoured by swirl fraction and on the right hand side, contours of non-dimensional adiabatic fluid temperature are depicted.

Baseline $30\,\mathrm{g\,s^{-1}}$ (top figures) Considering the upstream cavity first: the cavity is split into three main parts. At lower radii, the cooling air jet enters the upstream cavity radially through the drive arm at swirl equal to one and then is directed towards the stator

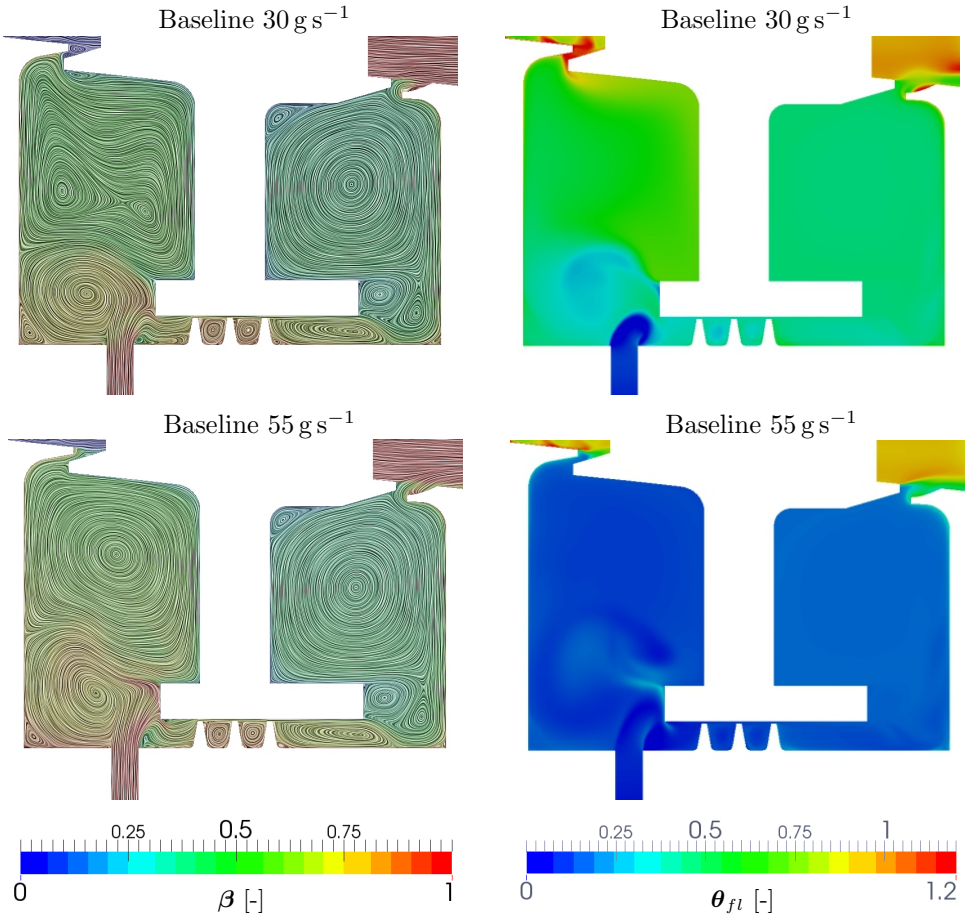

Figure 7.3: Surface LIC representation coloured by swirl fraction (left) and contours of non-dimensional fluid temperature (right) in an angular cutting plane obtained from the steady-state 3D CFD sector calculations of the two flow cases ($30\,\mathrm{g\,s^{-1}}$ top, $55\,\mathrm{g\,s^{-1}}$ bottom) for the baseline geometry using the cold built clearances

foot and the interstage labyrinth seal without penetrating the core region. This is also reflected in the temperature contours, where the cooling jet is cool as long as the swirl is maintained and then suddenly increases in temperature once it reaches the static part. At lower radii of the upstream cavity, a counter clockwise recirculating vortex is formed, which partially entrains the coolant towards the lower radii of the rotor disc before flowing through the interstage seal towards the downstream cavity. Having a look at the fluid temperature contours, this reflects in a small area of cooler air, which follows the shape of the recirculating vortex.

The second zone, is the core region at higher radii of the upstream cavity, where a large recirculating structure can be seen, which consists of two connected vortices. The temperatures in this area are larger than the inlet coolant temperature, which indicates that the cooling air does not fully penetrate this region, but mixes with hot air instead. This results from the radial momentum of the jet being too low and an insufficient amount of cooling air to seal the cavity. Thus, the cavity pressure is not strong enough to seal the cavity against the higher pressure of the main annulus, which, as a result, enters the

cavity. Furthermore, it can be seen that the air is pumped radially outwards inside the boundary layer along the rotor disc, and radially inwards along the stator disc boundary layer. This strongly infers the presence of a BATCHELOR cavity flow type, where the rotor boundary layer is an EKMAN layer and the stator one a BÖDEWADT layer.

This has already partially described the third feature, the rim region flow. In this area, a small vortex structure is detectable with negative swirl, which reflects in a very high temperature region. This is related to the main annulus air, which ingests into the cavity since the sealing requirement is not met. The contours of negative swirl are related to the recirculation zone when the main annulus gas detaches from the blades, whereas the hot spots in the temperature contours are solely related to the main annulus air, which enters the cavity.

Considering the literature, as described in Chap. 2.3 and in particular in Fig. 2.6, it can be seen that the described flow structure belongs to flow regime IV. With a cavity aspect ratio of $G = 0.62$ and a rotational REYNOLDS number of $Re_\phi \approx 1.9 \times 10^6$ this fits exactly in this regime as well. One very interesting aspect in the core, which is not expected, is the presence of the two vortices, rather than one large vortex. This is only apparent for this flow case and this particular geometry. One possible explanation could be that coolant and ingested air try to penetrate the core equally, constricting the large vortex from the top and the bottom, which results in this double vortex structure. We will see later, that for the more appropriate, i.e. hot running, clearance this separation is not visible anymore.

Evaluating the dominating effect for the externally induced hot gas ingestion into the cavity leads to a ratio of $Re_x/Re_\phi \approx 0.5$. According to PHADKE and OWEN (1988a,b) this means that ingestion is dominated by rotation. This also agrees with the turbulent flow coefficient calculated in Tab. 4.1, which is smaller than 0.1.

This brings us to the remaining flow structures of the TSW: the interstage seal and downstream cavity flows. The air flowing towards the downstream cavity passes the labyrinth seal fins and forms two highly swirled vortices in between those fins. Due to the high swirl, the fluid temperature is slightly reduced again and keeps the seal cool. Then one axially elongated vortex is formed until the flow separates and is entrained radially outwards along the disc. In this separation area, a highly turbulent two-vortex structure is formed at lower swirl due to the separation from the rotor wall. The fluid temperature slightly increases as well due to the loss in swirl. In the core region of the downstream cavity, one large recirculating vortex can be seen, as one would expect from the literature (DAILY and NECE, 1960). Similar to the upstream cavity, a BATCHELOR type flow is present. As no hot gas ingests into the cavity, the core flow is not perturbed and the flow is clearly separated into one inviscid recirculating vortex, a EKMAN layer along the rotor disc, which is pumped radially outwards, and a BÖDEWADT layer going radially inwards along the stator wall. In general, the fluid temperature in the downstream cavity is higher than in the upstream cavity due to the pickup of windage, i.e. viscous heating, while being

entrained along the rotating walls. In the rim region, the cavity air mixes with the highly swirled main annulus gas and exits the cavity.

Baseline $55\,\mathrm{g\,s^{-1}}$ (lower figures) Proceeding in the same manner as for the lower flow case, we will first consider the upstream cavity. Similar to the previous observations, the cooling air jet enters the upstream cavity radially through the drive arm hole with swirl equal to one. Since the mass flow rate is much larger, the swirl is kept longer and the jet impinges the stator foot at a higher radius. Then a similar small vortex structure is formed, where some of the coolant is recirculated towards the rotor disc and the other part enters the core flow of the cavity. Other than for the lower flow case, the cooling air flow rate satisfies the sealing requirements of the cavity and cools the complete upstream cavity, which can be seen from the temperature contours. Only at the impingement point at the stator foot local "hot spots" are visible, which is related to the sudden loss of swirl of the coolant.

In the core region, a typical BATCHELOR flow structure is formed, where the coolant is entrained radially outwards along the rotor towards the rim. As the geometry has not changed and the rotational REYNOLDS number is similar to the lower flow case, this is expected from the literature (DAILY and NECE, 1960).

From both contours it can clearly be seen, that the cavity is sealed in the rim region against hot gas ingestion. The main annulus flow at very low swirl ratio does not penetrate the rim gap, neither are there any red spots, i.e. hot air, detectable in that area. From the temperature contours it can be seen that the cool air (blue) coming from the cavity and the hot air (red) from the main annulus mix in the rim region to some intermediate temperature (green).

The remaining parts of the TSW are similar to the lower flow case. The coolant, which is not used to seal the upstream cavity, flows through the interstage labyrinth seal to the downstream cavity, forming the same vortex structure as mentioned before (recirculations between and after the fins, complex turbulent vortex structure, BATCHELOR type core flow). The fluid temperature is slightly elevated compared to the upstream cavity due to the windage pickup along the rotor disc. This heat pickup is better visible in these temperature contours than in the lower flow case representation as along the rotor wall a layer of higher temperature (turquoise to green colour) is detectable. This layer increases in thickness with increasing radius and then detaches at the downstream rim before it then mixes with the main annulus again.

In summary, we can conclude that in the baseline design, two different flow structures are observed depending on the level of cooling mass flow rate. Not only are there differences in the rim seal flows (i.e. ingestion or no ingestion), but also the upstream cavity flow structures show some significant differences. However, these steady-state CFD results are in good agreement with the classical rotor-stator cavity flows adjacent to a main gas path

that have been described in the early literature (DAILY and NECE (1960), BAYLEY and OWEN (1970), PHADKE and OWEN (1988b; 1988c)).

7.2.2 Deflector Plate Geometry

Similar to the baseline geometry, Fig. 7.4 summarises the steady-state CFD results of the deflector plate geometry for the $30\,\mathrm{g\,s^{-1}}$ flow case at the top and the $55\,\mathrm{g\,s^{-1}}$ at the bottom. On the left hand side a surface LIC representation is given, which is contoured by swirl fraction and on the right hand side, contours of non-dimensional adiabatic fluid temperature are depicted. Due to the deflector plate a completely different flow structure is formed inside the upstream cavity, while the downstream cavity is not affected.

Deflector $30\,\mathrm{g\,s^{-1}}$ (top figures) From the swirl fraction contours, it can be seen that the coolant jet enters the upstream cavity at disc speed and then impinges the lower tip of the deflector plate. Most of the jet is turned towards the rotor disc, while a small portion seems to be diverted, i.e. flowing straight towards the interstage seal. Once the jet impinges the deflector plate, all swirl is lost and the air heats up, as shown in the temperature contours. The portion of cooling air, which is deflected in direction of the rotor disc, is then entrained radially outwards.

The area enclosed by the deflector plate and the rotor disc is in a way a smaller rotor-stator cavity. Therefore, similar flow features as in the baseline design can be observed in this particular region. The vortex structure at low radius in the corner of the cavity represents a small recirculation area of the coolant before it is entrained radially outwards. The larger single vortex at higher radius is again a BATCHELOR type flow with its characteristic boundary layers. The gap between the upper deflector tip and the rotor wall is equivalent to a rim gap. The temperature contours clearly shows the benefit of the deflector plate: although the coolant artificially increases in temperature due to the impingement, the rotor disc is still exposed to relatively cool air before it mixes with the ingested hot gas.

However, checking the flow structure of the tiny portion of coolant, which is split from the main coolant jet and is directed towards the labyrinth seal straight away shows a small recirculation area in the mixing region with the cavity flow coming from the area between the stator foot and the deflector plate. Due to this recirculating vortex, hotter air is entrained back towards the region which is enclosed by the deflector plate and the rotor disc. This is also reflected in the fluid temperature contours, where hotter air (green) mixes with the cold air (blue). From a safety point of view this flow feature can cause serious damage and needs to be controlled. Depending on the amount of ingested hot gas, which is recirculated inside the upstream cavity, overheating of the rotor disc can be the consequence.

Evaluating the upstream rim flow shows that the complete rim is dominated by negative swirl and hot fluid temperatures, both of which are related to hot gas ingestion. As

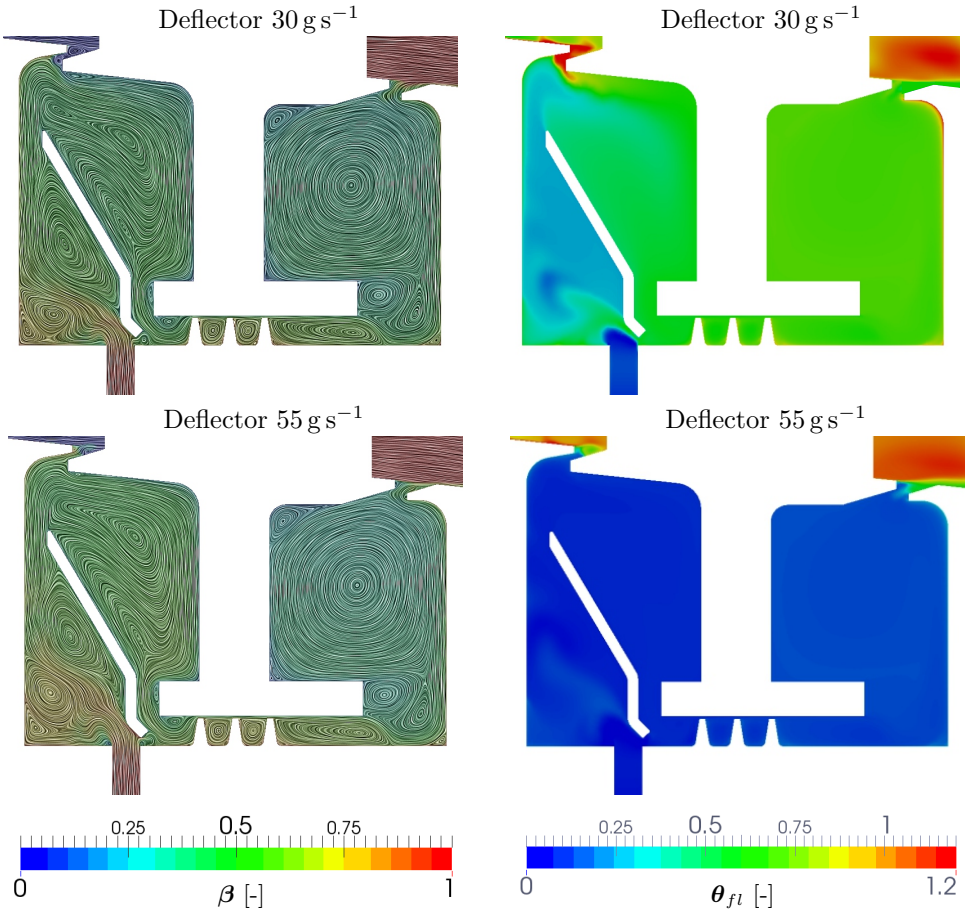

Figure 7.4: Surface LIC representation coloured by swirl fraction (left) and contours of non-dimensional fluid temperature (right) in an angular cutting plane obtained from the steady-state 3D CFD sector calculations of the two flow cases ($30\,\mathrm{g\,s^{-1}}$ top, $55\,\mathrm{g\,s^{-1}}$ bottom) for the deflector plate geometry using the cold built clearances

for the baseline design and low flow case, the amount of coolant is insufficient to seal the rim against ingestion appropriately. After the hot gas enters the cavity it mixes with the air coming from the rotor disc and then is entrained radially inwards through the area enclosed by the deflector plate and the stator foot. As the cavity air is swirled due to the rotation of the rotating parts, some vortices and recirculations are formed before being dragged to the interstage seal. This region is equivalent to a stator-stator cavity where a pre-swirled flow enters. To the author's best knowledge no such flow case has been studied in the literature so far and therefore it is not possible to associate this particular flow pattern to a distinct flow type as done before with the rotor-stator flows. However, it can be seen that along the stator as well as the deflector, a flow structure similar to the BÖDEWADT layer is formed.

Once the fluid enters the labyrinth seal and the downstream cavity, the same flow pattern as described for the baseline design is present. This is because no further modifications in geometry have been done. Only the temperatures are slightly different due to the different flow inlet boundary conditions and the mixing behaviour in the upstream cavity.

The same is true for the heat pickup due to windage, which is visible in the temperature contours.

Deflector $55\,\mathrm{g\,s^{-1}}$ (lower figures) The flow pattern of the $55\,\mathrm{g\,s^{-1}}$ with the deflector design is very similar to that of the $30\,\mathrm{g\,s^{-1}}$ flow case with the same geometry. The coolant jet enters at swirl equal to one into the upstream cavity and impinges the lower deflector tip. A small portion of the jet is split towards the interstage labyrinth seal whereas the main portion is directed towards the rotor disc. Compared to the lower flow case, in this case the jet has a higher radial momentum and penetrates deeper in the cavity before it loses most of its swirl. This is very similar to the comparison in the baseline design between the two flow cases. Due to the deeper penetration, the lower recirculation area in the corner becomes bigger and the one, which we associated to a BATCHELOR type of flow earlier (area between deflector plate and rotor disc at mid height), becomes smaller. Then the flow is entrained along the rotor disc towards the rim seal.

Due to the fact that the amount of cooling air is almost doubled in this flow case, the sealing requirement of the upstream cavity is met and very little hot gas can ingest into the cavity through the rim. This is clearly visible when checking the contours of swirl in that area: the blue contours of swirl (associated to the main annulus) do not enter the cavity but are blocked by the green contours from the coolant instead. Similar for the temperatures, where the red (main annulus) and the blue contours (coolant) mix in the rim region, but overall the cavity is kept blue, i.e. cool.

As there is no large temperature difference visible inside the upstream cavity, no serious comment can be made related to the small recirculation area at the lower deflector tip. The surface LIC representation shows that a small vortex can be detected similar to the lower flow case. However, as the temperatures are almost constant, it is hard to say whether air is recirculated or not.

The remaining flow patterns are again similar to the other three flow cases discussed previously. Again, it can be seen that the downstream cavity gets slightly hotter due to the heat pickup which is related to the viscous heating along the rotating walls (i.e. windage heating).

In summary, we can conclude that the deflector plate significantly changes the flow pattern in the upstream cavity. However, the downstream cavity is not affected. Although the flow patterns are different, the sealing requirements for both geometries seem to be similar. From a qualitative point of view, it looks like the deflector plate geometry is able to improve the upstream rotor disc cooling, although some ingested hot gas is recirculated and exposed to the disc again. Therefore, a back-to-back comparison between these four flow cases is given in the upcoming section.

7.2.3 Improved Geometry Benefits

This section focuses on a back-to-back comparison of the two different geometries and their benefits and drawbacks. From the literature it was stated that the deflector plate improves the cooling of the upstream rotor disc. In Fig. 7.5 the adiabatic near-wall temperatures are shown for the four test cases: from left to right the baseline geometry at low and high cooling mass flow rate is depicted followed by the two equivalent flow cases with the deflector plate geometry.

As already mentioned in the previous section, it can be seen that the two cases at low coolant flow rate do not cool the upstream disc as well as the high coolant flow cases. The discs are significantly hotter, which is shown by the green and red contours compared to the blue ones. The same behaviour can be concluded from the temperature plots along the upstream rotor disc on the left hand side in Fig. 7.6 ('disc up'). There it can also be seen that the rotor disc temperatures of the low coolant flow cases are hotter than for the high coolant flow cases. This can be associated to the hot gas ingestion into the cavity for the low coolant flow cases, which then mixes inside the cavity and thus heats up the cavity air temperature.

Comparing the isotherms, which are highlighted by the black lines in the disc temperature contours, it can be seen that the baseline design realises a more uniform angular temperature distribution and that the temperature increases consequently from lower to higher radii. In the deflector design, the isotherms are not as constant in angular direction as it is the case for the baseline design. Furthermore, the temperature at the disc do not increase permanently from lower to higher radii. This can be explained by the influence of the deflector plate, which turns the coolant jet towards the disc. At the disc impingement point, which is the area of the lower vortex structure described in the previous section, the cooling is more effective since the coolant does not completely mix with the remaining

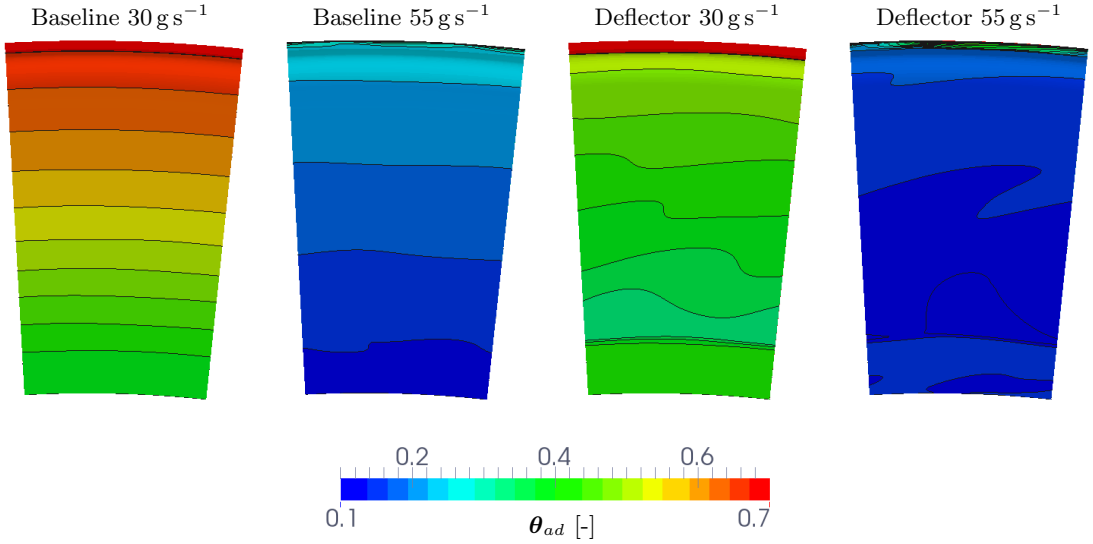

Figure 7.5: Comparison of the non-dimensional adiabatic temperatures at the upstream rotor disc for the four test cases

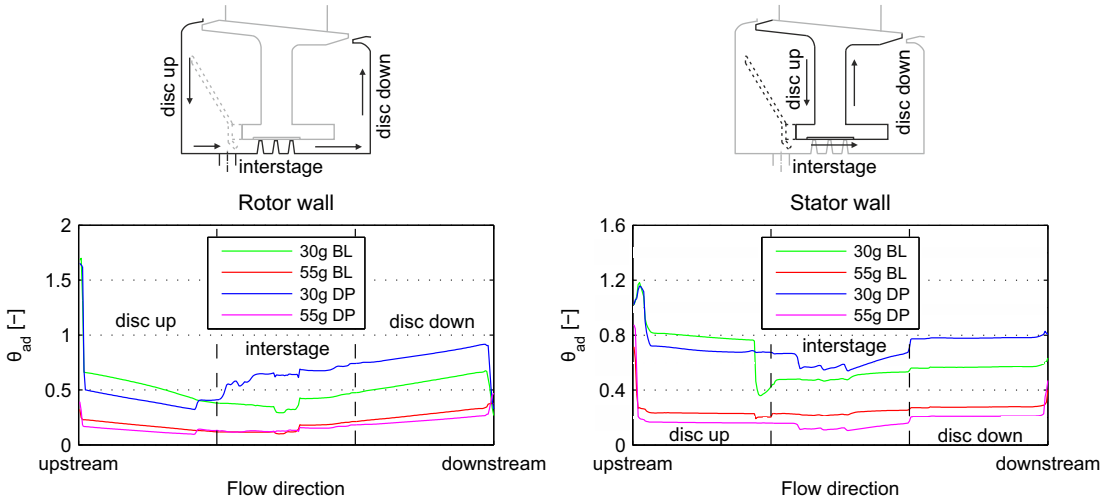

Figure 7.6: Comparison of non-dimensional adiabatic wall temperatures at the rotor (left) and stator (right) wall for the four different flow cases (BL: baseline, DP: deflector plate)

hotter cavity air. The non-uniformity in angular direction can be explained by the fact that the coolant jet is a 3D feature, which is directed towards the disc straight away before it can mix with the remaining cavity air. Thus a local stronger cool air impingement at the disc can be seen, which results in the non-uniformity of the temperatures.

To adequately distinguish the benefits of the different cavity designs and thus the direct impact of the deflector plate with respect to the cooling performance of the cavity components, the two flow cases are compared separately to each other.

The $30\,\mathrm{g\,s^{-1}}$ cases The comparison of the two different designs at $30\mathrm{g\,s^{-1}}$ in Figs. 7.5 and 7.6 suggests that the upstream disc is better cooled with a deflector plate than without. Only at the rim, the temperatures for both geometries are at a similar temperature level. However, further downstream ('interstage' and 'disc down'), the baseline geometry realises a better cooling than the deflector design. As in the baseline design the cooling air tends to flow directly through the interstage seal, while maintaining most of its swirl, without penetrating the upstream cavity, the downstream air is cooler than in the deflector design. In the latter, the vast majority of the coolant is used to keep the upstream disc cool. Then it mixes with the ingested gas from the main annulus flows through the area enclosed by the stator foot and the deflector plate, where it loses swirl and its temperature increases before passing the interstage seal compared to the baseline design.

Some comments on the stator temperatures are also made for completeness, although they do not represent engine life critical components. Similar to the upstream rotor disc, the upstream stator disc is at a similar adiabatic temperature at the rim for both geometries and then decreases. In the case with deflector plate, the upstream stator wall temperatures are generally lower than in the baseline case. Only at low radius, a temperature jump to much lower values can be seen in the baseline design. Going further

downstream, the adiabatic temperatures of the baseline design are consistently lower than in the deflector design.

These findings can be explained as described above. As for the deflector design, most of the coolant is entrained towards the rim, where it then mixes with the ingested gas, the temperatures are expected to be lower than for the baseline design, where only a small fraction of coolant enters the upstream cavity. The jump in temperature in the baseline design is due to the fact, that the coolant impinges the stator foot, which consequently results in an improved cooling at this particular position. Similar to the interstage and downstream rotor discs, the respective stator walls are better cooled in the baseline design, since more coolant flows straight away to the downstream area without mixing with the hot gas.

A quantitative comparison of the levels of ingestion of the two designs is not possible from these representations. This is done in the next section. However, these temperature contours and plots suggest that the levels of ingestion are of similar order of magnitude. Only the mixing area varies, which results in the difference in temperatures.

The $55\,\mathrm{g\,s^{-1}}$ cases The back-to-back comparison of the CFD results at higher cooling mass flow rate leads to similar conclusions as for the lower coolant flow cases. However, the differences are not that significant. From the temperature contours in Fig. 7.5 it can be seen that the deflector plate design provides a better rotor disc cooling, which is represented by the dark blue colours. The disc temperature is almost constant over the complete radius whereas in the baseline design a small temperature gradient is visible from low to high radii. In comparison to the low coolant flow cases no significant hot gas ingestion in the rim region is detectable for both designs.

With respect to the near wall temperature plots along all cavity walls as they are visualised in Fig. 7.6, it can be seen that the upstream rotor disc is cooled slightly more effectively when a deflector plate is included into the cavity. The interstage seal and the downstream rotor walls are also of similar magnitude with some advantages for the deflector plate design. This agrees with the descriptions for the low coolant flow cases. Due to the deflector the main fraction of the coolant is turned towards the upstream rotor disc, while in the baseline design, the coolant first interacts with the cavity air before cooling the upstream disc. However, the differences in temperature are not very large. As we have seen in the previous section, where the flow fields were analysed in detail, the high coolant flow cases seal the cavity appropriately with no net hot gas ingestion. Therefore, the temperature effects inside the cavity are only minor.

However, it is very interesting to compare the temperatures of both designs entering the interstage seal. Upstream the temperatures are almost identical but then going further downstream slight differences in temperature increase between the two designs are visible. The baseline design predicts hotter adiabatic wall temperatures than the deflector plate design. To find an explanation for this is not very obvious as the solver and turbulence models are identical for both cases. One possible reason for the difference could be associ-

ated with the different mesh generations and styles: structured and unstructured for the baseline and deflector plate design, respectively. Another explanation could be a difference in the interstage inlet flow of the two geometries. This can be linked to the mixing of the fraction of the coolant, which is directed towards the interstage, and the upstream cavity flow in the interstage inlet region. Due to this effect a different flow structure compared to the baseline design is present, which affects the fluid temperature.

Having a look at the adiabatic stator wall temperatures it can be seen that the deflector plate design realises slightly lower temperatures than the baseline design. The temperature jump at lower radii of the upstream stator disc is again visible for the baseline design. However, it is not as significant due to the lower temperature gradients inside the cavity, which is related to the lack of net hot gas ingestion. The small differences in the interstage seal and downstream cavity can again be associated to the different meshes and the different flow inlet.

In general, it can be stated that the outcome of this comparison summarised above agrees with the previous findings of Dixon et al. (2013); Da Soghe et al. (2011a); Coren et al. (2011), who assumed it is beneficial for the cooling of the upstream rotor disc to put the cooling hole near to the rotor disc or incline the hole in direction to the upstream disc. However, the statement of Pohl et al. (2015) that the amount of coolant can almost be halved by including the deflector plate, cannot be supported. The deflector plate surely improved the upstream disc cooling but does not reach the same efficiency of the high coolant flow of the baseline design. One possible explanation for that can be the use of different CFD codes, which result in a different flow pattern. In particular the flow recirculation through the area of the lower deflector tip and the rotor disc was not captured in earlier HYDRA versions.

7.2.4 Impact of Structural Deflections on the Flow Field

After having analysed the different flow fields of the four test cases at constant cold built seal clearances, now the effects of the thermo-mechanical displacements on the flow patterns inside the cavity are analysed. Therefore, the four geometries are remeshed using the hot running clearances measured during the experiments where available (see Sec. 7.1). Otherwise, the predicted displacement from the SC03 model is used.

As mentioned in the literature review (Chap. 2.4), the size of the interstage seal clearance is directly related to the level of hot gas ingestion through the rim seal, as the pressure gradient varies with leakage flow area. As a first validation step, the CFD results are used to calculate the labyrinth seal mass flows. Table 7.2 compiles the results of Eq. 2.45 for the simulated cold and hot running geometries using the measured clearances and the fluid variables from the steady-state CFD results. These calculated mass flows are compared to the results of Eq. 2.45 using the experimentally measured values for pressures and temperatures as described by Eastwood (2014).

Geometry	Flow case	$\dot{m}_{cold,Eq.1}$	$\dot{m}_{hot,Eq.1}$	$\dot{m}_{exp,Eq.1}$
Baseline	$30\,\mathrm{g\,s^{-1}}$	$31.84\,\mathrm{g\,s^{-1}}$	$37.23\,\mathrm{g\,s^{-1}}$	$38.04\,\mathrm{g\,s^{-1}}$
	$55\,\mathrm{g\,s^{-1}}$	$33.69\,\mathrm{g\,s^{-1}}$	$44.13\,\mathrm{g\,s^{-1}}$	$44.81\,\mathrm{g\,s^{-1}}$
Deflector	$30\,\mathrm{g\,s^{-1}}$	$33.14\,\mathrm{g\,s^{-1}}$	$44.19\,\mathrm{g\,s^{-1}}$	$44.54\,\mathrm{g\,s^{-1}}$
	$55\,\mathrm{g\,s^{-1}}$	$33.71\,\mathrm{g\,s^{-1}}$	$49.84\,\mathrm{g\,s^{-1}}$	$48.56\,\mathrm{g\,s^{-1}}$

Table 7.2: Overview of interstage seal flows for the four test cases with cold and hot running geometries calculated from Eq. 2.45

From the table, it can be seen that for all flow cases, the amount of air flowing through the interstage seal is significantly higher with an increased interstage seal clearance. An important difference between the low and high coolant flow cases is the amount of air passing the interstage seal: for the low coolant flow cases the interstage seal flows (cold and hot) are larger than the inlet cooling mass flow rate, which indicates the presence of hot gas ingestion. For the high coolant flow cases, the interstage seal flows are lower than the inlet cooling mass flow rate, which suggests the presence of a sealed cavity. These findings are in accordance with the flow field descriptions in the previous section.

Furthermore, the results of Eq. 2.45 show that the use of the cold interstage clearance does not match the measured values, whereas taking the hot running clearances into account, the predicted values are closer to the gas concentration experiments from which the measured mass flow rates in the interstage seal cavities are determined. Note that for low flow cases, the predicted and measured sealing mass flows are higher for the deflector plate geometry than for the baseline geometry. This will translate into a higher likelihood of ingestion which has become evident in the CFD.

Figures 7.7-7.14 provide an overview of the converged adiabatic steady-state solutions for each flow case for both cold and hot running geometries. Since the focus of this section is the quantification of the structural impact on the TSW heat transfer, flow pattern comparisons are only used for benchmarking purposes of the hot gas ingestion inside the cavity. Each figure pair shows on the left hand side a surface LIC representation coloured by swirl ratio of three angular cutting planes in the rim region and on the right hand side a surface LIC representation coloured by adiabatic fluid temperature in an angular midplane for the cold (top figures) and the hot geometries (bottom figures), respectively.

Baseline $30\,\mathrm{g\,s^{-1}}$ (Figs. 7.7 and 7.8) Although the levels of windage are comparable and the mass flow rates put in the system are similar for both seal clearances, significant differences can be detected from the swirl and temperature contours. From the close-up view of the rim region, it can be seen that the flow structure inside the rim differs, i.e. for the hot running clearance more hot gas is ingested into the cavity (larger recirculation area along the stator side). This directly reflects in the temperature contours, where the upstream cavity using the hot running clearance is significantly hotter (red contours), especially at the stator wall. This will have a direct impact on rim temperatures, especially

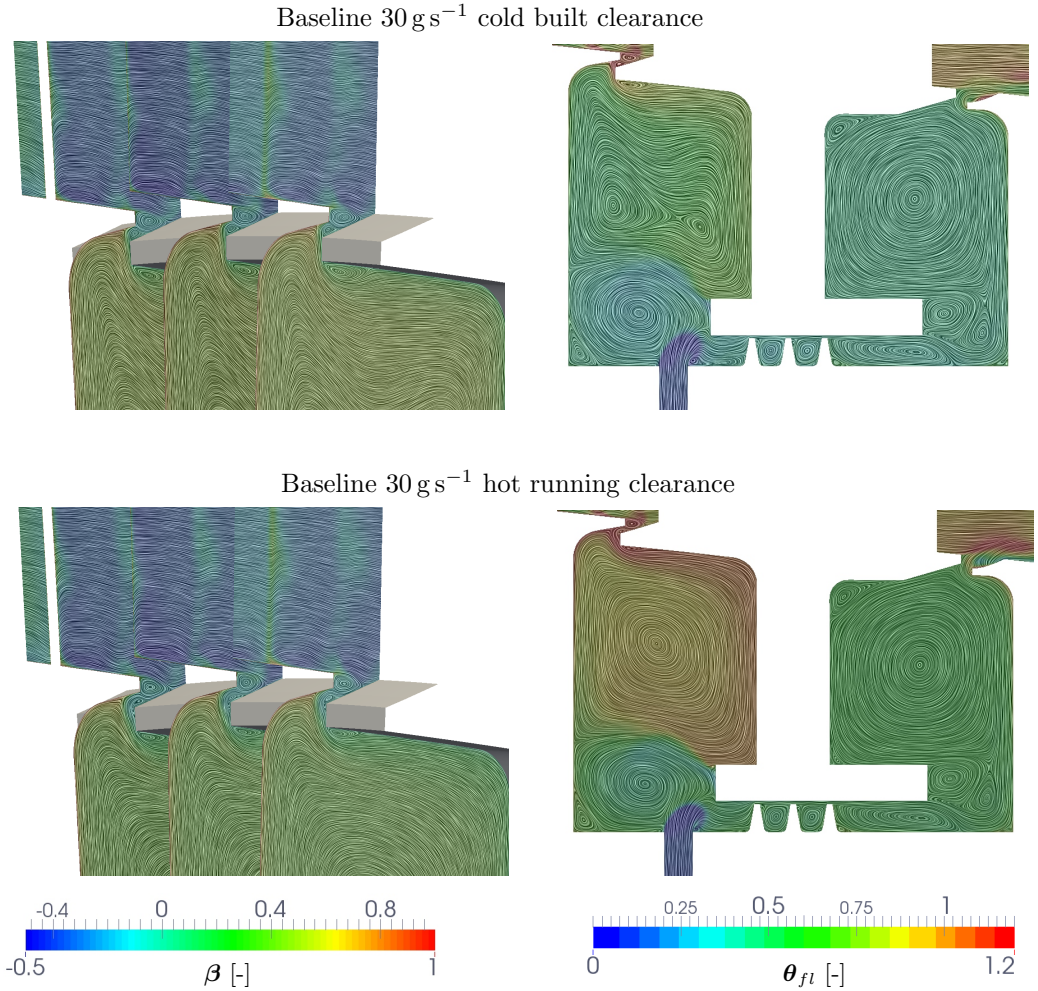

Figure 7.7: Swirl contours in three angular cutting planes in the rim region for the cold (top) and hot (bottom) geometry for the 30 g s^{-1} baseline design

Figure 7.8: Temperature contours in an angular cutting plane for the cold (top) and hot (bottom) geometry for the 30 g s^{-1} baseline design

on the stator side, anticipating a possible cause for the observed rim seal temperature underprediction (see Fig. 2.21).

Another interesting observation is the change of the flow field inside the upstream cavity when opening the seal clearance. Using the cold built clearance a vortex pair is formed in the core region, as described in the previous section. However, for the hot running clearance, this vortex pair merges to one large vortex and thus can be associated to a typical BATCHELOR type of flow as one would expect from the literature. An explanation for the change in flow structure, is strongly related to the amount of hot gas ingestion. In the hot geometry ingestion dominates the core flow, whereas in the cold geometry the core flow is also influenced from the coolant inlet jet.

In summary, it can be said that the flow field is strongly influenced by the structural changes. The flow pattern changes and more hot gas ingests into the upstream cavity, which results in higher air temperatures. This is in agreement with the hand-calculations using Eq. 2.45.

Baseline 55 g s^{-1} (Figs. 7.9 and 7.10) Having a look at the CFD results for the higher coolant flow case, similar conclusions can be drawn. The contours of swirl ratio in the rim region are slightly different again for the cold and hot geometries. Using the cold design, no hot air seems to penetrate the upstream cavity, whereas in the hot design, hot air seems to penetrate at least inside the rim and possibly also inside the upstream cavity. This again will have a direct impact on the rim temperatures, anticipating a possible cause for the observed rim seal temperature underprediction (see Fig. 2.21).

Comparing the temperature contours of the two designs, hardly any difference can be detected. The flow pattern is almost identical and the temperatures vary just slightly. In the case of the hot geometry, the fluid temperatures inside the cavities are slightly elevated. Only at the rim seal, a larger temperature increase is visible compared to the cold geometry. This latter finding is in agreement with the swirl ratio contours, where a similar conclusion can be drawn.

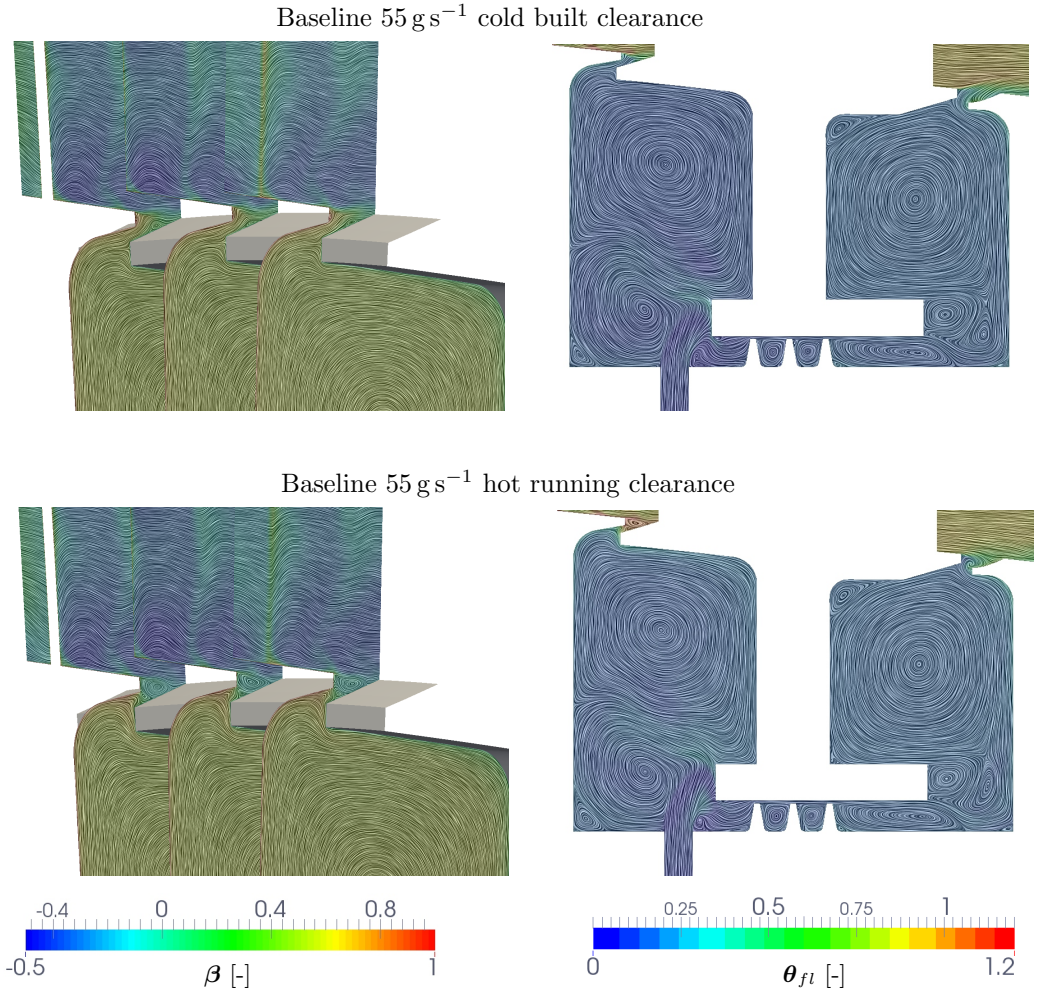

Figure 7.9: Swirl contours in three angular cutting planes in the rim region for the cold (top) and hot (bottom) geometry for the 55 g s^{-1} baseline design

Figure 7.10: Temperature contours in an angular cutting plane for the cold (top) and hot (bottom) geometry for the 55 g s^{-1} baseline design

These observations from the CFD results agree again very well with the calculation summarised in Tab. 7.2. Due to the larger interstage seal clearance, more gas flows through that seal instead of egressing into the main annulus. However, the cavity is sealed and no net hot gas ingestion is obvious.

Deflector 30 g s^{-1} (Figs. 7.11 and 7.12) This brings us to the deflector plate geometries. First we are having a look at the low coolant flow case. Similar to the baseline design flow cases, a difference in the rim seal flow pattern can be seen for both geometries. The area of recirculation of the hot gas seems to be larger in the hot geometry compared to the cold design. This is reflected in the temperature contours as well, where a larger portion of hot air (red contours) is present especially at the stator rim.

Overall the temperatures inside the upstream and downstream cavities are slightly higher for the hot geometry. Not only along the stator wall but also in the area between the deflector plate and the upstream rotor disc, where a portion of the hot gas is recircu-

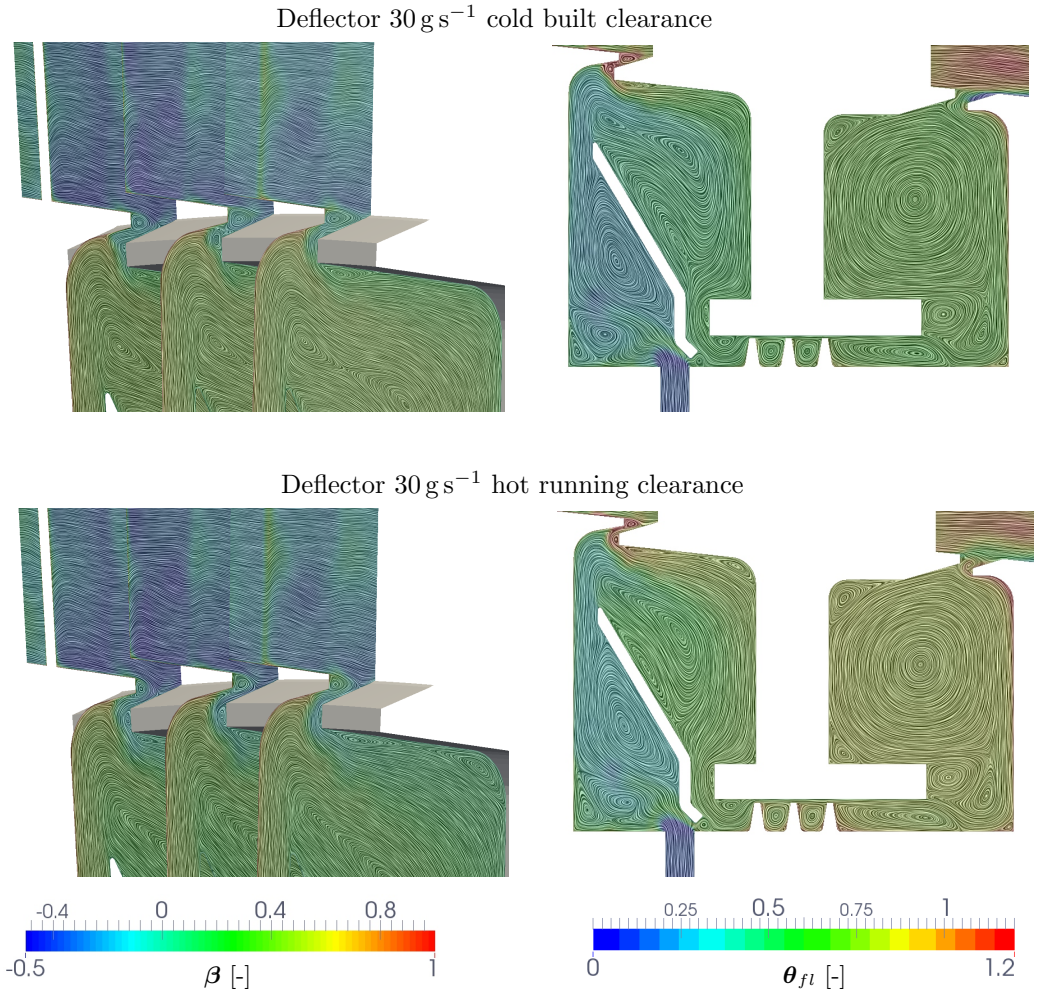

Figure 7.11: Swirl contours in three angular cutting planes in the rim region for the cold (top) and hot (bottom) geometry for the 30 g s^{-1} deflector design

Figure 7.12: Temperature contours in an angular cutting plane for the cold (top) and hot (bottom) geometry for the 30 g s^{-1} deflector design

lated and mixes with the coolant jet. This strictly underlines the importance of using hot running clearances in the design phase of an engine. From a safety point of view, the use of the results of the cold geometry could cause serious damage due to overheating if the design were to be based on cold clearance temperature predictions.

Comparing the outcome of the CFD results to the calculations in Tab. 7.2, it can be stated that both results are in good agreement. Due to the larger clearance more hot gas penetrates into the upstream cavity. This should also impact the metal temperature predictions, which are calculated using the coupled approach presented in the next section. From the temperature contours it can also be seen that the rim seal flow for the deflector geometry differs from the baseline design in such a way that more hot gas seems to penetrate into the cavity. An explanation for this can be the loss in radial momentum of the coolant jet once it impinges the deflector plate and thus does not seal the cavity as effectively.

Deflector $55\,\mathrm{g\,s^{-1}}$ (Figs. 7.13 and 7.14) The last comparison of the CFD results for the cold and hot geometry supports the previous findings as well. Since the interstage seal is increased during hot running, more hot gas ingests into the upstream cavity. This can be inferred from the swirl ratio contours and especially from the temperature contours in the mid-plane. The recirculation area in the three angular cutting planes penetrates much more into the cavity for the hot geometry than for the cold. This is in agreement with the temperatures, which are much higher (red) in the rim region for the hot geometry. This leads to an overall temperature increase in both cavities similar to the low coolant flow case of the deflector plate design.

Again the fluid temperatures in the life critical area enclosed by the deflector plate and the upstream rotor disc is higher once the interstage seal is increased. As mentioned previously, this can cause serious damage to the engine if only cold built clearances would be considered in the design phase.

With respect to the results from the hand calculations using Eq. 2.45, the CFD gives similar results. Although it is not obvious from the calculations how much air locally ingests and egresses. This is clearly different for the baseline and deflector plate design. From the swirl and temperature contours, it seems that during hot running more hot gas ingests into the cavity when a deflector plate is included inside the upstream cavity. Whether this is related to the different design and the assumption of a loss in radial momentum of the coolant jet due to the deflector or rather due to the larger interstage seal clearances during hot running in the deflector plate compared to the baseline design is not certain. However, it is obvious from these comparisons that the structural deformations impact the local flow fields and can cause significant differences in temperatures inside the cavities.

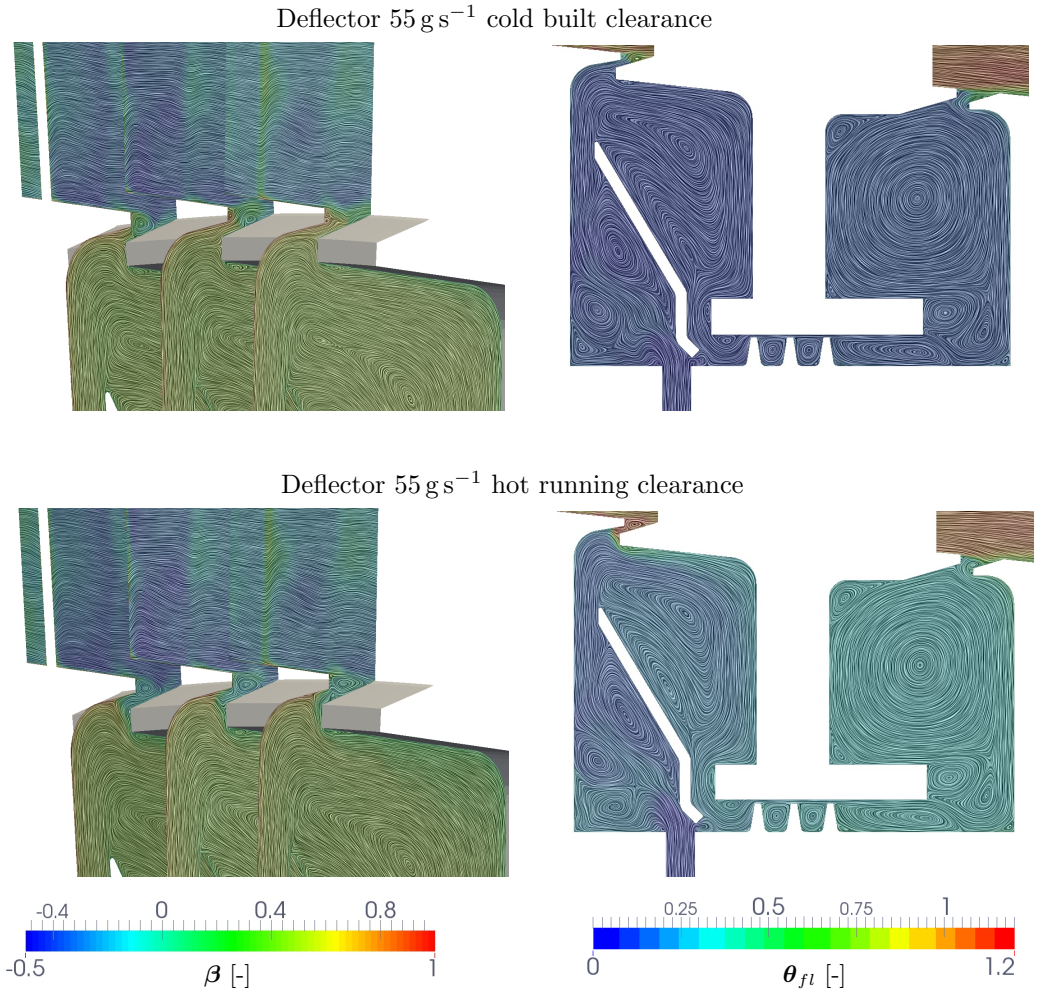

Figure 7.13: Swirl contours in three angular cutting planes in the rim region for the cold (top) and hot (bottom) geometry for the 55 g s^{-1} deflector design

Figure 7.14: Temperature contours in an angular cutting plane for the cold (top) and hot (bottom) geometry for the 55 g s^{-1} deflector design

7.3 Steady-State Against Unsteady CFD Results

Prior to embarking into the coupling analyses, further modeling uncertainties due to the averaging between the different reference frames by using mixing planes in the steady-state CFD need to be established. Special attention is given to the rim seal flows, where turbulent mixing and blade passage pressure variations are present. As already mentioned in the literature survey, previous studies have shown that steady-state CFD analyses are limited in their ability to predict this flow interaction appropriately.

Therefore, one flow case for each geometry is run in unsteady mode. At first, a comparison for the baseline design with 55 g s^{-1} cooling mass flow rate is conducted and then for the same flow case for the deflector plate geometry. Both comparisons are carried out by using the same type of flow representation as is shown in Figs. 7.15-7.18. On the left hand side a surface LIC representation coloured by swirl fraction in three angular cutting planes is shown and on the right hand side adiabatic fluid temperature contours in a

mid-plane are represented for the steady-state (top) and unsteady (bottom) CFD results, respectively.

7.3.1 Baseline Geometry

Figures 7.15 and 7.16 show a back-to-back comparison of the steady-state against unsteady CFD results of the baseline design geometry and a cooling mass flow rate of $55\,\mathrm{g\,s^{-1}}$. From a first look at the swirl ratio near the rim, slight differences are visible between both approaches. Compared to the steady-state result, the unsteady solution shows a larger penetration of the rim seal recirculation into the cavity.

The rim seal flow in the unsteady CFD also seems to be more attached to the rotor disc rather than only to the stator. However, from the swirl ratio contours, at the highest radii of the stator rim an impingement of the main annulus can be seen in the unsteady CFD

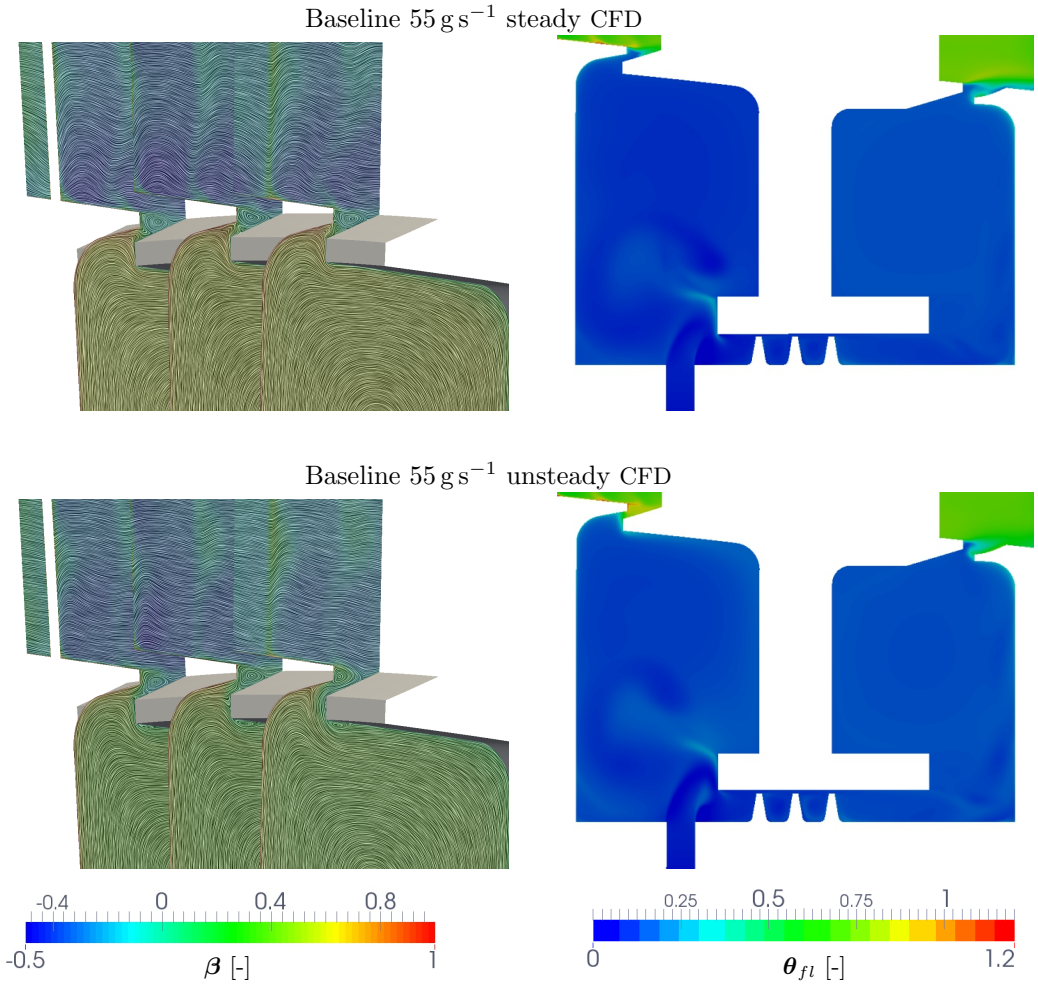

Figure 7.15: Swirl contours in three angular cutting planes in the rim region for the steady (top) and unsteady (bottom) CFD flow solutions of the $55\,\mathrm{g\,s^{-1}}$ baseline design

Figure 7.16: Fluid temperature contours in an angular cutting plane for the steady (top) and unsteady (bottom) CFD flow solutions of the $55\,\mathrm{g\,s^{-1}}$ baseline design

result, which should result in a local temperature elevation. From the fluid temperature contours similar conclusions can be drawn.

Compared to the steady-state solution more hot gas seems to penetrate into the rim. However, the temperatures inside the upstream and downstream cavities are only slightly increased. This indicates that the hot gas mainly mixes in the rim region with the cooling air and only partially penetrates into the upstream cavity. This supports the fact that the steady-state CFD does not accurately capture the rim seal mixing flow. When analysing and validating the coupling results later on using the steady-state CFD these drawbacks should be kept in mind in case of prediction discrepancies. Furthermore, these inaccuracies related to the steady-state CFD are possibly another reason for the rim seal temperature underprediction observed in previous studies (see Fig. 2.21), and steady to unsteady solution differences could be expected to be similar or even greater where more hot gas ingestion is present.

7.3.2 Deflector Plate Geometry

A similar back-to-back comparison between steady-state and unsteady CFD results for the deflector plate design with a $55\,\mathrm{g\,s^{-1}}$ cooling mass flow rate is shown in Figs. 7.17 and 7.18. From the swirl ratio contours in the rim region, one can already see slight differences in the flow solutions. The unsteady flow result predicts a larger recirculation area in the rim region, where a portion of the main annulus is entrained towards the cavity. This flow pattern is not visible in the steady-state solution and this may be related to the use of mixing planes, which do not reproduce the turbulent mixing correctly due to the averaging procedure at the rotor-stator interfaces.

Other than in the comparison between cold and hot running clearances, the hot air entering the rim does not fully penetrate the cavity. This can be concluded from the fluid temperature contours in the mid-plane. In the rim region of the unsteady result, the temperature is much higher than in the steady-state solution. However, this increase in temperature does not fully progress into the cavity. Only a slightly higher temperature level compared to the steady-state result can be observed. This again supports the theory that the turbulent mixing inside the rim region is not captured by the steady-state CFD or at least it poses an additional source of uncertainty when coupling to the FEA solver. Similar to the baseline design, this is also an explanation for the mismatch in predicting the rim temperatures correctly.

Having said that, it can be seen that not only the mesh and the use of different turbulent models represent sources of uncertainties but also the use of steady-state CFD can lead to misleading results. This is especially critical where engine life limiting component temperatures are underpredicted. Furthermore, it is essential to use the correct clearance size in order to draw the appropriate conclusions in the design phase.

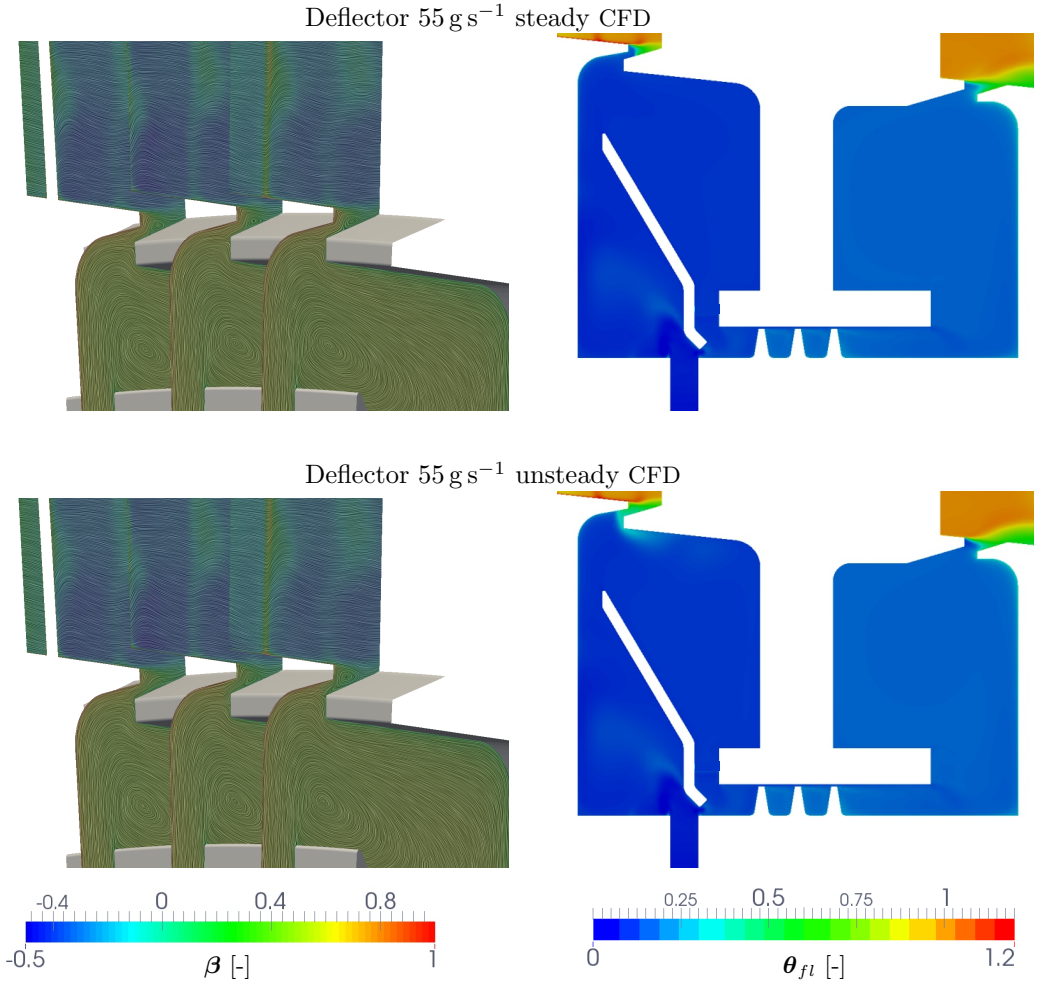

Figure 7.17: Swirl contours in three angular cutting planes in the rim region for the steady (top) and unsteady (bottom) CFD flow solutions of the 55 g s^{-1} deflector design

Figure 7.18: Fluid temperature contours in an angular cutting plane for the steady (top) and unsteady (bottom) CFD flow solutions of the 55 g s^{-1} deflector design

7.4 Aerothermal FEA to Steady-State CFD Coupling

This brings us to the final analysis part of the numerical validation: the aerothermal coupling. As explained in the methodology chapter, the steady-state CFD solution is coupled in an automated way to the FEA solver in order to calculate the conjugate heat transfer and thus predict the air and component metal temperatures. These final temperature predictions inside the fluid and the metal are then benchmarked against the experimental measurement. At first, the baseline geometry for the two coolant flow cases are validated which is followed by the validation of the deflector plate geometry. Both geometries are run at cold and hot running clearances in order to highlight the structural impact on the TSW heat transfer. Since the different flow fields and the influence of the deflector plate have already been discussed in earlier sections, the upcoming paragraphs only focus on the temperature results.

7.4.1 Baseline Geometry

The results of the aerothermal coupling for the baseline design and both flow cases with cold and hot clearances are shown in Figs. 7.19 and 7.21. On the left hand side the temperature predictions for the cold geometry are shown and on the right hand side for the hot one. As the differences are hard to distinguish from these two separate representations, a difference plot for each flow case is illustrated in Figs. 7.20 and 7.22. The difference is taken by subtracting the cold from the hot solution.

Analysing the low coolant flow case first (Fig. 7.20), it can be seen that the differences in temperature between the cold and hot geometry are minor as the temperature band is within $\pm 2\,\mathrm{K}$. However, these small temperature differences are present at the upstream rotor disc and in proximity to the interstage seal. The remaining parts are almost at an identical temperature. The temperature increase along the rotor disc can be explained with the larger amount of hot gas penetrating the cavity during hot running. As we have

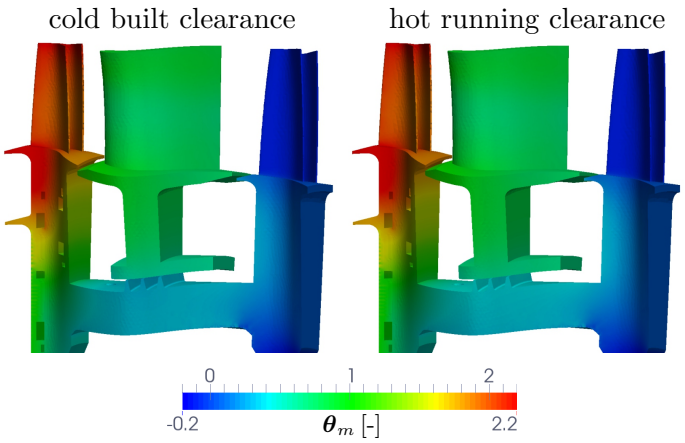

Figure 7.19: Metal temperature contours of the $30\,\mathrm{g\,s^{-1}}$ baseline test case for the cold (left) and hot (right) geometries

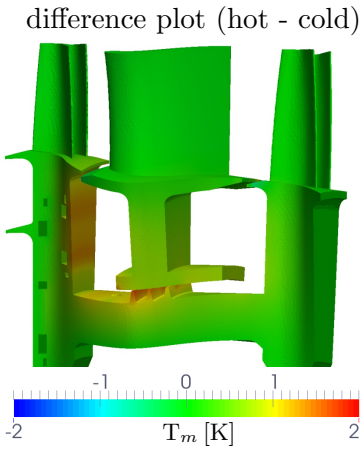

Figure 7.20: Temperature difference contours (hot - cold) of the $30\,\mathrm{g\,s^{-1}}$ baseline test case

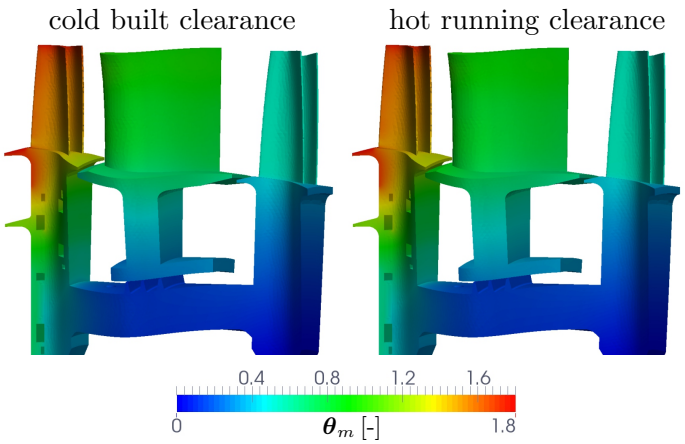

Figure 7.21: Metal temperature contours of the $55\,\mathrm{g\,s^{-1}}$ baseline test case for the cold (left) and hot (right) geometries

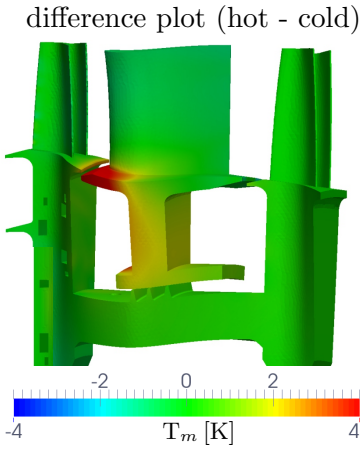

Figure 7.22: Temperature difference contours (hot - cold) of the $55\,\mathrm{g\,s^{-1}}$ baseline test case

seen in the cavity flow pattern, the hot gas mixes with the coolant in the upstream core region and is then recirculated along the rotor disc. The downstream cavity is barely affected.

The difference plot of the high coolant flow case (Fig. 7.22) shows larger discrepancies between the temperature predictions of the cold and hot geometries. First of all, the temperature differences are of higher magnitude and second, the temperatures in the upstream rim and the stator foot are strongly affected when opening the interstage seal clearance. Small differences are also detectable on the rotor side of the rim. This is in accordance with the flow field descriptions, where it was concluded that hot gas locally penetrates the cavity along the stator once the interstage seal opens. As the amount of hot gas ingestion is only minor compared to the amount of coolant, the core flow is marginally affected and so is the rotor disc temperature.

The temperature contours give already an impression how important it is to take into account the hot running clearances when calculating the conjugate heat transfer in TSW. To appropriately quantify the importance of the structural impact in predicting metal temperatures, the final coupled FEA-CFD solutions are compared to the available experimental test data.

Air temperatures are extracted from the CFD at the thermocouple locations and compared to the test data as shown in Fig. 7.23. Significantly better agreement is achieved at all thermocouple locations when the hot running geometry is used. For both baseline cases, the simulations at both cavity sides are generally improved. Only around thermo-

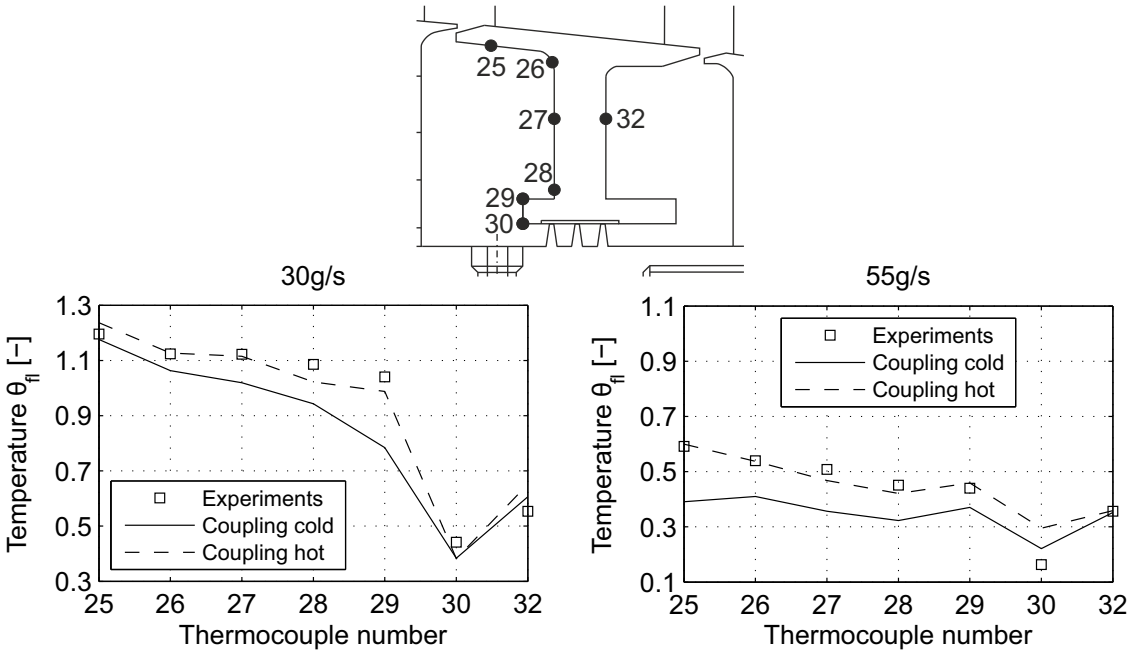

Figure 7.23: Comparison of air temperatures between CFD coupling results and experimental test data for the baseline geometry

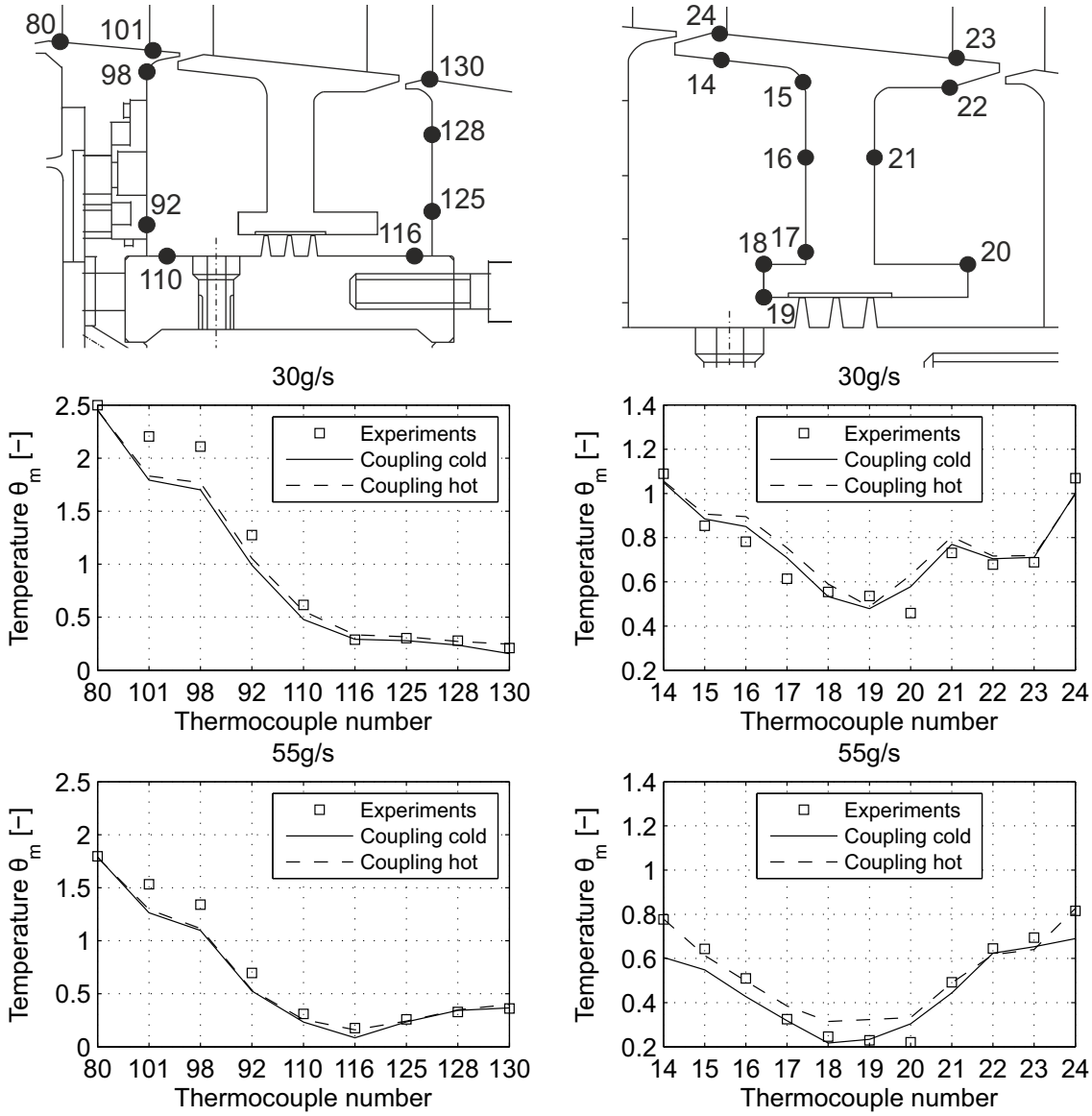

Figure 7.24: Comparison of metal temperatures between coupling results and experimental test data for the baseline geometry

couple number 30, the agreement is not necessarily enhanced, probably explained by being directly in the mixing region location where the air temperature gradients are larger.

In a final phase, the results of the 3D coupled FEA thermal baseline models are compared to the respective experimental test data. Figure 7.24 shows the metal temperature predictions of the rotor (left) and the stator (right) side by side with the metal thermocouple positions in the rig. The results for the $30\,\mathrm{g\,s^{-1}}$ case are shown on the top and the results for the $55\,\mathrm{g\,s^{-1}}$ case at the bottom, where the squares represent the experimentally measured values, the continuous line the cold geometry results and the dashed line the temperature prediction obtained from the hot geometry. Note: Actual flows from the

measured data have been used rather than the 'nominal' or 'target' cooling flow supply levels during the validation process.

Figure 2.21 showed the discrepancies observed in predicting the rim metal temperatures by several authors which led to this investigation. From the plots in Fig. 7.24, it can be postulated that the use of the hot running clearances slightly corrects the temperature underprediction at the rim. This is more evident at the stator especially as a small fraction of ingested gas mixes inside the cavity, but still is insufficient at the rotor side (positions 101 and 98) suggesting that the heat transfer coefficients downstream of the rotor blade are underestimated.

The predictions in the remaining areas are in good agreement with the experiments. The additional ingestion mixes in the cavity with the coolant for the lower mass flow rate case and the temperatures inside the downstream cavity remain similar. This is even more evident for the higher cooling flow level, as the cavity is sealed. However, the local mixing of hot gas also increases the temperature near the rim. This is in line with the gas concentration measurements shown in Fig. 4.5. Although the discrepancies in predicting the stator temperatures at lower radii are slightly increased for the hot running clearance, the predictions are still in an acceptable tolerance of $\pm 2\,\mathrm{K}$.

Generally, it can be concluded that the outcome of the coupled conjugate analyses of the baseline geometry support the findings of the stand-alone steady-state CFD results. Due to a different amount of hot gas ingestion into the cavity and a different mixing procedure, the metal temperatures are elevated when the interstage seal clearance is increased. Therefore, it is important to use the correct seal clearances for heat transfer predictions in life critical features. However, the rotor rim temperatures are still significantly underpredicted compared to the experiments, which might be caused by the limitations of the steady-state CFD solutions to accurately calculate the turbulent mixing in the rim region. The implementation of unsteady CFD into the coupling process might be able to correct these discrepancies since the mixing behaviour has been found to be noticeably different (see previous chapter).

7.4.2 Deflector Plate Geometry

As for the baseline design, the deflector geometries with cold and hot clearances at both coolant mass flow rate are analysed using the coupled conjugate heat transfer method. The metal temperature contours for both seal clearances (cold on the left and hot on the right) are represented in Figs. 7.25 and 7.27 for the respective low and high coolant flow cases. In order to highlight the key differences by running the simulation at a hot interstage clearance, two difference plots - the cold temperature predictions are subtracted from the hot - are shown in Figs. 7.26 and 7.28.

Compared to the baseline simulations, the impact of taking into account the structural deformations on the metal temperature predictions is more significant. For the $30\,\mathrm{g\,s^{-1}}$ flow case, the rim as well as the stator foot are significantly hotter when using the hot

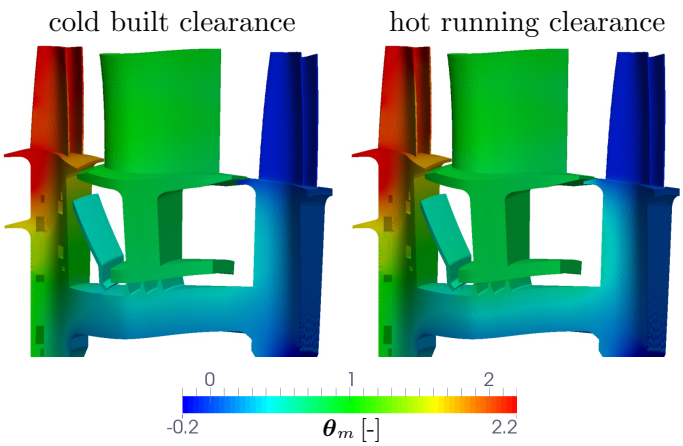

Figure 7.25: Metal temperature contours of the $30\,\mathrm{g\,s^{-1}}$ deflector test case for the cold (left) and hot (right) geometries

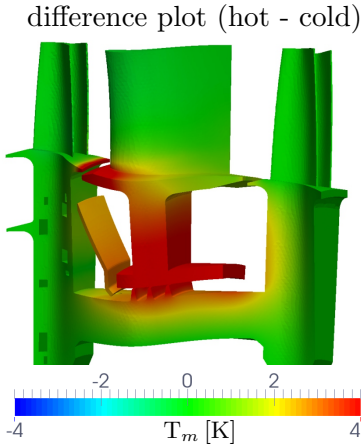

Figure 7.26: Temperature difference contours (hot - cold) of the $30\,\mathrm{g\,s^{-1}}$ deflector test case

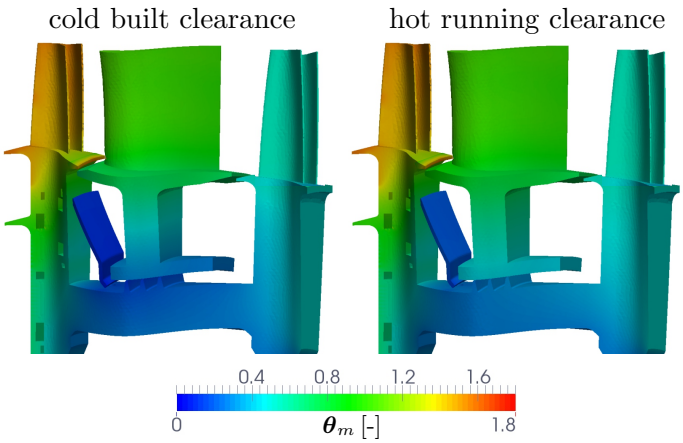

Figure 7.27: Metal temperature contours of the $55\,\mathrm{g\,s^{-1}}$ deflector test case for the cold (left) and hot (right) geometries

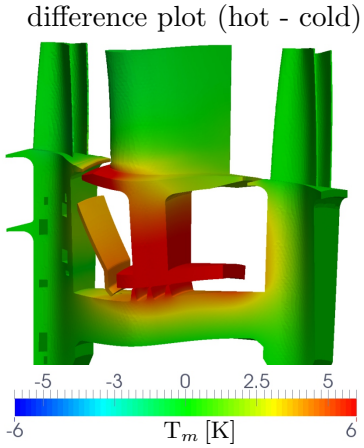

Figure 7.28: Temperature difference contours (hot - cold) of the $55\,\mathrm{g\,s^{-1}}$ deflector test case

running clearance. Furthermore, the rotor rim is hotter as well as the interstage seal fins. However, the uptream rotor disc is only marginally affected. This agrees with the conclusions from the steady-state CFD solutions of the cold and hot geometries, where a significant amount of hot gas seemed to penetrate the upstream cavity at a larger seal clearance. As this test case has not been validated before, it cannot be compared to previous studies. However, the comparison against the thermocouple measurements later in this section will give an indication whether the use of the hot running clearance improves the metal temperature predictions. But prior doing this, the $55\,\mathrm{g\,s^{-1}}$ flow case metal temperature contours are compared to each other for the cold and hot geometry. Generally, a similar trend as for the $30\,\mathrm{g\,s^{-1}}$ flow case is visible. The stator rim and the stator foot are significantly hotter for the hot geometry, whereas the upstream rotor disc is only slightly affected. The interstage seal fins are also of higher temperature. Again, these higher temperatures can be associated to the findings from the steady-state CFD, which showed a significant increase in ingestion for the hot running clearance.

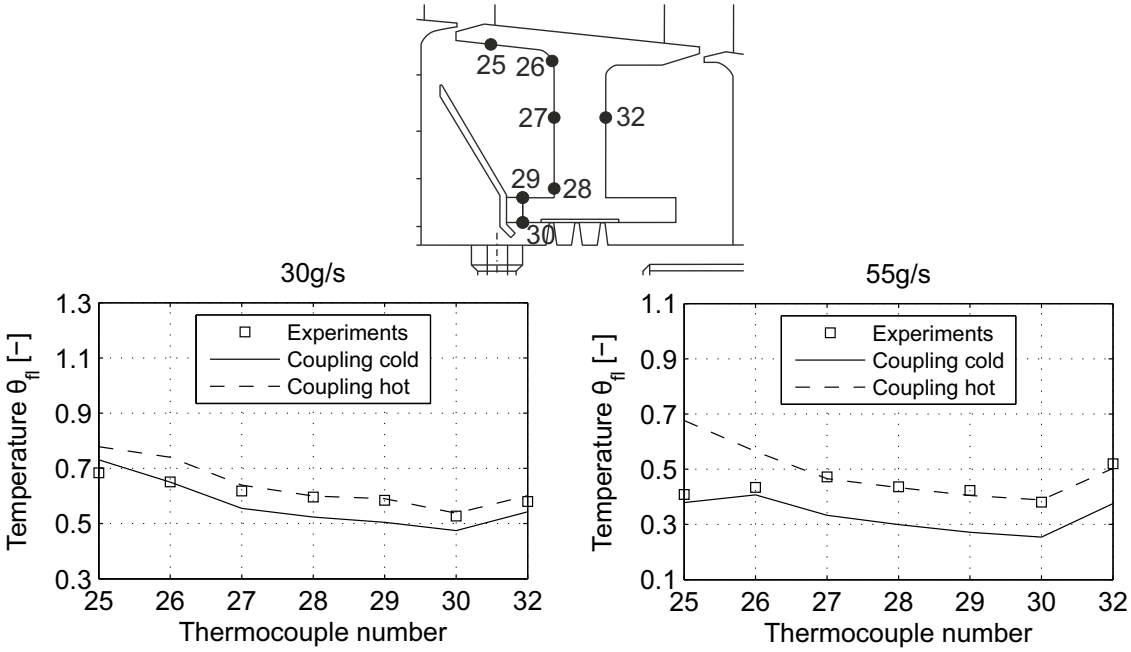

Figure 7.29: Comparison of air temperatures between CFD coupling results and experimental test data for the deflector geometry

The quantitative evaluation of the results is conducted by benchmarking the predicted metal temperature values at the thermocouple measurement points to the actually experimentally measured values. At first, the air temperatures are compared, as shown in Fig. 7.29. For the deflector cases, most of the data at the air thermocouples located at the stator foot are in better agreement when the hot interstage seal clearance is used. However, near the stator rim, air temperatures are overpredicted (positions 25 and 26). This is particularly evident on the higher mass flow rate case. Comparing this finding to the associated CFD contours of the hot running model shown in Fig. 7.13 and 7.14, the increase in temperature can be explained by the local hot gas ingestion observed, later on diluted near the stator rim. This discrepancy is likely to be caused by limitations of the steady-state CFD modeling as mentioned above.

Finally, the metal temperature predictions need to be validated against the experimental data. The results for both flow cases of the deflector plate geometry are summarised in Fig. 7.30. The comparison of the coupled results of the deflector geometry shows partly the same behaviour as described for the baseline geometry for the rotors. The data at the thermocouples is well matched in all the regions except at the rim, although the discrepancies are not as high as for the baseline geometry. The effect of blowing the coolant directly to the rim, mitigates the gradient and hence the inaccuracy is suspected to be caused by the underprediction of heat transfer at the rotor blade wake. Furthermore, as the coolant is confined in between the rotor and the deflector plate the impact of changes in seal clearance is less significant.

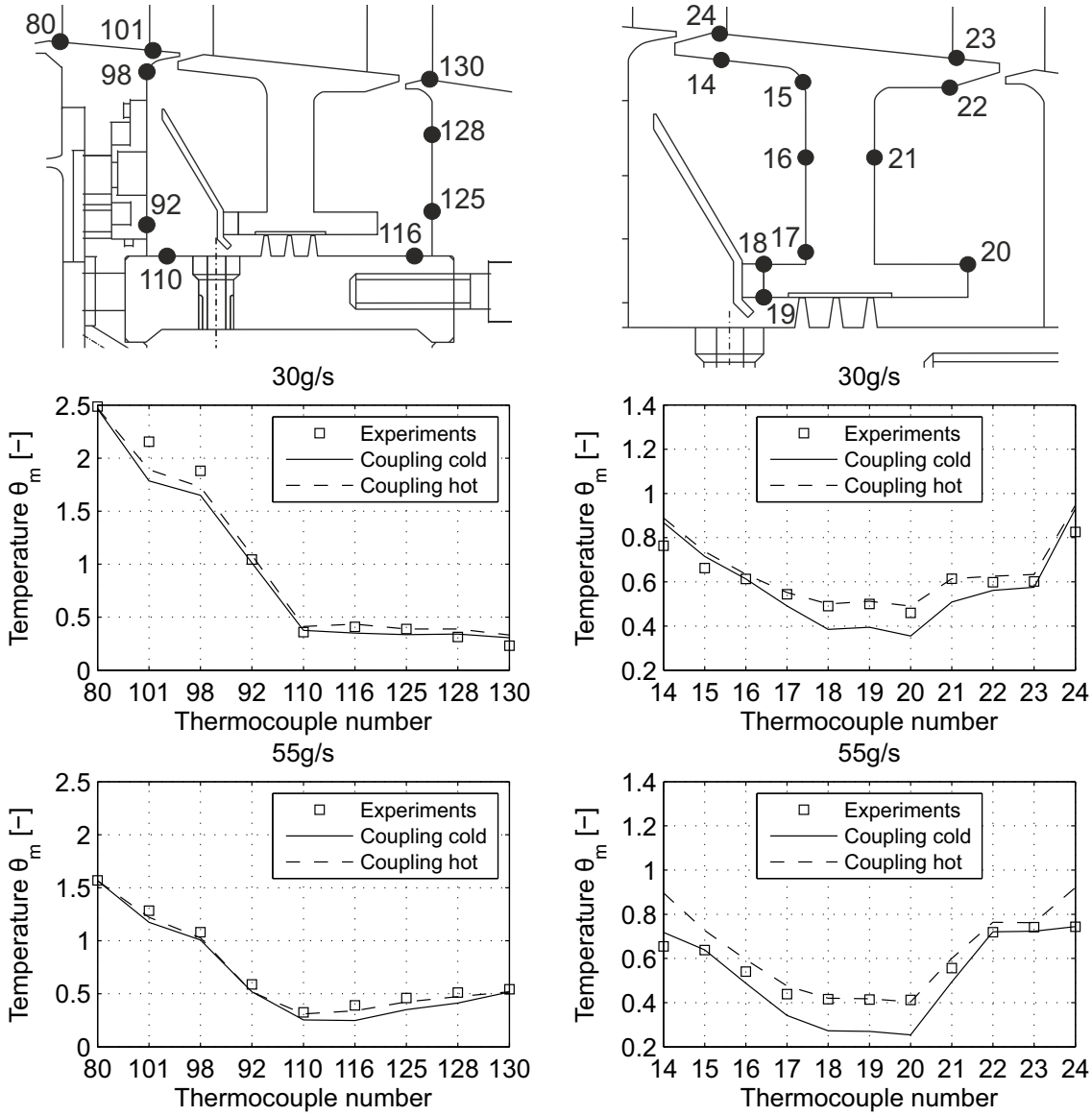

Figure 7.30: Comparison of metal temperatures between coupling results and experimental test data for the deflector geometry

The predictions of the stator foot temperatures show a slightly different behaviour. The increased clearance shifts the predicted curves towards higher temperatures. While the cold models significantly underpredict the temperatures at the stator foot, the hot running models are in very good agreement with the experiments. Only at the rim, where even the cold geometry overpredicts the measurement, the discrepancy becomes larger with larger seal clearances. This is in agreement with the air temperature measurements discussed earlier in this section. Any small amount of ingestion will be evident as the hot gas impacts directly at its surface.

For the $30\,\mathrm{g\,s^{-1}}$ case the effect is not as high as it is for the $55\,\mathrm{g\,s^{-1}}$ case. The likelihood is that the displacement sensor is reading a bigger displacement in the second rig build phase as suggested by Tab. 7.1. Thermocouples 23 and 24 are roughly at the same temperature as would be expected if the coolant is perfectly sealing the cavity and being egressed to the main stream. The predictions suggest in line with the temperature contours from the adiabatic CFD that slightly less air penetrated into the cavity.

As for the baseline geometry, from the discussion above it becomes obvious that the use of steady-state CFD reaches its limitations in predicting the rim seal flows. Although the remaining component temperature predictions are improved, the rim temperatures still cannot be matched. Therefore, capturing of the unsteadiness becomes important for improving the rotor rim metal temperatures.

7.5 Aerothermal FEA to Unsteady CFD Coupling

After having analysed all four test cases using steady-state CFD during the aerothermal coupling process, it was concluded that the rim temperatures cannot be predicted at a desired accuracy compared to the experiments. As we have seen in the back-to-back comparison of the steady against unsteady CFD, a different kind of mixing is present in the rim region when the CFD is fully time-resolved. To prove that this assumption is valid, the $55\,\mathrm{g\,s^{-1}}$ flow case of the baseline design is analysed by coupling the unsteady CFD to the FEA solver. As the procedure of this fully unsteady coupling requires around 20 times more computational power, only one test case is evaluated.

The results can be seen in Fig. 7.31, where the metal temperature contours of the steady-state (left) and unsteady (right) solutions are visualised. In order to better distinguish the differences, Fig. 7.32 shows the metal temperature contour differences obtained from a subtraction of the steady-state from the unsteady solution. The legend shows that the differences reach up to 10 K in distinct regions, especially the upstream rotor disc.

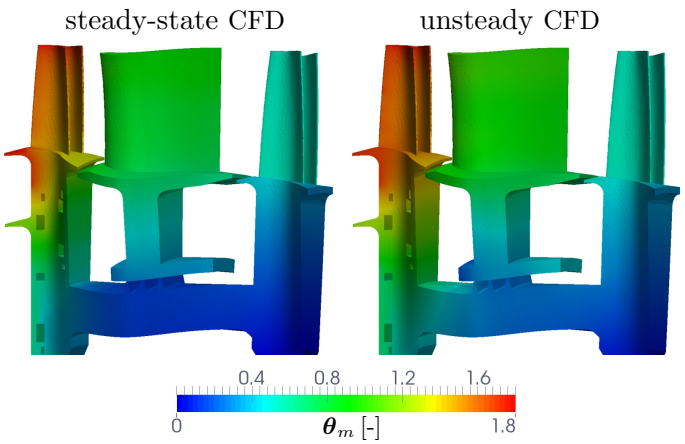

Figure 7.31: Metal temperature contours of the hot $55\,\mathrm{g\,s^{-1}}$ baseline test case for the steady (left) and unsteady (right) CFD coupling

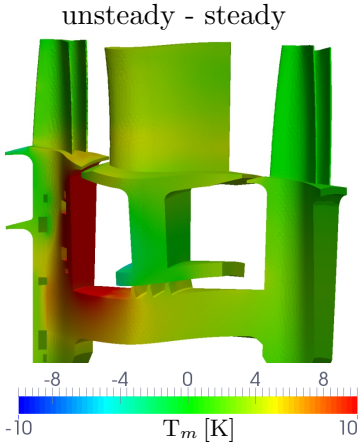

Figure 7.32: Temperature difference contours (unsteady - steady) of the hot $55\,\mathrm{g\,s^{-1}}$ baseline test case

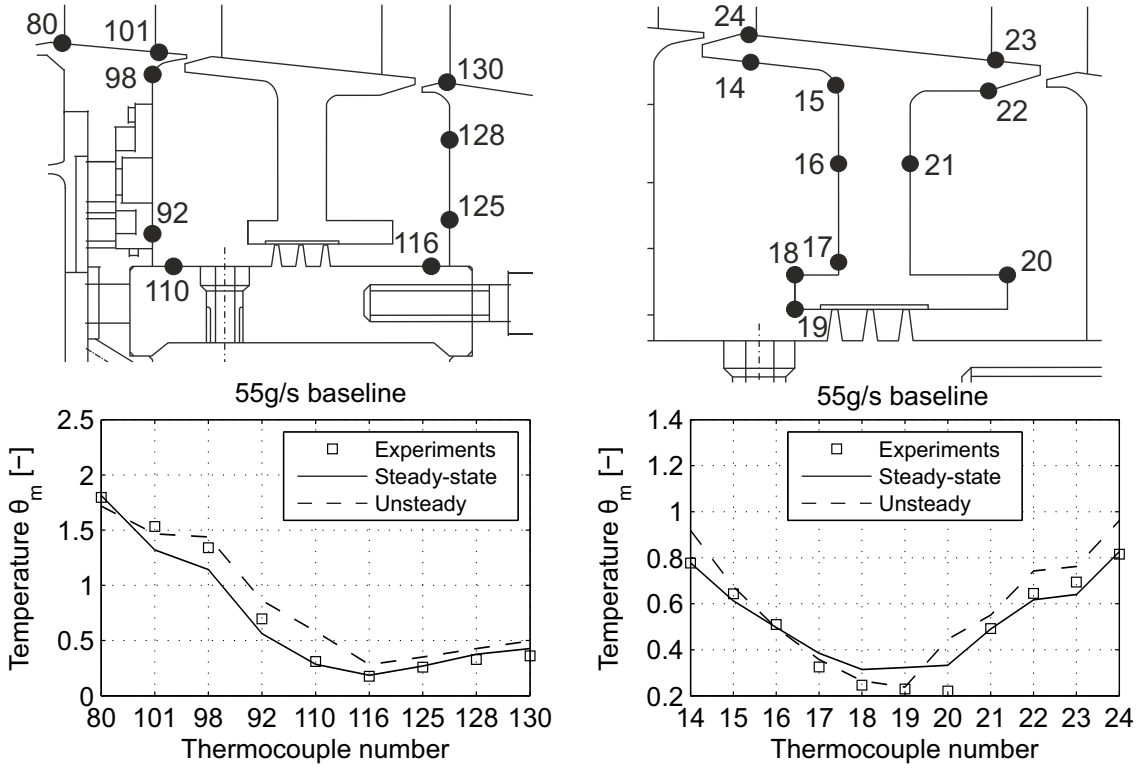

Figure 7.33: Comparison of metal temperatures between steady and unsteady coupling results against experimental test data for the $55\,\mathrm{g\,s^{-1}}$ baseline test case

From this comparison, a significant improvement can be expected for the rim seal temperature validation since the predictions using unsteady CFD are significantly higher. Such a benchmarking against the experimental test data is shown in Fig. 7.33. The rotor metal temperature comparison represented on the left hand side, supports the previous statement: the temperature predictions are now in very good agreement near the rim (position 101 and 98) when unsteady CFD solutions are coupled to the FEA code. This is due to its ability to capture the turbulent mixing more accurately, thus predicting a higher heat transfer coefficient in the rim region. However, the remaining temperature predictions are all slightly higher than in the steady-state solution, which increases the discrepancies again. Especially position 110 is significantly worse.

Along the stator wall, the impact of the unsteadiness is not as promising as it is at the rotor wall. From the temperature plot comparison on the right hand side of Fig. 7.33, it can be seen that the stator rim temperatures are now overpredicted compared to the steady-state and experimental solutions. However, thermocouple positions 18 and 19 are now in better agreement than before. Since this is a mixing region of the coolant entering the cavity, the improvement is strongly related to the different solution approach. Going further downstream to thermocouple position 20, a large discrepancy between the predictions and the measurements can be seen. The unsteadiness worsens the predictions significantly. The author cannot find a physical explanation for this mismatch. A possi-

bility is that the CFD might not be fully converged in this area although the residuals, mass flow and energy balances as well as the monitor surfaces seemed to have reached convergence. Alternatively the exact geometry of the rig may not be fully reproduced by the CFD and the FEA models of these features. As this area is a non-critical area for disc lifing purposes and the calculation of the unsteady aerothermal coupling is computationally very expensive, it was decided not to run the case again.

In summary, it can be concluded that the use of unsteady CFD improves the prediction of the rotor rim metal temperatures but still leaves some room for improvement in the remaining parts. Whether it is financially attractive to run this very expensive method to get the rim temperatures right in the design phase, is left to the aero-engine manufacture, their designer and their experience.

7.6 Summary

As a last section of this chapter, a small summary is given of the achievements. In general, FEA and CFD models of the MAGPI turbine rig configuration have been produced and run to replicate the test conditions for two geometries and at two relevant cooling flow conditions: ingestion and balanced cavity with no expected net ingestion. The flow fields were analysed in detail pointing out benefits and drawbacks of the particular geometries. Furthermore, the impact of the structural deformations on the flow field were captured as well as the effects of unsteadiness.

A fully automated FEA-CFD coupling capability was demonstrated and results from these models were compared with the available test data. The process was streamlined also to incorporate hot running geometries and evaluate the impact of structural deflections. Furthermore, it was achieved for the first time, to automatically couple a fully unsteady CFD solution to the FEA code in order to take the unsteadiness of the flow into account for conjugate heat transfer calculations. In brief:

1. Thermo-mechanical analyses with a matched set of temperatures were used. The results were compared to measurements of radial displacement and used to bound the variation in seal clearance to create representative CFD models. The predictions were in good agreement with the measurements.

2. The FEA-CFD coupling reflected those changes as a direct impact in the CFD solution. The most recent developments showed its potential as a predictive tool for seal running clearances. The methodology helped in matching the thermocouple measurements and resolving the uncertainty of the displacement sensor measurements.

3. The use of unsteady CFD incorporated in the aerothermal coupling process further reduced the uncertainties in rim temperature predictions as the turbulent mixing and thus the heat transfer was better captured in the time-resolved solution.

4. This capability may provide gas turbine engineers with the tools to optimise the internal air system as well as providing improved confidence in the analysis, particularly in relation to assessing trends and working towards less reliance on engine test data.

Finally, whilst improvements were achieved in matching the upstream rim seal thermocouples, an excellent match is achieved in areas of the turbine disc critical life limiting features, e.g. bucket groove hoop stress carrying material, discrepancies still persist in the predictions. It will be desirable to incorporate unsteadiness and higher order turbulence models for the remaining test cases in order to gain further confidence in the methodology.

8 Kriging Based Design Optimisation

In the previous chapter it was shown that the use of steady-state CFD can be a useful method to analyse the flow field inside the TSW and to draw conclusions on the disc and rim cooling. In this chapter, the steady-state CFD approach is used to optimise the shape and position of the deflector plate inside the cavity. As mentioned earlier, the initial design of the actual deflector plate was chosen more or less arbitrarily. Therefore, it is expected that there is room for considerable improvement with respect to the upstream disc cooling.

The Kriging-based optimisation is considered first. The number of evaluated designs, the simulation failures and the convergence history are presented and discussed. The converged response surfaces for the respective design variables are shown and interpreted and the final optimised design is "validated". The benefits of the optimised design are highlighted compared to the baseline design without a deflector plate and the standard initial deflector plate design. This is achieved by using stand-alone steady-state CFD in order to analyse the flow fields of the respective deflector plate designs. Furthermore, the aerothermal coupling method is applied to the three test cases (optimised DP and initial DP both with reduced cooling mass flow rate and the BL with 100 % coolant) in order to extract and compare the metal temperatures.

8.1 Optimisation Results

This section summarises the raw data of the automated optimisation process. Fig. 8.1 shows the convergence history of the Kriging-based optimisation, where the green crosses represent feasible and the red ones non-feasible solutions. A design is considered feasible when the solution stays within the limits of the constraint, i.e does not overshoot the pre-defined area mean averaged upstream disc temperature.

Overall, 98 design points are evaluated, where five mesh failures are recorded, one in the DOE and four in the optimisation process. As a reminder: mesh failures are generated geometries by the optimiser, which could not be successfully meshed. Although, at first, only non-feasible designs are found, the optimisers manage to find feasible designs for small amounts of cooling air. The optimised deflector design only needs around 35 % of the cooling air for the baseline geometry without a deflector plate. Compared to the non-optimised deflector, where earlier studies showed that $30 \mathrm{gs}^{-1}$, which is equivalent to

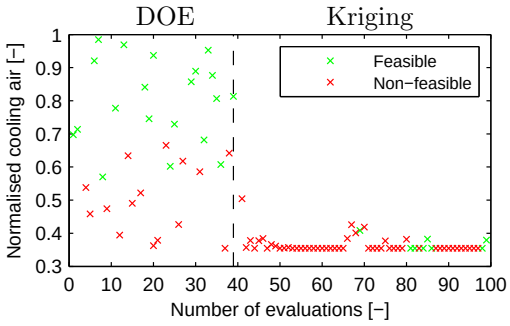

Figure 8.1: Convergence history of the Optimisation

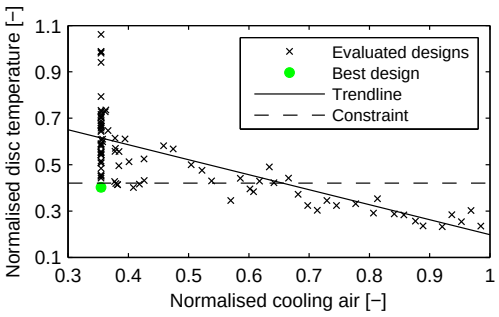

Figure 8.2: Objective function plotted against constraint

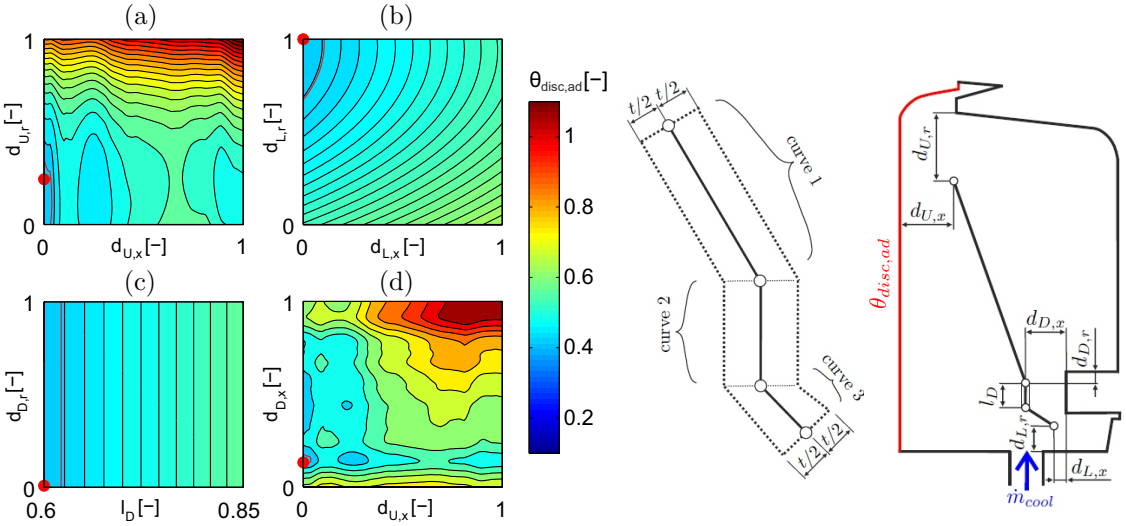

Figure 8.3: Overview of the Kriging prediction contoured by the adiabatic rotor disc temperature $\theta_{disc,ad}$

$0.6\,\dot{m}_{cool}$, achieve a similar performance to the baseline geometry (DIXON et al. (2013), POHL et al. (2015)), the optimised deflector reduces the coolant air flow rate required by another 40%. However, this last comparison should be handled with care. In Sec. 7.2.3 of this thesis, the geometry benefits were not as significant as in the studies by DIXON et al. (2013); POHL et al. (2015). Therefore, the improvements due to an optimised position and design should be even higher.

A different representation of the evaluated results is presented in Fig. 8.2, where the amount of normalised cooling air is plotted against the normalised area mean averaged adiabatic wall temperature at the disc. The optimum design is highlighted by the green filled circle whereas the dashed line represents the constraint. All points below that line are considered feasible, the others non-feasible. A linear trend is observed in this representation, which was not expected before hand. The cooling performance reduces with a reduction of coolant air, as one would expect. Interestingly, for all cooling mass flow rates above the value of around $0.66\,\dot{m}_{cool}$ (cutting point between continuous and the dashed line, which represent the trendline and the constraint respectively), all deflector designs

meet the required cooling performance of the disc. This infers that any shape and position of a deflector plate potentially reduces the amount of cooling air for the upstream disc by around 30%.

On the left hand side of Fig. 8.3, subfigures (a) – (d) show the Kriging predictions coming from the optimisation for all geometrical design parameters. The response surfaces are obtained from the optimisation process as presented above. The four different plots are coloured by the non-dimensional area mean adiabatic disc temperature $\theta_{disc,ad}$ and represent slices through the eight dimensional design space. With these plots it is possible to analyse the influence of each design parameter on the cooling performance of the disc. The optimum values for each parameter are highlighted by the red dots in each figure. As a reminder and to help to understand the outcome of the final response surfaces, the parameterisation of the deflector plate is shown on the right hand side of Fig. 8.3.

Examining the values of the optimised design, which are highlighted by the red dots, it is clearly visible that the optimiser moves the design points to the extreme values of the design space. In order to get a better understanding of the four figures the final response surfaces are interpreted one by one and the impact of the respective optimum values is discussed in the below paragraph.

Figure 8.3 (a) shows the response surface for the two design variables $d_{U,x}$ and $d_{U,r}$, i.e. the position of the upper deflector plate tip. It can be seen that the profile is *hilly* and contains several valleys (blue and turquoise contours) and mountains (red contours). The design variable $d_{U,x}$ is minimised to the lower bound of the design space, which means that the distance between the upper deflector tip and the upstream rotor disc is reduced to the defined minimum. It is very likely that this value is not the optimum value from a pure optimisation point of view but from an engineering perspective the distance cannot be further reduced. Especially with respect to axial displacements during hot running, this lower bound, i.e. the smallest possible gap size between upper deflector plate tip and upstream rotor disc, was already chosen very optimistically, meaning that almost no axial displacements are allowed in order to avoid component rubbing at the defined running conditions. For real engine conditions, this distance may already be too small. Therefore, preliminary analyses are indispensable for each running condition.

It is expected that the positioning of the upper deflector tip very close to the rotor disc, keeps the coolant in close proximity to the rotor disc and thus results in an improved cooling performance of the upstream rotor disc. However, this needs to be verified by the CFD and the FEA-CFD coupling, which is done in the next sections.

Other than the previous design variable, $d_{U,r}$ is not moved to one of its extreme boundaries but to a value of around 0.25. This position of the deflector plate may avoid the ingested hot gas entering the area enclosed by the deflector plate and the rotor disc through the upper gap and also minimises the amount of hot gas ingestion coming into contact with the rotor disc. These are just assumptions which need to be verified later.

In Fig. 8.3 (b), the interdependency between the two design variables $d_{L,x}$ and $d_{L,r}$ is visualised, i.e. the position of the lower deflector plate tip. From a first glance, it can be

seen that both values are moved to their limits of the design space and that only one large valley is present. As the two variables touch the limits of the design space, similar to the variable $d_{U,x}$, it is not certain that the optimum solution is found from an optimisation point of view. But from an engineering point of view with respect to the available meshing capabilities no more extreme design can be modeled.

The axial position of the lower deflector tip is defined by $d_{L,x}$. The optimiser reduces it to its lower bound of the design space which means that the tip is moved as close as possible towards the stator foot. This result on its own is hardly interpretable since the design variables $d_{L,r}$ and $d_{D,x}$ have an important influence on the flow characteristics.

In contrast to $d_{L,x}$, the radial position of the lower tip, which is defined by $d_{L,r}$, is maximised during the optimisation process. However, this means that the deflector tip is moved as close as possible towards the stator foot, which is a similar trend to the axial position ($d_{L,x}$). Ultimately, the optimiser tries to minimise the gap between the lower deflector tip and the stator foot.

If there were no constraints on the design space, the optimiser would possibly completely close the gap between the deflector plate and the stator foot, i.e. fully attach the deflector to the stator. By doing this, a basin of hot air would be generated in the area enclosed by the deflector plate and the stator wall. This could either result in an overheating of these components or in a partial air penetration in the area enclosed by the deflector plate and the rotor disc. Especially the latter could damage the engine. Both assumptions are only valid for the case that significant hot gas ingestion into the cavity is present for the reduced coolant mass flow rate.

Figure 8.3 (c) shows the response surface for the two design parameters l_D and $d_{D,r}$. The isolines (black) show that the design variable $d_{D,r}$, which defines the overlap of curve 2 with respect to the stator foot, only has a very marginal influence on the cooling performance. It is almost constant over its entire design space. This might be caused by the definition of the design space, which is rather small. However, the optimum value is found for a value of 0, which means that the upper point of curve 2 is at the same height as the upper edge of the stator foot.

The length of curve 2, which is defined by the design variable l_D, is minimised as well. By doing this, the lower point of curve 2 is moved radially upwards as the upper point is fixed (see previous paragraph) and thus the connection between curve 2 and curve 3 is straightened. The optimisers may try to minimise curve 2 to 0 and rather directly connect curve 1 to curve 3. However, this is not possible from a assembly point of view, as curve 2 serves to fix the deflector plate to the stator foot through perpendicular connecting bolts.

The final response surface, which needs to be discussed, is shown in Fig. 8.3 (d), where the interdependency between the two design variables $d_{U,x}$ and $d_{D,x}$ is visualised. The former was already discussed previously and the latter is the axial position of curve 2 with respect to the stator foot. For small values of $d_{D,x}$ the deflector plate is close to the stator foot and for larger values the distance increases. Similar to Fig. 8.3 (a), this response surface shows a *hilly* behaviour with a couple of valleys and mountains. The absolute

minimum is found for a value of $d_{D,x} \approx 0.15$, which means that the deflector plate needs to be at a certain distance from the stator foot for an optimum cooling of the rotor disc.

Other than in Fig. 8.3 (b), the optimisers do not try to close the gap between the deflector plate and the stator foot, which is in a way contradictory to the previous discussion. This suggests that the optimisers do not aim to fully close the gap between the lower deflector tip and the stator foot but highlight further potential in the design and positioning. However, in this current automated setup, it is not possible to further close the gap due to the limitations of the automated meshing tool, where the boundary layers would collapse.

This highlights the limitations of the applied method. A converged solution of a parameterised design has been achieved by using state of the art optimisation algorithms which are combined effectively. Not only is it very expensive to evaluate each design in a 3D steady-state CFD but also the degree of the parameterisation is limited to the capabilities of the meshing tool. As mentioned in the literature (e.g. PIRONNEAU (1984); GILES and PIERCE (2000); ROTH (2012)) the use of adjoint based optimisation techniques might improve the speed of the overall optimisation process significantly. Unfortunately, this is out of the scope of the current study and therefore is recommended as future work in this field.

Now, that the response surfaces have been analysed, the information gained is taken to model the new position and design of the deflector plate in the upstream cavity. This final design is then included in the complete two stage sector geometry to analyse the flow field and verify the benefits of the new design. The results are shown in the following section.

8.2 Validation

In this section, first steady-state adiabatic CFD analyses are carried out in order to evaluate the optimised TSW flow field with a reduced amount of cooling air and then the outcome of the optimisation, i.e. confirm or disprove the assumptions made in the previous section, is validated. Furthermore, this new flow field is compared against the flow field of the non-optimised design with the same amount of coolant. By doing this, the main advantages of the new design are highlighted together with the drawbacks and limitations in the optimisation setup.

In the second part, a back-to-back comparison of the metal temperatures of the optimised and non-optimised design with a reduced amount of cooling air as well as the baseline design with 100% coolant mass flow rate is carried out. This is done to gain even more confidence in the current methodology of the optimisation process, where standalone CFD simulations are used to improve the metal component cooling. Furthermore, the comparison highlights the main differences between the baseline design with increased coolant and both deflector designs with reduced coolant.

8.2.1 The Optimised Deflector Plate - Steady-State CFD

A comparison of the flow fields of the optimised deflector plate design (top) against the non-optimised (bottom) with respect to the position and shape based on the findings presented in the previous section can be seen in Figs. 8.4 and 8.5: the upper tip of the deflector is moved close to the rotor disc, whereas the lower parts are moved close to the stator foot. The depicted mid-plane cuts are surface LIC representations contoured by swirl fraction β (Fig. 8.4) and contours of normalised relative total fluid temperature θ_{fl} (Fig. 8.5). Both simulations are run with the reduced cooling mass flow rate of $0.35\,\dot{m}_{cool}$.

For the optimised deflector plate geometry, it can be seen that the cooling air enters the cavity swirled at disc speed ($\beta = 1$) and almost keeps its swirl constant as long as it does not impinge the deflector plate. This maintenance of swirl due to the position of the deflector close to the stator foot is beneficial for the cooling performance of the disc. Considering the non-optimised deflector, the cooling air loses all its swirl quickly after entering the cavity even before impinging the deflector.

Another interesting phenomenon can be seen at the lower tip of the deflector plate, where - for the optimised design - part of the highly swirled cooling air seems to move to the interstage seal straight away without cooling the disc. This ensures that the gap between the deflector lower tip and the rotor wall is sealed against hot gas coming from higher radii. This is not the case for the non-optimised geometry.

Examining the temperature contours inside the cavity for the optimised design, it can be seen that the cooling air enters the cavity and then partially splits up, as one could infer from the swirl ratio contours and the mass flow comparison. The disc is cooled all along the area enclosed by the deflector. It can also clearly be seen that hot gas from the main annulus ingests through the rim into the upstream cavity since the amount of cooling air does not meet the sealing requirements anymore. This results in a strong heatup of the area between the deflector and the stator foot as well as the downstream cavity. The cooling air however does seal the region between the lower tip of the deflector and the rotor wall avoiding hot gas entering the critical area between deflector and rotor disc.

A comparison of mass flow rates passing the gap between the upper deflector plate tip and the rotor disc shows a significant difference in the two designs and supports the previous assumptions: for the optimised deflector plate a mass flow rate of around $0.28\,\dot{m}_{cool}$ passes the gap whereas for the non-optimised design the mass flow rate is $0.76\,\dot{m}_{cool}$. This indicates that, for the optimised design, a portion of cooling air is used to seal the gap at the lower tip from hot gas recirculation and in the non-optimised design a significant amount of hot gas is recirculated instead.

In the non-optimised geometry, the air, which is used to cool the disc, is of higher relative total temperature than that in the optimised design. This is mainly due to two reasons: firstly, the cooling air loses all its swirl after entering the cavity, which results in an increase in relative total temperature. Secondly, the gap between the lower deflector tip and the rotor disc is not sealed, which results in hot air coming from higher radii entering

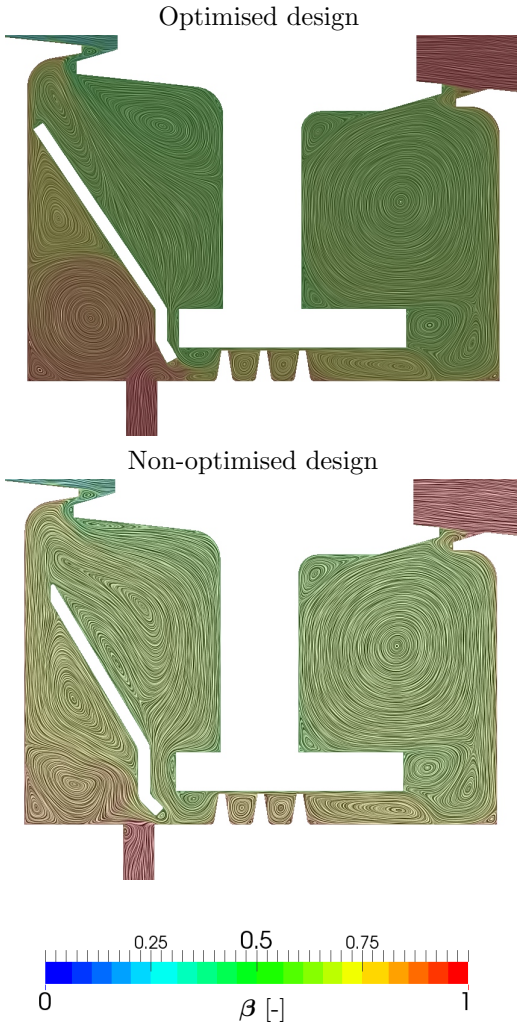

Figure 8.4: Surface LIC representation contoured by swirl fraction for the optimised (top) and non-optimised (bottom) deflector plate design with the minimised cooling mass flow rate

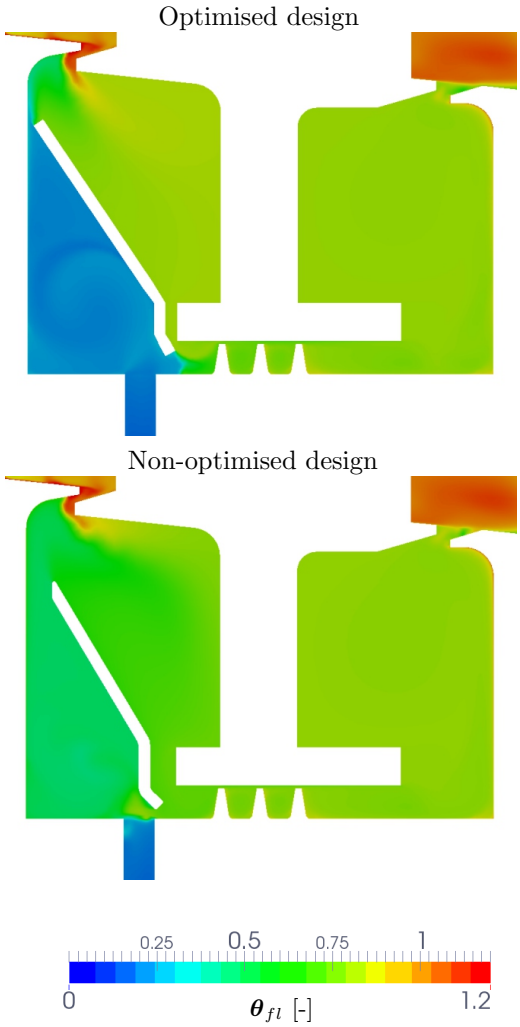

Figure 8.5: Contours of temperature for the optimised (top) and non-optimised (bottom) deflector plate design with the minimised cooling mass flow rate

the area between the deflector and the rotor disc. However, the air temperatures along the stator wall are slightly lower for the non-optimised design than those for the optimised one. While in the former the entire cooling flow penetrates the upstream cavity and mixes with the ingested flow, in the latter a fraction of the coolant is directly diverted towards the interstage seal.

Having analysed the steady-state CFD results for the optimised deflector, it can be concluded that the optimisation converged to a better deflector design, keeping the rotor disc cool while reducing the amount of cooling air. However, the fact that a large amount of hot gas enters the cavity, which inevitably results in a heatup of the metal of the stationary components, needs further investigation. Therefore, aerothermal coupled FEA-CFD analyses are carried out in order to extract the metal temperatures for the optimised design, the non-optimised deflector plate (both for a cooling air mass flow rate of $0.35\,\dot{m}_{cool}$)

and the baseline design without a deflector ($1\,\dot{m}_{cool}$). Also it is worth mentioning that the simulations are run with a constant interstage seal clearance only. The thermo-mechanical impact of the stator heating on the interstage seal clearance is not considered although this would need to be taken into consideration in any real engine design (as covered in Chap. 7).

8.2.2 Aerothermal Coupling - Metal Temperature Comparison

In Fig. 8.6, the final temperature contours for the three cases are depicted. On the left hand side the contours for the optimised deflector plate design, in the middle the non-optimised design, both at a reduced amount of coolant and on the right hand side the baseline design without deflector plate and 100% coolant. At a first glance two main comments can be made: firstly, the baseline geometry with high amount of coolant realises a better cooling of the downstream parts. Secondly, it is not obvious to determine differences in the upstream rotor disc cooling. The former can be linked to the significant hot gas ingestion, which is present for the low coolant flow cases. The latter needs further investigation.

Therefore, the temperature contours of the upstream disc are depicted in Fig. 8.7, with the same arrangement of the test cases as before. These plots clearly show that the optimised design realises a similar cooling of the upstream disc to the baseline design without deflector plate, although 65% less cooling air is used. The non-optimised design (middle plot), shows larger temperatures at lower radii of the disc. This is due to the hot gas recirculation and the instant loss in swirl of the coolant jet when entering the cavity, as was highlighted in the steady-state CFD results.

A more quantitative comparison of the differences of the cavity component temperatures can be seen in Fig. 8.8, where the circumferentially averaged normalised metal temperatures of the rotor (left) and the stator walls (right) are plotted for the three test cases from the upstream towards the downstream components. The green line stands for the optimised design, the red one for the non-optimised design and the blue line represents the baseline design without deflector plate at the cooling inlet flow levels assigned to each case.

It can be seen that the temperatures inside the upstream rotor disc (left hand side 'disc up' region) are almost the same for the optimised deflector and the baseline geometry at the assigned cooling flow levels, as required in the optimisation. The non-optimised deflector is worse, especially at the lower radii of the rotor disc. Moving further downstream inside the cavity, the rotors of the deflector designs are hotter compared to the baseline geometry. A reason for that, as mentioned before, is due to the hot gas from the main annulus ingesting into the upstream cavity, which then heats up the interstage seal as well as the downstream cavity compared to the baseline geometry with a large amount of coolant. This has also an effect on the metal temperature, however this may not be so critical to the overall turbine rotor design.

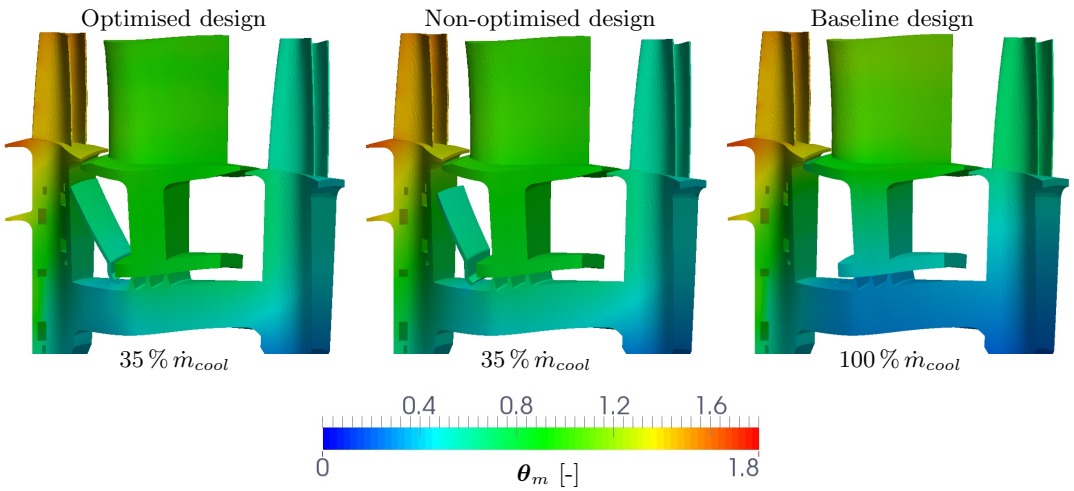

Figure 8.6: Non-dimensional metal temperature contours for the optimised, non-optimised and baseline design

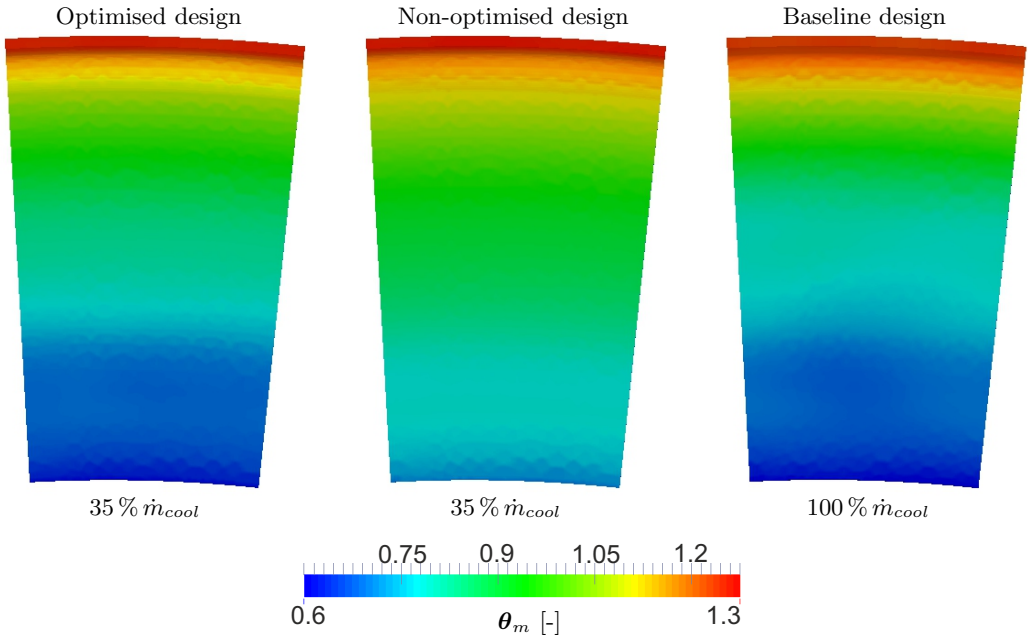

Figure 8.7: Comparison of the non-dimensional metal temperatures at the upstream rotor disc for the optimised, non-optimised and baseline design

Having a look at the temperature distribution along the rotor, it can be seen that despite the increase in temperature of the downstream rotor in the optimised design, the temperatures are still lower than in the upstream region. Hence, as a whole, from the thermal perspective, the optimised design with a reduced amount of cooling air is no worse, in the more critical upstream disc rim region than the baseline with the higher amount of cooling air. And for the same amount of coolant, the optimised deflector geometry performs better than the non-optimised deflector design.

The comparison of the stator metal temperatures shows larger differences between the deflector and the baseline designs due to the reasons mentioned above. Due to the hot gas

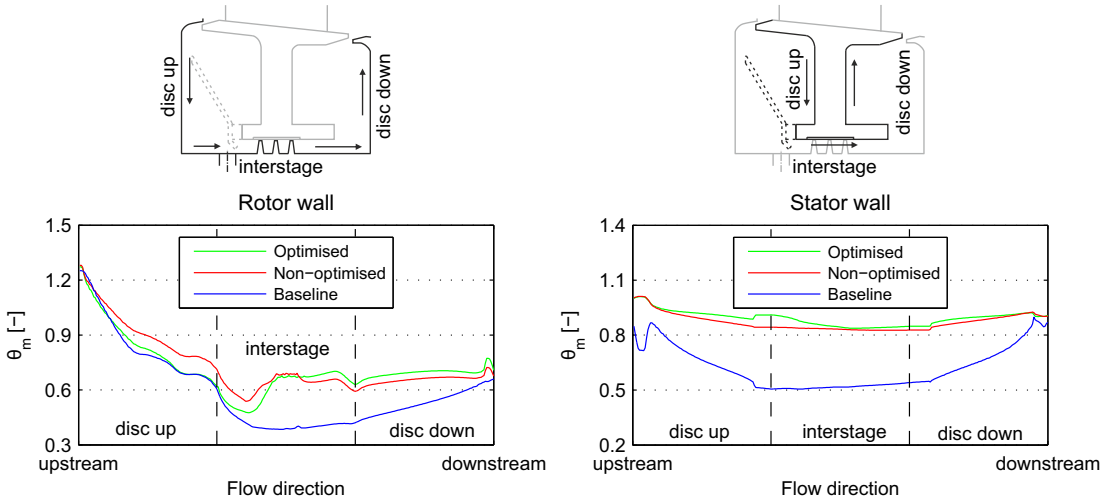

Figure 8.8: Comparison of non-dimensional metal temperatures at the rotor (left) and stator (right) wall for the three different geometries

ingestion, the stator temperatures are nearly constant over the radius and the axial position whereas in the baseline geometry the stator is cooled. Due to the higher amount of ingestion for the optimised design compared to the non-optimised deflector, the upstream stator ('disc up') is also slightly hotter for the optimised deflector design, which also agrees with the findings from the steady-state CFD in the previous section. Since the stator foot is not a life limiting part and the temperatures are still lower compared to the rotating components, it can be concluded that the insertion of the optimised deflector provides an efficient distribution of cooling air inside the cavity, keeping the critical parts cool and the non-critical parts in a reasonable temperature range.

The comparison of the optimised to the non-optimised deflector design for this rig test case shows a small improvement in disc cooling and differences in the flow physics, which might be more significant for real engine running conditions, where temperatures as well as temperature gradients are much higher. Especially, the fact that ingested hot gas is able to pass through the gap between the lower deflector tip and the rotor disc for the non-optimised design, which might cause life threatening conditions.

8.3 Summary

In this final section of the chapter, the main achievements of the optimisation process are summarised, some limitations which were observed during the study are highlighted and recommendations for future studies are given.

The first and most important point is the fact that the current parameterisation of the deflector plate in conjunction with Kriging assisted optimisation method gives a viable means of improving general cavity designs. By reducing the number of design variables to a minimum and by conducting preliminary studies such as mesh generation limits and

structural displacements, an optimised design is obtained after around 100 evaluations. Although the design evaluations within the optimisation process are conducted using stand-alone steady-state CFD, it was shown that it is a valid approach for disc cooling problems. The final verification of the optimised design compared to the reference design taking into account the conjugate effects, did not show any discrepancies.

On the downside, each evaluation takes around two days on 16 cores of a contemporary Linux cluster. Although running the jobs in parallel when possible, this still required a very long evaluation time. Therefore, this method should be used very carefully in a design process with tight deadlines when computational resources are only limited. However, just running the DOE and one or two optimisation loops can indicate to the designer where to tune the shape appropriately. Bearing in mind that in the current setup the flexibility and design space limits are either chosen from a thermo-mechanical point of view to avoid component rubbing or defined by the ability of the automated meshing tool, the final converged solution can still have potential for slight improvements.

In order to accelerate the optimisation loop, it is desirable to include adjoint techniques and mesh morphing algorithms. In general this should improve the convergence of the optimisation a lot and reduce the overall run time, since it is not necessary to explore the complete design space. As already mentioned, this approach is unfortunately out of the scope of this study and is therefore left as future work on this topic.

Although it was shown that the use of stand-alone CFD is a valid approach in an optimisation process for disc cooling, it is desirable to incorporate the coupled FEA-CFD method in the optimisation loop. This would give even more confidence in the outcome of the optimisation and also give the opportunity to carry out the optimisation in a multidisciplinary context. In addition to that, this would also avoid the CFD code exchange, which is currently necessary to switch from the optimisation setup to the aerothermal coupling method.

Furthermore, it would be possible to link thermo-mechanical analyses to the optimisation and thus further increase the confidence in the final result as each evaluation is done at the correct seal clearances. This impact has been already discussed in the previous chapter. In a final step, it would then also be possible to link a structural stress analysis to the optimisation to accurately predict the impact of the new temperatures on the component stress level, which also has a big effect on the component life.

Another important point to mention is the current boundary conditions which are taken from the test rig. In order to obtain an even more representative solution it is desirable to conduct the optimisation at real engine running conditions, i.e. much higher temperatures and temperature gradients. However, this requires additional considerations, since the relative displacements (clearances and gaps) can significantly differ from the current setup. As a consequence different bounds of the design space need to be defined.

Referring to real engine conditions and much higher temperatures, it is essential to define additional constraints in order to control the level of ingestion. In the current study, a large portion of hot gas ingests into the cavity, which is a valid point since the only

constraint is to keep the upstream disc cool. One option to control the amount of hot gas ingestion would be to define a maximum allowable temperature at the first interstage fin gap as constraint. This should definitely be done when optimising real engine seal/cavity designs.

As a last comment, it needs to be mentioned again that the use of steady-state CFD, both stand-alone or coupled to the FEA, poses a source of uncertainty in the design process, especially when hot gas ingestion is present. Ideally, one would include unsteady CFD into the optimisation process and - even better - couple it to the FEA for more confidence. But this requires even more computational resources and is not currently time-efficient from an industrial design point of view.

With respect to real engine simulations, where several transient flight cycle manoeuvres resulting from various operating conditions, must be evaluated, the fully coupled thermo-mechanical design optimisation process as outlined here, may not be fully justified except in the most critical of cases. However better preliminary interstage seal design is entirely possible using the less compute intensive approach, i.e. steady-state CFD analysis with some automated geometry optimisation, providing some care is taken to ensure cooling flow levels are maintained sufficiently above the absolute minimums, to ensure no significant hot gas ingestion.

9 Conclusion and Outlook

The thesis presents a detailed numerical investigation of TSW flows in aero-engines, with a focus on the MAGPI two-stage turbine test rig configuration. Different TSW flows adjacent to the main gas path are analysed with the objective of improving metal temperature predictions in the rim region. Therefore, the impact of both the structural deflections and the flow unsteadiness on the conjugate heat transfer is investigated in this thesis. Furthermore, the effects of improved geometry benefits on the rotor disc cooling are analysed by conducting an automated Kriging based design optimisation. The detailed conclusions of the different thorough investigations are given at the end of the respective chapters. In this final part of the thesis, the most important conclusions are summarised and an outlook for potential future work is given.

9.1 Concluding Remarks

9.1.1 Pointing Out Sources of Uncertainty

First of all some preliminary investigations were carried out, where general uncertainties arising from the numerical modeling strategies and CFD solver assumptions were pointed out and discussed (Chap. 6). Depending on the near-wall mesh resolution, significant differences in the adiabatic wall temperature predictions were detected. An increase in non-dimensional temperature of almost 0.2 was observed along most TSW walls, when applying y^+ values of 5 instead of 1. This could directly translate into increased metal temperature predictions from the coupled method and thus should always be considered as a source of error, when it is decided to use coarser meshes in order to reduce the computational effort.

Another source of uncertainty is the choice of the turbulence model in order to solve the RANS and URANS equations. From the current investigation, i.e. the preliminary studies, no final recommendation can be given as only steady-state stand-alone CFD simulations were carried out for four different turbulent models with no available experimental test data for benchmarking purposes. The evaluation of the four flow fields showed partial agreement between the models in certain areas of the cavity but also some significant discrepancies in other areas, i.e. each turbulence model predicted a slightly different flow solution. Therefore, the results were compared to the earlier findings in the literature,

providing evidence that the $k-\omega-SST$ approach is reasonably accurate. However, there is still scope for further investigations into the capabilities of other turbulence models.

The final preliminary study consisted of comparing the two available CFD codes, FLUENT and HYDRA. The former is predominantly used with the pressure-based solver for secondary air system flows at ROLLS-ROYCE and also the solver preferred for the aerothermal coupling. The latter is the ROLLS-ROYCE in-house CFD code, a density-based solver, which is preferentially used for aerodynamic main gas path investigations. Due to computational and license limitations both codes needed to be used in this project. The back-to-back comparison of the steady-state CFD results only showed minor differences between the codes in the cavity flow fields with an included deflector plate. Having said that, it can be concluded that a code exchange is a valid approach for this specific geometry and flow case. However, this approach may not be appropriate for every rotor-stator cavity geometry and flow case.

9.1.2 The MAGPI Deflector Plate and Its Benefits

As already mentioned in Sec. 1.3, the influence of a stationary deflector plate on the flow field and the heat transfer in TSWs has not been investigated in detail before, nor has the deflector plate disc cooling performance been compared to the performance of the baseline geometry studying a variety of coolant flow rates. Therefore, in this thesis, for the first time, the MAGPI deflector plate geometry is thoroughly analysed numerically from a fluid dynamical point of view, compared back-to-back against the baseline geometry and validated against the available experimental test data. For this purpose, different modeling approaches of the deflector plate geometry were proposed requiring different CFD setups and assumptions for solving the RANS and URANS equations in the CFD solver.

From the modeling point of view, it has been found that the flow field in the proximity of the bolt, which connects the deflector plate to the stator foot, is only marginally different whether the bolt is effectively modeled or not. For reasons of simplicity and with regard to the automated optimisation, it was concluded that the bolt could be neglected in subsequent investigations. However, it is not certain that this approximation is always valid. Therefore, this needs to be kept in mind when evaluating different geometries and the respective flow fields and temperatures.

As already said, considerable effort was put into the evaluation of different flow fields and the effect of the deflector plate with respect to the upstream rotor disc cooling compared to the baseline design (Sec. 7.2). For that reason two different amount of cooling air for each of the two geometries were compared to each other. In the literature it was found that including a deflector plate into the upstream cavity is beneficial for upstream rotor disc cooling and could potentially reduce the amount of coolant by almost 50 %. However, the current investigation has shown that the benefits were not as significant as it has been stated in the previous studies. These differences are basically due to the hot gas recirculation in the upstream cavity, which presumably was not captured in the earlier studies,

where different turbulence models were used (for details see the respective subsections in Sec. 7.2).

From that comparison, two major conclusions were drawn. Firstly, although the impact on the rotor disc cooling of the original MAGPI deflector plate is not as significant as expected, it does benefit the rotor disc cooling. However, there is still potential for further improvement, especially with regard to the hot gas recirculation. Secondly, the choice of the turbulence model is a source of uncertainty and can seriously affect the flow solution (over- or underestimating the disc cooling). This uncertainty can only be reduced by benchmarking the numerical results against experimental measurements.

Apart from comparing the steady-state CFD solutions to each other, in a second step, the limitations of the steady-state CFD approach for predicting the rim seal flows correctly were discussed. Therefore, steady-state CFD analyses were compared to unsteady CFD results for the two available geometries. Special interest was applied to the rim seal flow where it was shown that the steady-state solution did not capture the turbulent mixing and the potential field from the blade passage in the same manner as the time-averaged unsteady solution. This kind of investigation was already done for a different flow case of the baseline geometry where it was found that steady-state CFD underpredict the amount of ingestion. Therefore, it was interesting to find similarities in the current investigation that ingestion seems to be underpredicted using steady-state CFD, regardless of which geometry and amount of coolant is chosen. This also gave an indication of why, in previous works on CHT analyses using steady-state CFD, the rim seal temperatures were significantly underpredicted. Therefore, the current comparison supports the conclusions from earlier studies that it is crucial to account for unsteadiness when correctly predicting rim seal flows where cooling flow supply is limited and net or local hot gas ingestion is present. However, it was not clear at this point if the use of URANS is sufficient or if higher order turbulence models such as LES are necessary for this type of flow case.

9.1.3 Improving the Accuracy of TSW Component Temperature Predictions

Another of the key objectives of this thesis was to validate the coupled CHT methodology against the available experimental test data from the MAGPI project for both geometries and flow cases (Sec. 7.4). Since previous investigations on the same topic led to significant underpredictions of the rim temperatures in particular, the impact of the structural deflections during hot running was included in the current work. As the hot running clearances are effectively larger than the cold built clearances, the flow fields inside the cavities change, as do the rim seal flows. In particular the latter has a strong impact on the amount of net gas ingestion into the upstream cavity.

One particular test case of interest was the $55\,\mathrm{g\,s^{-1}}$ baseline case, which was evaluated several times in the past and compared to test data, but always lacking accuracy in matching the rotor and stator rim temperatures (see Fig. 2.21 in Sec. 2.4). The current investigation demonstrated that by taking into account the hot running clearances and

using the hFTB method with steady-state CFD as an aerothermal coupling approach, the stator rim temperatures can be matched within the desired range of accuracy ($\pm 2\,\mathrm{K}$), which has not been achieved before. The rotor temperature predictions were also slightly improved, however still not in the desired prediction tolerance. This mismatch was linked to the use of steady-state CFD and the reasons mentioned previously.

The same investigations were carried out for the three remaining test cases. One case, which has not been investigated as much as the one before in the past, is the $30\,\mathrm{g\,s^{-1}}$ baseline case. Comparing the temperature predictions of the cold and hot geometries it could be seen that the temperatures in the rim region were improved while using the hot running clearance. However, they were still lacking the desired accuracy at the rotor wall. The effect on the stator wall was only minor, since this case is in the presence of net ingestion in both cold and hot running conditions.

Since the deflector plate geometry cases were not investigated in such detail up to this point, there were no previous studies to compare the performance of the aerothermal computations against. As a general conclusion it can be said that the chosen hFTB method is also able to compute the CHT for modified TSW geometries in a stable and reliable way. Furthermore, it was found that the discrepancies in the rotor rim region were generally smaller than in the baseline cases, which was linked to the presence of the deflector plate affecting the flow pattern in the rim region.

With respect to the impact of the clearances, the rotor rim as well as the stator foot temperatures were significantly improved in the $30\,\mathrm{g\,s^{-1}}$ deflector case using the hot running clearances. However, the rotor and stator rim temperatures were still out of the desired tolerance, but interestingly under- and overpredicting the measurements, respectively. This might be related to the bad mesh interface in the rim region between the main annulus and the cavity as mentioned in the modeling part of the unstructured mesh (Sec. 5.2.3.3), which as a consequence might affect the ingestion/egress rate.

Similar findings were made for the $55\,\mathrm{g\,s^{-1}}$ deflector case. The rotor temperature predictions were in very good agreement compared to the experiments and slightly improved using the hot running clearances such that the predictions matched the measurements. On the stator side, the stator foot temperatures were significantly underpredicted using the cold geometry but spot on when applying the hot running clearances to the geometry. However, the stator rim temperatures were then significantly overpredicted, which again was explained with the bad mesh interface between the main annulus and the cavity.

Overall, as a main conclusion from the validation of the aerthermal coupling method using steady-state CFD, it can be said that the predictions of all four test cases were improved by taking into account the hot running clearances. However, the rim temperatures were only slightly better and were still not in the desired prediction tolerance.

Therefore, it was decided to modify and tune the original coupled CHT analysis - where generally steady-state CFD is linked to the transient FEA code - in such a way that the flow unsteadiness of the CFD is also accounted for. This means that a time-averaged unsteady CFD solution of the $55\,\mathrm{g\,s^{-1}}$ baseline case was coupled to the respective FEA

model (Sec. 7.5). By doing this, it was finally and for the first time, possible to predict the rotor rim temperatures in the desired range of accuracy compared to test data. This underlines the importance of taking into account unsteady effects when predicting rim flows and temperatures accurately. Furthermore, this proved that it is not mandatory to run full 3D models or LES simulations to predict the CHT in the rim region accurately. Since this method was very costly and time consuming, it was out of the scope of the current work to fully optimise the procedure with respect to run time and step size. The result of this achievement is that there is a way to capture the flow unsteadiness in CHT problems of TSWs and that this method allows accurate predictions of temperatures in distinct areas where flow unsteadiness is present such as rim seals. In addition to that, this finding helped to further advance the analysis tool-set of aeroengine manufacturers in designing TSWs.

9.1.4 Reduction of Cooling Mass Flow Rate Due to an Optimised Design

Another objective of the current research was to investigate the shape and position of the deflector plate in the upstream cavity with respect to its influence on the rotor disc cooling. This was covered in the last chapter, where a metamodel-assisted automated design optimisation was conducted on the deflector plate geometry in order to find an optimum position and shape with the target to minimise the cooling mass flow rate (and thus engine cycle efficiency) whilst still ensuring similar rotor disc cooling (Chap. 8). The very first achievement which needs to be mentioned is the fact that the chosen methodology worked and converged to a better design reducing the amount of cooling air by almost 70 % compared to the baseline design. This proved that the original shape of the deflector was not ideal and this investigation gave further insight into designing TSWs.

Thanks to the preliminary tests for mesh generation and the very careful choice of the design space boundaries for each parameter, almost no mesh failures were recorded. Furthermore, the approach of using regressing Kriging as a metamodel as well as two different optimisation search algorithms to tune the model, was a success in order to find a new design with only a few update points.

In order to save computational time and resources, it was decided to only use standalone steady-state CFD during the optimisation process. The final verification of the optimised design, where a coupled CHT methodology was used, supported the choice of this approach. Therefore, it can be concluded that in TSW and rotor-stator cavity cooling problems, steady-state CFD can be used in an optimisation instead of the more expensive CHT methods. The current method can be used to lead the designer to an improved cavity design without much manual input.

The last conclusion, which can be drawn from the optimisation study, is again the suitability of the code exchange. During the optimisation the CFD code HYDRA is used whereas for the verification of the results FLUENT is used as a benchmarked code. Although the preliminary studies showed that both codes predict similar flow fields and wall

temperatures for one particular test case, the suitability was now extended. The exchange is still valid for a new design and a completely different flow case.

9.2 Outlook for Future Work

From all the topics discussed in this thesis it is evident that there is still room for improvement in certain areas and that some of the developed methodologies are only a starting point for further thorough investigations.

In CFD the use of turbulence models always poses an important source of uncertainty. It is therefore worth investigating the performance of RSM or higher order turbulence models such as LES. At the moment, there is no turbulence model available which is able to predict ingestion correctly and accurately. Once this is developed at least one uncertainty could be omitted.

Although the code exchange is a suitable approach during this work, it should not be considered as the ideal way to conduct numerical analyses. It was shown that both codes can be used for such TSW geometries but in future it should be possible to focus only on one single code.

Among all the different topics, the most relevant and novel achievement was to couple the unsteady CFD to the FEA code, which resulted in a very good match of the rim temperatures. Unfortunately, this method is very time consuming and costly (approximately 15 - 20 times higher than the original method) and therefore needs to be further developed in order to make it suitable as a day-to-day analysis tool. Only one particular test case was run with this method. It would also be very interesting to see whether the rim temperatures of the three other test cases can be matched in a similar way.

A general recommendation from this work is that for heat transfer problems where CFD simulations are used, the hot running clearances should always be applied to the geometry. A possibility to account for this automatically is to extend the current aerothermal coupling methodology to an aerothermo-mechanical coupling approach, where after each aerothermal run, the structural deflections are calculated and applied to the geometry at the next iteration.

From an optimisation point of view, there is also plenty of improvement possible. As already mentioned, only stand-alone steady-state CFD are used in the current setup. Ideally this could be extended by the proposed aerothermo-mechanical methodology in order to further extending the number of disciplines within the optimisation process, i.e. to make it a multidisciplinary optimisation and to account for various physical phenomena, which would reduce the uncertainties during the optimisation. This method could then also be further extended taking stress analyses into account.

The main drawback of the current and proposed extended methodologies, which rely on the use of metamodels, is the computational effort which is currently infeasible for industrial applications. The use of adjoint methods, which are able to predict sensitivities

within one evaluation, is increasingly popular and may render optimisation more feasible. For future optimisation studies the use of adjoint methods should be a key priority.

Another important aspect, which arose from this work, is the verification of the suitability of the methods for real engine conditions. In the current setup, the rig conditions are used, i.e. the temperatures and temperature gradients are much lower compared to real engines. This will definitely affect the thermo-mechanical displacements and could result in different design space boundaries in order to avoid rubbing. Having said that, the basic principles of the optimisation process, as applied to this class of thermo-mechanical, fluid interaction problem, have been successfully demonstrated, with validation against good quality test data giving confidence in potential application to real engine turbine stator well cooling design. It can also be seen that each optimisation problem is always unique and requires a lot of pre-processing for a successful run. Reducing this effort further would be extremely helpful in future optimisation studies.

Bibliography

AMEDEO. Aerospace Multidisciplinary Enabling Design Optimisation. Grant reference: 316394, 2013.

T. Abe, J. Kikuchi, and H. Takeuchi. An Investigation of Turbine Disk Cooling: Experimental Investigation and Observation of Hot Gas Flow into a Wheel Space. In *13th CIMAC Congress*, number GT30, Vienna, Austria, May 1979.

D. Amirante and N. J. Hills. A Coupled Approach for Aerothermal Mechanical Modelling for Turbomachinery. In *1st International Conference on Computational Methods for Thermal Problems*, Napoli, Italy, September 2009.

D. Amirante, N. J. Hills, and C. Barnes. A Moving Mesh Algorithm for Aero-Thermo-Mechanical Modelling in Turbomachinery. *International Journal for Numerical Methods in Fluids*, 70 (9):1118–1138, 2012a.

D. Amirante, N. J. Hills, and C. Barnes. Thermo-Mechanical Finite Element Analysis/-Computational Fluid Dynamics Coupling of an Interstage Seal Cavity Using Torsional Spring Analogy. *Journal of Turbomachinery*, 134:051015–1–9, September 2012b.

D. Amirante, N. J. Hills, and C. Barnes. Use of Dynamic Meshes for Transient Metal Temperature Predictions. In *ASME Turbo Expo 2012*, number GT2012-68782, Copenhagen, Denmark, June 2012c.

A. Andreini, R. Da Soghe, and B. Facchini. Turbine Stator Well CFD Studies: Effects of Coolant Supply Geometry on Cavity Sealing Performance. In *ASME Turbo Expo 2009*, number GT2009-59186, Orlando, Florida, USA, June 2009.

J. S. Arora. *Introduction to Optimum Design.* Elsevier Academic Press, 2nd edition, 2012.

V. N. D. Autef. *Aerothermal Modelling for Axial Turbines.* PhD thesis, University of Surrey, Surrey, UK, 2007.

M. Avriel. *Nonlinear Programming: Analysis and Methods.* Dover Publishing, 2009.

L. Baert, C. Beauthier, M. Leborgne, and I. Lepot. Surrogate-Based Optimisation for a Mixed-Variable Design Space: Proof of Concept and Opportunities for Turboma-

chinery Applications. In *ASME Turbo Expo 2015, GT2015-43254*, Montréal, Canada, June 2015.

G. K. Batchelor. Note on a Class of Solutions of the Navier-Stokes Equations Representing Steady Rotationally-Symmetric Flow. *The Quaterly Journal of Mechanics and Applied Mathematics*, 4:29–41, 1951.

F. J. Bayley and J. M. Owen. The Fluid Dynamics of a Shrouded Disc System with Radial Outflow of Coolant. In *ASME Turbo Expo 1970*, number 70-GT-6, Brussels, Belgium, March 1970.

H. Bayraktar and F. S. Turalioglu. A Kriging-Based Approach for Locating a Sampling Site - in the Assessment of Air Quality. *Stochastic Environmental Research and Risk Assessment*, 19(4):301–305, 2005.

A. D. Belegundu and T. R. Chandrupatla. *Optimization Concepts and Applications in Engineering*. Cambridge University Press, 2nd edition, 2011.

F. J. Blom and P. Leyland. Analysis of Fluid-Structure Interaction on Moving Airfoils by Mean of an Improved ALE Method. In *AIAA Paper*, number 1997-1770, Snowmass Village, Colorado, USA, July 1997.

D. E. Bohn, B. Rudzinski, N. Suerken, and W. Gaertner. Experimental and Numerical Investigation of the Influence of Rotor Blades on Hot Gas Ingestion into the Upstream Cavity of an Axial Turbine Stage. In *ASME Turbo Expo 2000*, number 00-GT-284, Munich, Germany, May 2000.

D. E. Bohn, A. Decker, N. Ohlendorf, and R. Jakoby. Influence of an Axial and Radial Rim Seal Geometry on Hot Gas Ingestion into the Upstream Cavity of a 1.5-Stage Turbine. In *ASME Turbo Expo 2006*, number GT2006-90453, Barcelona, Spain, May 2006.

J. F. Bonnans, J. C. Gilbert, C. Lemaréchal, and C. Sagastizábal. *Numerical Optimization - Theoretical and Practical Aspects*. Springer Verlag, 2003.

J. Boudet, V. N. D. Autef, J. W. Chew, N. J. Hills, and O. Gentilhomme. Numerical Simulation of Rim Seal Flows in Axial Turbines. *The Aeronautical Journal*, 109:373–383, 2005.

J. Boudet, N. J. Hills, and J. W. Chew. Numerical Simulation of the Flow Interaction Between Turbine Main Annulus and Disc Cavities. In *ASME Turbo Expo 2006*, number GT2006-90307, Barcelona, Spain, May 2006.

J. F. Brady and L. Durlofsky. On Rotating Disk Flow. *Journal of Fluid Mechanics*, 175:363–394, 1987.

C. J. Brooks, A. I. J. Forrester, A. J. Keane, and S. Shahpar. Multi-Fidelity Design Optimisation of a Transonic Compressor Rotor. In *9th European Conference for Turbomachinery, Fluid Dynamics and Thermodynamics*, Istanbul, Turkey, March 2011.

C. Byun and G. P. Guruswamy. A Parallel, Multi-Block, Moving Grid Method for Aeroelastic Applications on Full Aircraft. In *AIAA Paper*, number 98-4782, Anaheim, California, USA, September 1998.

B. Cabral and L. C. Leedom. Imaging Vector Fields Using Line Integral Convolution. In *Proceedings of ACM SIGGRAPH '93*, pages 263–270, Anaheim, California, USA, August 1993.

S. Caloni and S. Shahpar. Investigation into Coupling Techniques for High Pressure Turbine Blade Tip. In *ASME Turbo Expo 2015*, number GT2015-43292, Montréal, Canada, June 2015.

C. Cao, J. W. Chew, P. R. Millington, and S. I. Hogg. Interaction of Rim Seal and Annulus Flows in an Axial Flow Turbine. *ASME Journal of Turbomachinery*, 126: 786–793, 2004.

C. Carcasci, S. Zecchi, and G. Oteri. Comparison of Blade Cooling Performance Using Alternative Fluids. In *ASME Turbo Expo 2002*, number 2002-GT-30551, Amsterdam, The Netherlands, June 2002.

J. X Chen, X. Gan, and J. M. Owen. Heat Transfer in an Air-Cooled Rotor-Stator System. In *ASME Turbo Expo 1994*, number 94-GT-55, The Hague, Netherlands, June 1994.

J. W. Chew. The Effect of Hub Radius on the Flow due to a Rotating Disc. *Journal of Turbomachinery*, 110:417–418, 1988.

J. W. Chew and C. Vaughan. Numerical Predictions for the Flow Induced by an Enclosed Rotating Disk. In *ASME Turbo Expo 1988*, number 88-GT-127, Amsterdam, Netherlands, June 1988.

J. W. Chew, S. Dadkhah, and A. B. Turner. Rim Sealing of Rotor-Stator Wheelspaces in the Absence of External Flow. *ASME Journal of Turbomachinery*, 114(2):433–438, 1992.

J. W. Chew, T. Green, and A. B. Turner. Rim Sealing of Rotor Stator Wheelspaces in the Presence of External Flow. In *ASME Turbo Expo 1994*, number 94-GT-126, The Hague, Netherlands, June 1994.

P. R. N. Childs. *Rotating Flow*. Butterworth-Heinemann, Elsevier, Paris, 2011.

W. G. Cochran. The Flow Due to a Rotating Disc. *Mathematical Proceedings of the Cambridge Philosophical Society*, 30:365–370, 1934.

D. D. Coren, N. R. Atkins, P. R. N. Childs, J. R. Turner, D. Eastwood, S. Davies, J. A. Dixon, and T. Scanlon. An Advanced Multi Configuration Turbine Stator Well Cooling Test Facility. In *ASME Turbo Expo 2010*, number GT2010-23450, Glasgow, Scotland, June 2010.

D. D. Coren, N. R. Atkins, C. A. Long, D. Eastwood, P. R. N. Childs, A. Guijarro Valencia, and J. A. Dixon. The Influence of Turbine Stator Well Coolant Flow Rate and Passage Configuration on Cooling Effectiveness. In *ASME Turbo Expo 2011*, number GT2011-46448, Vancouver, Canada, June 2011.

N. Cumpsty. *Jet Propulsion: A Simple Guide to the Aerodynamic and Thermodynamic Design and Performance of Jet Engines*. Cambridge University Press, 7th edition, 2009.

R. Da Soghe, A. Andreini, and B. Facchini. Turbine Stator Well CFD Studies: Effects of Coolant Supply Geometry on Cavity Sealing Performance. *Journal of Turbomachinery*, 133:021008–1–11, April 2011a.

R. Da Soghe, B. Facchini, L. Innocenti, and M. Micio. Analysis of Gas Turbine Rotating Cavities by One-Dimensional Model: Definition of New Disk Friction Coefficient Correlations Set. *Journal of Turbomachinery*, 133:021020–1–8, April 2011b.

J. Dacles Mariani, G. G. Zilliac, J. S. Chow, and P. Bradshaw. Numerical/Experimental Study of Wingtip Vortex in the Near Field. *AIAA Journal*, 33(9): 1561–1568, 1995.

S. Dadkhah, A. B. Turner, and J. W. Chew. Performance of Radial Clearance Rim Seals in Upstream and Downstream Rotor-Stator Wheelspaces. *ASME Journal of Turbomachinery*, 114(2):439–445, 1992.

J. W. Daily and R. E. Nece. Chamber Dimension Effects on Induced Flow and Frictional Resistance of Enclosed Rotating Disks. *ASME Journal of Basic Engineering*, 82:217–232, 1960.

J. W. Daily, W. D. Ernst, and V. V. Asbedian. Enclosed Rotating Disks with Superposed Throughflow: Mean Steady and Periodic Unsteady Characteristics of Induced Flow. Technical Report Report No. 64, Hydrodynamic Lab., Massachussets Institute of Technology, Cambridge, Massachusetts, USA, 1964.

W. A. Daniels, B. V. Johnson, D. J. Graber, and R. J. Martin. Rim Seal Experiments and Analysis for Turbine Applications. *ASME Journal of Turbomachinery*, 114(2):426–432, 1992.

C. Degand and C. Farhat. A Three-Dimensional Torsional Spring Analogy for Unstructured Dynamic Meshes. *Computers and Structures*, 80(3):305–316, 2002.

E. Divo, E. Steinthorsson, and A. J. Kassap. TFFB Coupling BEM/FVM Algorithm for Multi-Dimensional Conjugate Heat Transfer. In *Fourteenth International Conference on Boundary Element Technology*, number BETECH XIV, Orlando, Florida, USA, March 2001.

E. Divo, E. Steinthorsson, A. J. Kassap, and R. Bialecki. An Iterative BEM/FVM Protocol for Steady-State Multi-Dimensional Conjugate Heat Transfer in Compressible Flows. *Engineering Analysis with Boundary Elements*, 26(5):447–454, 2002.

J. A. Dixon. Personal communication. Technical discussion, July 2015.

J. A. Dixon, A. Guijarro Valencia, A. Bauknecht, D. Coren, and N. Atkins. Heat Transfer in Turbine Hub Cavities Adjacent to the Main Gas Path. *Journal of Turbomachinery*, 135:021025–1–14, March 2013.

J. A. Dixon, A. Guijarro Valencia, D. Coren, D. Eastwood, and C. Long. Main Annulus Gas Path Interactions - Turbine Stator Well Heat Transfer. *Journal of Turbomachinery*, 136:021010–1–16, February 2014.

M. Djaoui, A. Dyment, and R. Debuchy. Heat Transfer in a Rotor-Stator System with a Radial Inflow. *European Journal of Mechanics - B/Fluids*, 20:371–398, 2001.

L. A. Dorfman. *Hydrodynamic Resistance and the Heat Loss of Rotating Solids*. Oliver & Boyd, Edinburgh, Scotland, 1963.

O. Dubrule. Cross Validation of Kriging in Unique Neighbourhood. *Math. Geol.*, 15(6): 687–699, 1983.

F. Durst. *Grundlagen der Strömungsmechanik - Eine Einfürung in die Theorie der Strömungen von Fluiden*. Springer-Verlag, Berlin, Heidelberg, 2006.

N. Dyn, D. Levin, and S. Rippa. Numerical Procedures for Surface Fitting of Scattered Data by Radial Functions. *SIAM Journal of Scientific and Statistical Computing*, 7(2): 639–659, 1986.

D. Eastwood. *Investigaton of Rim Seal Exchange and Coolant Re-Ingestion in Rotor Stator Cavities Using Concentration Techniques*. PhD thesis, University of Sussex, Sussex, UK, 2014.

D. Eastwood, D. D. Coren, C. A. Long, N. R. Atkins, P. R. N. Childs, T. J. Scanlon, and A. Guijarro Valencia. Experimental Investigation of Turbine Stator Well Rim Seal, Re-Ingestion and Interstage Seal Flows Using Gas Concentration Techniques and Displacement Measurements. *Journal of Turbomachinery*, 134:082501–1–9,

August 2012.

C. J. Elkins and J. K. Eaton. Heat Transfer in the Rotating Disk Boundary Layer. Thermosciences Division Report TSD-103, Department of Mechanical Engineering, Stanford University, Standford, California, USA, 1997.

B. Facchini, A. Magi, and A. S. D. Greco. Conjugate Heat Transfer Simulation of a Radially Cooled Gas Turbine Vane. In *ASME Turbo Expo 2004*, number GT2004-54213, Vienna, Austria, May 2004.

C. Farhat, C. Degand, B. Koobus, and M. Lesoinne. Torsional Springs for Two-Dimensional Dynamic Unstructured Fluid Meshes. *Computer Methods in Applied Mechanics and Engineering*, 163:231–245, 1998.

J. H. Ferzinger and M. Perić. *Computational Methods for Fluid Dynamics*. Springer Verlag, 2002.

V. Fico. Personal communication. Technical discussion, November 2013.

Ansys Fluent. ANSYS FLUENT 12.0 - Theory Guide. 2009.

Ansys Fluent. ANSYS FLUENT User's Guide. 2013.

A. I. J. Forrester, A. J. Keane, and N. W. Bressloff. Design and Analysis of "Noisy" Computer Experiments. *AIAA Journal*, 44(10):2331–2339, 2006.

A. I. J. Forrester, A. Sobester, and A. J. Keane. *Engineering Design via Surrogate Modelling: A Practical Guide*. Wiley, Chichester, 2008.

M. B. Giles and N. A. Pierce. An Introduction to the Adjoint Approach to Design. *Flow, Turbulence and Combustion*, 65:393–415, 2000.

P. E. Gill, W. Murray, and M. H. Wright. *Practical Optimization*. Academic Press, 1981.

D. Goldberg. Genetic Algorithms in Search, Optimization and Machine Learning. *Addison-Wesley*, 1989.

L. F. Gonzàlez, L. Damp, J. Périaux, and K. Srinivas. High-Fidelity Multi-Criteria Aero-Structural Optimisation Using Hierarchical Parallel Evolutionary Algorithms. In *Computational Fluid Dynamics 2006 - Proceedings of the Fourth International Conference on Computational Fluid Dynamics, ICCFD 2006*, Ghent, Belgium, July 2006.

V. K. B. Gopalkrishna. *Aerothermal Analysis of Compressor Drum and Internal Fluid Flow*. PhD thesis, University of Surrey, Surrey, UK, 2014.

D. J. Graber, W. A. Daniels, and B. V. Johnson. Disk Pumping Test. Final Report AFWAL-TR-87-2050, Air Force Wright Aeronautical Laboratories, Ohio, USA, 1987.

T. Green and A. B. Turner. Ingestion into the Upstream Wheelspace of an Axial Turbine Stage. *ASME Journal of Turbomachinery*, 116(2):327–332, 1994.

A. Guijarro Valencia, J. A. Dixon, A. Guardini, D. D. Coren, and D. Eastwood. Heat Transfer in Turbine Hub Cavities Adjacent to the Main Gas Path Including FE-CFD Coupled Thermal Analysis. In *ASME Turbo Expo 2011*, number GT2011-45695, Vancouver, Canada, June 2011.

A. Guijarro Valencia, J. A. Dixon, R. Da Soghe, B. Facchini, P. E. J. Smith, J. Munoz, D. Eastwood, C. A. Long, D. Coren, and N. R. Atkins. An Investigation into Numerical Analysis Alternatives for Prediciting Re-Ingestion in Turbine Disc Rim Cavities. In *ASME Turbo Expo 2012*, number GT2012-68592, Copenhagen, Denmark, June 2012.

F. Haaser, J. Jack, and W. McGreehan. Windage Rise and Flowpath Gas Ingestion in Turbine Rim Cavities. In *ASME Turbo Expo 1987*, number 87-GT-164, Anaheim, California, USA, May 1987.

G. A. Halls. Air Cooling of Turbine Blades and Vanes. *Aircraft Engineering and Aerospace Technology*, 39(8):4–14, 1967.

S. P. Han. Superlinearly Convergent Variable Metric Algorithms for General Nonlinear Programming Problems. *Mathematical Programming*, 11:263–282, 1976.

S. P. Han. A Globally Convergent Method for Nonlinear Programming. *Journal of Optimization Theory and Applications*, 22:297–309, 1977.

Z. Han, B. Dennis, and G. Dulikrawich. Simultaneous Prediction of External Flow-Field and Temperature in Internally Cooled 3D Turbine Blade Material. In *ASME Turbo Expo 2000*, number 2000-GT-253, Munich, Germany, May 2000.

S. Harmand, J. Pellé, S. Poncet, and I. V. Shevchuk. Review of Fluid Flow and Convective Heat Transfer within Rotating Disk Cavities with Impinging Jet. *International Journal of Thermal Sciences*, 67:1–30, 2013.

J. Heidmann, D. Rigby, and A. Ameri. A Three-Dimensional Coupled External/Internal Simulation of a Film-Cooled Turbine Vane. *ASME Journal of Turbomachinery*, 124: 348–359, 2000.

J. Heidmann, A. J. Kassab, E. A. Divo, F. Rodriguez, and E. Steinthorsson. Conjugate Heat Transfer Effects on a Realistic Film-cooled Turbine Vane. In *ASME Turbo Expo 2003*, number GT2003-38533, Atlanta, Georgia, USA, June 2003.

A. Heselhaus. A Hybrid Coupling Scheme and Stability Analysis for Coupled Solid/Fluid Turbine Blade Temperature Calculations. In *ASME Turbo Expo 1998*, number 98-GT-88, Stockholm, Sweden, June 1998.

A. Heselhaus, D. T. Vogel, and H. Karain. Coupling of 3D N-S External Flow Calculations and Internal 3D Heat Conduction Calculations for Cooled Turbine Blades. In *Proceedings of Propulsion Energetics Pathel* 80^{th} *Symposium*, number AGARD CP 527, Antalya, Turkey, 1992.

N. J. Hills, J. W. Chew, and A. B. Turner. Computational and Mathematical Modelling of Turbine Rim Seal Ingestion. In *ASME Turbo Expo 2001*, number 2001-GT-204, New Orleans, Louisiana, USA, June 2001.

B. Hodkinson. Estimation of the Leakage Through a Labyrinth Gland. *Proceedings of the Institute of Mechanical Engineering*, 141:283–288, 1940.

J. H. Holland. Adaption in Natural and Artificial Systems. *University of Michigan Press*, 1975.

J. Illingworth, N. Hills, and C. J. Barnes. 3D Fluid-Solid Heat Transfer Coupling of an Aero-Engine Preswirl System. In *ASME Turbo Expo 2005*, number GT2005-68939, Reno, Nevada, USA, June 2005.

B. Irons and S. Ahmad. *NAFEMS: Introduction to Nonlinear Finite Element Analysis*. NAFEMS, 1992.

M. Itoh and I. Hasegawa. Turbulent Boundary Layer on a Rotating Disk in Infinite Quiescent Fluid. *JSME International Journal Series B: Fluids and Thermal Enginnering*, 37:449–456, 1994.

JR. J. D. Anderson. *Computational Fluid Dynamics - The Basics with Applications*. McGraw-Hill, New York, 1995.

U. Javiya. *Aerothermal Analysis of Cooling Air Delivery System for Turbine Disc*. PhD thesis, University of Surrey, Surrey, UK, 2012.

B. V. Johnson, C.-Z. Wang, and R. P. Roy. A Rim Seal Orifice Model With 2 Cds and Effects of Swirl in Seals. In *ASME Turbo Expo 2008*, number GT2008-50650, Berlin, Germany, June 2008.

D. R. Jones, M. Schonlau, and W. J. Welch. Efficient Global Optimization of Expensive Black-Box Functions. *Journal of Global Optimization*, 13:455–492, 1998.

J. C. Jouhaud, P. Sagaut, M. Montagnac, and J. Laurenceau. A Surrogate-Model Based Multidisciplinary Shape Optimization Method with Application to a 2D Subsonic Airfoil. *Computers and Fluids*, 36:520–529, 2007.

A. G. Journel and C. J. Huijbregts. *Mining Geostatistics*. Academic Press, 1978.

M. K. Karakasis, K. C. Giannakoglou, and D. G. Koubogiannis. Hierarchical, Distributed, Metamodel-Assisted Evolutionary Algorithms in Shape Optimization. *In-*

ternational Journal for Numerical Methods in Fluids, 53(3):455–469, 2007.

T. S. Kim and K. S. Cha. Comparative Analysis of the Influence of Labyrinth Seal Configuration on Leakage Behaviour. *Journal of Mechanical Science and Technology*, 23:2830–2838, 2009.

S. Kirkpatrick, C. D. Gelatt, and M. P. Vecchi. Optimisation by Simulated Annealing. *Science*, 220:671–680, 1983.

A. N. Kolmogorov. The Local Structure of Turbulence in Incompressible Viscous Fluid for Large Reynolds Numbers. *Dokl. Akad. Nauk. SSSR*, 30:299–303, 1941.

D. G. Krige. A Statistical Approach to Some Basic Mine Valuations and Allied Problems at the Witwatersrand. Master's thesis, University of Witwatersrand, South Africa, 1951.

L. Lapworth. Hydra-CFD: A Framework for Collaborative CFD Development. In *ICSEC*, Singapore, July 2004.

G. Lassaux, S. Daux, and L. Descamps. Conjugate Heat Transfer Analysis of a Tri-Dimensional Turbine Blade Internal Cavity. In *Proceedings of the* 24^{th} *International Congress of the Aeronautical Sciences ICAS*, Yokohama, Japan, 2004.

B. E. Launder and D. B. Spalding. The Numerical Computation Of Flows. *Computer Methods in Applied Mechanics and Engineering*, 3:269–289, 1974.

R. J. Lingwood. An Experimental Study of Absolute Instability of the Rotating-Disk Boundary Layer Flow. *Journal of Fluid Mechanics*, 314:373–405, 1996.

X. Liu, N. Qin, and H. Xia. Fast Dynamic Grid Deformation Based on Delaunay Graph Mapping. *Journal of Computational Physics*, 211:405–423, 2006.

E. A. H. Love. *The Mathematical Theory of Elasticity*. Cambridge University Press, 1905.

H. Lück, M. Schäfer, and H.-P. Schiffer. Simulation of Thermal Fluid-Structure Interactions in Blade-Disc Configuration of an Aircraft Turbine Model. In *ASME Turbo Expo 2014*, number GT2014-26316, Düsseldorf, Germany, June 2014a.

H. Lück, M. Schäfer, and H.-P. Schiffer. Thermal Fluid-Structure Interaction Based Optimization of Secondary Air Flows in Rotor Stator Cavities of Aircraft Turbines. In *WCCM-ECCM-ECFD 2014*, Barcelona, Spain, July 2014b.

A. Luikov, V. Akeksashenko, and A. Akeksashenko. Analytical Methods of Solution of Conjugate Problems in Convective Heat Transfer. *International Journal of Heat and Fluid Flow*, 14(8):1047–1056, 1971.

MAGPI. Main Annulus Gas Path Interaction - Specific Targeted Research Project. Proposal Contract no.: 30874, 2006.

R. Maffulli and L. He. Wall Temperature Effects on Heat Transfer Coefficient for High-Pressure Turbines. *AIAA Journal of Propulsion and Power*, 30(4):1080–1090, 2014.

G. A. Marcou, Z. S. Mouroutis, D. C. Carmpis, and M. Papadrakakis. The Orto-Semi-Torsional (OST) Spring Analogy Method for 3D Mesh Moving Boundary Problems. *Computer Methods in Applied Mechanics and Engineering*, 196(4):747–765, 2007.

G. Matheron. Principles of Geostatistics. *Economic Geology*, 58:1246–1266, 1963.

M. D. McKay, W. J. Conover, and R. J. Beckman. A Comparison of Three Methods for Selecting Values of Input Variables in the Analysis of Output from a Computer Code. *Technometrics*, 21(2):239–245, 1979.

F. R. Menter. Two-Equation Eddy-Viscosity Turbulence Models for Engineering Applications. *AIAA Journal*, 32(8):1598–1605, 1994.

F. R. Menter, M. Kuntz, and R. Langtry. *Turbulence*, chapter Heat and Mass Transfer 4, pages 625–632. Begell House Inc., 2003.

D. C. Montenay, L. Paté, and J. Duboué. Conjugate Heat Transfer Analysis of an Engine Internal Cavity. In *ASME Turbo Expo 2000*, number 2000-GT-282, Munich, Germany, May 2000.

D. Montgomery. *Design and Analysis of Experiments*. Wiley, 2000.

F. Montomoli, P. Adami, S. Gatta Della, and F. Martelli. Conjugate Heat Transfer Modeling in Film Cooled Blades. In *ASME Turbo Expo 2004*, number GT2004-53177, Vienna, Austria, May 2004.

F. Montomoli, D. Amirante, S. Shahpar, and M. Massini. Uncertainty Quantification, Rare Events and Mission Optimization: Stochastic Variations of Metal Temperature During a Transient. In *ASME Turbo Expo 2014*, number GT2014-25398, Düsseldorf, Germany, June 2014.

H. Mühlenbein, M. Schomisch, and J. Born. The Parallel Genetic Algorithm as Function Optimizer. *Parallel Computing*, 17:619–632, 1991.

A. Northrup and J. M. Owen. Heat Transfer Measurements in Rotating-Disc Systems, Part 1: The Free Disc. *International Journal of Heat and Fluid Flow*, 9(1):19–26, 1988.

F. A. Nour, S. Poncet, R. Debuchy, and G. Bois. A Combined Analytical, Experimental and Numerical Investigation of Turbulent Air Flow Behaviour in a Rotor-Stator Cavity. In *19ème Congrès Français de Mécanique*, pages 1–6, Marseille, France, August 2009.

T. S. D. O'Mahoney, N. J. Hills, J. W. Chew, and T. Scanlon. Large-Eddy Simulation of Rim Seal Ingestion. *Proceedings of the Institution of Mechanical Engineers,*

Part C - Journal of Mechanical Engineering Science, 225 (C12):2881–2891, 2011. DOI: 10.1177/0954406211409285.

Y. Okita and S. Yamawaki. Conjugate Heat Transfer Analysis of Turbine Rotor-Stator System. In *ASME Turbo Expo 2002*, number 2002-GT-30615, Amsterdam, The Netherlands, June 2002.

M. A. Oliver and R. Webster. Krigung: A Method of Interpolation for Geographical Interpolation System. *International Journal for Geographical Information Systems*, 4(3): 313–332, 1990.

S. A. Orszag, V. Yakhot, W. S. Flannery, F. Boysan, D. Choudhury, J. Maruzewski, and B. Patel. Renormalization Group Modeling and Turbulence Simulations. In *International Conference on Near-Wall Turbulent Flows*, Tempe, Arizona, USA, 1993.

J. M. Owen. *Heat and Mass Transfer in Rotating Machinery*, chapter Fluid Flow and Heat Transfer in Rotating Disk Systems, pages 81–104. Springer, 1984.

J. M. Owen. Prediction of Ingestion Through Turbine Rim Seals - Part 1: Rotationally-Induced Ingress. *ASME Journal of Turbomachinery*, 133(3):031005–1–9, 2010.

J. M. Owen and R. H. Rogers. *Flow and Heat Transfer in Rotating-Disc Systems, Vol. 1: Rotor-Stator Systems*, volume 1. Research Studies Press, Taunton, UK, 1989.

J. M. Owen, O. Pountney, and G. D. Lock. Prediction of Ingestion Through Turbine Rim Seals - Part 2: Combined Ingress. *ASME Journal of Turbomachinery*, 134(3): 031013–1–7, 2012.

T. Perelman. On Conjugated Problems of Heat Transfer. *International Journal of Heat and Fluid Flow*, 3(4):293–303, 1969.

U. P. Phadke and J. M. Owen. An Investigation of Ingress for a Simple Shrouded Rotating Disc System With a Radial Outflow of Coolant. In *ASME Turbo Expo 1980*, number 80-GT-49, New Orleans, Louisiana, USA, March 1980.

U. P. Phadke and J. M. Owen. An Investigation on Ingress for an 'Air Cooled' Shrouded Rotating Disk System with Radial Clearance Seals. *ASME journal of Engineering, Gas Turbines & Power*, 105:178–183, 1983.

U. P. Phadke and J. M. Owen. Aerodynamic Aspects of the Sealing of Gas Turbine Rotor-Stator Systems - Part 1: The Behaviour of Simple Shrouded Rotating Disk Systems in Quiescent Environment. *International Journal of Heat and Fluid Flow*, 9:98–105, 1988a.

U. P. Phadke and J. M. Owen. Aerodynamic Aspects of the Sealing of Gas Turbine Rotor-Stator Systems - Part 2: The Behaviour of Simple Seals in Quasi-Axisymmetric External Flow. *International Journal of Heat and Fluid Flow*, 9:106–112, 1988b.

U. P. Phadke and J. M. Owen. Aerodynamic Aspects of the Sealing of Gas Turbine Rotor-Stator Systems - Part 3: The Effect of Non-Axisymmetric External Flow on Sealing Performance. *International Journal of Heat and Fluid Flow*, 9:113–117, 1988c.

O. Pironneau. *Optimal Shape Design for Elliptical Systems*. Springer Verlag, 1984.

T. Poggio and F. Girosi. Regularization Algorithms for Learning that are Equivalent to Multilayer Networks. *Science*, 247:978–982, 1990.

J. Pohl, V. Fico, and J. A. Dixon. Turbine Stator Well Cooling - Improved Geometry Benefits. In *ASME Turbo Expo 2015, GT2015-42658*, Montréal, Canada, June 2015.

A. Polynkin, V. Toropov, and S. Shahpar. Multidisciplinary Optimization of Turbomachinery Based on Meta-Model Built bt Genetic Programming. In *AIAA Paper 2010-9397*, Fort Worth, Texas, USA, September 2010.

S. Poncet, M.-P. Chauve, and P. Le Gal. Turbulent Rotating Disk Flow with Inward Throughflow. *Journal of Fluid Mechanics*, 522:253–1–14, 2005a.

S. Poncet, M.-P. Chauve, and R. Schiestel. Batchelor Versus Stewartson Flow Structures in a Rotor-Stator Cavity with Throughflow. *Physics of Fluids*, 17:075110–1–15, 2005b.

S. B. Pope. *Turbulent Flows*. Cambridge University Press, 2000.

M. J. D. Powell. Variable Metric Methods for Constrained Optimization. In A. Bachem, B. Korte, and M. Grätschel, editors, *Mathematical Programming: The State of the Art*, pages 288–311. Springer, Berlin, Heidelberg, 1983.

K. Price and N. Storn. Differential Evolution. *Dr. Dobb's Journal*, pages 18–24, April 1997.

A. M. Raimundo, A. R. Figueiredo, and L. A. Oliveira. Heat Transfer in a Rotor-Stator System with Three Dimensional Non Axisymmetric Flow Conditions. *Experimental Thermal and Fluid Science*, 27:47–58, 2002.

A. Randriamampianina, L. Elena, J. P. Fontaine, and R. Schiestel. Numerical Predicition of Laminar, Transitional and Turbulent Flows in Shrouded Rotor-Stator Systems. *Physics of Fluids*, 9(6):1696–1713, 1997.

S. S. Rao. *Engineering Optimization: Theory and Practice*. John Wiley & Sons, 4th edition, 2009.

I. Rechenberg. Evolutionsstrategie - Optimierung technischer Systeme nach Prinzipien der biologischen Evolution. *Fommann-Holzboog*, 1973.

J. Reuther, A. Jameson, J. Farmer, L. Martinelli, and D. Saunders. Aerodynamic Shape Optimization of Complex Aircraft Configurations via an Adjoint Formulation. In *AIAA Paper*, number 96-0094, San Diego, California, USA, January 1996.

O. Reynolds. On the Dynamical Theory of Incompressible Viscous Flows and the Determination of the Criterion. *Philosophical Transactions of the Royal Society of London*, 186:121–161, 1894.

W. C. Reynolds. Fundamentals of Turbulence for Turbulence Modeling and Simulation. Agard Report No. 755, Von Karman Institute, 1987.

A. F. P. Ribeiro, A. M. Awruch, and H. M. Gomes. An Airfoil Optimization Technique for Wind Turbines. *Applied Mathematical Modelling*, 36(10):4898–4907, 2012.

L. F. Richardson. *Weather Prediction by Numerical Process*. Cambridge University Press, 1922.

Rolls-Royce plc. SC03 Manual - The SC03 User's Guide. 1999.

Rolls-Royce plc. The HYDRA User's Guide. 2009.

Rolls-Royce plc. 2050 Environmental Targets. Technical report, Rolls-Royce plc., 2013. www.rolls-royce.com.

T. J. Ross. *Fuzzy Logic with Engineering Applications*. McGraw Hill, New York, 1995.

R. Roth. *Multilevel Optimization of Turbulent Flows by Discrete Adjoint Techniques*. PhD thesis, Technische Universität Darmstadt, Darmstadt, Germany, 2012.

R. P. Roy, D. W. Zhou, S. Ganesan, C. Z. Wang, and R. E. Paolillo. The Flow Field and Main Gas Ingestion in a Rotor-Stator Cavity. In *ASME Turbo Expo 2007*, number GT2007-27671, Montréal, Canada, May 2007.

C. M. Sangan, O. J. Pountney, K. Zhou, J. M. Owen, M. Wilson, and G. D. Lock. Experimental Measurements of Ingestion through Turbine Rim Seals - Part II: Rotationally Induced Drag. *ASME Journal of Turbomachinery*, 135(2):021013–1–9, 2012a.

C. M. Sangan, O. J. Pountney, K. Zhou, M. Wilson, J. M. Owen, and G. D. Lock. Experimental Measurements of Ingestion through Turbine Rim Seals - Part I: Externally Induced Ingress. *ASME Journal of Turbomachinery*, 135(2):021012–1–10, 2012b.

C. M. Sangan, O. J. Pountney, J. A. Scobie, M. Wilson, J. M. Owen, and G. D. Lock. Experimental Measurements of Ingestion through Turbine Rim Seals - Part III: Single and Double Seals. *ASME Journal of Turbomachinery*, 135(5):051011–1–11, 2013.

C. M. Sangan, J. A. Scobie, J. M. Owen, G. D. Lock, K. M. Tham, and V. P. Laurello. Performance of a Finned Turbine Rim Seal. In *ASME Turbo Expo 2014*, number GT2014-25626, Düsseldorf, Germany, June 2014.

D. Sasaki and S. Obayashi. Efficient Search for Trade-Offs by Adaptive Range Multi-Objective Genetic Algorithms. *Journal of Aerospace Computing, Information and Communication*, 2:44–64, 2005.

M. J. Sasena. *Flexibilty and Efficiency Enhancements for Constrained Global Design Optimization with Kriging Approximations*. PhD thesis, University of Michigan, Detroit, Michigan, USA, 2002.

T. Scanlon and J. Wilkes. A Simple Method for Estimating Ingestion of Annulus Gas into a Turbine Rotor Stator Cavity in the Presence of External Pressure Variations. In *ASME Turbo Expo 2004*, number GT2004-53097, Vienna, Austria, June 2004.

R. C. Schlaps, S. Shahpar, and V. Gümmer. Automatic Three-Dimensional Optimisation of a Modern Tandem Compressor Vane. In *ASME Turbo Expo 2014, GT2014-26762*, Düsseldorf, Germany, June 2014.

H. Schlichting and K. Gersten. *Grenzschicht-Theorie*. Springer Verlag, Berlin, Heidelberg, 10th edition, 2006.

S. Shahpar. SOFT: A New Design And Optimisation Tool for Turbomachinery. In K. Ginnakoglou et al., editor, *CIMNE 2002*, Athens, Greece, 2002.

S. Shahpar. SOPHY: An Integrated CFD Based Automatic Design Optimisation System. Report No. ISABE-2005-1086, 2005.

S. Shahpar and L. Lapworth. PADRAM: Parametric Design and Rapid Meshing System for Turbomachinery Optimisation. In *ASME Turbo Expo 2003, collocated with 2003 International Joint Power Generation Conference*, number GT2003-38698, Atlanta, Georgia, USA, June 2003.

S. Shahpar, A. Polynkin, and V. Toropov. Large Scale Optimization of Transonic Axial Compressor Rotor Blades. In *AIAA Paper 2008-2056*, Schaumburg, Illinois, USA, April 2008.

I. V. Shevchuk. *Convective Heat and Mass Transfer in Rotating Disk Systems*. Springer Verlag, Berlin, Heidelberg, 2009.

T.-H. Shih, W. W. Liou, A. Shabbir, Z. Yang, and J. Zhu. A New k-ϵ Eddy-Viscosity Model for High Reynolds Number Turbulent Flows - Model Development and Validation. *Computers Fluids*, 24(3):227–238, 1995.

P. E. J. Smith, J. Mugglestone, K. M. Tham, D. D. Coren, and C. A. Long. Conjugate Heat Transfer CFD Analysis in Turbine Disc Cavities. In *ASME Turbo Expo 2012*, number GT2012-69597, Copenhagen, Denmark, June 2012.

P. R. Spalart and S. R. Allmaras. A One Equation Turbulence Model For Aerodynamic Flows. In *30th Aerospace Sciences Meeting & Exhibit AIAA*, number AIAA-92-0439, Reno, Nevada, USA, January 1992.

F. W. Staub. Rotor Cavity Flow and Heat Transfer with Inlet Swirl and Radial Outflow of Cooling Air. In *ASME Turbo Expo 1992*, number 92-GT-378, Cologne, Germany, June 1992.

M. Stein. Large Sample Properties of Simulations Using Latin Hypercube Sampling. *Technometrics*, 29(2):143–151, 1987.

K. Stewartson. On the Flow between Two Rotating Coaxial Disks. *Proceedings of the Cambridge Philosophical Society*, 49:333–341, 1953.

Z. Sun, J. W. Chew, N. J. Hills, K. N. Volkov, and C. Barnes. Efficient Finite Element Analysis/Computational Fluid Dynamics Thermal Coupling for Engineering Applications. *Journal of Turbomachinery*, 132:031016–1–9, July 2010.

Z. Sun, J. W. Chew, N. J. Hills, C. J. Barnes, and A. Guijarro Valencia. 3D Coupled Fluid-Solid Thermal Simulation of a Turbine Disc Through a Transient Cycle. In *ASME Turbo Expo 2012*, number GT2012-68430, Copenhagen, Denmark, June 2012.

T. von Karman. Über Laminare und Turbulente Reibung. *Zeitschrift für Angewandte Mathematik und Mechanik (ZAMM) - Journal of Applied Mathematics and Mechanics*, 1:233–252, 1921.

T. Takahashi, K. Watanabe, and T. Sakai. Conjugate Heat Transfer Analysis of a Rotor Blade with Rib-Roughened Internal Cooling Passages. In *ASME Turbo Expo 2005*, number GT2005-68227, Reno, Nevada, USA, June 2005.

C. L. Tien and D. T. Campbell. Heat and Mass Transfer from Rotating Cones. *Journal of Fluid Mechanics*, 17:105–112, 1963.

J. A. Verdicchio. *The Validation and Coupling of Computational Fluid Dynamics and Finite Element Codes for Solving Industrial Problems*. PhD thesis, University of Sussex, Sussex, UK, 2001.

T. Verstraete. *Multidisciplinary Turbomachinery Component Optimization Considering Performance, Stress, and Internal Heat Transfer*. PhD thesis, Universiteit Gent, Gent, Belgium, 2008.

T. Verstraete and R. Van Den Braembussche. A Novel Method for the Computation of Conjugate Heat Transfer with Coupled Solvers. In *International Symposium on Heat Transfer in Gas Turbine Systems*, Antalya, Turkey, August 2009.

T. Verstraete, F. Coletti, J. Bulle, T. Vanderwielen, and T. Arts. Optimization of a U-Bend for Minimal Pressure Loss in Internal Cooling Channels - Part I: Numerical Method. *Journal of Turbomachinery*, 135:051015–1–10, September 2013.

E. J. Whitney, M. Sefrioui, K. Srinivas, and J. Périaux. Advances in Hierarchical, Parallel Evolutionary Algorithms for Aerodynamic Shape Optimization. *Japan Society of Mechanical Engineers (JSME) International Journal*, 45(1):23–28, 2002.

D. C. Wilcox. *Turbulence Modeling for CFD*. DCW Industries, 1998.

R. B. Wilson. *A Simplicial Algorithm for Concave Programming*. PhD thesis, Harvard University, Harvard, Massachusetts, USA, 1963.

S. Wittig, U. Schelling, S. Kim, and K. Jacobsen. Numerical Predictions and Measurements of Discharge Coefficients in Labyrinth Seals. In *ASME Turbo Expo 1987*, number 87-GT-188, Miami Beach, Florida, USA, October 1987.

V. Yakhot and S. A. Orszag. Renormalization Group Analysis of Turbulence: I. Basic Theory. *Journal of Scientific Computing*, 1(1):1–51, 1986.

T. Yamane and Y. Tanaka. A Method for Conjugate Heat Transfer with Unsteady RANS Simulation. In *ASME Turbo Expo 2014*, number GT2014-25582, Düsseldorf, Germany, June 2014.

C. Young, G. D. Snowsill, P. W. Ferra, and C. P. Gravett. Turbine Apparatus. Patent number: US8186938, May 2012. PatBase number: 41140158.

Z. X. Yuan, N. Saniei, and X. T. Yan. Turbulent Heat Transfer on the Stationary Disc in a Rotor Stator System. *Journal of Heat and Mass Transfer*, 46:2207–2218, 2003.

D. W. Zhou, R. P. Roy, C. Z. Wang, and J. A. Glahn. Main Gas Ingestion in a Turbine Stage for Three Rim Cavity Configurations. In *ASME Turbo Expo 2009*, number GT2009-59851, Orlando, Florida, USA, June 2009.

D. W. Zhou, S. Wood, and J. M. Owen. Statistical and Theoretical Models of Ingestion through Turbine Rim Seals. In *ASME Turbo Expo 2011*, number GT2011-45139, Vancouver, Canada, June 2011.

K. Zhou, M. Wilson, J. M. Owen, and G. D. Lock. Computation of Ingestion through Gas Turbine Rim Seals. *Proceedings of the Institution of Mechanical Engineers, Part G: Journal of Aerospace Engineering*, 227(7):1101–1113, 2013.

H. Zimmermann and K. H. Wolff. Air System Correlations Part 1: Labyrinth Seals. In *ASME Turbo Expo 1998*, number 98-GT-206, Stockholm, Sweden, June 1998.

N. Zuckermann and N. Liord. Impingement Heat Transfer: Correlations and Numerical Modeling. *Journal of Heat Transfer*, 127:544–552, 2005.